Andreas Eitzlmayr, Dipl.-Ing.

Modeling of High-Viscous Flow and Mixing in Co-Rotating Twin-Screw Extruders

DOCTORAL THESIS

to achieve the university degree of

Doktor der technischen Wissenschaften

submitted to

Graz University of Technology

Supervisor

Univ.-Prof. Dipl.-Ing. Dr.techn. Johannes Khinast

Institute of Process and Particle Engineering

Research Center Pharmaceutical Engineering GmbH

Graz, March 2015

Andreas Eitzlmayr

Modeling of High-Viscous Flow and Mixing
in Co-Rotating Twin-Screw Extruders

Dissertation

First assessor

Univ.-Prof. Dipl.-Ing. Dr.techn. Johannes Khinast
Institute of Process and Particle Engineering
Research Center Pharmaceutical Engineering GmbH
Graz University of Technology

Second assessor

Univ.-Prof. Dr.-Ing. habil. Günter Brenn
Institute of Fluid Mechanics and Heat Transfer
Graz University of Technology

AFFIDAVIT

I declare that I have authored this thesis independently, that I have not used other than the declared sources/resources, and that I have explicitly indicated all material which has been quoted either literally or by content from the sources used. The text document uploaded to TUGRAZonline is identical to the present doctoral thesis.

Date

Signature

"*Do not worry about your difficulties in mathematics.*
I can assure you mine are still greater."

(Albert Einstein)

Preface

The origin of my interest in computer simulations was in the years when I attended a technical college. Here, my preference for mathematics, physical and technical calculations and programming drove me to write simple calculation programs in order to improve my physical understanding. When I learned that computers can be used to compute the flow of liquids and gasses, even combustion, chemical reactions and the weather, I was fascinated. However, in these years I could not imagine that a decade later I would develop simulation programs myself.

Soon after I started to attend lectures of Prof. Khinast during my undergraduate studies at Graz University of Technology, I recognized that computer simulations play an important role in the research activities of his institute. Once, he asked me if I am interested to contribute to a project, and introduced me to his assistant Stefan Radl. I agreed and joined the institute in September 2009. Some months later I delivered the construction drawings for a 60 liters bubble column for the lab of the institute, including a simple compartment model for gas/liquid mass transfer and reactive mixing. After that, I continued with my diploma thesis at the Research Center Pharmaceutical Engineering, supported by Stefan Radl and Daniele Suzzi, where I used the population balance equation to model a precipitation process for the production of organic nanoparticles.

During this time, Prof. Khinast asked me if I am interested in a dissertation. Honestly, I did not consider this before, but it was not difficult to convince me. He told me that there will be a new project about hot-melt extrusion which includes modeling and simulation. Without detailed knowledge about extruders and the challenges in their modeling I agreed, and started to work on this thesis in February 2011. The first challenge was to choose an appropriate numerical method, and I found that an ideal method did actually not exist for this problem and that there was no chance to develop a fully resolved model of the entire extrusion process at this time. Some people told me even that I should never start with this topic, because modeling of extrusion is impossible.

Four years later, after numerous pages of mathematical derivations, programming thousands of code lines, running hundreds of simulations, extruding dozens of kilograms

Soluplus® during the experiments, writing a couple of papers and guiding two master students I found that I should come to an end. However, there is still a lot to do and it will take numerous years of research and development until someone achieves a fully resolved simulation of an entire twin-screw extruder. I hope that my thesis contributes to that, and that the presented results provide some useful insights which help to understand flow and mixing in extruders.

Acknowledgement

I am grateful to all people who contributed to this work and supported me during the last years. Some of them I would like to mention here.

First, my thanks go to Prof. Johannes Khinast for the opportunity to work in his group and for offering me this challenging topic. Being the first in his group advancing towards the simulation of co-rotating twin-screw extruders was not easy. Nevertheless, the support of Johannes enabled me to approach our goals step by step and to achieve an excellent basis for publications and for gaining new industrial partners.

I acknowledge Prof. Günter Brenn for being the second assessor of my thesis. This is a great pleasure for me, since I really enjoyed his lectures about fluid mechanics, mass and heat transfer during my undergraduate studies. These contributed a lot to develop a robust basis of fundamental knowledge, which was an important requirement for this work.

Further thanks go to all members of the RCPE who contributed to provide the financial basis, in particular Gerold Koscher, who leaded most projects for which I worked during the last years. For the financial funding I acknowledge the Austrian COMET Program, initiated by the Federal Ministries BMVIT and BMWFW and the Styrian Funding Agency SFG. I also want to thank NAWI Graz and the ZID of the Graz University of Technology for access to high performance computing systems.

My specific gratitude goes to all colleagues who supported me technically: Stefan Radl for guiding me during my first steps in running and programming LIGGGHTS, Josip Matić for running numerous LIGGGHTS simulations, István Kondor for critical in-depth discussions and feedback about SPH results, Johann Grubbauer for his ideas concerning the experimental setup and for assembling die valve and temperature sensor, Sarah Windhab for her help in measuring the rheology of Soluplus®, Daniel Markl for his assistance with the SIPAT system, Gudrun Hörl, Markus Gamsriegler, Mario Unterreiter and Daniel Kaiser for their support during the experiments and Olya Reis for her proofreading efforts.

I am very grateful to all current and former colleagues from the IPPE and the RCPE who contributed to the pleasant atmosphere in our offices, during lunch time and coffee breaks.

This made periods of hard work much easier. In particular, I want to thank Daniel Treffer, whose work had many connections to mine, for all our discussions in the office and on several business trips. Further, my thanks go to Prof. Eva Roblegg, Ramona Baumgartner and Diana Dujmovic for our cooperation in the “NanEx” project, which was always a pleasure for me. I also want to thank our administrative staff Michaela Cibulka, Adela Roller and Silvia Houben for their assistance, sometimes I would have been lost without your help!

Moreover, I acknowledge our industrial partners from Astra Zeneca and Leistritz Extrusionstechnik for their cooperation and support. I thank Dr. Christoph Kloss from DCS Computing for sharing his LIGGGHTS developments, Dr. Andreas Gryczke from BASF for providing Soluplus®, Reinhardt-Karsten Mürb from Automatik Plastics Machinery for providing ZSK18 screw elements and his valuable time during lots of detailed discussions, and Dr. Michael Bierdel and Dr. Carsten Conzen from Bayer Technology Services for their critical feedback during their visits at RCPE, which led to a new cooperation with BTS.

My thanks go to all scientists and experts who supported me with knowledge, feedback and comments: Gottfried Yelin, who gave me a detailed introduction to extrusion based on decades of practical experience and helped me with the layout of the experiments, Markus Schörgenhumer for several telephone discussions about numerical details of SPH, Dr. Martin Robinson for answering my burning email questions about his SPH papers, Prof. François Bertrand, Prof. Suzanne Kresta and Dr. Minye Liu for their questions and outstanding feedback after my talk at AIChE 2013 in San Francisco, Dr. Kalman Geiger for his contributions to our Rheology Workshops and Klaus Straka and Herwig Juster for our discussions about the simulation of extrusion and injection molding.

Last but not least I want to thank my family and friends, in particular my parents and my sister for all their support and that they have always time for me.

Kurzfassung

Gleichläufige Doppelschneckenextruder spielen eine wichtige Rolle für das Mischen von hochviskosen Stoffen. Sie sind seit Jahrzehnten unter anderem in der Polymer-, Kautschuk- und Nahrungsmittelindustrie etabliert, und zogen in den letzten Jahren steigendes Interesse der pharmazeutischen Industrie für die Herstellung von festen Arzneiformen auf sich. Die üblicherweise verwendete modulare Schneckenbauweise bietet zahlreiche Möglichkeiten hinsichtlich der Auslegung und Optimierung von Extrudern. Durch die Komplexität der Schneckengeometrie und der involvierten physikalischen Phänomene erfordern diese Aufgaben in der Regel einen beträchtlichen Versuchsaufwand. Modellbasierte Auslegungsmethoden wären höchst vorteilhaft, jedoch unterliegt die Modellierung von Extrusionsprozessen heutzutage noch immer starken Einschränkungen. Zum Beispiel stoßen die etablierten, gitterbasierten Simulationsmethoden (Computational Fluid Dynamics, CFD) bei den freien Oberflächenströmungen in teilgefüllten Schneckenzonen an ihre Grenzen, und voll aufgelöste Simulationen von ganzen Extrusionsprozessen auf der Basis von Naturgesetzen waren bisher noch nicht möglich. Abgesehen von der physikalischen Komplexität wäre der erforderliche Rechenaufwand dafür extrem hoch.

In dieser Arbeit wurde die „Smoothed Particle Hydrodynamics“ (SPH) Methode für die Untersuchung von Strömung und Vermischung in verschiedenen Schneckenelement-geometrien verwendet. SPH ist eine gitterfreie Lagrange-Partikelmethode für hydro-dynamische Simulationen. Im Gegensatz zu den etablierten CFD Methoden ist SPH in der Lage, freie Oberflächenströmungen ohne zusätzlichen Aufwand zu erfassen. Darüber hinaus wird Konvektion inhärent abgebildet, was für die Untersuchung der Vermischung vorteilhaft ist. Jedoch existiert noch keine einheitliche Methode für die Umsetzung der Randbedingungen an festen Wänden in SPH, und die Modellierung von komplexen Wandgeometrien ist nicht trivial. Deshalb wurde in dieser Arbeit eine neue Methode für die Randbedingungen an beliebig geformten Wandoberflächen entwickelt. Zusätzlich wurde ein neues Modell für die Newtonsche, laminare Strömung in nicht aufgelösten Spalten entwickelt und in die SPH Methode integriert. Auf Basis dieser Entwicklungen wurde die Newtonsche Strömung in einem vollgefüllten Förderelement unter Berücksichtigung der Spaltströmungen untersucht. Die Ergebnisse zeigten eine exzellente

Übereinstimmung mit CFD Daten aus der Literatur. Darüber hinaus wurde die Methode sowohl für die Untersuchung dieses Förderelementes in teilgefüllten Betriebszuständen, als auch für die detaillierte Analyse der Vermischung mittels Tracerpartikeln in allen betrachteten Betriebszuständen angewendet.

Bedingt durch den hohen Rechenaufwand von voll aufgelösten Modellen haben vereinfachte Modelle noch immer große Bedeutung für die Betrachtung von Gesamtprozessen. Eindimensionale (1D) Modelle lösen die Prozessvariablen (z.B. Füllgrad, Druck, Temperatur) nur in der axialen Richtung auf. Dies ist eine starke Vereinfachung, die jedoch zu technisch sinnvollen Ergebnissen führt, insbesondere wenn ein 1D Modell mit voll aufgelösten Simulationen und/oder Experimenten kalibriert wird. In dieser Arbeit wurde ein 1D Modell neu implementiert, und die charakteristischen Parameter verschiedener Schneckenelemente wurden mit einem typischen pharmazeutischen Polymer experimentell bestimmt. Unter Verwendung dieser Parameter zeigte das Modell eine gute Übereinstimmung mit Messdaten. Weiters konnten experimentelle Daten für die Verweilzeitverteilung aus der Literatur mit dem Modell gut wiedergegeben werden. Darüber hinaus wurden mit dem dreidimensionalen SPH Modell die Strömung und die Vermischung in verschiedenen Schneckenelementgeometrien untersucht, um erforderliche Parameter für das 1D Modell zu generieren. Diese Daten ermöglichen auch eine 1D Beschreibung der Vermischung entlang einer Doppelschnecke.

Abstract

Co-rotating twin-screw extruders play an important role in mixing of high-viscous materials. Established since decades for example in the polymer, rubber and food industries, they attracted increasing interest in the pharmaceutical industry in recent years for the manufacturing of solid drug products. The usually used modular screw design provides numerous options for the design and optimization of extrusion processes. Due to the complexity of the geometry and the involved physical phenomena, these tasks often require a significant amount of experimental effort. Model based design approaches would be highly beneficial, however, there are still strong limitations in the modeling of extrusion processes today. For example, the well established computational fluid dynamics (CFD) methods are limited concerning the free surface flows occurring in partially filled screw sections. Fully resolved first principles simulations of entire extrusion processes have not yet been achieved. Apart from the physical complexity, the required computational expense for that would still be extremely high.

In this work, the smoothed particle hydrodynamics (SPH) method was employed to investigate flow and mixing in various screw element geometries. SPH is a Lagrangian, mesh-free particle method for hydrodynamics simulations. In contrast to the well established CFD methods, SPH accounts for free surface flows without additional complications. Moreover, convection is inherently represented, which is beneficial for the investigation of mixing. However, a unique approach to model solid walls in SPH does not yet exist, and the modeling of complex wall geometries is not trivial. To overcome that, a new boundary method applicable to arbitrarily shaped wall surfaces was developed in this work. In addition, a novel model accounting for the Newtonian, laminar flow in unresolved clearances was developed and integrated into SPH. Based on these developments, the Newtonian flow in a completely filled conveying element of a co-rotating twin-screw extruder was investigated with specific attention to the clearance flows. The results showed excellent agreement with CFD data from the literature. Beyond that, the method was employed for the investigation of this screw element in partially filled operation states, as well as a detailed analysis of mixing with tracer particles in all considered operation states.

Due to the high computational expense required for fully resolved models, simplified models are still important when entire extrusion processes should be considered. One-dimensional (1D) models resolve the process variables (e.g., filling ratio, pressure, temperature) only in the axial direction. This is a strong simplification, however, it leads to technically reasonable results, specifically, when fully resolved simulations and/or experiments are used to calibrate a 1D model. In this work, a 1D model was newly implemented. Experiments with a typical pharmaceutical polymer were conducted for the determination of characteristic parameters of different screw elements. Using these parameters, the model showed good agreement with measurements. Moreover, experimental data from the literature for the residence time distribution could be well reproduced with the model. Additionally, the three dimensional SPH model was employed for the investigation of flow and mixing in various screw element geometries in order to provide required input parameters for the 1D model. These data enable also a reasonable description of mixing along the twin-screw in 1D.

Table of Contents

List of Figures

List of Tables

"*Your assumptions are your windows on the world. Scrub them off every once in a while, or the light won't come in.*"

(Isaac Asimov)

1 Introduction

1.1 Extrusion

Extrusion is an important unit operation, which has been established in various industries for many decades. Besides major applications in the polymer and food industries, extruders are also used, for example, in the manufacturing of rubber, building materials and ceramics. Beyond that, extrusion attracted increasing interest in pharmaceutical manufacturing in recent years.

Basically, extrusion is defined as the process of forcing a material through an orifice. A very simple and well known example of extrusion is squeezing out toothpaste. However, the typical machinery denoted as "extruder" today, performs more than that. Clearly, to force a material through an orifice requires a certain pressure. The different mechanisms of pressure generation lead to a classification of extruders. Screw extruders, where most of the existing extrusion devices belong to, apply one or more rotating screws to generate the required pressure. Besides that, the pressure can also be generated by a plunger (plunger or ram extruders), or by rotating disks or drums (disk and drum extruders). However, these types are of minor industrial significance.[1]

Screw extruders can be further classified according to the number of their screws in single-screw, twin-screw and multi-screw extruders. Twin-screws can be either co-rotating or counter-rotating. Extruders with more than one screw can be intermeshing or non-intermeshing. For more details about different types please refer to the literature.[1–3]

Extrusion is used for various purposes. The most obvious function, directly related to the definition of extrusion, is shaping. A variety of different geometries can be manufactured by extrusion, for example, strands, foils, pipes, tubes, and more complex profiles. By using cutting and granulation machinery downstream to the extrusion die, granules of various shapes can be obtained. Calandering allows the efficient manufacturing of defined shapes directly after the extrusion. An important shaping process, which also applies basic principles of extrusion, is injection molding. This allows the efficient manufacturing of complex shaped parts in high quantities by injecting the molten material into a mold. However, in contrast to typical extrusion processes, injection molding is operated discontinuously, and requires specific machinery to achieve the required injection pressures and flow rates.[4]

Shaping is usually only the final step conducted in extrusion processes. Often the materials are solid and have to be molten prior to the extrusion (also called plastification). Screw extruders are well appropriate for plastification due to the high shear rates exerted to the material and the corresponding high energy input. If the main targets are plastification and pressure generation, single-screws are typically chosen.[2]

In many applications, the material consists of different components which have to be sufficiently mixed. Since the materials in extrusion are typically high-viscous (e.g., polymer melts), the benefits of turbulence for mixing down to small length scales cannot be utilized, which makes mixing much more challenging. Screw extruders, specifically twin-screws, strongly facilitate mixing in the laminar regime due to their complex geometry, which causes a complete deformation of the material during the rotation as well as splitting and merging of parts of the flow. This is a reason for the dominance of screw extruders among other types. Due to their excellent mixing capabilities, twin-screw extruders are often preferred instead of single screws, for applications where mixing is of importance.[2,3]

If the mixture includes volatile components (e.g. moisture, solvents or monomers), which should be removed, devolatilization can be employed. This requires a vented extruder, which is equipped with one or more openings in the barrel, where the gas phase is continuously removed, typically with a vacuum pump. For applications with extremely

high devolatilization requirements, multi-screw extruders are beneficial due to the higher specific surface, facilitating the mass transfer to the gas phase.[1,5]

More specific applications of extrusion are foam extrusion or co-extrusion. Foam extrusion applies gaseous foaming agents, which strongly increase the volume of the extrudate due to the expansion in the die. In co-extrusion, two or more extruders are operated together. The materials are extruded through a single die, where the extrudates merge and form a laminar-layered structure.[6]

1.2 Pharmaceutical Applications

During recent years extrusion became increasingly interesting for the manufacturing of pharmaceutical solid dosage products.[7] It is particularly promising for poorly soluble drugs by dispersing or dissolving the API (active pharmaceutical ingredient) in a solid matrix, often based on polymers. The obtained solid dispersions or solid solutions can lead to an increased solubility of the API, and further to an increased bioavailability.[8–11] Moreover, extrusion processes can be conducted solvent-free, which avoids costs for solvents and their recovery, separation and disposal, as well as problems associated with residues of solvent in the drug product.

In the extruder, the matrix must be plasticized in order to facilitate mixing and extrusion. For this, polymers typically have to exceed the melting point. Then the process is called “hot-melt extrusion”, which is analogous to the so-called “compounding” processes known from the polymer industry. Similar to that is “solid-lipid extrusion”, where the matrix is a lipid or similar material, which can be sufficiently plasticized below the melting point.[12] On the contrast, “wet-extrusion” does usually not require increased temperature levels, because here the material is a solid, granular material which is processed together with a liquid. Instead of an extrusion die, wet-extrusion typically extrudes through a plate with a large number of small holes (almost a sieve). The extrudates of wet-extrusion can be spheronized and dried subsequent to the extrusion to obtain spherical granules.[12,13]

Further targets of pharmaceutical extrusion processes can be, for example, controlled release systems[14,15], taste masking or the stabilization of API nanoparticles[16–18] by

incorporation into a solid matrix. Also co-extrusion and injection molding are considered as promising tools for pharmaceutical manufacturing.[19–21]

The product quality is usually critical in pharmaceutical manufacturing and continuous monitoring systems are required to avoid large amounts of nonconforming product. It was demonstrated that existing monitoring tools can be utilized to acquire critical quality attributes such as API content and pellet size.[22–26] For more details about pharmaceutical applications of extrusion please refer to the literature.[6,8,12,27–30]

1.3 Co-Rotating Twin-Screw Extruders

In extrusion applications with high mixing requirements, the most frequently used extruder type is the co-rotating twin-screw extruder with the self-wiping screw profile invented by Meskat and Erdmenger[31] in the 1940s. Its beneficial mixing performance and the self-wiping screws led to this dominant position, specifically in compounding and pharmaceutical extrusion processes.[27,32] Also for devaporization, the self-wiping screws are beneficial since their tight clearances cause an intensive surface renewal during the rotation.[5]

In order to improve the mixing capabilities, further modifications of the original, threaded screw geometry were invented in the 1940s and 1950s by Erdmenger and others (for a detailed review see, e.g., Kohlgrüber[2]). Most important and widely used is the geometry of kneading discs/elements, which consist of prismatic discs with the same self-wiping cross-section profile as used for the threaded screw elements. Beyond that, a variety of other screw geometries has been invented up to now for various purposes, e.g., different types of specific mixing elements.[2]

A further invention of Erdmenger was the modular screw design, which means that the screw consists of individual elements which can be arranged according to the actual requirements of the extrusion process. This provides numerous options for the design and optimization of the screw configuration and provides high flexibility in practical operation. Today, most co-rotating twin-screw extruders are based on the modular design.[2]

Some examples for frequently used screw elements are shown in Figure 1.1. Screw elements based on the original, threaded screw geometry are mostly called “conveying

elements" (e.g., Figure 1.1a and b), since they mainly convey the processed material along the screws. The most common mixing elements used today (e.g., Figure 1.1c) are based on conveying elements and allow an exchange of material between adjacent screw channels through their openings.

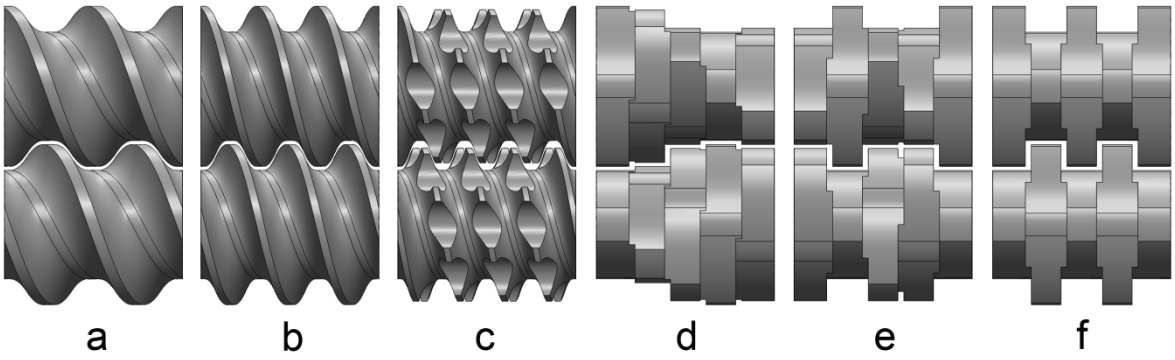

Figure 1.1: Frequently used types of screw elements (a and b: conveying elements with different pitches, c: mixing element, d – f: kneading elements with stagger angles of 30°, 60° and 90°).

Kneading elements (e.g., Figure 1.1d – f) consist of a series of prismatic discs, arranged in a staggered manner. Different kneading elements can be mainly distinguished by the thickness of the discs and the angle between two adjacent discs, the so-called stagger-angle. The most common stagger angles are 30, 45, 60 and 90°, whereas 90° kneading elements are symmetrical with respect to the extrusion direction and therefore, do not convey by themselves and have to be overdriven by pressure (so-called non-conveying elements). In contrast, kneading elements with stagger angles different from 90° have a certain conveying capability.

The intention behind kneading and mixing elements is similar, i.e., to facilitate mixing. However, the kneading elements involve a relatively high energy input, whereas mixing elements are typically designed in order to facilitate mixing together with minimal energy input.

Screw elements with conveying capabilities mostly exist in two variants, "right-handed" and "left-handed". This means conveying forward or backward, respectively, and implies two mirror-inverted variants of the geometry. Clearly, mostly used are right-handed elements (conveying forward), however, in some cases left-handed elements are used to generate a completely filled zone, which generates the required pressure to overdrive the

left-handed element. This can be required to intensify energy input and mixing or to separate a vacuum zone (devaporization) from other parts of the process.

A schematic of the screw configuration of a co-rotating twin-screw extruder together with the related process zones is shown in Figure 1.2 (the length is not realistic here, the typical length of melt extruders is ca. 40 screw diameters). The following process steps are typical for co-rotating twin-screw extruders:[2]

- intake
- compression
- atmospheric venting
- plastification (melting)
- conveying
- feeding additional components
- mixing
- devaporization
- pressure build-up

The intake zone mainly has to convey the feed material (powder, granules) sufficiently fast to avoid clogging. After that, the compression of the material and the removal of entrapped air is achieved by the decreasing pitch of the conveying elements. Depending on the feed material, atmospheric venting can be required to support the air removal.

To provide appropriate temperature conditions in each zone, the barrel is typically divided into a number of temperature zones, each of them being temperature controlled. This requires not only heating, but also cooling due to the relatively high amount of dissipation heat generated by the flow, depending on the material and the operation conditions. The barrel temperature in the intake zone is usually low, to avoid sticking of the granular feed material.

The plastification (melting) mainly starts at the hot surfaces of the heated barrel, whereas the complete melting of the material is mainly achieved by friction and dissipation heat. Kneading elements are often used to support the melting by their high energy input and dispersing solid particles, depending on the feed material.

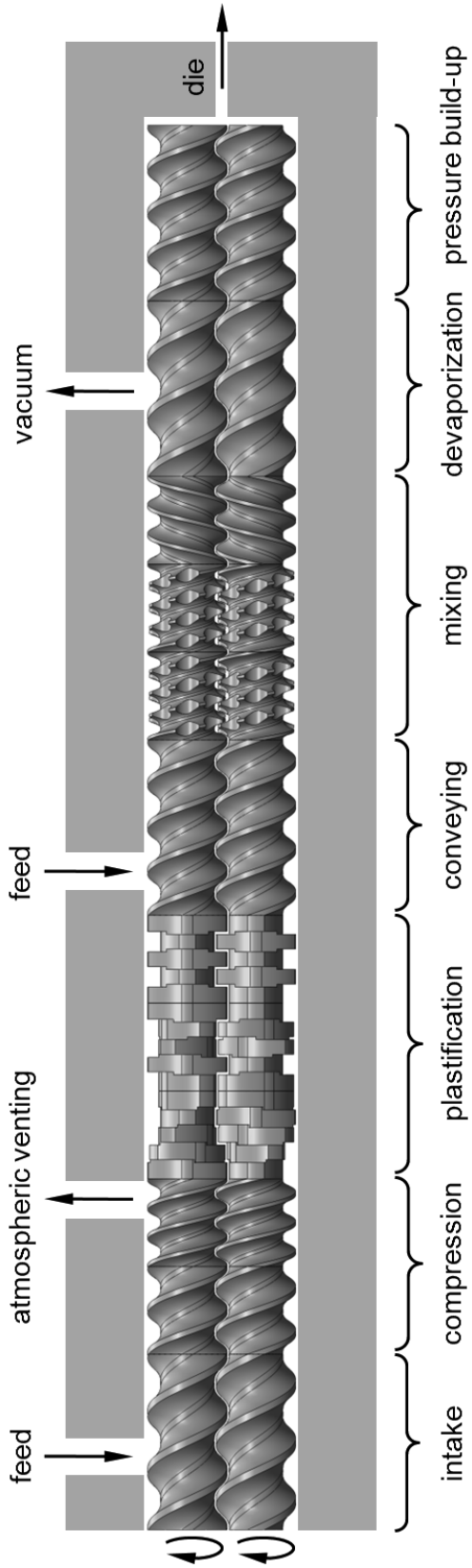

Figure 1.2: Schematic of the co-rotating, self cleaning twin-screw extruder and an example arrangement of different process zones.

The plastification zone is typically followed by conveying elements, which are usually partially filled. Here, additional materials can be added, e.g., liquid additives/excipients or sensitive materials which should not pass the plastification zone.

Two different types of mixing are generally distinguished in extrusion, dispersive and distributive mixing. Dispersive mixing means the size reduction of a dispersed phase (particles or droplets) by shear forces, while distributive mixing is the homogenization of a continuous phase by distributing the components among each other. Depending on the requirements, kneading elements or mixing elements can be used for this.

Before the pressure build-up, a devaporization zone is often used which applies vacuum to remove volatile components (e.g. moisture or residues of solvents/monomers). Here, usually conveying elements with large pitches are used in order to achieve a low filling ratio and a large gas/liquid interface to support the mass transfer. Finally, the pressure build-up zone generates the die pressure.

Clearly, in the real extruder the process zones cannot be strictly isolated from each other, since a certain extent of conveying, energy input and mixing occurs practically everywhere along the screws. However, the process zones are designed in order to perform their intended function best possible, which depends on the used screw elements and the operation parameters.

1.4 Parameters

Besides the screw geometry, lots of other parameters impact the extrusion process. This starts from the material properties, which are typically complex and diverse (e.g., density, rheology, glass transition point, melting point, melting enthalpy, specific heat capacity, thermal conductivity, miscibility of different components, phase transitions, etc.). Usually, the possibilities to change the material properties are limited (e.g., using plasticizers to reduce the viscosity), thus, the extrusion process must be adequately designed and operated depending on the used materials.

The operation parameters (screw speed, throughput and barrel temperatures) must be appropriate for the used materials. Also, the used machine size must be in agreement with the desired throughput. The actual die geometry (e.g., number of die channels, diameter

and length) influences the required die pressure and thus, the length of the pressure build-up zone. The die must be appropriate for the used materials and the desired throughput.

The actual distances of the tight clearances (screw/barrel and screw/screw) are crucial for the amount of viscous dissipation heat and, thus, have a considerable impact on the obtained melt temperature (which is typically higher than the barrel temperature). However, in practical applications the clearance distances underlie a certain evolution during the life time of an extruder, caused by abrasion (strongly depending on the processed materials). It is important to note that this can cause significant changes in the extrusion process during the life time.

A variety of process parameters can be used to characterize the extrusion process. Some parameters which can be measured are pressure, power consumption, mixedness of the extrudate or the residence time distribution. Other important parameters cannot be measured easily, for example, the screw filling ratio, the local melt temperature or the evolution of the mixedness along the screws. However, knowledge about these parameters would strongly support the rational design, optimization and scale-up of extruders. There is still a lack of systematic design approaches for extrusion processes, and a high amount of experience, empirical knowledge and experimental work are required to overcome these challenges.

1.5 Modeling Approaches

An essential advantage of modeling and simulation methods compared to the reality is that they are fully transparent, i.e., provide complete access to all computed variables. This can significantly contribute to the understanding of complex systems, as the flow and mixing in extrusion processes.

1.5.1 Challenges

Modeling of co-rotating twin-screw extruders involves several complications, starting from the complex and rotating geometry of the screws, which causes a complete deformation of the processed material. Together with the free surface flows in partially filled screw sections, this is particularly challenging for the application of simulation methods which are based on Eulerian meshes, e.g., the well-established computational fluid dynamics

(CFD) methods. Moreover, these geometries cause additional challenges in terms of length scales, since the tight clearance distances are typically at least two orders of magnitude smaller than the screw diameter and four orders of magnitude smaller than the length of an entire screw. Consequently, the computational expense for entire extruders is high when the flow through the clearances should be resolved, which is usually essential.

Moreover, the involved physical phenomena introduced by the materials are complex, for example, the transition of the materials during the plastification, the rheology, viscoelasticity, additional phase transitions or the variation of the macroscopic material properties during the mixing process. Apart from numerical challenges, the sufficient description of the material behavior is highly challenging on its own. Due to these complications, the simulation of entire co-rotating twin-screw extruders without significant simplifications is not possible today.

1.5.2 Beginnings of Extruder Flow Modeling

In the early days of extruder modeling, the available computation power was clearly far away from the requirements of spatially resolved simulations of the flow in entire extruders. Analytical techniques were applied to describe the isothermal flow of Newtonian liquids in co-rotating twin-screw extruders (e.g., Booy[33,34], Tayeb[35]). Guo and Chung[36] developed a model for the dependency of the melt temperature on the screw speed and compared it to measurements. Denson and Hwang[37] used the finite element method and studied the isothermal, Newtonian flow in a co-rotating twin-screw extruder. A similar method, proposed by Tadmor[38], was applied by Szydlowski and White[39] for Newtonian flow and by Szydlowski and White[40] and Wang and White[41] for non-Newtonian flow in different geometries of co-rotating twin-screws. Kalyon et al.[42] employed the finite element method for the investigation of non-Newtonian, non-isothermal flow and mixing. Main results of these studies were the relationships of flow rate, axial pressure gradient and screw speed for different screw element geometries (the so-called pumping or pressure characteristic). Pawlowski[43,44] presented a general concept for the description of the pressure characteristic and similar relationships of screw machines based on dimensional analysis.

1.5.3 One-Dimensional Modeling

Due to the large extension of extruders in the axial direction compared to the radial direction, the simplification of the so-called one-dimensional (1D) modeling approach was an obvious step. Here, the spatial dependencies of process variables (e.g., filling ratio, pressure, material temperature) are considered only in the axial direction, whereas distributions over the cross section are neglected. Clearly, this is a significant simplification, however, 1D modeling leads to reasonable results for practical applications. Due to the lack of resolution, 1D models usually require input parameters which describe the pressure characteristic of individual screw elements. These parameters have to be determined by other methods, e.g., analytical techniques, spatially resolved flow simulations or experiments.

1D models were presented, for example, by Yacu[45], White and Szydlowski[46], Meijer and Elemans[47], White and Chen[48], Potente et al.[49–51], Vergnes et al.[52], White et al.[53], Prat et al.[54,55] and Teixeira et al.[56]. 1D models for reactive extrusion were presented, for example, by Choulak et al.[57], Zagal et al.[58], Puaux et al[59], Vergnes and Berzin[60] and Bahloul et al.[61]. Similarly, the transport mechanisms along the screws were used to model the residence time distribution (RTD) of extruders, e.g., Todd[62], Potente and Koch[63], Chen et al.[64], Oberlehner et al.[65], De Ruyck[66], Giudici et al.[67], Gao et al.[68], Prat et al.[69], Puaux et al.[70], Kumar et al.[71], Baron et al.[72] and Amedu et al.[73]. Mudalamane and Bigio[74] studied the transient behavior of extruders.

Today, the 1D approach still plays an important role in modeling of extrusion processes, specifically in industrial and engineering applications, where efficient and fast methods with reasonable results are required. Commercial software is available for these purposes, and, clearly, the provided details about the implemented models are rare. Also the literature does not reveal every detail required for the proper implementation of a 1D model, for example, details about the simplified calculation of the viscous dissipation or the heat transfer in co-rotating twin-screw extruders are hardly available. A reason might be, that a material-independent 1D model does not exist in the strict sense, since the 1D simplification (i.e., the averaging over the cross section) also involves the spatial variability of material properties, which is clearly a huge drawback. However, the 1D approach is still the only way to efficiently model entire extruders.

1.5.4 Mesh-based CFD Methods

With increasing computational possibilities, three-dimensional (3D) numerical models of the flow in co-rotating twin-screw extruders were developed, mainly based on mesh-based CFD methods as the finite element and finite volume methods (FEM and FVM).

For example, Yang and Manas-Zloczower[75] analyzed the flow field in the kneading disc region by FEM. Ishikawa et al.[76] used FEM to analyze the non-Newtonian, non-isothermal flow and the mixing performance of kneading elements. Bertrand et al.[77] proposed a mesh refinement strategy for the FEM simulation of fluid flow in complex, moving geometries with small gaps, and applied it to the geometry of a co-rotating twin-screw. Pokriefke[78,79] used FVM with an Eulerian two-phase model to study the flow in completely filled and partially filled sections of co-rotating twin-screw extruders. Ficarella et al.[80,81] analyzed the flow in a co-rotating twin-screw extruder based on FEM. Barrera et al.[82] employed FEM to obtain flow curves (i.e., similar to the pressure characteristic) of co-rotating twin-screw extruder elements. Bierdel[83] showed detailed results for the flow field, the pressure and power characteristic of a conveying element obtained with FVM. Conzen[84] employed FVM to study the non-isothermal flow field in single screw and co-rotating twin-screw extruders. Rodriguez[85] investigated reactive extrusion in co-rotating twin-screw extruders by 1D modeling and FEM. Haghayeghi et al.[86] employed FVM to analyze the solidification process in a co-rotating twin-screw melt conditioner. Vyakaranam et al.[87] investigated the effect of the stagger angle of kneading elements on the velocity profiles using FEM. Sobhani et al.[88] modeled non-Newtonian, non-isothermal flow with FEM and the fictitious domain method. Sarhangi Fard et al.[89–91] extended FEM by an adaptive non-conformal mesh refinement and studied flow and mixing in different screw geometries of co-rotating twin-screw extruders. Hétu and Ilinca[92] used FEM and the immersed boundary method to avoid involved and computationally expensive remeshing techniques. Rathod and Kokini[93] studied the effect of the mixer geometry and operating conditions on the mixing efficiency in a twin-screw mixer with FEM. Several studies focused on the flow in extrusion dies.[94–99] Most of these studies considered completely filled screw sections, since the free surface flows in partially filled screw sections are highly challenging for mesh-based methods.

Clearly, CFD methods are well-established and robust tools which led to significant advances in the understanding of flow and mixing in co-rotating twin-screws. However, their limitations for free surface flows and the required highly sophisticated mesh treatment due to the deformation of the fluid suggest to investigate also other methods, which might have benefits for these particular challenges.

1.5.5 Smoothed Particle Hydrodynamics

The smoothed particle hydrodynamics[100] method (SPH) is a Lagrangian method for hydrodynamic simulations, which is mesh-free and thus, implies significant benefits for complex, rotating geometries as co-rotating twin-screws. Originally, SPH was developed in the 1970s to study astrophysical phenomena,[101,102] later it was found that this concept can also be applied to continuum equations, as the hydrodynamics equations of motion.[103] The flow is represented by moving fluid elements (so-called particles). This allows to model free surface flows without additional modeling effort.[104] Moreover, due to the Lagrangian nature SPH accounts inherently for convective species transport,[105] which is beneficial for the investigation of mixing. For example, Robinson et al.[106] employed SPH to study flow and mixing in a twin-cam mixer at low Reynolds numbers and obtained good agreement with experimental and FEM results of Avalosse and Crochet[107]. Moreover, Robinson and Cleary[108] studied a helical ribbon mixer based on SPH. These advantages make the SPH method very promising for studies of flow and mixing in co-rotating twin-screw extruders, as recently reported by Cleary and Robinson[109].

Although, SPH was invented decades ago and employed to various problems up to now, there is still no unique way of modeling boundaries.[110] The most obvious way is, to model walls consisting of particles (e.g., boundary particles[111,105], fixed fluid particles[112,113], ghost particles[114–118]). These particle based techniques are often not practicable for complex shaped, technical geometries, as extruder screws, or lead to complications at edges and corners.[110,119] Normalization techniques[120,121] have been used, which avoid the use of additional particles for the boundary modeling, however, they are typically involved and computationally expensive in 3D.

In technical applications, the geometries are usually created by CAD (computer aided design) software and a direct use of the related file formats would be desirable. A

frequently used format for the representation of complex, three-dimensional geometries is the *.stl format, which approximates the surface by a tessellation consisting of triangles. Thus, a simple model for the interaction of a single fluid element with a continuous wall surface would be highly beneficial to enable the efficient and practicable processing of complex geometries in SPH simulations. Such a model was proposed for example by Kruisbrink et al.[122], who modeled the wall interaction based on normal and tangential forces acting on fluid particles in the vicinity of a continuous wall.

1.6 Conclusions

Extrusion is important in various applications. The complexity of the physical phenomena together with the geometry of co-rotating twin-screw extruders make the modeling of extrusion processes highly complex, and significant simplifications are still required. 1D modeling of extruders implies strong simplifications, however, is still required for fast and efficient models of entire extrusion processes, as required for industrial and engineering applications. For spatially resolved simulations of the flow and mixing, the conventional, mesh-based CFD methods are limited due to the usually included free surface flows together with the strongly deformed fluid domain. Mesh-free, Lagrangian methods, as the SPH method, provide significant benefits for these challenges and their further investigation is a promising way towards a deeper understanding and quantification of flow and mixing in co-rotating twin-screw extruders.

1.7 Abbreviations

1D	one-dimensional
3D	three-dimensional
API	active pharmaceutical ingredient
CAD	computer aided design
CFD	computational fluid dynamics
FEM	finite element method
FVM	finite volume method
RTD	residence time distribution
SPH	smoothed particle hydrodynamics

1.8 References

(1) Rauwendaal, C. *Polymer Extrusion*; 4th ed.; Hanser Publishers: Munich, 2001.

(2) Kohlgrüber, K. *Co-Rotating Twin-Screw Extruders*; Carl Hanser Publishers: Munich, 2008.

(3) Paul, E. L.; Atiemo-Obeng, V. A.; Kresta, S. M. *Handbook of Industrial Mixing*; John Wiley & Sons, Inc.: Hoboken, New Jersey, 2004.

(4) Rosato, D.; Rosato, D.; Rosato, M. *Injection Molding Handbook*; 3rd Ed.; Kluwer Academic Publishers Group: Dordrecht, Netherlands, 2000.

(5) Kohlgrüber, K.; Bierdel, M.; Conzen, C.; Hepperle, J.; Kirchhoff, J.; König, T.; Thiele, H. Optimierter Betrieb und Scale-up von Doppelschnecken-Extrudern. In *Seminar Handout*; VDI Wissensforum: Leverkusen, Germany, 2012.

(6) Repka, M. A.; Langley, N.; DiNunzio, J. *Melt Extrusion - Materials, Technology and Drug Product Design*; Springer: New York, Heidelberg, Dordrecht, London, 2013.

(7) Crowley, M. M.; Zhang, F.; Repka, M. A.; Thumma, S.; Upadhye, S. B.; Battu, S. K.; McGinity, J. W.; Martin, C. Pharmaceutical Applications of Hot-Melt Extrusion: Part I. *Drug Dev. Ind. Pharm.* **2007**, *33*, 909–926.

(8) Breitenbach, J. Melt Extrusion: From Process to Drug Delivery Technology. *Eur. J. Pharm. Biopharm.* **2002**, *54*, 107–117.

(9) Lang, B.; McGinity, J. W.; Williams, R. O. Dissolution Enhancement of Itraconazole by Hot-Melt Extrusion Alone and the Combination of Hot-Melt Extrusion and Rapid Freezing - Effect of Formulation and Processing Variables. *Mol. Pharm.* **2014**, *11*, 186–196.

(10) Pina, M. F.; Zhao, M.; Pinto, J. F.; Sousa, J. J.; Craig, D. Q. M. The Influence of Drug Physical State on the Dissolution Enhancement of Solid Dispersions Prepared Via Hot-Melt Extrusion: A Case Study Using Olanzapine. *J. Pharm. Sci.* **2014**, *103*, 1214–1223.

(11) Repka, M. A.; Battu, S. K.; Upadhye, S. B.; Thumma, S.; Crowley, M. M.; Zhang, F.; Martin, C.; McGinity, J. W. Pharmaceutical Applications of Hot-Melt Extrusion: Part II. *Drug Dev. Ind. Pharm.* **2007**, *33*, 1043–1057.

(12) Kleinebudde, P. Pharmazeutisches Produktdesign: Gezielte Freisetzung von Wirkstoffen durch unterschiedliche Extrusionstechniken. *Chemie Ing. Tech.* **2011**, *83*, 589–597.

(13) Roblegg, E.; Schrank, S.; Griesbacher, M.; Radl, S.; Zimmer, A.; Khinast, J. Use of the Direct Compression Aid Ludiflash® for the Preparation of Pellets via Wet Extrusion/Spheronization. *Drug Dev. Ind. Pharm.* **2011**, *37*, 1231–1243.

(14) Roblegg, E.; Jäger, E.; Hodzic, A.; Koscher, G.; Mohr, S.; Zimmer, A.; Khinast, J. Development of Sustained-Release Lipophilic Calcium Stearate Pellets via Hot Melt Extrusion. *Eur. J. Pharm. Biopharm.* **2011**, *79*, 635–645.

(15) Repka, M. A.; Gutta, K.; Prodduturi, S.; Munjal, M.; Stodghill, S. P. Characterization of Cellulosic Hot-Melt Extruded Films Containing Lidocaine. *Eur. J. Pharm. Biopharm.* **2005**, *59*, 189–196.

(16) Baumgartner, R. Nanoextrusion: Verarbeitung von Nanosuspensionen durch das Verfahren der Schmelzextrusion, Karl-Franzens-Universität Graz, 2012.

(17) Khinast, J. G.; Baumgartner, R.; Roblegg, E. Nano-Extrusion: A One-Step Process for Manufacturing of Solid Nanoparticle Formulations Directly from the Liquid Phase. *AAPS PharmSciTech* **2013**, *14*, 601–604.

(18) Baumgartner, R.; Eitzlmayr, A.; Matsko, N.; Tetyczka, C.; Khinast, J.; Roblegg, E. Nano-Extrusion: A Promising Tool for Continuous Manufacturing of Solid Nano-Formulations. *Int. J. Pharm.* **2014**, *477*, 1–11.

(19) Dierickx, L.; Van Snick, B.; Monteyne, T.; De Beer, T.; Remon, J. P.; Vervaet, C. Co-Extruded Solid Solutions as Immediate Release Fixed-Dose Combinations. *Eur. J. Pharm. Biopharm.* **2014**, *88*, 502–509.

(20) Quinten, T.; De Beer, T.; Vervaet, C.; Remon, J. P. Evaluation of Injection Moulding as a Pharmaceutical Technology to Produce Matrix Tablets. *Eur. J. Pharm. Biopharm.* **2009**, *71*, 145–154.

(21) Zema, L.; Loreti, G.; Melocchi, A.; Maroni, A.; Gazzaniga, A. Injection Molding and Its Application to Drug Delivery. *J. Control. Release* **2012**, *159*, 324–331.

(22) Markl, D.; Wahl, P. R.; Menezes, J. C.; Koller, D. M.; Kavsek, B.; Francois, K.; Roblegg, E.; Khinast, J. G. Supervisory Control System for Monitoring a Pharmaceutical Hot Melt Extrusion Process. *AAPS PharmSciTech* **2013**, *14*, 1034–1044.

(23) Wahl, P. R.; Treffer, D.; Mohr, S.; Roblegg, E.; Koscher, G.; Khinast, J. G. Inline Monitoring and a PAT Strategy for Pharmaceutical Hot Melt Extrusion. *Int. J. Pharm.* **2013**.

(24) Treffer, D.; Wahl, P. R.; Hörmann, T. R.; Markl, D.; Schrank, S.; Jones, I.; Cruise, P.; Mürb, R.-K.; Koscher, G.; Roblegg, E.; et al. In-Line Implementation of an Image-Based Particle Size Measurement Tool to Monitor Hot-Melt Extruded Pellets. *Int. J. Pharm.* **2014**, *466*, 181–189.

(25) Saerens, L.; Dierickx, L.; Lenain, B.; Vervaet, C.; Remon, J. P.; De Beer, T. Raman Spectroscopy for the in-Line Polymer-Drug Quantification and Solid State Characterization during a Pharmaceutical Hot-Melt Extrusion Process. *Eur. J. Pharm. Biopharm.* **2011**, *77*, 158–163.

(26) Saerens, L.; Dierickx, L.; Quinten, T.; Adriaensens, P.; Carleer, R.; Vervaet, C.; Remon, J. P.; De Beer, T. In-Line NIR Spectroscopy for the Understanding of Polymer-Drug Interaction during Pharmaceutical Hot-Melt Extrusion. *Eur. J. Pharm. Biopharm.* **2012**, *81*, 237–230.

(27) Ghebre-Sellassie, I.; Martin, C. *Pharmaceutical Extrusion Technology*; Marcel Dekker Inc.: New York, 2003.

(28) Douroumis, D. *Hot-Melt Extrusion: Pharmaceutical Applications*; John Wiley & Sons, Ltd.: Chichester, 2012.

(29) Kolter, K.; Karl, M.; Gryczke, A. *Hot-Melt Extrusion with BASF Pharma Polymers; Extrusion Compendium*; 2nd ed.; BASF: Ludwigshafen, 2012.

(30) Chokshi, R.; Zia, H. Hot-Melt Extrusion Technique: A Review. *Iran. J. Pharm. Res.* **2004**, *3*, 3–16.

(31) Meskat, W.; Erdmenger, R. Gleichdrall Doppelschnecke mit Dichtprofil. DBP 862 668, 1944.

(32) Hornberger, C.; Saddey, A.; Huber, A. Automatisierung und Validierung von Pharmaextrudern. *TechnoPharm* **2011**, *1*, 144–151.

(33) Booy, M. L. Geometry of Fully Wiped Twin-Screw Equipment. *Polym. Eng. Sci.* **1978**, *18*, 973–984.

(34) Booy, M. L. Isothermal Flow of Viscous Liquids in Corotating Twin Screw Devices. *Polym. Eng. Sci.* **1980**, *20*, 1220–1228.

(35) Tayeb, J.; Vergnes, B.; Della Valle, G. Theoretical Computation of the Isothermal Flow Through the Reverse Screw Element of a Twin Screw Extrusion Cooker. *J. Food Sci.* **1988**, *53*, 616–625.

(36) Guo, Y.; Chung, C. I. Dependence of Melt Temperature on Screw Speed and Size in Extrusion. *Polym. Eng. Sci.* **1989**, *29*, 415–419.

(37) Denson, C. D.; Hwang, B. K. J. The Influence of the Axial Pressure Gradient on Flow Rate for Newtonian Liquids in a Self Wiping , Co-Rotating Twin Screw Extruder. *Polym. Eng. Sci.* **1980**, *20*, 965–971.

(38) Tadmor, Z.; Broyer, E. Flow Analysis Network (FAN) - A Method for Solving Flow Problems in Polymer Processing. *Polym. Eng. Sci.* **1974**, *14*, 660–665.

(39) Szydlowski, W.; White, J. L. An Improved Theory of Metering in an Intermeshing Corotating Twin-Screw Extruder. *Adv. Polym. Technol.* **1987**, *7*, 177–183.

(40) Szydlowski, W.; White, J. L. A Non-Newtonian Model of Flow in a Kneading Disc Region of a Modular Intermeshing Corotating Twin Screw Extruder. *J. Nonnewton. Fluid Mech.* **1988**, *28*, 29–46.

(41) Wang, Y.; White, J. L. Non-Newtonian Flow Modelling in the Screw Regions of an Intermeshing Corotating Twin Screw Extruder. *J. Nonnewton. Fluid Mech.* **1989**, *32*, 19–38.

(42) Kalyon, D. M.; Gotsis, A. D.; Yilmazer, U.; Gogos, C. G.; Sangani, H.; Aral, B.; Tsenoglou, C. Development of Experimental Techniques and Simulation Methods To Analyze Mixing in Co-Rotating Twin Screw Extrusion. *Adv. Polym. Technol.* **1988**, *8*, 337–353.

(43) Pawlowski, J. *Die Ähnlichkeitstheorie in der physikalisch-technischen Forschung*; Springer-Verlag: Berlin/Heidelberg/New York, 1971.

(44) Pawlowski, J. *Transportvorgänge in Einwellen-Schnecken*; Otto Salle Verlag, Verlag Sauerländer: Aarau, Frankfurt am Main, Salzburg, 1990.

(45) Yacu, W. A. Modelling a Twin Screw Co-Rotating Extruder. *J. Food Eng.* **1985**, *8*, 1–21.

(46) White, J. L.; Szydlowski, W. Composite Models of Modular Intermeshing Corotating and Tangential Counterrotating Twin Screw Extruders. *Adv. Polym. Technol.* **1987**, *7*, 419–426.

(47) Meijer, H. E. H.; Elemans, P. H. M. The Modeling of Continuous Mixers. Part I: The Corotating Twin-Screw Extruder. *Polym. Eng. Sci.* **1988**, *28*, 275–290.

(48) White, J. L.; Chen, Z. Simulation of Non-Isothermal Flow in Modular Co- Rotating Twin Screw Extrusion. *Polym. Eng. Sci.* **1994**, *34*, 229–237.

(49) Potente, H.; Hanhart, W. Design and Processing Optimization of Extruder Screws. *Polym. Eng. Sci.* **1994**, *3*, 937–945.

(50) Potente, H.; Bastian, M.; Flecke, J. Design of a Compounding Extruder by Means of the SIGMA Simulation Software. *Adv. Polym. Technol.* **1999**, *18*, 147–170.

(51) Potente, H.; Kretschmer, K. Simulation and Evaluation of Compounding Processes. *Macromol. Mater. Eng.* **2002**, *287*, 758–772.

(52) Vergnes, B.; Della Valle, G.; Delamare, L. A Global Computer Software for Polymer Flows in Corotating Twin Screw Extruders. *Polym. Eng. Sci.* **1998**, *38*, 1781–1792.

(53) White, J. L.; Kim, E. K.; Keum, J. M.; Jung, H. C. Modeling Heat Transfer in Screw Extrusion With Special Application to Modular Self-Wiping Co-Rotating Twin-Screw Extrusion. *Polym. Eng. Sci.* **2001**, *41*, 1448–1455.

(54) Prat, L.; Guiraud, P.; Rigal, L.; Gourdon, C. A One Dimensional Model for the Prediction of Extraction Yields in a Two Phases Modified Twin-Screw Extruder. *Chem. Eng. Process.* **2002**, *41*, 743–751.

(55) Prat, L.; N'Diaye, S.; Rigal, L.; Gourdon, C. Solid–liquid Transport in a Modified Co-Rotating Twin-Screw Extruder—dynamic Simulator and Experimental Validations. *Chem. Eng. Process.* **2004**, *43*, 881–886.

(56) Teixeira, C.; Gaspar-Cunha, A.; Covas, J. A. Flow and Heat Transfer Along the Length of a Co-Rotating Twin Screw Extruder. *Polym. Plast. Technol. Eng.* **2012**, *51*, 1567–1577.

(57) Choulak, S.; Couenne, F.; Le Gorrec, Y.; Jallut, C.; Cassagnau, P.; Michel, A. Generic Dynamic Model for Simulation and Control of Reactive Extrusion. *Ind. Eng. Chem. Res.* **2004**, *43*, 7373–7382.

(58) Zagal, A.; Vivaldo-Lima, E.; Manero, O. A Mathematical Model for the Reactive Extrusion of Methyl Methacrylate in a Co-Rotating Twin-Screw Extruder. *Ind. Eng. Chem. Res.* **2005**, *44*, 9805–9817.

(59) Puaux, J.-P.; Cassagnau, P.; Bozga, G.; Nagy, I. Modeling of Polyurethane Synthesis by Reactive Extrusion. *Chem. Eng. Process.* **2006**, *45*, 481–487.

(60) Vergnes, B.; Berzin, F. Modeling of Reactive Systems in Twin-Screw Extrusion: Challenges and Applications. *Comptes Rendus Chim.* **2006**, *9*, 1409–1418.

(61) Bahloul, W.; Oddes, O.; Bounor-Legaré, V.; Mélis, F.; Cassagnau, P.; Vergnes, B. Reactive Extrusion Processing of Polypropylene/TiO2 Nanocomposites by In Situ Synthesis of the Nanofillers: Experiments and Modeling. *AIChE J.* **2011**, *57*, 2174–2184.

(62) Todd, D. B. Residence Time Distribution in Twin-Screw Extruders. *Polym. Eng. Sci.* **1975**, *15*, 437–443.

(63) Potente, H.; Koch, M. Residence Time Behavior in Grooved-Barrel Extruders. *Adv. Polym. Technol.* **1989**, *9*, 119–127.

(64) Chen, L.; Pan, Z.; Hu, G.-H. Residence Time Distribution in Screw Extruders. *AIChE J.* **1993**, *39*, 1455–1464.

(65) Oberlehner, J.; Cassagnau, P.; Michel, A. Local Residence Time Distribution Screw Extruder in a Twin. *Chem. Eng. Sci.* **1994**, *49*, 3897–3907.

(66) De Ruyck, H. Modelling of the Residence Time Distribution in a Twin Screw Extruder. *J. Food Eng.* **1997**, *32*, 375–390.

(67) Giudici, R.; Nascimento, C. A. O.; Beiler, I. C.; Scherbakoff, N. Transient Experiments and Mathematical Modeling of an Industrial Twin-Screw Extruder Reactor for Nylon-6,6 Polymerization. *Ind. Eng. Chem. Res.* **1997**, *36*, 3513–3519.

(68) Gao, J.; Walsh, G. C.; Bigio, D.; Briber, R. M.; Wetzel, M. D. Residence-Time Distribution Model for Twin-Screw Extruders. *Process Syst. Eng.* **1999**, *45*, 2541–2549.

(69) Prat, L.; Guiraud, P.; Rigal, L.; Gourdon, C. Two Phase Residence Time Distribution in a Modified Twin Screw Extruder. *Chem. Eng. Process.* **1999**, *38*, 73–83.

(70) Puaux, J. .; Bozga, G.; Ainser, A. Residence Time Distribution in a Corotating Twin-Screw Extruder. *Chem. Eng. Sci.* **2000**, *55*, 1641–1651.

(71) Kumar, A.; Ganjyal, G. M.; Jones, D. D.; Hanna, M. A. Modeling Residence Time Distribution in a Twin-Screw Extruder as a Series of Ideal Steady-State Flow Reactors. *J. Food Eng.* **2008**, *84*, 441–448.

(72) Baron, R.; Vauchel, P.; Kaas, R.; Arhaliass, A.; Legrand, J. Dynamical Modelling of a Reactive Extrusion Process: Focus on Residence Time Distribution in a Fully Intermeshing Co-Rotating Twin-Screw Extruder and Application to an Alginate Extraction Process. *Chem. Eng. Sci.* **2010**, *65*, 3313–3321.

(73) Amedu, O. K.; Penlington, R.; Busawon, K.; Morgan, A. Application of Statistical Techniques and Mechanistic Modelling to the Mixing Process in Co-Rotating Twin-Screw Extruders. In *2013 AIChE Annual Meeting Conference Proceedings*; San Francisco, 2013.

(74) Mudalamane, R.; Bigio, D. I. Process Variations and the Transient Behavior of Extruders. *AIChE J.* **2003**, *49*, 3150–3160.

(75) Yang, H.-H.; Manas-Zloczower, I. Flow Field Analysis of the Kneading Disc Region in a Co-Rotating Twin Screw Extruder. *Polym. Eng. Sci.* **1992**, *32*, 1411–1417.

(76) Ishikawa, T. 3-D Non-Isothermal Flow Field Analysis and Mixing Performance Evaluation of Kneading Blocks in a Co-Rotating Twin Srew Extruder. *Polym. Eng. Sci.* **2001**, *41*, 840–849.

(77) Bertrand, F.; Thibault, F.; Delamare, L.; Tanguy, P. A. Adaptive Finite Element Simulations of Fluid Flow in Twin-Screw Extruders. *Comput. Chem. Eng.* **2003**, *27*, 491–500.

(78) Pokriefke, G. Numerische Analyse reibungsbehafteter Strömungen in teilgefüllten Extrudern, Universität der Bundeswehr Hamburg, 2005.

(79) Pokriefke, G. Numerical Simulation of 2d Fluid Flow in an Partially Filled Simplified Extruder Model. *Proc. Appl. Math. Mech.* **2003**, *3*, 418–419.

(80) Ficarella, A.; Milanese, M.; Laforgia, D. Numerical Study of the Extrusion Process in Cereals Production: Part I. Fluid-Dynamic Analysis of the Extrusion System. *J. Food Eng.* **2006**, *73*, 103–111.

(81) Ficarella, A.; Milanese, M.; Laforgia, D. Numerical Study of the Extrusion Process in Cereals Production: Part II. Analysis of Variance. *J. Food Eng.* **2006**, *72*, 179–188.

(82) Barrera, M. A.; Vega, J. F.; Martínez-Salazar, J. Three-Dimensional Modelling of Flow Curves in Co-Rotating Twin-Screw Extruder Elements. *J. Mater. Process. Technol.* **2008**, *197*, 221–224.

(83) Bierdel, M. Computational Fluid Dynamics. In *Co-Rotating Twin-Screw Extruders*; Kohlgrüber, K., Ed.; Carl Hanser Publishers: Munich, 2008.

(84) Conzen, C. Numerische und experimentelle Untersuchungen zu Transportvorgängen in Schneckenmaschinen, Universität Kassel, 2008.

(85) Rodríguez, E. O. Numerical Simulations of Reactive Extrusion in Twin Screw Extruders, Waterloo, Canada, 2009.

(86) Haghayeghi, R.; Khalajzadeh, V.; Farahani, M. F.; Bahai, H. Experimental and CFD Investigation on the Solidification Process in a Co-Rotating Twin Screw Melt Conditioner. *J. Mater. Process. Technol.* **2010**, *210*, 1464–1471.

(87) Vyakaranam, K. V.; Ashokan, B. K.; Kokini, J. L. Evaluation of Effect of Paddle Element Stagger Angle on the Local Velocity Profiles in a Twin-Screw Continuous Mixer with Viscous Flow Using Finite Element Method Simulations. *J. Food Eng.* **2012**, *108*, 585–599.

(88) Sobhani, H.; Anderson, P. D.; Meijer, H. H. E.; Ghoreishy, M. H. R.; Razavi-Nouri, M. Non-Isothermal Modeling of a Non-Newtonian Fluid Flow in a Twin Screw Extruder Using the Fictitious Domain Method. *Macromol. Theory Simulations* **2013**, *22*, 462–474.

(89) Sarhangi Fard, A.; Hulsen, M. A.; Meijer, H. E. H.; Famili, N. M. H.; Anderson, P. D. Adaptive Non-Conformal Mesh Refinement and Extended Finite Element Method for Viscous Flow inside Complex Moving Geometries. *Int. J. Numer. methods fluids* **2012**, *68*, 1031–1052.

(90) Sarhangi Fard, A.; Hulsen, M. A.; Meijer, H. E. H.; Famili, N. M. H.; Anderson, P. D. Tools to Simulate Distributive Mixing in Twin-Screw Extruders. *Macromol. Theory Simulations* **2012**, *21*, 217–240.

(91) Sarhangi Fard, A.; Anderson, P. D. Simulation of Distributive Mixing inside Mixing Elements of Co-Rotating Twin-Screw Extruders. *Comput. Fluids* **2013**, *87*, 79–91.

(92) Hétu, J.-F.; Ilinca, F. Immersed Boundary Finite Elements for 3D Flow Simulations in Twin-Screw Extruders. *Comput. Fluids* **2013**, *87*, 2–11.

(93) Rathod, M. L.; Kokini, J. L. Effect of Mixer Geometry and Operating Conditions on Mixing Efficiency of a Non-Newtonian Fluid in a Twin Screw Mixer. *J. Food Eng.* **2013**, *118*, 256–265.

(94) Carneiro, O. S.; Nóbrega, J. M.; Pinho, F. T.; Oliveira, P. J. Computer Aided Rheological Design of Extrusion Dies for Profiles. *J. Mater. Process. Technol.* **2001**, *114*, 75–86.

(95) Lin, Z.; Juchen, X.; Xinyun, W.; Guoan, H. Optimization of Die Profile for Improving Die Life in the Hot Extrusion Process. *J. Mater. Process. Technol.* **2003**, *142*, 659–664.

(96) Patil, P. D.; Feng, J. J.; Hatzikiriakos, S. G. Constitutive Modeling and Flow Simulation of Polytetrafluoroethylene (PTFE) Paste Extrusion. *J. Nonnewton. Fluid Mech.* **2006**, *139*, 44–53.

(97) Mitsoulis, E.; Hatzikiriakos, S. G. Steady Flow Simulations of Compressible PTFE Paste Extrusion under Severe Wall Slip. *J. Nonnewton. Fluid Mech.* **2009**, *157*, 26–33.

(98) Radl, S.; Tritthart, T.; Khinast, J. G. A Novel Design for Hot-Melt Extrusion Pelletizers. *Chem. Eng. Sci.* **2010**, *65*, 1976–1988.

(99) Ardakani, H. A.; Mitsoulis, E.; Hatzikiriakos, S. G. Thixotropic Flow of Toothpaste through Extrusion Dies. *J. Nonnewton. Fluid Mech.* **2011**, *166*, 1262–1271.

(100) Monaghan, J. J. Smoothed Particle Hydrodynamics and Its Diverse Applications. *Annu. Rev. Fluid Mech.* **2012**, *44*, 323–346.

(101) Gingold, R. A.; Monaghan, J. J. Smoothed Particle Hydrodynamics: Theory and Application to Non-Spherical Stars. *Mon. Not. R. Astron. Soc.* **1977**, *181*, 375–389.

(102) Lucy, L. B. A Numerical Approach to the Testing of the Fission Hypothesis. *Astron. J.* **1977**, *82*, 1013–1024.

(103) Gingold, R. A.; Monaghan, J. J. Kernel Estimates as a Basis for General Particle Methods in Hydrodynamics. *J. Comput. Phys.* **1982**, *46*, 429–453.

(104) Monaghan, J. J. Simulating Free Surface Flows with SPH. *J. Comput. Phys.* **1994**, *110*, 339–406.

(105) Monaghan, J. J. Smoothed Particle Hydrodynamics. *Reports Prog. Phys.* **2005**, *68*, 1703–1759.

(106) Robinson, M.; Cleary, P.; Monaghan, J. Analysis of Mixing in a Twin Cam Mixer Using Smoothed Particle Hydrodynamics. *AIChE J.* **2008**, *54*, 1987–1998.

(107) Avalosse, T.; Crochet, M. J. Finite-Element Simulation of Mixing: 1. Two-Dimensional Flow in Periodic Geometry. *AIChE J.* **1997**, *43*, 577–587.

(108) Robinson, M.; Cleary, P. W. Flow and Mixing Performance in Helical Ribbon Mixers. *Chem. Eng. Sci.* **2012**, *84*, 382–398.

(109) Cleary, P. W.; Robinson, M. Understanding Viscous Fluid Transport and Mixing in a Twin Screw Extruder. In *8th International Conference on CFD in Oil & Gas, Metallurgical and Process Industries*; Trondheim, Norway, 2011.

(110) Monaghan, J. J.; Kajtar, J. B. SPH Particle Boundary Forces for Arbitrary Boundaries. *Comput. Phys. Commun.* **2009**, *180*, 1811–1820.

(111) Monaghan, J. J.; Kos, A. Solitary Waves on a Cretan Beach. *J. Waterw. Port, Coast. Ocean Eng.* **1999**, *125*, 145–154.

(112) Dalrymple, R. A.; Knio, O. SPH Modelling of Water Waves. *Coast. Dyn.* **2001**, 779–787.

(113) M. Gómez-Gesteira; Dalrymple, R. A. Using a Three-Dimensional Smoothed Particle Hydrodynamics Method for Wave Impact on a Tall Structure. *J. Waterw. Port, Coast. Ocean Eng.* **2004**, *130*, 63–69.

(114) Takeda, H.; Miyama, S. M.; Sekiya, M. Numerical Simulation of Viscous Flow by Smoothed Particle Hydrodynamics. *Prog. Theor. Phys.* **1994**, *92*, 939–960.

(115) Randles, P. W.; Libersky, L. D. Smoothed Particle Hydrodynamics : Some Recent Improvements and Applications. *Comput. Methods Appl. Mech. Eng.* **1996**, *139*, 375–408.

(116) Colagrossi, A.; Landrini, M. Numerical Simulation of Interfacial Flows by Smoothed Particle Hydrodynamics. *J. Comput. Phys.* **2003**, *191*, 448–475.

(117) De Leffe, M.; Le Touzé, D.; Alessandrini, B. A Modified No-Slip Condition in Weakly-Compressible SPH. In *6th International SPHERIC Workshop*; Rung, T.; Ulrich, C., Eds.; Schriftenreihe Schiffbau: Hamburg, 2011; pp. 291–297.

(118) Børve, S. Generalized Ghost Particle Method for Handling Boundaries. In *6th International SPHERIC Workshop*; Rung, T.; Ulrich, C., Eds.; Schriftenreihe Schiffbau: Hamburg, 2011; pp. 313–320.

(119) Gomez-Gesteira, M.; Rogers, B. D.; Dalrymple, R. A.; Crespo, A. J. C. Numerical Simulation of Interfacial Flows by Smoothed Particle Hydrodynamics. *J. Hydraul. Res.* **2010**, *48*, 6–27.

(120) Feldman, J.; Bonet, J. Dynamic Refinement and Boundary Contact Forces in SPH with Applications in Fluid Flow Problems. *Int. J. Numer. Methods Eng.* **2007**, *72*, 295–324.

(121) Ferrand, M.; Violeau, D.; Rogers, B. D.; Laurence, D. Consistent Wall Boundary Treatment for Laminar and Turbulent Flows in SPH. In *6th International SPHERIC Workshop*; Rung, T.; Ulrich, C., Eds.; Schriftenreihe Schiffbau: Hamburg, 2011; pp. 275–282.

(122) Kruisbrink, A. C. H.; Pearce, F. R.; Yue, T.; Cliffe, K. A.; H. P. Morvan. *SPH Concepts for Continuous Wall and Pressure Boundaries*; Rung, T.; Ulrich, C., Eds.; Schriftenreihe Schiffbau: Hamburg, 2011; pp. 298–304.

"*The aim of science is not to open the door to infinite wisdom,*
but to set a limit to infinite error."

(Bertolt Brecht)

2

Goals and Content

2.1 Goals

This thesis is the beginning of research activities in the field of modeling co-rotating twin-screw extruders in the group of Prof. Khinast (Institute of Process and Particle Engineering and Research Center Pharmaceutical Engineering GmbH). In this first step, the modeling should be focused on viscous flow and mixing. The plastification is more complex and should not be addressed in this thesis.

Spatially resolved flow simulations of co-rotating twin-screws are computationally still too expensive for their extensive application to entire extruders. The less expensive one-dimensional (1D) models do not spatially resolve the flow, and therefore require predefined parameters which describe the behavior of different screw elements. Thus, the combination of the 1D approach and a spatially resolved model could afford more than a single approach, and the goal was to explore how the benefits of these approaches could support each other.

Specifically, a 1D model should be newly implemented based on first principles and available models from the literature. This model should allow to investigate the impact of the actual screw configuration as well as operation and material parameters on the process. Moreover, it should facilitate the scale-up of extrusion processes. Experiments with a typical polymer used for pharmaceutical hot-melt extrusion and literature data should be used to validate the model results.

The spatially resolved model should be based on the smoothed particle hydrodynamics (SPH) method. It should be explored, if SPH can be applied to study flow and mixing in typical screw geometries of co-rotating twin-screws, and if SPH facilitates the simulation of partially filled screw sections, which typically occur in the reality and are highly challenging for the mesh-based computational fluid dynamics (CFD) methods. The results should be validated with CFD data from the literature for a completely filled geometry.

2.2 Content

The main part of this thesis consists of six articles, which include the most important results of the conducted research (Chapters 3-8). Chapters 3, 4 and 5 were published and Chapters 6 and 7 submitted before the printing date of the thesis, the remaining Chapter 8 is also intended for publication. For details, see the publication list at the end of the thesis.

Chapter 3 presents experimental results for the pressure characteristic of different screw element types (including conveying and kneading elements) with a typical non-Newtonian polymer available for pharmaceutical hot-melt extrusion. In order to obtain reasonable data for the melt temperature, a specific design for the location of the temperature probe was developed in order to avoid impact of the barrel wall temperature. Measured data and fitted model parameters for the temperature dependent density and rheology of the polymer melt are included. A pressure characteristic model was used to fit the measured pressure and temperature data. It was shown that two empirical parameters for each screw element were sufficient to describe the measured pressure drop for all investigated variations of screw speed, throughput, and the corresponding variations of the melt temperature.

Chapter 4 shows, how the pressure characteristic model of Chapter 3 can be employed in a 1D model of the co-rotating twin-screw extruder with modular screws. Since the reasonable computation of the viscous dissipation and the heat transfer between melt and barrel were essential, specific modeling effort was addressed to these aspects. The 1D model yielded profiles of process variables along the screws, as the screw filling ratio, pressure and melt temperature for a defined configuration of the modular screws and given material and operation parameters. Furthermore, the associated residence time distribution (RTD) was obtained. The results include a comparison of the power input to CFD data from the literature[1] for a Newtonian fluid and a comparison of model results to the

experimental measurements of Chapter 3. Moreover, a comparison of model results for the RTD to experimental data from the literature is included.[2]

Chapter 5 is not related to the previous Chapters, and reports preliminary preparations required for the application of the SPH method to the complex geometry of twin-screw extruders. Specifically, the development of a model for the interaction of fluid elements with continuous walls is presented, based on the investigation of a wall consisting of fixed fluid particles. The resulting model was implemented into the open-source particle simulator LIGGGHTS[3] and velocity profiles for different scenarios in a channel flow were compared to analytical solutions and SPH solutions with fixed fluid particles. Moreover, mixing in a twin-cam mixer was simulated and compared to experimental and numerical results from the literature.[4–6]

In Chapter 6, the Newtonian flow in a conveying element of a co-rotating twin-screw extruder is analyzed based on SPH and the developed wall interaction of Chapter 5. Since the spatial resolution is usually constant in SPH (apart from emerging, sophisticated techniques for variable resolution), the flow through the tight clearances could not be resolved. To overcome this, a clearance model was developed, which accounts for the unresolved clearance flow. The detailed derivation and validation of the clearance model is included in Chapter 6. The results showed excellent agreement with CFD data from the literature for the completely filled state.[1] Beyond that, the filling ratio was varied and an analysis of the flow field in the partially filled state is included.

Chapter 7 focuses on the mixing phenomena associated with the results presented in Chapter 6. Tracer particles were tracked during several screw revolutions and the intensity of segregation was evaluated using a grid of cubed cells. The resulting time evolution of the intensity of segregation was used to determine mixing rates for all investigated operation states. The separate evaluation of axial mixing allowed an in-depth analysis of the observed mixing phenomena.

In Chapter 8, the SPH method and the achieved developments were applied to study the Newtonian flow and mixing in different types of screw elements, including conveying elements, kneading elements and a mixing element. The results highlighted the differences

in conveying, pressure generation, power input and mixing among the investigated screw elements. Moreover, these results provide essential input data for the 1D model presented in Chapter 4.

Chapters 9 provides general conclusions of the presented results, and points out which aspects should be addressed in future work.

2.3 Abbreviations

1D	one-dimensional
CFD	computational fluid dynamics
RTD	residence time distribution
SPH	smoothed particle hydrodynamics

2.4 References

(1) Bierdel, M. Computational Fluid Dynamics. In *Co-Rotating Twin-Screw Extruders*; Kohlgrüber, K., Ed.; Carl Hanser Publishers: Munich, 2008.

(2) Puaux, J. .; Bozga, G.; Ainser, A. Residence Time Distribution in a Corotating Twin-Screw Extruder. *Chem. Eng. Sci.* **2000**, *55*, 1641–1651.

(3) Kloss, C.; Goniva, C.; Hager, A.; Amberger, S.; Pirker, S. Models, Algorithms and Validation for Opensource DEM and CFD-DEM. *Prog. Comput. Fluid Dyn. An Int. J.* **2012**, *12*, 140–152.

(4) Avalosse, T.; Crochet, M. J. Finite-Element Simulation of Mixing: 1. Two-Dimensional Flow in Periodic Geometry. *AIChE J.* **1997**, *43*, 577–587.

(5) Bertrand, F.; Thibault, F.; Delamare, L.; Tanguy, P. A. Adaptive Finite Element Simulations of Fluid Flow in Twin-Screw Extruders. *Comput. Chem. Eng.* **2003**, *27*, 491–500.

(6) Robinson, M.; Cleary, P.; Monaghan, J. Analysis of Mixing in a Twin Cam Mixer Using Smoothed Particle Hydrodynamics. *AIChE J.* **2008**, *54*, 1987–1998.

"*Measure what can be measured, and make measureable what cannot be measured.*"

(Galileo Galilei)

3

Experimental Characterization and Modeling of Twin-Screw Extruder Elements for Pharmaceutical Hot-Melt Extrusion*

In this study we characterized various screw elements of a co-rotating twin-screw extruder used for pharmaceutical hot-melt extrusion (HME) and measured the pressure characteristic, i.e., the correlation between the axial pressure gradient and the material throughput in a completely filled screw section at different screw speeds. A typical HME matrix material, Soluplus, was used for the experiments and its required rheological properties were determined. A three-parameter model based on a dimensionless formulation of the measured quantities was used. These parameters could not be determined uniquely by fitting to experimental data. Therefore we developed an approach to approximate one empirical parameter based on the mechanistic consideration of a pressure-driven channel flow. The model was extended to account for the variable melt temperature. The results confirmed the expected tendencies and established an essential input parameter set for one-dimensional simulations of co-rotating twin-screw extruders.

---

* This chapter is based on: Eitzlmayr, A.; Khinast, J.; Hörl, G.; Koscher, G.; Reynolds, G.; Huang, Z.; Booth, J.; Shering, P. Experimental Characterization and Modeling of Twin-Screw Extruder Elements for Pharmaceutical Hot Melt Extrusion. *AIChE J.* 2013, 59, 11, 4440–4450.

3.1 Introduction

Hot-melt extrusion (HME) has been used for many decades in various industries (e.g., plastics and food) and, in recent years, has become an important pharmaceutical manufacturing operation.[1] Extrusion is defined as the process of forcing a material through a die under controlled conditions and high pressure. HME applies temperature levels above the melting (or softening) point in order to extrude the material in a viscous state.[2] In pharmaceutical manufacturing, HME can potentially increase the bioavailability of poorly soluble drugs,[3] form solid solutions and amorphous solid dispersions[4] and enhance the product quality due to the mixing efficiency of extruders.[2] Moreover, in a single step raw materials can be converted into a final delivery form, e.g., through calandering.

Screw extruders (single-, twin- and multi-screw) are the most common extrusion devices,[1] which combine various process steps such as mixing, melting, conveying, degassing and dissolution of particles in a single device. These properties increase the manufacturing efficiency and reduce operation costs.[2] In pharmaceutical manufacturing, typically co-rotating twin-screw extruders with self-cleaning screws and modular screw design are used, i.e., the screws are divided into different types of screw elements (e.g., conveying elements, kneading elements), which can be individually arranged to accommodate actual process requirements. While this feature offers high flexibility, achieving optimal process conditions is a challenge since developing optimal screw configurations requires experience and/or experimental work based on trial and error.

Mechanistic models can provide useful insights into the effects of various screw configurations, improve understanding of the underlying mechanisms and reduce the experimental and empirical effort. Although different models describing the flow field in screw extruders have been developed, not all aspects of the extrusion process can be predicted in detail. For example, to date no detailed methods exist for the simulation of the flow in partially filled screws. The involved physical phenomena (non-Newtonian flow, wall slip, small gaps, free surfaces, etc.) are highly complex and first principles design methods are not available.[5]

Existing mechanistic models of the entire HME process are based on one-dimensional (1D) models of the flow along co-rotating twin screws, resolving the pressure and filling ratio

along the screw axis.[6–9] These models basically account for the pressure-throughput correlation of single screw elements, describing the pressure gradient versus flow rate in completely filled screw sections.[5,10–14] The resulting predictions of the material transport along the screw have been used to develop models of the residence time distribution in extruders.[15–19] In recent years, this approach has been extended to models of reactive extrusion.[20–22] Spatially resolved simulations of the flow field in completely filled screw sections have been performed using computational fluid dynamics (CFD),[14,23–28] but they cannot be applied to an entire twin screw due to the required calculation effort and the challenge of partially-filled screw sections in three-dimensional simulations. Thus, simplified descriptions of extrusion processes are still prevalent.

Pawlowski[10] showed that for single screw extruders and Newtonian fluids in the creeping flow regime the axial pressure gradient is linearly correlated with the throughput, and described the correlation by an empirical model termed “pressure characteristic”, based on dimensionless numbers. Since the pressure characteristic is determined by the detailed screw geometry, the used empirical parameters are called “screw parameters”. Kohlgrüber[5] applied this concept to co-rotating twin-screw extruders and extended it to shear-thinning polymer melts described by the Carreau model.

In our work, we developed a 1D simulation for co-rotating twin-screw extruders based on the pressure-characteristic model by Kohlgrüber[5]. To simulate a real extrusion process, screw parameters for all used screw elements must be provided as input parameters. Thus, we present pressure-characteristic measurements for different screw elements and the resulting screw parameters using Soluplus, a typical matrix material for pharmaceutical HME. The required temperature-dependent rheological material parameters of Soluplus have been measured. In the extrusion experiments, we found a slight variation of the melt temperature with the throughput, which is not negligible due to the strong temperature dependency of the viscosity. To account for this effect, the pressure characteristic was corrected for the temperature-dependence of the material parameters. Moreover, we developed an approach to estimate the empirical shear rate parameter A_3 to overcome an underdetermined fitting problem. In summary, input parameters for the 1D simulation of co-rotating twin-screw extruders were established.

3.2 Mathematical Model

3.2.1 Pressure Characteristic Model

The description of Pawlowski[10] and Kohlgrüber[5] is based on a dimensionless formulation of the volumetric throughput and the axial pressure gradient in completely filled screw sections (similarly to [11]), where the dimensionless throughput $\dot{V}^*$ is defined as the volumetric throughput $\dot{V}$ over the screw speed n and the nominal screw diameter D cubed:

$$\dot{V}^* = \frac{\dot{V}}{nD^3} \tag{3.1}$$

For measurement purposes, the axial pressure gradient $\partial p/\partial x$ is approximated by the quotient of pressure difference and axial distance $\Delta p/\Delta x$ (see Figure 3.7). The dimensionless axial pressure gradient $\Delta p^*/\Delta x^*$ is defined using the dynamic viscosity of the material η, the screw speed n and the nominal screw diameter D as follows:

$$\left(\frac{\Delta p^*}{\Delta x^*}\right) = \frac{\Delta p}{\eta \cdot n} \cdot \frac{D}{\Delta x} \tag{3.2}$$

The correlation between dimensionless throughput $\dot{V}^*$ and dimensionless axial pressure gradient ($\Delta p^*/\Delta x^*$) is termed pressure characteristic. Using the described dimensionless quantities, Pawlowski[10] experimentally showed that the pressure characteristic of a certain screw element is invariant for different screw speeds n, screw diameters D and viscosities η under the following conditions:

- Creeping flow, i.e., sufficiently low Reynolds number $Re = \rho \cdot n \cdot D^2/\eta$ (ρ being the density). The limiting Reynolds number depends on the screw geometry. In a specific case (D=60mm) Re<100 satisfied this condition.[10] Typically, high-viscosity materials used in HME generally lead to Reynolds numbers below 1 and thus in technically-relevant cases the creeping flow regime can be assumed.

- Newtonian fluid.

- Geometrical similarity of the entire flow-relevant geometry.

Furthermore, it was demonstrated that for Newtonian fluids in the creeping flow regime the pressure characteristic follows a linear function, which is described as:[5,10]

$$\frac{\Delta p^*}{\Delta x^*} = \frac{\Delta p}{\eta \cdot n} \cdot \frac{D}{\Delta x} = A_2 \cdot \left(1 - \frac{\dot{V}^*}{A_1}\right) \tag{3.3}$$

where A_1 and A_2 are the screw parameters, i.e., the axis intercepts of the linear function (i.e., $\Delta p^*/\Delta x^* = 0$ for $\dot{V}^* = A_1$ and $\Delta p^*/\Delta x^* = A_2$ for $\dot{V}^* = 0$). Thus, parameter A_1 represents the throughput in a completely filled screw section without back pressure (i.e., inherent conveying capacity), whereas A_2 represents the pressure gradient in a completely filled screw section conveying towards a closed die. An approximation for A_1 is given as:[29]

$$A_1 \approx \frac{1}{2} \frac{A_{cr} \cdot T_S}{D^3} \tag{3.4}$$

where A_{cr} is a free cross-section area illustrated as a shaded area in Figure 3.2 and T_S is the screw pitch. In reality, typical materials used for HME are not Newtonian fluids but rather shear-thinning materials that can often be described via the Carreau model for constant temperature:[5,30]

$$\eta(\dot{\gamma}) = \frac{\eta_0}{\left[1 + \frac{|\dot{\gamma}|}{\dot{\gamma}_{crit}}\right]^m} \tag{3.5}$$

where η_0 is the zero-shear-rate viscosity, $\dot{\gamma}_{crit}$ is the critical shear rate and m the Carreau exponent. Kohlgrüber[5] extended the linear pressure characteristic for Newtonian fluids to non-Newtonian fluids described by the Carreau model. For this purpose, the Newtonian viscosity in Eq. 3.3 was substituted by Eq. 3.5:

$$\frac{\Delta p^*}{\Delta x^*} = \frac{\Delta p}{\frac{\eta_0}{\left[1 + \frac{|\dot{\gamma}|}{\dot{\gamma}_{crit}}\right]^m} \cdot n} \cdot \frac{D}{\Delta x} = A_2 \cdot \left(1 - \frac{\dot{V}^*}{A_1}\right) \tag{3.6}$$

Then the dimensionless axial pressure gradient was re-defined for a Carreau fluid (indicated by index *C*) using the zero-shear-rate viscosity η_0 as:

$$\frac{\Delta p_C^*}{\Delta x^*} = \frac{\Delta p}{\eta_0 \cdot n} \cdot \frac{D}{\Delta x} = \frac{A_2 \cdot \left(1 - \frac{\dot{V}^*}{A_1}\right)}{\left[1 + \frac{|\dot{\gamma}|}{\dot{\gamma}_{crit}}\right]^m} \tag{3.7}$$

This pressure characteristic function is non-linear and predicts lower pressure gradients compared to the linear function in the Newtonian case caused by the shear-thinning effect of the melt. However, the issue of how to determine the shear rate $\dot{\gamma}$ is critical for a correct representation of the problem.

In the real flow field around the screws the shear rate is varying strongly, e.g., in the smallest gaps of O(10^{-4}-10^{-3} m) higher shear rates can be expected than in the screw channels of O(10^{-3}-10^{-2} m). Thus, using a single value for the shear rate in Eq. 3.7 ("representative shear rate" $\dot{\gamma}_r$) is a simplification. However, Kohlgrüber[5] created a model that describes the representative shear rate proportional to the pressure-induced backflow (1-$\dot{V}^*/A_1$). At the inherent conveying point ($\dot{V}^* = A_1$), where no pressure-induced backflow occurs, the representative shear rate is zero. The representative shear rate increases with the increasing backflow. Furthermore, the shear rate is set to be proportional to the screw speed and an empirical fitting parameter A_3:

$$\dot{\gamma}_r = A_3 \cdot n \cdot \left(1 - \frac{\dot{V}*}{A_1}\right) \tag{3.8}$$

Substituting this in Eq. 3.7 leads to the following pressure characteristic function:[5]

$$\frac{\Delta p_C^*}{\Delta x^*} = \frac{\Delta p}{\eta_0 \cdot n} \cdot \frac{D}{\Delta x} = \frac{A_2 \cdot \left(1 - \frac{\dot{V}^*}{A_1}\right)}{\left[1 + \frac{A_3 \cdot n}{\dot{\gamma}_{crit}} \cdot \left|1 - \frac{\dot{V}^*}{A_1}\right|\right]^m} \tag{3.9}$$

Eq. 3.9 can be used to fit the measured pressure gradients for shear-thinning fluids described by the Carreau model.[5] Kohlgrüber[5] also presented a formulation equivalent to Eq. 3.9, which is based on the representative viscosity η_r (with $\eta_r = \eta(\dot{\gamma}_r)$ from Eq. 3.5 and $\dot{\gamma}_r$ from Eq. 3.8):

$$\frac{\Delta p^*}{\Delta x^*} = \frac{\Delta p}{\eta_r \cdot n} \cdot \frac{D}{\Delta x} = A_2 \cdot \left(1 - \frac{\dot{V}^*}{A_1}\right) \tag{3.10}$$

Here, the shear thinning effect is incorporated into the representative viscosity η_r, leading to a representation in which the measured data points of shear-thinning fluids are located along the linear pressure characteristic function of Newtonian fluids.

3.2.2 Approximation of A_3

Our study showed that establishing the three screw parameters (A_1, A_2, A_3) by fitting the measured data leads to an underdetermined problem, i.e., different combinations of A_1, A_2, A_3 can describe the measurements equally well. Furthermore, the calculated pressure gradient is significantly less sensitive to variations of parameter A_3 than of parameters A_1 and A_2 (which can easily be demonstrated by varying parameters in Eq. 3.9). Thus, we approximate the value of A_3 based on a simplified model of a two-dimensional channel flow between two plates (see Figure 3.1). Assuming a stationary and developed flow, the force balance relates the pressure gradient $\partial p/\partial x$ and the wall shear stress τ_W as:

$$\frac{\partial p}{\partial x} \cdot l \cdot b \cdot h = 2 \cdot \tau_W \cdot b \cdot l \tag{3.11}$$

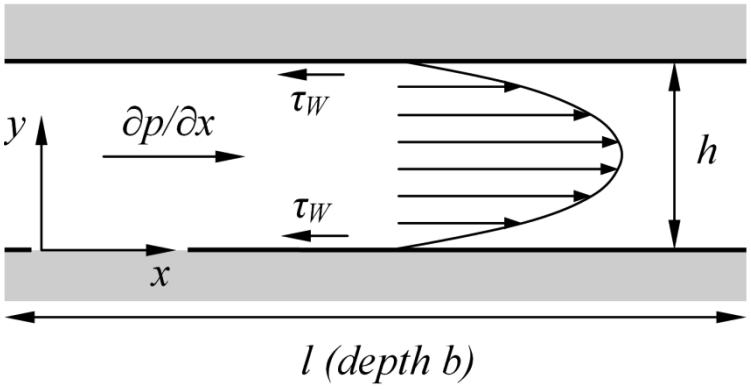

Figure 3.1: Two-plate model.

The wall shear stress can be written as product of wall shear rate and the corresponding viscosity $\tau_W = \eta_W \cdot \dot{\gamma}_W$ with $\eta_W = \eta(\dot{\gamma}_W)$. If so, Eq. 3.11 leads to

$$\dot{\gamma}_W = \frac{1}{\eta_W}\frac{\partial p}{\partial x}\cdot\frac{h}{2} \tag{3.12}$$

Considering Eq. 3.8 and substituting the term in brackets with Eq. 3.10 results in

$$\dot{\gamma}_r = \frac{1}{\eta_r}\cdot\frac{\Delta p}{\Delta x}\cdot\frac{A_3}{A_2}\cdot D \tag{3.13}$$

Comparing the simplified two-plate model with the real situation of a twin-screw, and assuming, that $\dot{\gamma}_W$ and η_W are estimates for $\dot{\gamma}_r$ and η_r, Eqs. 3.12 and 3.13 yield the following approximation for A_3:

$$A_3 \approx \frac{A_2 \cdot h}{2 \cdot D} \tag{3.14}$$

In this equation, the gap distance *h* is not known. In fact, the gap distance between the screw and the barrel in an extruder varies depending on the cross sectional profile of the screws (see Figure 3.2).

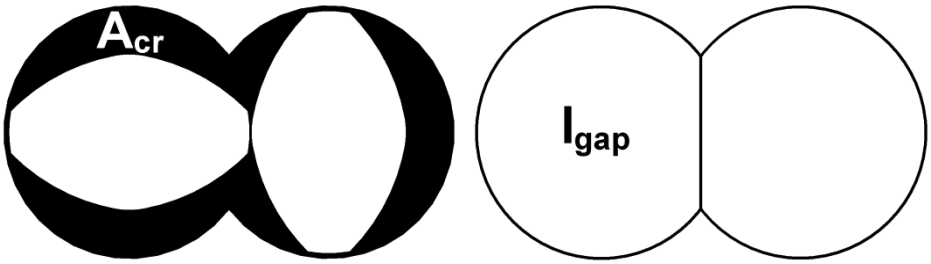

Figure 3.2: Schematic of gap cross section area A_{cr} (left) and gap length l_{gap} (right).

To create an average, the parameter h was estimated as ratio between the gap cross section area A_{cr} (i.e., shaded area in Figure 3.2 top) and the gap length l_{gap} (estimated as the entire length of the lines shown in Figure 3.2 bottom). Parameter h was calculated as:

$$h = \frac{A_{cr}}{l_{gap}} \tag{3.15}$$

The use of Eqs. 3.14 and 3.15 reduces the number of free parameters to two (A_1, A_2), and the solution of the fitting problem is unique.

3.2.3 Temperature Dependency

As expected, the melt temperature was not constant during our measurements. In addition to the expected dependence of the melt temperature on the screw speed, the melt temperature also slightly varied with the throughput. Due to the strong temperature dependency of the viscosity we could not neglect this effect and incorporated the temperature dependency in the pressure characteristic of Kohlgrüber[5], using a temperature shift factor a_T in the Carreau model Eq. 3.5:[31]

$$\eta(\dot{\gamma},T)=\frac{\eta_0 \cdot a_T}{\left(1+\frac{|\dot{\gamma}|\cdot a_T}{\dot{\gamma}_{crit}}\right)^m} \tag{3.16}$$

The temperature shift factor in our case can be described by the Williams-Landel-Ferry (WLF) equation (often used for amorphous thermoplasts[30]), where C_1 and C_2 are material constants, i.e.,

$$a_T=\exp\left[\frac{-C_1\cdot(T-T_r)}{C_2+T-T_r}\right] \tag{3.17}$$

Using this and the approximation of A_3 (Eq. 3.14), the pressure characteristic function Eq. 3.9 becomes:

$$\frac{\Delta p_C^*}{\Delta x^*}=\frac{\Delta p}{\eta_0\cdot a_T\cdot n}\cdot\frac{D}{\Delta x}=\frac{A_2\cdot\left(1-\frac{\dot{V}^*}{A_1}\right)}{\left[1+\frac{A_2\cdot n\cdot a_T}{\dot{\gamma}_{crit}}\cdot\frac{h}{2D}\cdot\left|1-\frac{\dot{V}^*}{A_1}\right|\right]^m} \tag{3.18}$$

Eq. 3.10 remains unchanged. The representative viscosity is described by Eq. 3.16 for non-isothermal conditions.

3.2.4 Non-Conveying Elements

The proposed concept was shown by Kohlgrüber[5] for actively conveying elements. Here we derived a modification for non-conveying elements (e.g., kneading elements with 90° offset angle) for which parameters A_1 and A_2 are zero (i.e., the inherent conveying capacity and the ability to generate pressure are zero). In the limit of A_1, A_2 going to zero in Eq. 3.18, the following equation is recovered, where $A_0=A_2/A_1$ for $A_1, A_2 \rightarrow 0$:

$$\frac{\Delta p_C^*}{\Delta x^*} = \frac{\Delta p}{\eta_0 \cdot a_T \cdot n} \cdot \frac{D}{\Delta x} = \frac{-A_0 \cdot \dot{V}^*}{\left[1 + \frac{A_0 \cdot n \cdot a_T}{\dot{\gamma}_{crit}} \cdot \frac{h}{2D} \cdot \left|\dot{V}^*\right|\right]^m} \tag{3.19}$$

Similarly, Eq. 3.8 including the approximation of A_3 (Eq. 3.14) and Eq. 3.10 can be used for non-conveying screw elements:

$$\dot{\gamma}_r = A_0 \cdot n \cdot \frac{h}{2D} \cdot \dot{V}^* \tag{3.20}$$

$$\frac{\Delta p^*}{\Delta x^*} = \frac{\Delta p}{\eta_r \cdot n} \cdot \frac{D}{\Delta x} = -A_0 \cdot \dot{V}^* \tag{3.21}$$

where the representative viscosity $\eta_r = \eta(\dot{\gamma}_r, T)$ is described by Eq. 3.16.

3.3 Material Properties

In our experiments the pharmaceutical-grade matrix material Soluplus was used, which is a polyvinyl caprolactam-polyvinyl acetate-polyethylene glycol graft copolymer specifically designed for HME. Soluble in water and many organic solvents, it is well-suited as a solubilizer for poorly soluble drugs. More detailed information can be obtained from the manufacturer.[32] To evaluate our measurements, the equation of state and viscosity depending on the temperature and shear rate are required.

3.3.1 Equation of State

The equation of state of Soluplus was measured with a PVT-device of type PVT100 (SWO Polymertechnik GmbH, Germany) according to the standard ISO 17744.[33] Isobar-cooling

with 6 K/min at 5 different pressure levels from 200-1200 bar was used. The measured data were fitted with the Menges model[34] (parameters K_1 – K_4 are different for solid and liquid state), which describes the specific volume v [m^3/kg] depending on pressure p and temperature T:

$$v = \frac{K_1}{p + K_4} + \frac{K_2 \cdot T}{p + K_3} \tag{3.22}$$

The transition temperature between solid and liquid states (in this case the glass transition temperature) depending on pressure p is described by:

$$T_{trans} = K_8 + K_9 \cdot p \tag{3.23}$$

Table 3.1: Menges model parameters.

	Solid	Liquid
K_1 [bar cm³/g]	29716	29519
K_2 [bar cm³/g°C]	0.35526	1.1618
K_3 [bar]	1671.5	2614.4
K_4 [bar]	34326	34783
	Transition temperature	
K_8 [°C]	72.729	
K_9 [°C/bar]	0.020912	

The parameters established through the experiments are provided in Table 3.1. The resulting dependence of the specific volume on temperature and pressure is shown in Figure 3.3. Clearly, the pressure impact is low (variation < 1% between 0 and 100 bar) compared to the temperature variability (about 10% between 40 and 240°C). A discontinuity in the curves indicates the glass transition point of Soluplus (approximately 70°C[32]).

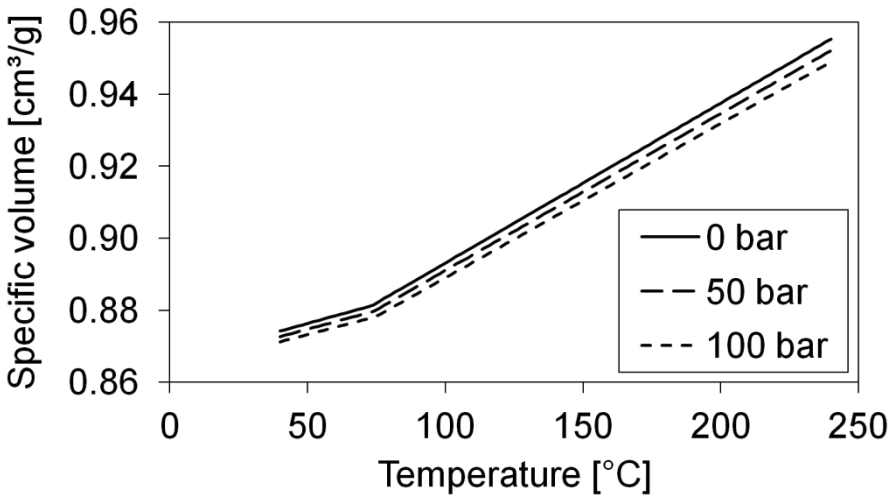

Figure 3.3: Specific volume as a function of temperature and pressure.

3.3.2 Melt Viscosity

The viscosity of the Soluplus melt was measured with a MCR301 (Anton Paar, Austria) equipped with electric temperature control systems P-EDT400 and H-EDT400 and a cone-to-plate measurement body with a diameter of 25mm and 1° cone angle. Different types of measurements were performed: three frequency sweeps (FS) at 130, 170 and 200°C, a rotation test with controlled shear rate (CSR) at 170°C and a temperature sweep (TS) at 10 rad/s. Although the shear viscosity (i.e., the result of CSR tests) was required, FS tests are preferable since they allow a wider measurement range of angular frequency (and shear rate). As shown in Figure 3.4, FS and CSR at 170°C are in agreement, confirming the validity of the Cox-Merz rule,[31] under which the result of the FS (complex viscosity depending on the angular frequency) is equal to the CSR result (shear viscosity depending on shear rate). In addition, to confirm the temperature dependency established via the FS at three different settings, a TS at a constant angular frequency of 10 rad/s was performed (Figure 3.5).

The model (Carreau and WLF equation, Eq. 3.16 and 3.17) was fitted, and the yielding parameters are shown in Table 3.2. Calculated model curves vs. the measured data are shown in Figure 3.4 and Figure 3.5. The measurements were in agreement with the data supplied by the manufacturer.[32]

Table 3.2: Viscosity parameters.

η_0	2999.9 Pa·s
$\dot{\gamma}_{crit}$	5.7852 s^{-1}
m	0.39489
T_r	170 °C
C_1	10.7203
C_2	135.4020 °C

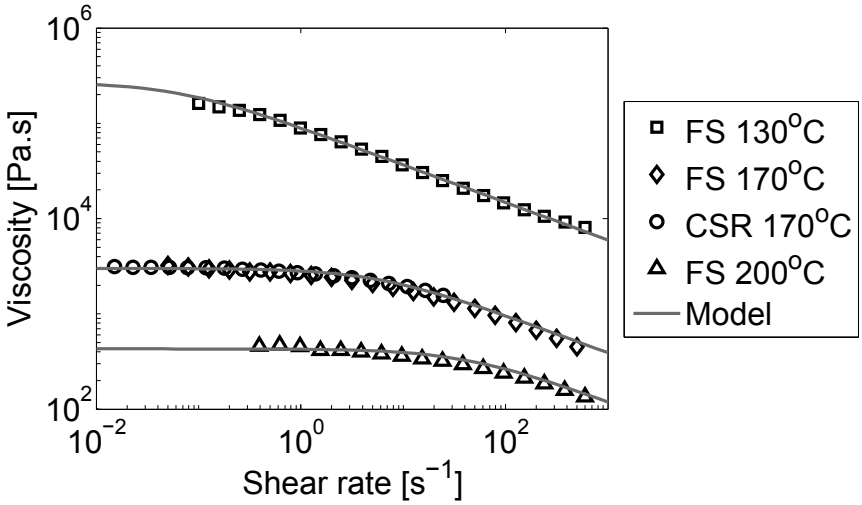

Figure 3.4: Viscosity over shear rate. The shown measurements are frequency sweeps (FS) and a rotation test under controlled shear rate (CSR).

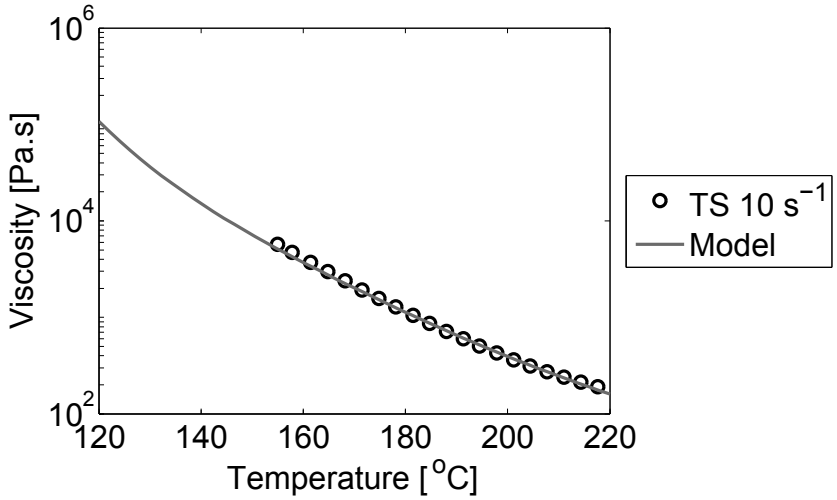

Figure 3.5: Viscosity over temperature. The shown measurement is a temperature sweep (TS).

3.4 Experiments

Experiments were performed to measure the axial pressure gradient and material temperature for different throughputs, screw speeds and screw element configurations. The extruder used was a ZSK 18 from Coperion (Germany) with a nominal screw diameter D = 18 mm. The characterization was performed for 6 different types of screw elements (all two-flighted), i.e., two conveying screw elements termed “24/24” and “16/16” with different pitch of 24 and 16 mm, respectively, two kneading elements “KB 45/5/8” and “KB 45/5/8 LH” (45° offset angle, 5 discs, 8 mm length, right- and left-handed), a kneading element “KB 90/5/8” and a kneading element “KB 45/5/16”. All elements are depicted in Figure 3.6. From the geometry of the cross section (Figure 3.2), a free cross section area A_{cr} = 187.8 mm² was calculated. The gap length l_{gap} was 101.6 mm, leading to an average gap size h = 1.847 mm based on Eq. 3.15.

Two pressure sensors (melt pressure sensors from Gefran, Italy; I-Series, 0-35bar) were installed close to the screw end at an axial distance of Δx = 43.2 mm (see Figure 3.7). The built-in temperature sensors of the extruder are planar with the wall (similar to the pressure sensors) and their readings are strongly influenced by the barrel temperature. These sensors always measure some average of melt and barrel temperature. Thus, another temperature sensor (fast-response thermometer Thermapen from ETI Electronic Temperature Instruments Ltd, UK) was placed in the clearance volume directly behind the screw, which was the only option for inserting it directly in the melt flow. To avoid wall contact, the shaft of this additional temperature sensor was covered with a PTFE (poly-tetra-fluor-ethylene) casing. The measured temperature was significantly higher (approximately 3-10°C) than that indicated by the built-in temperature sensors, obviously significant viscous dissipation occurs. The screw section between both pressure sensors was configured with the screw element type being investigated. To ensure that the filled screw section extended over both pressure sensors, an adjustable die valve was constructed (Figure 3.7).

The barrel temperature was set to 180°C. Vacuum devaporization was used (200 mbar) to avoid foaming caused by moisture in Soluplus. The measurements were performed for three screw speeds (60, 120, 180 rpm) and throughputs of 0.5 – 4 kg/h and 0.5-2 kg/h for the conveying and kneading elements, respectively. Each change of throughput or screw

speed was maintained for at least 15 min to achieve a steady state before collecting data for 6 min using the SIPAT System (Siemens, Belgium) with a data acquisition rate of 5s. Since the measured pressure data showed significant oscillations, steady state in this case meant that the pressure difference was oscillating around a constant value over the considered time period. The measured temperature did not show oscillations and was recorded manually by the operator.

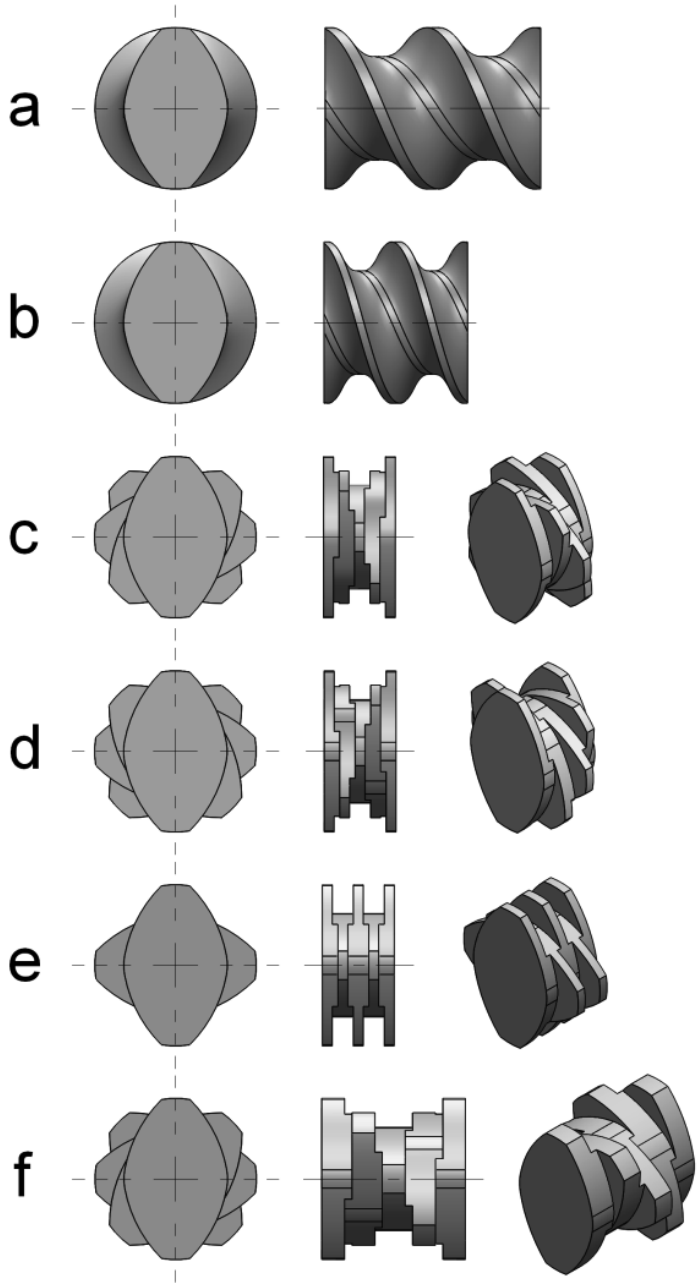

Figure 3.6: ZSK18 screw elements evaluated in our study: a) 24/24, b) 16/16, c) KB 45/5/8, d) KB 45/5/8 LH, e) KB 90/5/8 and f) KB 45/5/16.

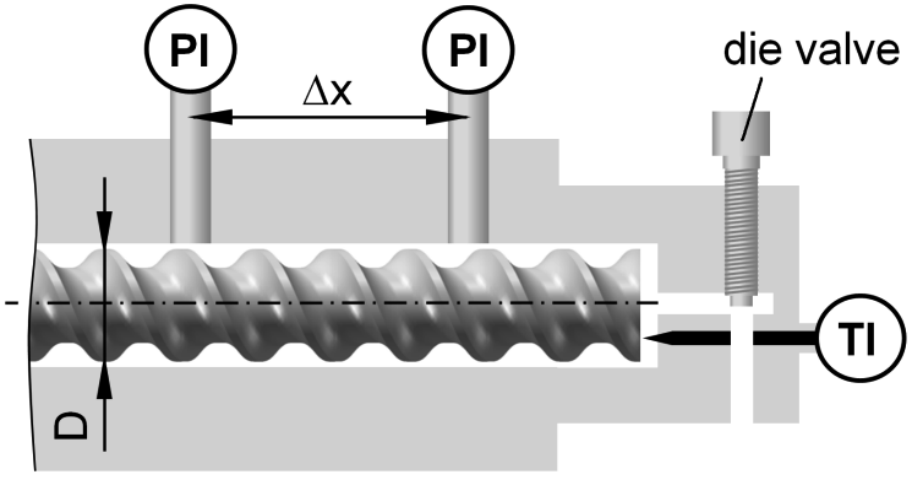

Figure 3.7: Experimental set-up. PI are the pressure indicators, TI the temperature indicator.

3.5 Results and Discussion

3.5.1 Measured Data

The resulting data of the measured melt temperature and pressure gradient for the 24/24 screw element (Figure 3.6a) are shown in Figure 3.8 and Figure 3.9. The melt temperature T_M was significantly higher than the barrel temperature due to the considerable amount of heat generated by viscous dissipation, even in the case of conveying elements. As expected, the temperature increased with the increasing screw speed due to greater dissipation and slightly decreased with increasing throughput due to the reduced axial pressure gradient (i.e., reduced viscous dissipation) and an increased cooling due to convective heat transport. The axial pressure gradient $\Delta p/\Delta x$ was averaged over 6 min for each measured data point, the error bars indicate the standard deviation of the observed oscillations. With increasing screw speed, the axial pressure gradient increased due to increased shear forces balanced by pressure gradients and decreased with increasing throughput due to a decreased backflow in the completely filled section, as it also shown by the linear pressure characteristic model for Newtonian fluids (Eq. 3.3).

The dependency of the axial pressure gradient on the throughput becomes weaker with increasing screw speed. At 180 rpm the pressure gradient was rather constant for the 24/24 screw element. This can be explained by the viscosity increase due to the corresponding temperature decrease of approximately 2°C, which dominates the slight decrease of the

axial pressure gradient with increasing throughput expected due to the pressure characteristic (note, that also at 180rpm an inherent conveying capacity exists, i.e., a throughput, where the axial pressure gradient becomes zero. However, that throughput is relatively high at 180 rpm).

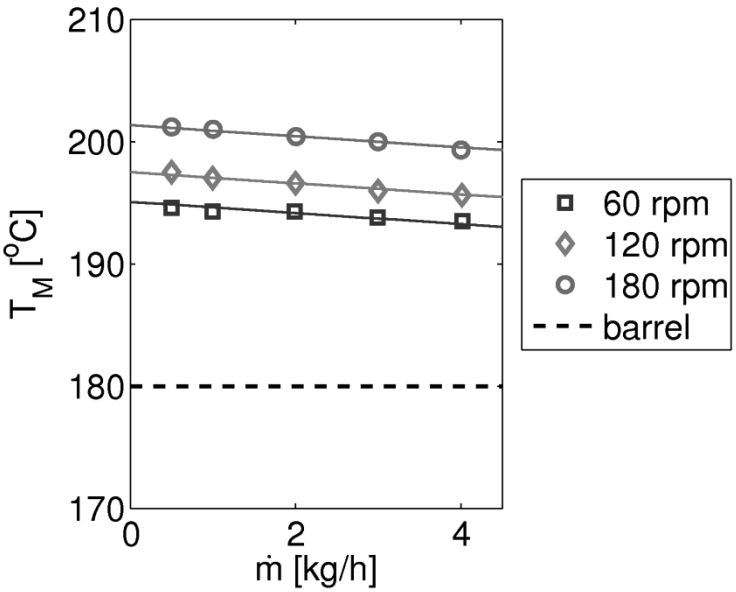

Figure 3.8: Melt temperature (points: measurement, lines: fit) over throughput at different screw speeds for the conveying screw element 24/24.

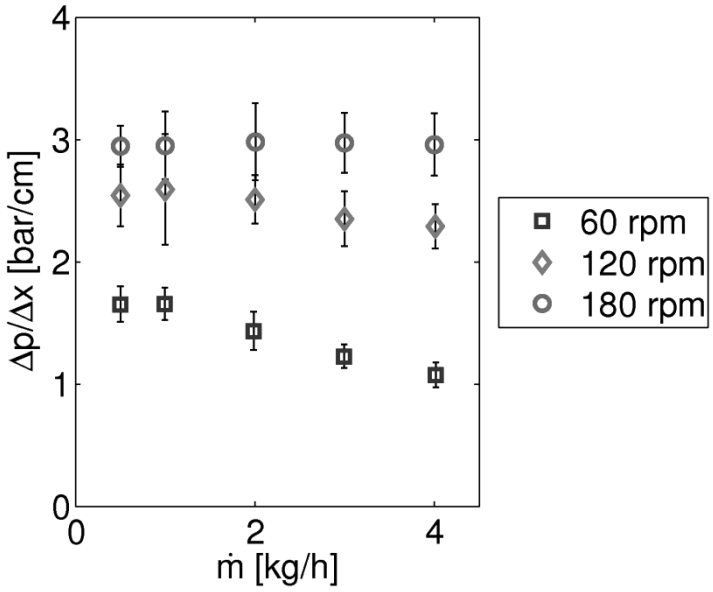

Figure 3.9: Axial pressure gradient over throughput at different screw speeds for the conveying screw element 24/24.

The data for all other screw elements were qualitatively similar and are not shown in detail. Specifically, we did not find a significant difference in the melt temperature for all investigated screw elements, indicating, that the heat generation by viscous dissipation is not significantly different, even for kneading elements. Note, that the local viscous dissipation rate is proportional to viscosity and shear rate squared ($q_{Diss} = \eta \cdot \dot{\gamma}^2$). The dominating shear rates are mainly caused by the screw rotation and the gap distance between screws and barrel, which is equal for all investigated screw elements due to the invariant cross section profile of the screws. In the case of kneading elements, the offset of the single discs causes additional gaps in the intermeshing region of the screws where high shear rates occur. However, this does not dominate the heat generation, since only a small amount of material is located in the crossover of offset regions and the intermeshing region.

3.5.2 Fitted Model

The measurements were used to fit parameters A_1 and A_2 in Eq. 3.18 for all of the investigated screw elements and parameter A_0 in Eq. 3.19 for the non-conveying screw element KB 90/5/8. The specific volume per Eq. 3.22, which was required to convert mass throughput $\dot{m}$ [kg/h] into volumetric throughput $\dot{V}$ [m³/h], was evaluated at the measured melt temperature T_M and the pressure p = 0, i.e., the (small) pressure dependency was neglected (see Figure 3.3). The material parameters given in Table 3.1 and Table 3.2 were used, and the temperature shift factor a_T per Eq. 3.17 was calculated based on the measured melt temperature T_M.

Table 3.3: Fitted screw parameters and relative variations due to h ± 50%.

Screw element	A_1	A_2	A_3
24/24	0.3593 +15.3% / -7.6%	766.5 ±18.8%	39.33 +77% / -59%
16/16	0.2257 +6.4% / -3.4%	808.6 ±18.9%	41.49 +77% / -59%
KB 45/5/8	0.1545 +7.4% / -5.0%	259.1 ±10.2%	13.29 +65% / -55%
KB 45/5/16	0.1448 +4.8% / -3.6%	217.7 ±8.5%	11.17 +63% / -54%
KB 90/5/8	A_0 = 1214.4 ±2.9%		

The fitted parameters for all of the investigated screw elements are shown in Table 3.3. In order to demonstrate the sensitivity of the fitted screw parameters A_0, A_1 and A_2 on the developed estimate of parameter h and A_3, the estimate h was varied by ±50% (1.847 mm ± 0.924 mm). The resulting deviations in A_0, A_1, A_2 and A_3 are shown by relative errors in Table 3.3. The values of parameter A_3 deviated in the range of 54 - 77%, while the corresponding deviations of A_0, A_1 and A_2 were in the ranges of 3%, 3 - 15% and 8 - 19%, respectively. This indicates that deviations in A_0, A_1 and A_2 that were caused by deviations in A_3 were significantly lower than deviations in A_3, i.e., the model is hardly sensitive to the estimated parameter A_3. As such, the used approximation is a valid approach and it can be expected that the data reported here allow the simulation of extruders and the prediction of their performance within technical accuracy ranges.

Using the determined parameters A_0, A_1 and A_2, the pressure characteristic curves were calculated according to Eq. 3.18 for conveying elements and Eq. 3.19 for non-conveying element KB 90/5/8. The calculated curves describe changes in the dimensionless axial pressure gradient as a function of throughput and screw speed. The corresponding melt temperature is required for the evaluation of Eqs. 3.18 and 3.19 due to the temperature dependency of the viscosity, but cannot be predicted by the pressure characteristic model. Thus, the melt temperature was determined from a linear fit of the measured temperature data $T_M(n,\dot{m}) = a_n - b \cdot \dot{m}$ (see solid lines in Figure 3.8, fitted parameters a_n and b are provided in Table 3.4).

Table 3.4: Fitted temperature parameters.

Screw element	a_n [°C]			b [°C.h/kg]
	60rpm	120rpm	180rpm	
24/24	195.05	197.48	201.33	0.4545
16/16	191.73	195.88	200.48	0.3566
KB 45/5/8	194.02	198.33	200.97	0.3360
KB 45/5/16	193.91	199.97	202.74	1.0076
KB 90/5/8	195.97	199.90	203.53	0.7424

A comparison between the calculated pressure characteristic curves and the measured data is shown in Figure 3.10 - Figure 3.15 for all investigated screw elements. The dashed lines represent the linear model of Newtonian fluids with axis intercepts A_1 and A_2 (calculated in Eq. 3.3). The discrepancy between the linear model and the measured data was due to shear-thinning and temperature variations.

Clearly, the model fits the measured data well and is a good basis for extruder design and performance prediction. The model fit is better for the conveying screw elements 24/24 (Figure 3.10) and 16/16 (Figure 3.11) than for the kneading elements (Figure 3.12 - Figure 3.15). This can be explained by the stronger relative pressure oscillations observed for the kneading elements (represented by error bars). The ratio of the inherent conveying capacity (i.e., parameter A_1) for both of the investigated conveying screw elements 0.3593 / 0.2257 = 1.59 is comparable with the ratio of their pitch 24 / 16 = 1.5. This is in agreement with the data reported by Kohlgrüber et al.[29], who stated that A_1 is approximately proportional to the screw pitch. Both A_1 parameters are comparable to the approximation calculated in Eq. 3.4 (0.3864 and 0.2576). In contrast, A_2 of the 24/24 and 16/16 are relatively similar, i.e., the generated pressure gradient at zero throughput is not significantly different. Kohlgrüber[5] demonstrated that A_2 generally increases with the decreasing pitch, except for cases when there is a large gap between the screw and the barrel (typical for relatively small machines, such as ZSK 18 that we used).

Parameters A_1 and A_2 are significantly lower for the kneading elements KB 45/5/8 (Figure 3.12) and KB 45/5/16 (Figure 3.13) than for the conveying elements due to the geometry of the kneading elements (Figure 3.6) with discontinuous steps rather than a smooth surface that reduces the conveying effect and pressure build-up. KB 45/5/16 has a slightly decreased A_1 and A_2 compared to KB 45/5/8, i.e., the stretched geometry of KB 45/5/16 resulted in reduced conveying and pressure build-up.

The measured data of the screw element KB 45/5/8 LH were not fitted, since they should be identical to the pressure characteristic of KB 45/5/8 except for the inversed direction (negative throughput) due to its backward conveying effect (also see the corresponding literature[5,11]). The data points for KB 45/5/8 LH and KB 45/5/8 are shown together in Figure 3.14. Although the data approximately match at zero throughput, the axial pressure

gradient of KB 45/5/8 LH showed an unexpected discrepancy compared to the fitted curves of KB 45/5/8, even a decreasing axial pressure gradient with increasing negative throughput in some regions.

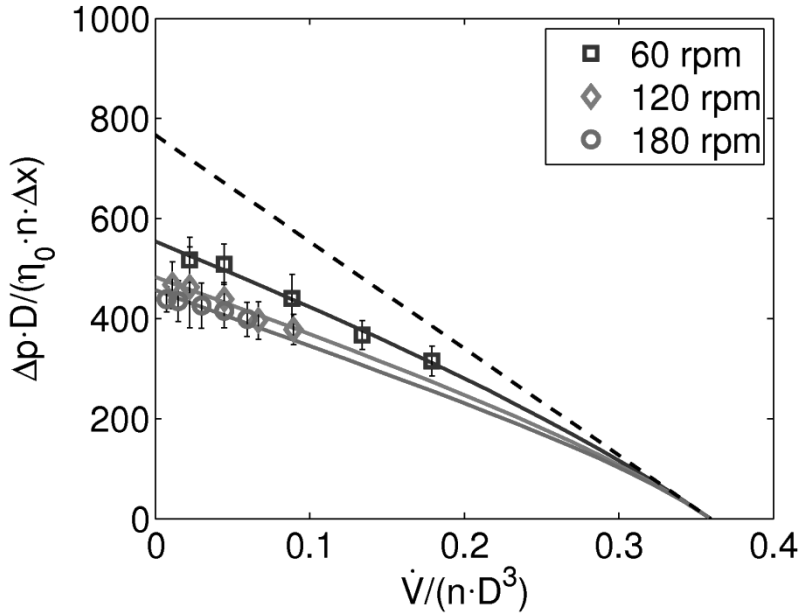

Figure 3.10: Pressure characteristic based on η_0 for the conveying screw element 24/24. Dots: measurements, solid lines: model for Soluplus, dashed line: model for Newtonian fluids.

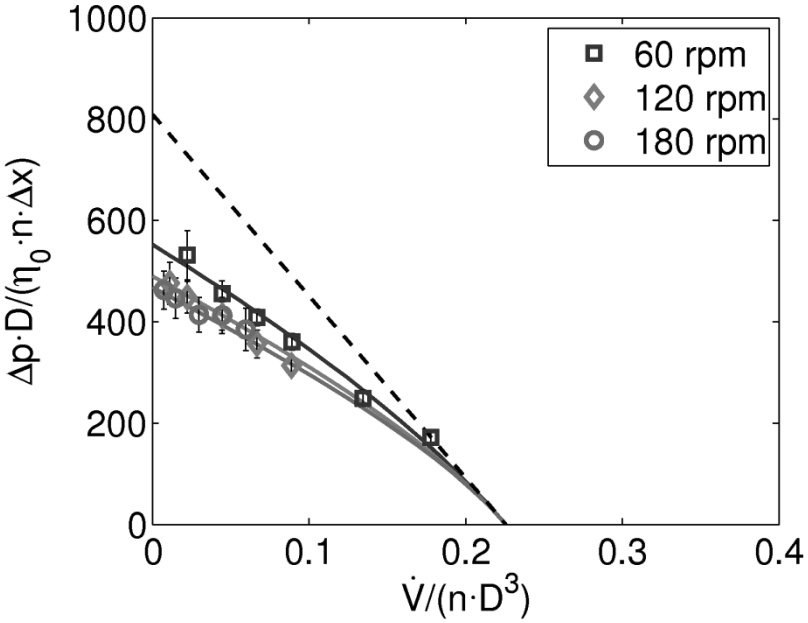

Figure 3.11: Pressure characteristic based on η_0 for the conveying screw element 16/16. Dots: measurements, solid lines: model for Soluplus, dashed line: model for Newtonian fluids.

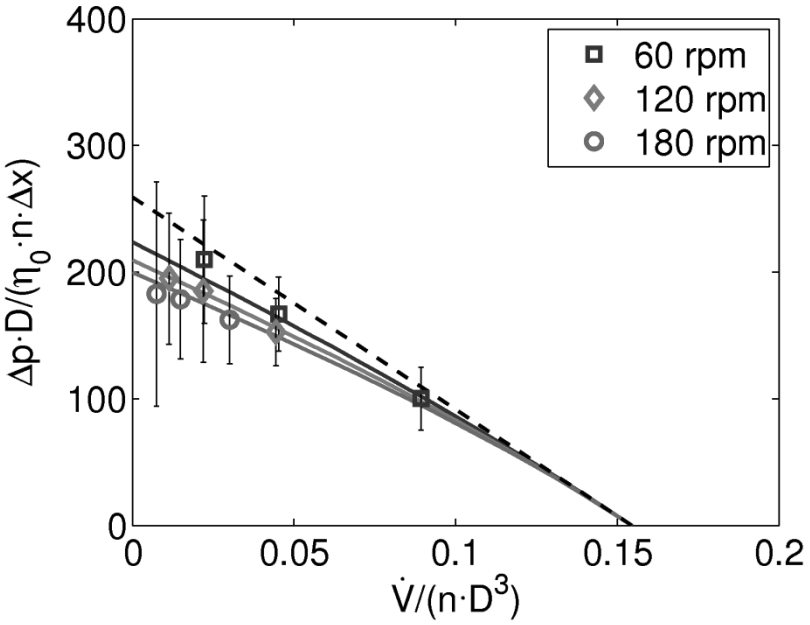

Figure 3.12: Pressure characteristic based on η_0 for the kneading element KB 45/5/8. Dots: measurements, solid lines: model for Soluplus, dashed line: model for Newtonian fluids.

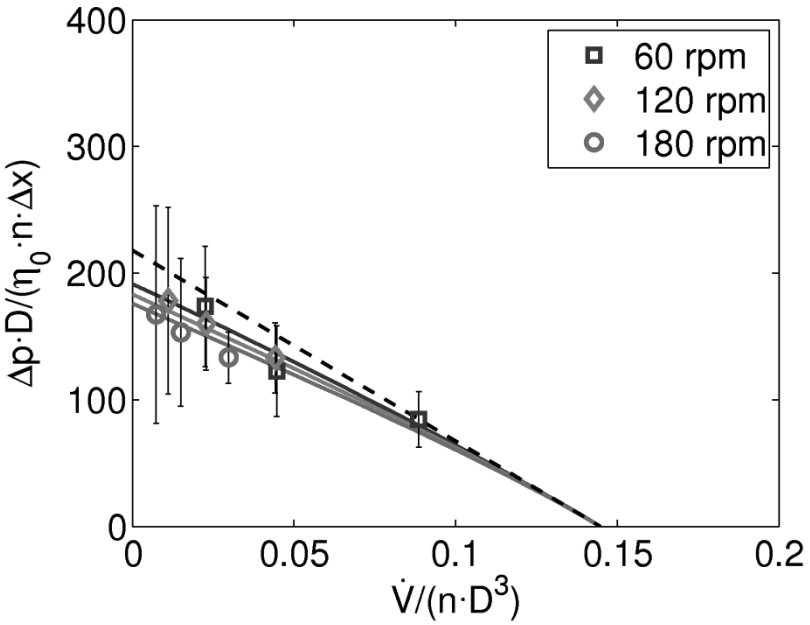

Figure 3.13: Pressure characteristic based on η_0 for the kneading element KB 45/5/16. Dots: measurements, solid lines: model for Soluplus, dashed line: model for Newtonian fluids.

As expected, the kneading element KB 90/5/8 (Figure 3.15) had a pressure-characteristic line passing the origin since its geometry does not cause a preferred conveying direction

and is thus non-conveying. The curve slope was similar to the other kneading elements, meaning that the change in the flow resistance with varying throughput was similar.

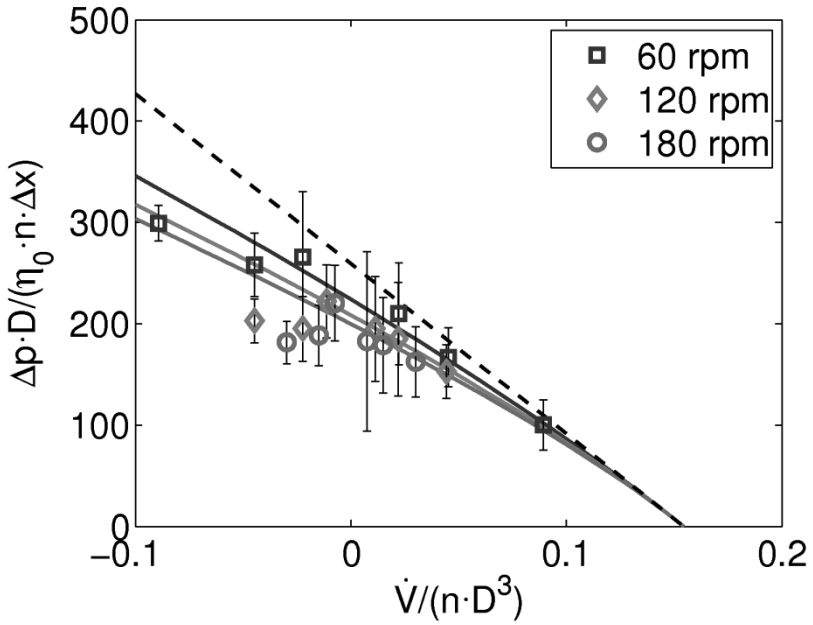

Figure 3.14: Pressure characteristic based on η_0 for the kneading element KB 45/5/8 together with KB 45/5/8 LH. Dots: measurements, solid lines: model for Soluplus, dashed line: model for Newtonian fluids.

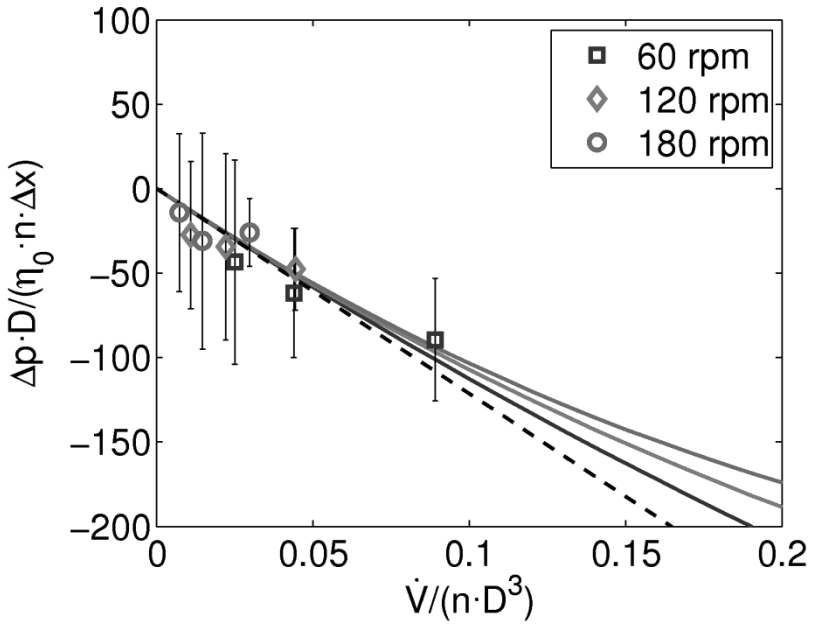

Figure 3.15: Pressure characteristic based on η_0 for the kneading element KB 90/5/8. Dots: measurements, solid lines: model for Soluplus, dashed line: model for Newtonian fluids.

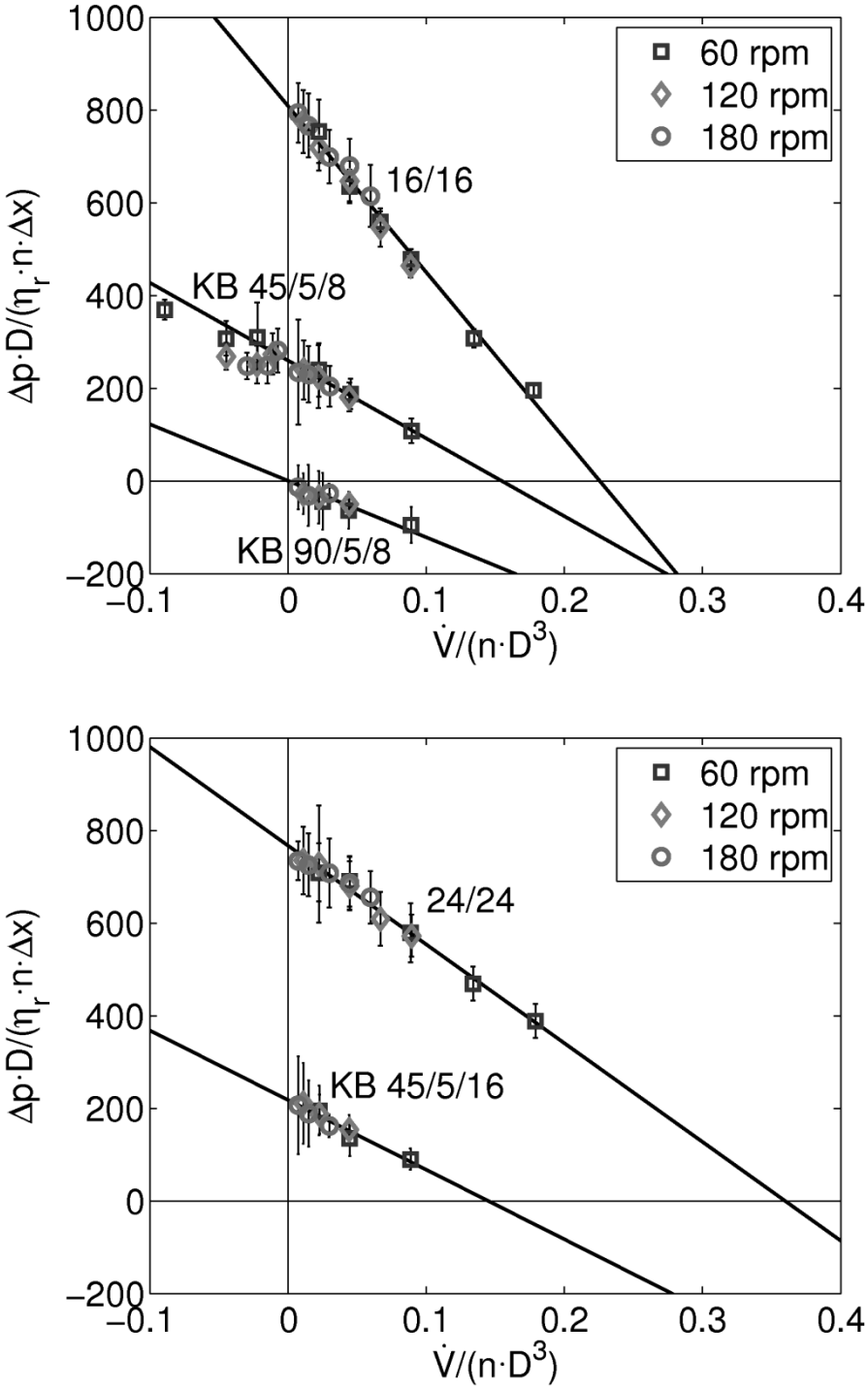

Figure 3.16: Pressure characteristic curves based on η_r for all of the investigated screw elements in comparison (dots: measurements, lines: model).

The resulting linear pressure characteristic curves of all of the investigated screw elements are compared in Figure 3.16. For a clear graphical representation, the dimensionless axial pressure gradient $\Delta p^*/\Delta x^* = \Delta p \cdot D/(\eta_r \cdot n \cdot \Delta x)$ according to Eq. 3.10 (Eq. 3.21 for non-

conveying elements) was used, in contrast to $\Delta p_C^*/\Delta x^* = \Delta p \cdot D/(\eta_0 \cdot n \cdot \Delta x)$ as used for Figure 3.10 - Figure 3.15. The obvious difference is the shear-rate-dependent representative viscosity η_r (in contrast to η_0), which leads to a linear correlation, since the shear-thinning effect of the melt rheology is incorporated in η_r. Thus, all data points of a screw element are located along the pressure characteristics for Newtonian Fluids in Figure 3.16 which is independent of the screw speed.

Although the relative oscillations of the kneading elements were significantly higher than those of the conveying elements, the absolute oscillations of the dimensionless pressure gradient were similar for the investigated screw elements (see Figure 3.16). The cross section profile of the screw elements was equal for all considered elements. This indicates, that the observed oscillations of the axial pressure gradient are caused by the rotation of the screws, which led to pressure maxima in front of and minima behind the screw flights with respect to the rotational direction (This conjecture, however, cannot be proven based on the shown data, since the data acquisition rate of 5s does not resolve the circulation time of the screws). However, this effect has been shown by three-dimensional simulations of twin screws[5] for the pressure distribution over the cross section.

3.6 Summary and Conclusions

This work presents the first detailed experimental characterization of completely filled screw elements for pharmaceutical HME with Soluplus on a co-rotating twin-screw extruder. Specifically, the pressure characteristic (i.e., the correlation between the axial pressure gradient and the volumetric throughput in a completely filled screw section) was measured at different screw speeds and for different screw elements. The required rheological properties and the specific volume of Soluplus were determined in detail the first time by precise measurements and described via the Carreau model combined with the WLF equation, and the Menges model respectively. The pressure characteristic model[10,5] was fitted to describe the measured data. Since fitting of three parameters was found to be an underdetermined problem, an approximation of the parameter A_3, which has a lower impact on the results than parameters A_1 and A_2, was developed based on a mechanistic understanding of the pressure-driven flow. The effect of the approximation was significantly lower for A_1 and A_2 than for A_3, i.e., deviations in A_1 and A_2 were lower than

deviation in A_3 introduced by the approximation. Since it was established that the melt temperature was not constant for variable throughput and the screw speed, a temperature dependency was included into the model using a linear fit of the measured temperature over the throughput.

The results show significantly different pressure characteristic curves and corresponding screw parameters for the investigated screw elements. A comparison of the screw parameters for the different elements confirm the expected tendencies, such as the proportionality of the inherent conveying capacity and the screw pitch of conveying screw elements, as well as the same axial pressure gradient for right- and left-handed elements of the same type (i.e., inverse conveying direction) at zero throughput.

More detailed studies (e.g., via numerical simulations) are required to investigate why the backward-conveying kneading element KB 45/5/8 LH deviated from the model curves of element KB 45/5/8 and, in some regions, had decreased pressure gradients at increased throughputs. Extensive three-dimensional simulations (e.g., CFD) of the investigated screw elements are necessary to confirm the determined screw parameters and pressure characteristic curves and to analyze the developed approximation of A_3. A comparison between the numerical results for different underlying material rheologies and the presented measurements could establish if the screw parameters depend on the material and if they can be determined via a simulation of simplified cases, e.g., under isothermal conditions. This could open a ways of determining such parameters for other types of screw elements without performing experiments.

The determined parameters confirm an essential premise for a 1D model of a co-rotating twin-screw extruder, which cannot predict the transport processes caused by the screw elements based directly on the three-dimensional geometry. Using the obtained screw parameters, such a model can predict process variables (e.g., filling ratio, pressure and melt temperature along the twin screw). Although the shown experiments have exclusively been performed for a completely filled screw section, the results can be used to estimate filling ratio and pressure in partially filled screw sections. Axial pressure gradients in partially filled screw sections are zero due to the connected gas phase. The dependency of the filling ratio on the throughput can be estimated linearly[5] $f = \dot{V} / \left(A_1 \cdot n \cdot D^3 \right)$, i.e., filling ratio = 0

at throughput = 0, filling ratio = 1 at the inherent conveying capacity. Moreover, based on the calculated flow rates along the screw such a 1D model can predict residence time distributions, i.e., characterize the mixing performance of the process.

3.7 Abbreviations

1D	one-dimensional
CSR	controlled shear rate test
FS	frequency sweep
HME	hot-melt extrusion
PTFE	poly-tetra-fluor-ethylene
TS	temperature sweep
WFL	Williams-Landel-Ferry

3.8 Nomenclature

Latin symbols

A_0	screw parameter for non-conveying elements [-]
A_1, A_2	screw parameters for conveying elements [-]
A_3	empirical shear rate parameter [-]
a_T	temperature shift factor (Carreau model, WLF equation) [-]
C_1 , C_2	parameters of the WLF equation
D	nominal screw diameter [m]
H	gap distance [m]
$K_1 - K_9$	parameters of the Menges model
$\dot{m}$	mass throughput [kg/s]
M	Carreau exponent [-]
n	screw speed [s^{-1}]
p	Pressure [Pa]
$\frac{\Delta p^*}{\Delta x^*}$	dimensionless axial pressure gradient based on η_r or η [-]
$\frac{\Delta p_C^*}{\Delta x^*}$	dimensionless axial pressure gradient based on η_0 [-]
Re	Reynolds number [-]

T	temperature [°C]
T_M	measured melt temperature [°C]
T_r	reference temperature (WLF equation) [°C]
T_S	screw pitch [m]
T_{trans}	transition temperature (Menges model) [°C]
$\dot{V}$	volumetric throughput [m³/s]
$\dot{V}^*$	dimensionless volumetric throughput [-]
v	specific volume [m³/kg]
x	axial coordinate [m]

Greek symbols

$\dot{\gamma}$	shear rate [s^{-1}]
$\dot{\gamma}_{crit}$	critical shear rate (Carreau model) [s^{-1}]
$\dot{\gamma}_r$	representative shear rate [s^{-1}]
η	dynamic viscosity [Pas]
η_o	zero-shear-rate viscosity (Carreau model) [Pas]
η_r	representative viscosity [Pas]
ρ	density [kg/m³]
τ_W	wall shear stress [Pa]

3.9 References

(1) Kleinebudde, P. Pharmazeutisches Produktdesign: Gezielte Freisetzung von Wirkstoffen durch unterschiedliche Extrusionstechniken. *Chemie Ing. Tech.* **2011**, *83*, 589–597.

(2) Ghebre-Sellassie, I.; Martin, C. *Pharmaceutical Extrusion Technology*; Marcel Dekker Inc.: New York, 2003.

(3) Breitenbach, J. Melt Extrusion: From Process to Drug Delivery Technology. *Eur. J. Pharm. Biopharm.* **2002**, *54*, 107–117.

(4) Repka, M. A.; Battu, S. K.; Upadhye, S. B.; Thumma, S.; Crowley, M. M.; Zhang, F.; Martin, C.; McGinity, J. W. Pharmaceutical Applications of Hot-Melt Extrusion: Part II. *Drug Dev. Ind. Pharm.* **2007**, *33*, 1043–1057.

(5) Kohlgrüber, K. *Co-Rotating Twin-Screw Extruders*; Carl Hanser Publishers: Munich, 2008.

(6) Yacu, W. A. Modelling a Twin Screw Co-Rotating Extruder. *J. Food Eng.* **1985**, *8*, 1–21.

(7) Meijer, H. E. H.; Elemans, P. H. M. The Modeling of Continuous Mixers. Part I: The Corotating Twin-Screw Extruder. *Polym. Eng. Sci.* **1988**, *28*, 275–290.

(8) White, J. L.; Chen, Z. Simulation of Non-Isothermal Flow in Modular Co- Rotating Twin Screw Extrusion. *Polym. Eng. Sci.* **1994**, *34*, 229–237.

(9) Potente, H.; Hanhart, W. Design and Processing Optimization of Extruder Screws. *Polym. Eng. Sci.* **1994**, *3*, 937–945.

(10) Pawlowski, J. *Die Ähnlichkeitstheorie in der physikalisch-technischen Forschung*; Springer-Verlag: Berlin/Heidelberg/New York, 1971.

(11) Szydlowski, W.; White, J. L. An Improved Theory of Metering in an Intermeshing Corotating Twin-Screw Extruder. *Adv. Polym. Technol.* **1987**, *7*, 177–183.

(12) Potente, H.; Fornefeld, A.; Michel, P.; Wittemeier, R. Analyse und Berechnung der Strömungsvorgänge im zylindrischen Scherspalt von Plastifizieraggregaten. *Rheol. Acta* **1987**, *26*, 193–199.

(13) Wang, Y.; White, J. L. Non-Newtonian Flow Modelling in the Screw Regions of an Intermeshing Corotating Twin Screw Extruder. *J. Nonnewton. Fluid Mech.* **1989**, *32*, 19–38.

(14) Barrera, M. A.; Vega, J. F.; Martínez-Salazar, J. Three-Dimensional Modelling of Flow Curves in Co-Rotating Twin-Screw Extruder Elements. *J. Mater. Process. Technol.* **2008**, *197*, 221–224.

(15) Potente, H.; Koch, M. Residence Time Behavior in Grooved-Barrel Extruders. *Adv. Polym. Technol.* **1989**, *9*, 119–127.

(16) De Ruyck, H. Modelling of the Residence Time Distribution in a Twin Screw Extruder. *J. Food Eng.* **1997**, *32*, 375–390.

(17) Giudici, R.; Nascimento, C. A. O.; Beiler, I. C.; Scherbakoff, N. Transient Experiments and Mathematical Modeling of an Industrial Twin-Screw Extruder Reactor for Nylon-6,6 Polymerization. *Ind. Eng. Chem. Res.* **1997**, *36*, 3513–3519.

(18) Puaux, J. .; Bozga, G.; Ainser, A. Residence Time Distribution in a Corotating Twin-Screw Extruder. *Chem. Eng. Sci.* **2000**, *55*, 1641–1651.

(19) Baron, R.; Vauchel, P.; Kaas, R.; Arhaliass, A.; Legrand, J. Dynamical Modelling of a Reactive Extrusion Process: Focus on Residence Time Distribution in a Fully Intermeshing Co-Rotating Twin-Screw Extruder and Application to an Alginate Extraction Process. *Chem. Eng. Sci.* **2010**, *65*, 3313–3321.

(20) Choulak, S.; Couenne, F.; Le Gorrec, Y.; Jallut, C.; Cassagnau, P.; Michel, A. Generic Dynamic Model for Simulation and Control of Reactive Extrusion. *Ind. Eng. Chem. Res.* **2004**, *43*, 7373–7382.

(21) Zagal, A.; Vivaldo-Lima, E.; Manero, O. A Mathematical Model for the Reactive Extrusion of Methyl Methacrylate in a Co-Rotating Twin-Screw Extruder. *Ind. Eng. Chem. Res.* **2005**, *44*, 9805–9817.

(22) Puaux, J.-P.; Cassagnau, P.; Bozga, G.; Nagy, I. Modeling of Polyurethane Synthesis by Reactive Extrusion. *Chem. Eng. Process.* **2006**, *45*, 481–487.

(23) Bertrand, F.; Thibault, F.; Delamare, L.; Tanguy, P. A. Adaptive Finite Element Simulations of Fluid Flow in Twin-Screw Extruders. *Comput. Chem. Eng.* **2003**, *27*, 491–500.

(24) Potente, H.; Többen, W. H. Improved Design of Shearing Sections with New Calculation Models Based on 3D Finite-Element Simulations. *Macromol. Mater. Eng.* **2002**, *287*, 808–814.

(25) Pokriefke, G. Numerical Simulation of 2d Fluid Flow in an Partially Filled Simplified Extruder Model. *Proc. Appl. Math. Mech.* **2003**, *3*, 418–419.

(26) Ficarella, A.; Milanese, M.; Laforgia, D. Numerical Study of the Extrusion Process in Cereals Production: Part I. Fluid-Dynamic Analysis of the Extrusion System. *J. Food Eng.* **2006**, *73*, 103–111.

(27) Rodríguez, E. O. Numerical Simulations of Reactive Extrusion in Twin Screw Extruders, Waterloo, Canada, 2009.

(28) Cleary, P. W.; Robinson, M. Understanding Viscous Fluid Transport and Mixing in a Twin Screw Extruder. In *8th International Conference on CFD in Oil & Gas, Metallurgical and Process Industries*; Trondheim, Norway, 2011.

(29) Kohlgrüber, K.; Bierdel, M.; Conzen, C.; Hepperle, J.; Kirchhoff, J.; König, T.; Thiele, H. Optimierter Betrieb und Scale-up von Doppelschnecken-Extrudern. In *Seminar Handout*; VDI Wissensforum: Leverkusen, Germany, 2012.

(30) Rauwendaal, C. *Polymer Extrusion*; 4th ed.; Hanser Publishers: Munich, 2001.

(31) Mezger, T. *Das Rheologie-Handbuch*; Curt R. Vinzentz Verlag: Hannover, 2000.

(32) Kolter, K.; Karl, M.; Gryczke, A. *Hot-Melt Extrusion with BASF Pharma Polymers; Extrusion Compendium*; 2nd ed.; BASF: Ludwigshafen, 2012.

(33) Germuth, A. *Untersuchungsbericht: Messung von thermodynamischen Stoffdaten an einem Copolymer der Type Soluplus*; Montanuniversität Leoben, Lehrstuhl für Kunststoffverarbeitung: Leoben, 2012.

(34) D. G. F. Huilier. Modeling of Injection Mold Post-Filling: A Review and Some Critical Problems to Solve. *J. Polym. Eng.* **1990**, *9*, 237–302.

"*Life is and will ever remain an equation incapable of solution,*
but it contains certain known factors."

(Nikola Tesla)

4

Mechanistic Modeling of Modular Co-Rotating Twin-Screw Extruders*

In this study, we present a one-dimensional (1D) model of the metering zone of a modular, co-rotating twin-screw extruder for pharmaceutical hot-melt extrusion (HME). The model accounts for filling ratio, pressure, melt temperature in screw channels and gaps, driving power, torque and the residence time distribution (RTD). It requires two empirical parameters for each screw element to be determined experimentally or numerically using computational fluid dynamics (CFD). The required Nusselt correlation for the heat transfer to the barrel was determined from experimental data. We present results for a fluid with a constant viscosity in comparison to literature data obtained from CFD simulations. Moreover, we show how to incorporate the rheology of a typical, non-Newtonian polymer melt, and present results in comparison to measurements. For both cases, we achieved excellent agreement. Furthermore, we present results for the RTD, based on experimental data from the literature, and found good agreement with simulations, in which the entire HME process was approximated with the metering model, assuming a constant viscosity for the polymer melt.

---

* This chapter is based on: Eitzlmayr, A.; Koscher, G.; Reynolds, G.; Huang, Z.; Booth, J.; Shering, P.; Khinast, J. Mechanistic Modeling of Modular Co-Rotating Twin-Screw Extruders. *Int. J. Pharm*. 2014, 474, 157–176.

4.1 Introduction

Developed in the 1940s and 1950s, intermeshing extruders have been firmly established in various industries for many decades. Examples include the manufacture of polymers, chemicals and foodstuffs. The most common type of extrusion devices is the co-rotating twin screw extruder, specifically for the purpose of mixing of highly viscous materials. Single-screw extruders are typically used as a melting device in injection molding machines. Other types of extruder, such as counter-rotating twin-screws, multi-screws or ram-extruders are preferred for more specific applications.[1]

In recent years, co-rotating twin-screw extruders have attracted increasing interest in the pharmaceutical industry, mainly for wet extrusion, solid lipid extrusion, hot-melt granulation and hot-melt extrusion (HME) processes.[2] The latter, in particular, is used for the preparation of solid solutions and amorphous solid dispersions for improving the bioavailability of poorly water-soluble drugs.[3,4] For this and other pharmaceutical applications, the good mixing performance, the self-wiping properties, the short residence time and the resulting product quality and yield of the co-rotating intermeshing twin-screws are a major advantage.[5] In addition, the process is solvent-free, which is highly beneficial in day-to-day manufacturing as costs associated with solvent use, recovery, separation and disposal are high. Furthermore, the commonly used modular screw design provides high operational flexibility. However, a major challenging is the complexity of developing an appropriate screw configuration to accommodate the actual process requirements. This task usually requires extensive experience and/or experimental (and mostly empirical) work.

Modeling and simulation methods can help to increase the understanding of the complex interaction between screw geometry, material properties and the operating conditions. In experimental studies, extruders are essentially black-box systems, since detailed measurements of the filling ratio, the pressure distribution and the local material temperature along the screws are very difficult to achieve. A simulation has the potential to provide complete access to critical parameters in a twin screw extrusion process. This is a particularly powerful approach for scaling-up the process. However, it is still not possible to develop a comprehensive HME model.[1] In part, this arises from the complex behavior of

the processed materials, which are, typically, polymers. Although adequate models have been developed for pure polymers, most applications of HME involve the mixture of two, three or even more components. In these cases, the actual values of the macroscopic material properties (e.g., viscosity, density) depend on the degree of mixing. Due to dissipative heating in small gaps, flows are non-isothermal with the associated effect on the local viscosity. A further challenge is that for the detailed simulation of the flow in partially filled screw sections, well-established methods are currently not available. Similarly, a detailed simulation of the transition from granular to molten state has not yet been developed.

Computational methods for the three-dimensional (3D) simulation of screw sections are available, e.g., the discrete element method (DEM) for the granular flow in the intake zone and computational fluid dynamics methods (CFD, mainly finite element and finite volume methods) for the simulation of viscous flow. However, CFD is mostly limited to completely filled screw sections, e.g., Ishikawa[6], Bertrand et al.[7], Barrera et al.[8], Potente and Többen[9], Ficarella et al. [10], Rodrigurez[11], Sarhangi Fard et al.[12–14], Hétu and Ilinca[15] or Rathod and Kokini[16]. Pokriefke[17] used an Eulerian multiphase CFD method to simulate the flow in partially filled screw sections. Cleary and Robinson[18] applied the smoothed particle hydrodynamics method (SPH) to study mixing in a completely filled co-rotating twin-screw section. Also the die flow was studied by CFD methods, e.g., Carneiro et al.[19], Lin et al.[20], Patil et al.[21], Mitsoulis and Hatzikiriakos[22], Ardakani et al.[23] or Radl et al.[24]. Although, extensive work was devoted to the development of 3D simulation methods, it is still not possible to apply a 3D simulation to the entire HME process, not only due to the difficulties in the simulation of melting and partially filled screw sections, but also due to the extremely high computational effort as a high resolution in the small gaps between screw and wall in the order of 100µm is needed. Thus, computationally less intensive, simplified models are still prevalent.

Existing models for the entire HME process are typically based on the one-dimensional (1D) discretization of screws in axial direction. Such 1D models usually yield profiles of pressure, filling ratio and temperature along the screws, e.g., Yacu[25], Meijer and Elemans[26], White and Chen[27], Potente and Hanhart[28], Vergnes et al.[29]. These models use the pressure-throughput correlation of different types of screw elements, e.g., the axial

pressure gradient versus throughput in a completely filled screw section,[1,8,30–33] and calculate profiles for a given screw configuration. Heat transfer was also considered by investigators, such as Guo and Chung[34] and White et al.[35]. The underlying transport mechanisms along the screws have also been used to model the residence time distribution (RTD), e.g., Todd[36], Potente and Koch[37], Chen et al.[38], Oberlehner et al.[39], De Ruyck[40], Giudici et al.[41], Gao et al.[42], Prat et al.[43], Puaux et al.[44], Kumar et al.[45], Baron et al.[46], Amedu et al.[47]. It was also demonstrated, that this approach can be used to model reactive extrusion, for example, Choulak et al.[48], Zagal et al.[49], Puaux et al.[50].

However, some detailed aspects of these 1D models are still challenging. For example, it is not completely clear, how to model the viscous dissipation in a twin-screw extruder or the heat transfer to the barrel in a simplified way without using extensive CFD simulations. Also, the melting zone is difficult to model, and, often excluded in 1D models. In our work, we developed a 1D model for the metering zone of co-rotating twin-screw extruders with focus on pharmaceutical manufacturing, based on models presented by Choulak et al.[48], Kohlgrüber[1] and Pawlowski[30]. Parts of our model have been shown in our previous work[51], where we presented an experimental investigation of various types of screw elements in terms of axial pressure gradient and melt temperature depending on screw speed and throughput. We used these data to evaluate empirical screw parameters, which must be provided as input parameters for our 1D model.

Here, we show the complete model in detail. To our knowledge, we are the first to present a simplified 1D model for the metering zone of co-rotating twin-screw extruders, including a detailed and well-founded approach for calculating the viscous dissipation and the local gap temperatures for a non-Newtonian polymer melt. Our model requires only two empirical parameters for each type of screw element. Instead of additional empirical parameters to calculate viscous dissipation and driving power these are calculated using geometrical and physical parameters. Furthermore, we are the first to apply this approach to pharmaceutical HME, and, specifically, to the pharmaceutical-grade polymer Soluplus®.

The main purpose of the HME process in pharmaceutical manufacturing is usually to induce intimate mixing of the component materials. However, the capabilities of the 1D

approach to account for mixing are limited, for example, the local uniformity of the mixture cannot be resolved and requires more intensive 3D simulation approaches. However, our model accounts for the RTD, which is a measure of axial mixing and is often of practical interest, for example, to gain knowledge about the residence time of the excipients in the process or to study if oscillations at the input (typically caused by the feeding equipment) can be compensated by the extruder.

Our model is a step towards the detailed simulation and rational design of pharmaceutical HME systems. Together with advanced 3D simulation methods, which we will report in an upcoming publication, it constitutes a combined approach to increase the understanding of the HME process and to support the development, design, optimization and scale-up of extrusion processes.

4.2 Proposed Model

4.2.1 Mass Flow Rates and Mass Balances

Similar to the approach of Choulak et al.[48], who modeled the extruder as a cascade of continuous stirred tank reactors (CSTR), we discretized the twin-screw in the axial direction, obtaining *N* numerical elements (see Figure 4.1). The numerical elements are connected by mass flow rates accounting for the mass transfer along the screws. Two different types of mass flow are considered: screw-driven flow, which represent conveying caused by the geometry of the screw elements, and pressure-driven flow, accounting for mass flow due to pressure gradients in axial direction.

Since the numerical elements have to represent different types of physical screw elements (e.g., forward conveying, backward conveying, non-conveying), we designed a general numerical element, which is able to represent all types of physical screw elements depending on its parameter setting. Three different mass flow rates are assigned to each single numerical element *i* (see Figure 4.2). Two of them are screw-driven mass flow rates, one for conveying in the forward direction ($\dot{m}_{f,i}$) and one for conveying in the backward direction ($\dot{m}_{b,i}$). At least one of them is zero to represent either a screw element conveying forward, or a screw element conveying backward. For non-conveying elements, both are

zero. The third mass flow rate of each single numerical element accounts for the pressure-driven flow ($\dot{m}_{p,i}$), whose direction depends on the actual pressure values of adjacent (numerical) elements.

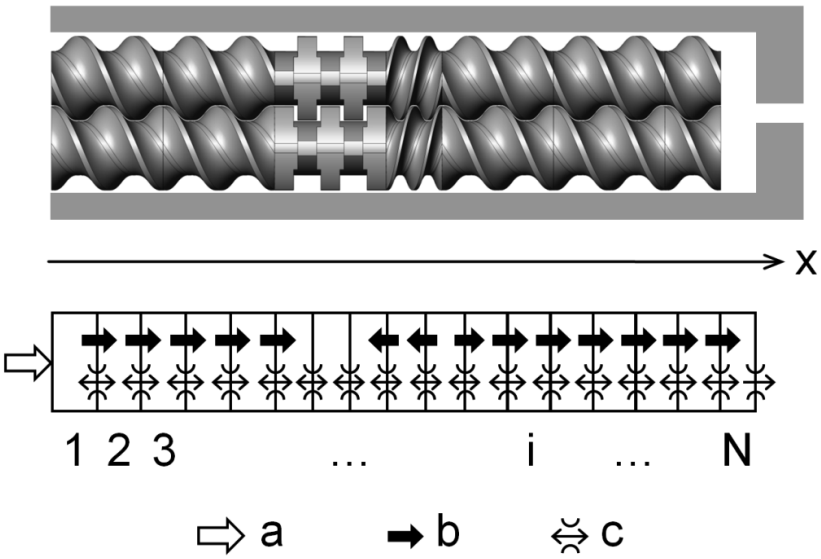

Figure 4.1: An example for the axial discretization of a twin-screw with numerical elements 1 ... *N* and the assigned mass flow rates (a: feed flow, b: screw-driven flow, c: pressure-driven flow).

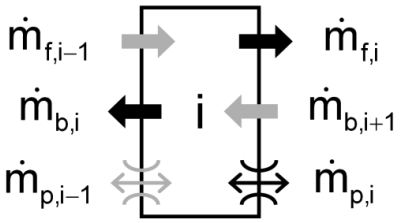

Figure 4.2: A single numerical element *i* and the associated mass flow rates (grey arrows belong to the adjacent elements).

To model the screw-driven mass flow rates $\dot{m}_{f,i}$ and $\dot{m}_{b,i}$ (denoted as $\dot{m}_{fb,i}$ below since modeled equally), Choulak et al.[48] proposed to describe them as proportional to the screw speed n, the filling ratio f_i (i.e., the filled volume fraction) and the free volume V_i of element i. Since the free volume V_i of the numerical elements depends on the axial resolution, we replaced it by the free cross-section area A_{cr} of the twin-screw (see Appendix B) times the screw diameter D as a unit length:

$$\dot{m}_{fb,i} = \rho_i \cdot K_{fb,i} \cdot n \cdot f_i \cdot A_{cr} \cdot D \tag{4.1}$$

The dimensionless coefficient $K_{fb,i}$ (i.e., either $K_{f,i}$ or $K_{b,i}$) is an empirical parameter describing the conveying effect of the considered screw element, ρ_i is the melt density. For the pressure-driven mass flow rates, Choulak et al.[48] proposed to describe them as proportional to the axial pressure difference $\Delta p_i = p_{i+1} - p_i$ between adjacent numerical elements and inversely proportional to the dynamic viscosity η_i. Since the axial pressure difference Δp_i depends on the axial resolution, we normalized it with the axial distance to the adjacent element $\Delta x_i = x_{i+1} - x_i$. To obtain a dimensionless flow resistance parameter $K_{p,i}$, we multiplied with D^4:

$$\dot{m}_{p,i} = -\frac{D^4}{K_{p,i}} \cdot \frac{\rho_i}{\eta_i} \cdot \frac{\Delta p_i}{\Delta x_i} \tag{4.2}$$

The negative sign accounts for the flow direction against increasing pressure. Based on Eqs. 4.1 and 4.2, we formulate mass balances for the numerical elements. The values of the parameters $K_{f,i}$, $K_{b,i}$ and $K_{p,i}$ are assigned appropriately for each numerical element, depending on the physical screw element being represented (illustrated in Table 4.1 and Figure 4.3). $K_{p,i}$ is always > 0, since pressure-driven flow is possible in all types of screw elements. The parameter $K_{f,i}$ is > 0 for forward-conveying elements (type a), the parameter $K_{b,i}$ is > 0 for backward-conveying elements (type b). For non-conveying elements (type c) $K_{f,i}$ and $K_{b,i}$ are both 0. At positions where the conveying direction changes, we used so-called transition elements, for which either $K_{f,i}$ and $K_{b,i}$ are both 0 (change from forward to backward, type d), or $K_{f,i}$ and $K_{b,i}$ are both > 0 (change from backward to forward, type e).

Table 4.1: Parameters for different types of physical screw elements (fwd: forward, bwd: backward).

Type	Description	$K_{f,i}$	$K_{b,i}$	$K_{p,i}$
a	fwd-conveying	> 0	0	> 0
b	bwd-conveying	0	> 0	> 0
c	non-conveying	0	0	> 0
d	transition fwd→bwd	0	0	> 0
e	transition bwd→fwd	> 0	> 0	> 0
f	die element (N)	0	0	> 0

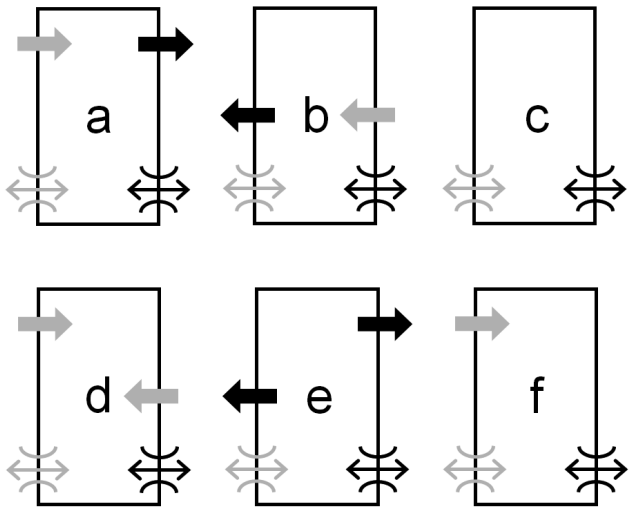

Figure 4.3: Configuration of numerical elements for different types of physical screw elements (grey arrows are exemplary and belong to adjacent elements). For a description of indices a – f see Table 4.1.

At the end of the extruder, we used a die element (type f), representing the clearance volume between screws and the die via a pressure-driven mass flow rate.

For the mass balance of each numerical element i (see Figure 4.2), inflowing mass flow rates minus outflowing mass flow rates yield the time derivative of the mass content m_i within i (expressing the mass content as $m_i = \rho_i \cdot V_i \cdot f_i$):

$$\frac{dm_i}{dt} = \rho_i \cdot V_i \cdot \frac{df_i}{dt} = \dot{m}_{f,i-1} + \dot{m}_{b,i+1} + \dot{m}_{p,i-1} - \dot{m}_{f,i} - \dot{m}_{b,i} - \dot{m}_{p,i} \tag{4.3}$$

For completely filled elements, the filling ratio is constant (f_i = 1), which simplifies the mass balance to:

$$f_i = 1: \quad \dot{m}_{f,i-1} + \dot{m}_{b,i+1} + \dot{m}_{p,i-1} = \dot{m}_{f,i} + \dot{m}_{b,i} + \dot{m}_{p,i} \tag{4.4}$$

Substituting the mass flow rates in Eq. 4.4 from Eqs. 4.1 and 4.2 yields a linear system of algebraic equations for the pressures p_i of the involved numerical elements in a completely filled screw section.

Partially filled screw elements do not generate pressure, thus the value of the pressure in partially filled screw sections is equal to the ambient pressure p_0 (or vacuum pressure in devaporization zones) and constant along the partially filled screw section. Thus, the

pressure-driven flow rates $\dot{m}_{p,i}$ for partially filled numerical elements are zero, which simplifies the balance in this case to:

$$f_i < 1: \quad \rho_i \cdot V_i \cdot \frac{df_i}{dt} = \dot{m}_{f,i-1} + \dot{m}_{b,i+1} - \dot{m}_{f,i} - \dot{m}_{b,i} \tag{4.5}$$

For a partially filled screw section, Eq. 4.5 yields a linear system of ordinary differential equations (ODE) for the filling ratios f_i of the involved numerical elements.

4.2.2 Screw Parameters

For the framework presented above, determination of the actual values of $K_{f,i}$, $K_{b,i}$ and $K_{p,i}$ is required, which is the main challenge of this work. Pawlowski[30] and Kohlgrüber[1] developed a model describing the correlation of axial pressure gradient and throughput of a completely filled, actively conveying screw element in dimensionless form. This is called the "pressure characteristic",

$$\frac{\Delta p}{\eta_r \cdot n} \cdot \frac{D}{\Delta x} = A_2 \cdot \left(1 - \frac{\dot{V}}{A_1 \cdot n \cdot D^3}\right) \tag{4.6}$$

The left-hand side represents the dimensionless pressure gradient in the axial direction, nondimensionalized by the representative viscosity η_r, the screw speed n and the screw diameter D. The group $\dot{V}/(n \cdot D^3)$ at the right hand side is the dimensionless throughput, i.e., the volumetric throughput per screw revolution and unit volume D^3. In case of a Newtonian fluid, the representative viscosity η_r is simply the viscosity of the fluid. However, for non-Newtonian fluids η_r is defined as viscosity of a fictitious Newtonian fluid, which leads to the same Δp and $\dot{V}$ as the non-Newtonian fluid.

Eq. 4.6 represents a linear correlation of the dimensionless axial pressure gradient and the dimensionless throughput, defined by the coefficients A_1 and A_2, which are characteristic of the respective screw element. It was shown, that A_1 and A_2 are independent of length scale, screw speed and viscosity.[1,30] A_1 is a measure for the inherent throughput of the screw element (i.e., the achieved throughput when conveying without backpressure), whereas A_2 describes the ability of the screw element to generate pressure. For a detailed description of

the pressure characteristic and the corresponding parameters we refer to Pawlowski[30], Kohlgrüber[1] and our previous work[51].

It can be easily shown, that the pressure characteristic model Eq. 4.6 is equivalent to the flow rate models, i.e., Eqs. 4.1 and 4.2. Expressing the volumetric throughput from Eq. 4.6 yields:

$$\dot{V} = A_1 \cdot n \cdot D^3 - \frac{A_1}{A_2} \cdot \frac{D^4}{\eta_r} \cdot \frac{\Delta p}{\Delta x} \tag{4.7}$$

The corresponding expression of the volumetric net-throughput in a completely filled, actively conveying screw element (f_i = 1) based on Eqs. 4.1 and 4.2 is obtained as the sum of the screw-driven flow rate (Eq. 4.1) and the pressure-driven flow rate (Eq. 4.2), acting against the conveying direction:

$$\dot{V} = \frac{\dot{m}_{fb,i} + \dot{m}_{p,i}}{\rho_i} = K_{fb,i} \cdot n \cdot A_{cr} \cdot D - \frac{1}{K_{p,i}} \frac{D^4}{\eta_i} \cdot \frac{\Delta p_i}{\Delta x_i} \tag{4.8}$$

Note, that Eqs. 4.7 and 4.8 have an equivalent dependence on screw speed, axial pressure gradient and viscosity, if the viscosity η_i in Eqs. 4.2 and 4.8 is assumed to be equal to the representative viscosity η_r. A comparison yields the following correlations for the empirical parameters $K_{fb,i}$ and $K_{p,i}$ of actively-conveying screw elements:

$$K_{fb,i} = A_1 \cdot \frac{D^2}{A_{cr}} \tag{4.9}$$

$$K_{p,i} = \frac{A_2}{A_1} \tag{4.10}$$

Kohlgrüber[1] reported how to determine A_1 and A_2 for a given screw element geometry either experimentally or by using CFD simulations. Moreover, for conveying elements Kohlgrüber et al.[52] showed the following estimation for the parameter A_1, using the free cross-section area A_{cr} and the pitch T_S:

$$A_1 \approx \frac{1}{2} \frac{A_{cr} \cdot T_s}{D^3} \tag{4.11}$$

For $K_{fb,i}$, this would mean $K_{fb,i} \approx ½\ T_s/D$ (substituting Eq. 4.11 in Eq. 4.9). In our previous work,[51] we determined the parameters A_1 and A_2 for different types of screw elements experimentally.

In addition to actively conveying screw elements, there are also non-conveying elements, for example, kneading blocks with a 90° offset angle. As we showed in our previous work[51], the description based on the pressure characteristic can be extended to non-conveying elements, for which the pressure gradient is zero at zero throughput $\dot{V}$. Instead of Eq. 4.6, the following correlation between the dimensionless throughput $\dot{V}/(n \cdot D^3)$ and the dimensionless axial pressure gradient $\Delta p \cdot D / (\eta_r \cdot n \cdot \Delta x)$ is obtained:

$$\frac{\Delta p}{\eta_r \cdot n} \cdot \frac{D}{\Delta x} = -A_0 \cdot \left(\frac{\dot{V}}{n \cdot D^3} \right) \tag{4.12}$$

The parameters A_1 and A_2 in Eq. 4.6 are replaced by the parameter A_0 in case of non-conveying elements, which is defined as $A_0 = A_2/A_1$ for $A_1, A_2 \rightarrow 0$ and describes the flow resistance in axial direction. Thus, the parameters $K_{fb,i}$ and $K_{p,i}$ for non-conveying elements are:

$$K_{fb,i} = 0 \tag{4.13}$$

$$K_{p,i} = A_0 \tag{4.14}$$

4.2.3 Representative Viscosity

Kohlgrüber[1] reported how to describe the representative viscosity in Eq. 4.6. Due to the analogy of Eqs. 4.1 and 4.2 to Eq. 4.6, we used the same calculation for η_i in the pressure-driven mass flow rate Eq. 4.2. For a shear-thinning fluid, described by the Carreau-model, which is often used to describe the rheology of polymer melts, the representative viscosity is[1]:

$$\eta_r = \frac{\eta_0}{\left[1 + \frac{|\dot{\gamma}_r|}{\dot{\gamma}_{crit}} \right]^m} \tag{4.15}$$

where η_0 is the zero-shear-rate viscosity, $\dot{\gamma}_{crit}$ is the critical shear rate and m the Carreau exponent. For actively conveying elements, the following model for the representative shear rate $\dot{\gamma}_r$ was proposed[1], including an empirical parameter A_3:

$$\dot{\gamma}_r = A_3 \cdot n \cdot \left(1 - \frac{\dot{V}}{A_1 \cdot n \cdot D^3}\right) \tag{4.16}$$

In our previous work,[51] we showed that A_3 can be estimated from A_2, using an average gap distance h between screw and barrel, i.e., $A_3 \approx A_2 \cdot$ h / 2D, where we calculated h from the free cross-section area A_{cr} and the gap length in the cross-sectional plane l_{gap} ($h = A_{cr} / l_{gap}$, illustrated in Figure 4.4).

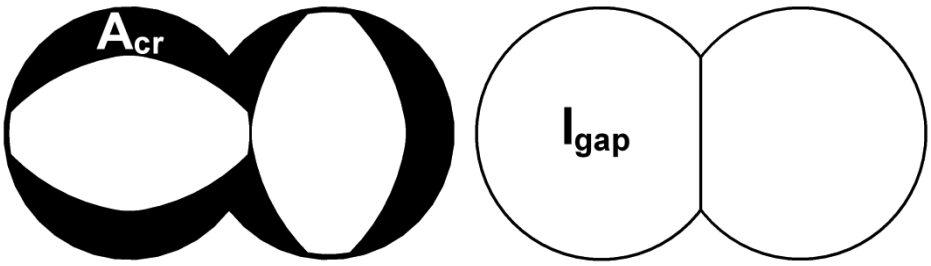

Figure 4.4: Schematic of gap cross-section area A_{cr} (left) and gap length l_{gap} (right).

For non-conveying elements, Eq. 4.16 changes to the following (where $A_3 \approx A_0 \cdot$ h / 2D):[51]

$$\dot{\gamma}_r = A_3 \cdot n \cdot \frac{\dot{V}}{n \cdot D^3} \tag{4.17}$$

4.2.4 Die Pressure Drop

The die is modeled by a pressure-driven flow (Eq. 4.2) after element N, which represents the clearance volume between the screws and the die. The flow resistance parameter $K_{p,N}$ was derived from the pressure drop in a cylindrical pipe flow in the following way. Kohlgrüber[1] showed, that the wall shear rate in a cylindrical pipe flow for a shear-thinning fluid, based on the power law, can be calculated by

$$\dot{\gamma}_W = \frac{3(1-m)+1}{1-m} \cdot \frac{8\dot{V}}{d^3\pi} \tag{4.18}$$

where d is the pipe diameter and $(1 - m)$ the Power law index, substituted by the Carreau exponent m. For the lack of a corresponding equation for Carreau fluids, we used the one above based on the power law. Note, that the power law and the Carreau law converge for high shear rates $\dot{\gamma} > \dot{\gamma}_{crit}$, as is typically the case in the die.

From the force balance of the wall shear forces against the pressure difference over the die length L_{Die}, we can calculate the die pressure drop, substituting the wall shear rate from Eq. 4.18 (τ_W is the wall shear stress):

$$\tau_W \cdot d \cdot \pi \cdot L_{Die} = \Delta p \cdot \frac{d^2 \pi}{4} \tag{4.19}$$

$$\Delta p = \tau_W \cdot \frac{4L_{Die}}{d} = \eta(\dot{\gamma}_W) \cdot \dot{\gamma}_W \cdot \frac{4L_{Die}}{d} = \eta(\dot{\gamma}_W) \cdot \frac{3(1-m)+1}{1-m} \cdot \frac{32\dot{V} \cdot L_{Die}}{d^4 \pi} \tag{4.20}$$

From the pressure-driven mass flow rate Eq. 4.2, the pressure loss of the numerical element N is (with $L_{Die} = x_{N+1} - x_N$):

$$\Delta p = p_N - p_{N+1} = \eta_N \cdot \frac{K_{p,N}}{D^4} \cdot \dot{V} \cdot L_{Die} \tag{4.21}$$

Comparison of Eqs. 4.20 and 4.21 yields the following flow resistance parameter of element N $K_{p,N}$, while the viscosity η_N has to be calculated as $\eta(\dot{\gamma}_W)$ using $\dot{\gamma}_W$ from Eq. 4.18:

$$K_{p,N} = \frac{3(1-m)+1}{1-m} \cdot \frac{32}{\pi} \cdot \left(\frac{D}{d}\right)^4 \tag{4.22}$$

4.2.5 Species Mass Balances

In order to evaluate the RTD, we implemented mass balances for a species mass fraction. Analogous to the overall mass balance for a numerical element Eq. 4.3, we can write the species mass balance for the mass fraction w_i in element i as (considering diffusion to be negligible in high-viscous flows):

$$\frac{d}{dt}(\rho_i \cdot V_i \cdot f_i \cdot w_i) = \sum_{i-1 \to i} \dot{m} \cdot w_{i-1} + \sum_{i+1 \to i} \dot{m} \cdot w_{i+1} - \left(\sum_{i \to i-1} \dot{m} + \sum_{i \to i+1} \dot{m} \right) \cdot w_i \tag{4.23}$$

where the first and second sums denote the mass flow rates flowing from element *i*-1 to *i* and from *i*+1 to *i*, respectively, and the third and fourth sums describe the mass flow rates leaving element *i*. The actual contributions to the summations depend on the values of the pressure in elements *i*-1, *i* and *i*+1, determining the direction of the pressure-driven flow rates.

4.2.6 Energy Balances

Thermal energy sources in hot-melt extrusion are viscous dissipation and active heating (or cooling) in the barrel. Different types of heat fluxes distribute the heat as convective transport by the melt, heat exchange between melt and screws, melt and barrel, heat conduction in screws and barrel, and heat loss to the environment.[48] For this purpose, we assigned sections of screws and barrel to each numerical element *i* (see Figure 4.5), which are described by the temperatures T_i^b (barrel) and T_i^s (screws), whereas the melt temperature is T_i^m.

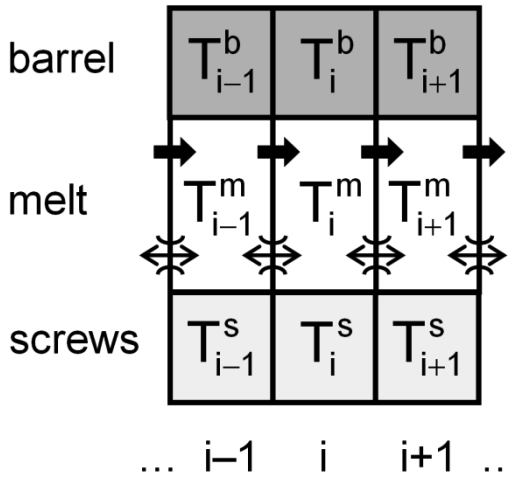

Figure 4.5: Temperature values assigned to the numerical elements.

The energy balance equation for the melt in element *i* accounts for convective heat transfer from/to adjacent elements *i*-1 and *i*+1, heat exchange with barrel and screws and viscous dissipation:

$$\frac{d}{dt}\left(\rho_i \cdot V_i \cdot f_i \cdot c_{p,i}^m \cdot T_i^m\right) = \sum_{i-1\to i} \dot{m} \cdot c_{p,i-1}^m \cdot T_{i-1}^m + \sum_{i+1\to i} \dot{m} \cdot c_{p,i+1}^m \cdot T_{i+1}^m$$
$$-\left(\sum_{i\to i-1} \dot{m} + \sum_{i\to i+1} \dot{m}\right) \cdot c_{p,i}^m \cdot T_i^m + \dot{Q}_{bm,i} + \dot{Q}_{sm,i} + \dot{Q}_{diss,i} \tag{4.24}$$

where $c_{p,i}^m$ is the heat capacity of the melt in element *i*. The dissipated power $\dot{Q}_{diss,i}$ is calculated via the mean volume-specific viscous dissipation rate $\dot{q}_{diss,i}$, which is derived in the next section. The heat fluxes between barrel and melt $\dot{Q}_{bm,i}$ and screws and melt $\dot{Q}_{sm,i}$ are:

$$\dot{Q}_{bm,i} = \alpha_{b,i} \cdot A_{bm,i} \cdot \left(T_i^b - T_i^m\right) \tag{4.25}$$

$$\dot{Q}_{sm,i} = \alpha_{s,i} \cdot A_{sm,i} \cdot \left(T_i^s - T_i^m\right) \dot{m}_{fb,i} = \rho_i \cdot K_{fb,i} \cdot n \cdot f_i \cdot A_{cr} \cdot D \tag{4.26}$$

where $\alpha_{b,i}$ is the heat transfer coefficient (HTC) between melt and barrel, $A_{bm,i} = 2 \cdot D_B \cdot (\pi - \psi) \cdot \Delta x_i$ the inner barrel surface area, $\alpha_{s,i}$ the HTC between screws and melt and $A_{sm,i}$ is the surface area of the screws contributing to heat transfer in element *i*. We assumed, that even for partially filled screws the entire barrel surfaces contribute to the heat transfer, since a melt film is established at the barrel which is exchanged periodically with every pass of the melt bulk (see Figure 4.6).

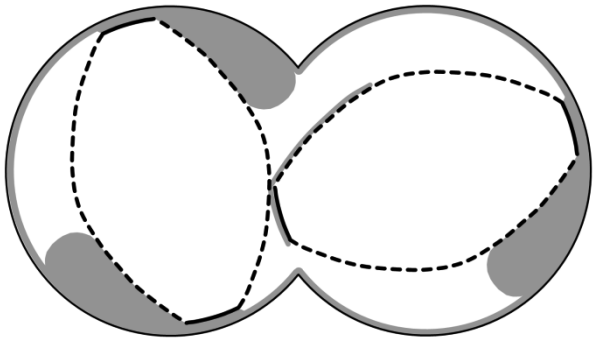

Figure 4.6: Melt film at the barrel surface (shaded line) for partially filled screws and division of the screw surfaces into tip surface (solid lines) and channel surface (dashed lines).

The screw surface consists of two different parts: the tip surface, which forms the gap between screw and barrel (solid lines in Figure 4.6), and the channel surface (dashed lines in Figure 4.6). Similar to the barrel surface, the gap flow causes a continuous exchange at

the tip surfaces. Thus, we assumed that the tip surfaces contribute to the heat transfer completely. However, depending on the filling ratio, some regions of the channel surface will not be into contact with the melt bulk during the revolution and, thus, are assumed not to contribute to the heat transfer. For that reason, we scaled the channel surface of the screws with the filling ratio ($A_{s,tip,i}$ is the tip surface area in element i and $A_{s,ch,i}$ the channel surface area in element i):

$$A_{sm,i} = A_{s,tip,i} + A_{s,ch,i} \cdot f_i \tag{4.27}$$

where the tip surface of the screws is $A_{s,tip,i} = \alpha \cdot D \cdot n_F \cdot \Delta x_i$ and $A_{s,ch,i}$ can be calculated from the screw surface area A_{surf} given in Appendix B.

The energy balance equation for the barrel section in element i accounts for heat conduction in the axial direction, heat exchange with melt and environment and the active barrel heating:

$$m_i^b \cdot c_p^b \cdot \frac{dT_i^b}{dt} = -\lambda_b \cdot A_b \cdot \frac{T_i^b - T_{i-1}^b}{x_i - x_{i-1}} + \lambda_b \cdot A_b \cdot \frac{T_{i+1}^b - T_i^b}{x_{i+1} - x_i} - \dot{Q}_{e,i} - \dot{Q}_{bm,i} + P_{heat,i} \tag{4.28}$$

where m_i^b is the mass of barrel in element i, c_p^b and λ_b the heat capacity and thermal conductivity of the barrel steel, A_b the barrel cross-section area, $\dot{Q}_{e,i}$ the heat loss to the environment and $P_{heat,i}$ is the barrel heating power (or cooling power when negative). The heat loss to the environment is described as:

$$\dot{Q}_{e,i} = \alpha_{e,i} \cdot A_{e,i} \cdot \left(T_e - T_i^b\right) \tag{4.29}$$

where $\alpha_{e,i}$ is the HTC between barrel and environment, $A_{e,i}$ the barrel surface area in element i and T_e the environment temperature. Analogously, the energy balance equation for the screws in element i is:

$$m_i^s \cdot c_p^s \cdot \frac{dT_i^s}{dt} = -\lambda_s \cdot A_s \cdot \frac{T_i^s - T_{i-1}^s}{x_i - x_{i-1}} + \lambda_s \cdot A_s \cdot \frac{T_{i+1}^s - T_i^s}{x_{i+1} - x_i} - \dot{Q}_{sm,i} \tag{4.30}$$

where m_i^s is the mass of the screws in element i, c_p^s and λ_s the heat capacity and thermal conductivity of the screw steel and A_s the cross-section area of both screws.

4.2.7 Viscous Dissipation Rate

The viscous dissipation is the heat generated from viscous stresses (i.e., shear rates), which, for high-viscous fluids typically yields a significant contribution to the thermal energy balance. It can be calculated from the spatially-resolved velocity field using tensor analysis. To account for the viscous dissipation rate in our 1D model, we developed an approximation based on a detailed consideration of the flow field. For a partially filled screw section (also a completely filled screw section without backpressure) we assumed, that the circumferential shear rates caused by the rotation of the screws yield the dominating contribution to the viscous dissipation rate. However, in a completely filled screw section with backpressure, the pressure-driven backflow against the conveying direction causes an additional contribution which has to be taken into account. Thus, we calculated the viscous dissipation rate as a sum of two parts, one caused by the flow in the circumferential direction ($\dot{q}_{diss,circ,i}$) and one caused by the pressure-driven flow in the axial direction ($\dot{q}_{diss,ax,i}$):

$$\dot{q}_{diss,i} = \dot{q}_{diss,circ,i} + \dot{q}_{diss,ax,i} \quad \dot{m}_{fb,i} = \rho_i \cdot K_{fb,i} \cdot n \cdot f_i \cdot A_{cr} \cdot D \tag{4.31}$$

The axial part can be calculated as energy loss of the pressure-driven flow $\dot{Q}_{diss,ax,i} = -\dot{V}_{p,i} \cdot \Delta p_i$ (the minus is required since the pressure-driven flow rate is directed against increasing pressure in Eq. 4.2) divided by the volume in element *i* ($V_i = \Delta x_i \cdot A_{cr}$):

$$\dot{q}_{diss,ax,i} = \frac{\dot{Q}_{diss,ax,i}}{V_i} = -\frac{\dot{m}_{p,i} \cdot \Delta p_i}{\rho_i \cdot \Delta x_i \cdot A_{cr}} \tag{4.32}$$

Substituting the pressure-driven flow rate $\dot{m}_{p,i}$ from Eq. 4.2 yields:

$$\dot{q}_{diss,ax,i} = \frac{D^4}{K_{p,i} \cdot \eta_i \cdot A_{cr}} \cdot \left(\frac{\Delta p_i}{\Delta x_i} \right)^2 \tag{4.33}$$

In order to calculate the circumferential contribution of the viscous dissipation rate, we considered the cross-section of the twin-screw (see Figure 4.7). Although, the volume fraction of the gap regions is small (highlighted in black, typically in the order of 1%), the

gap regions contribute significantly to viscous dissipation, since the circumferential shear rate is maximized there. Thus, we calculated the viscous dissipation rate for gap and channel regions separately ($\dot{q}_{diss,ga,i}$, $\dot{q}_{diss,ch,i}$) using a weighted average based on the volume fractions of melt located in each region. For partially filled screws, we assumed that the gaps are always completely filled, since the melt is pushed in front of the screw flights (as shown in Figure 4.7), whereas the channels are partially filled according to the actual filling ratio f_i:

$$\dot{q}_{diss,circ,i} = \frac{\dot{q}_{diss,ga,i} \cdot \varepsilon_{ga} + \dot{q}_{diss,ch,i} \cdot \varepsilon_{ch} \cdot f_i}{\varepsilon_{ga} + \varepsilon_{ch} \cdot f_i} \tag{4.34}$$

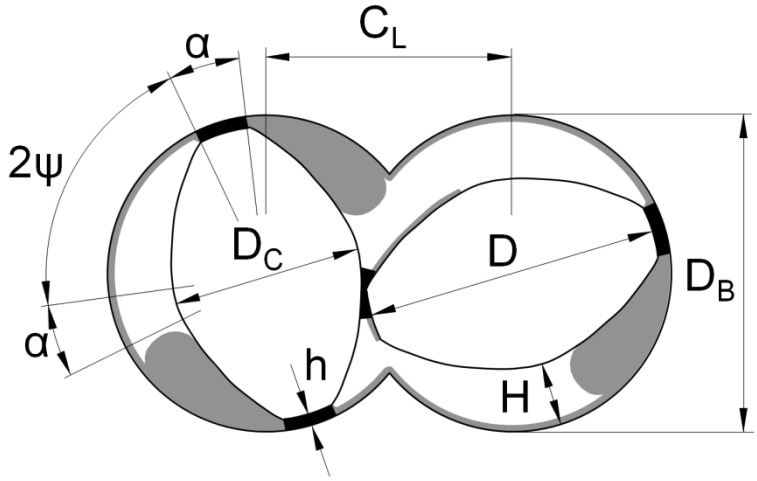

Figure 4.7: Cross-section of a partially filled twin-screw (two-flighted, $n_F = 2$), gap regions are highlighted in black, geometrical dimensions: outer screw diameter D, screw core diameter D_C, barrel diameter D_B, centerline distance C_L, gap distance h, channel depth H, tip angle α, angle ψ.

The volume fractions of gap and channel regions (ε_{ga}, ε_{ch}) can be calculated from the geometry (see Figure 4.7):

$$\varepsilon_{ga} = \frac{\alpha \cdot D \cdot h \cdot n_F}{A_{cr}} \tag{4.35}$$

$$\varepsilon_{ch} = 1 - \varepsilon_{ga} \tag{4.36}$$

where A_{cr} is the free cross-section area of the twin-screw. How the latter and the tip angle α can be calculated is shown in Appendix B.

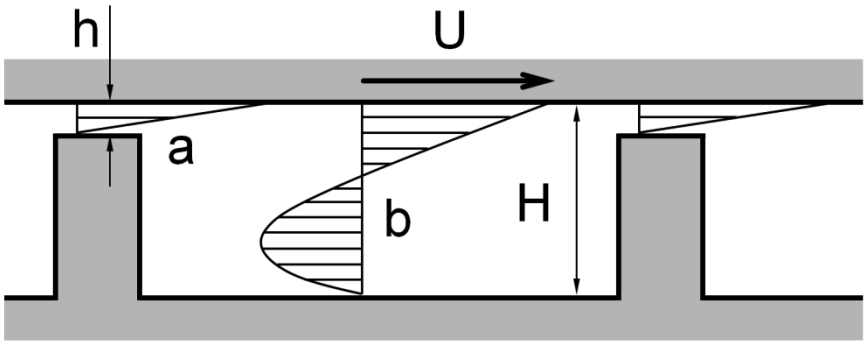

Figure 4.8: Velocity profiles in a two-plate model (a: gap region, b: channel region).

In order to establish the viscous dissipation rate in the gap and channel regions, we considered a simplified two-plate model of the screws (see Figure 4.8), which consists of a steady plate at the bottom including periodic ridges (i.e., simplified screw flights) and a moving plate at the top (i.e., a simplified barrel). In the gap regions between barrel and screw flights (region "a" in Figure 4.8) we assumed linear velocity profiles. This is not exactly true, since a pressure-driven flow superposes a drag flow over the screw flights, however, the linear profile is a good approximation (as also shown by Bierdel[53] using CFD). Then, the volume-specific viscous dissipation rate in the gap region can be calculated as:

$$\dot{q}_{diss,ga,i} = \eta_{ga,i} \cdot \dot{\gamma}_{ga}^{\,2} \tag{4.37}$$

with $\eta_{ga,i} = \eta\left(\dot{\gamma}_{ga}, T_{m,i}\right)$ for a shear-thinning melt. The shear rate in the gaps $\dot{\gamma}_{ga}$ is circumferential velocity per gap distance h (for simplicity, the gap between both screws is not distinguished from the gaps between screws and barrel):

$$\dot{\gamma}_{ga} = \frac{D\pi n}{h} \tag{4.38}$$

However, the approximation of a linear velocity profile is not suitable for the channel regions (region "b" in Figure 4.8), since the screw channels in the cross-section form cavities where instead of a pure shear flow a circulation is established due to the drag of the barrel. Thus, we assumed a 2D channel flow with a boundary velocity U, a channel depth H and a throughput of zero (i.e., a Couette-Poiseuille flow, as illustrated in region "b" in Figure 4.8), for which the velocity profile is:

$$u(y) = U\frac{y}{H} - \frac{H^2}{2\eta}\cdot\frac{\partial p}{\partial x}\cdot\frac{y}{H}\cdot\left(1-\frac{y}{H}\right) \tag{4.39}$$

Setting the throughput to zero yields a condition for the pressure gradient which can be substituted in Eq. 4.39:

$$\dot{V} = \int_{y=0}^{H} u(y)\cdot dy = \frac{U\cdot H}{2} - \frac{H^3}{12\eta}\cdot\frac{\partial p}{\partial x} = 0 \Rightarrow \frac{\partial p}{\partial x} = \frac{6\eta\cdot U}{H^2} \tag{4.40}$$

$$u(y) = U\cdot\frac{y}{H}\cdot\left[3\frac{y}{H}-2\right] \tag{4.41}$$

Using this, the average viscous dissipation rate in the channel yields:

$$\dot{q}_{diss} = \frac{1}{H}\int_{y=0}^{H}\eta\cdot\left(\frac{\partial u}{\partial y}\right)^2 dy = 4\eta\cdot\left(\frac{U}{H}\right)^2 \tag{4.42}$$

Applying this to the channel region:

$$\dot{q}_{diss,ch,i} = 4\eta_{ch,i}\cdot\dot{\gamma}_{ch}^{\ 2} \tag{4.43}$$

$$\dot{\gamma}_{ch} = \frac{D_C\pi n}{H_{av}} \tag{4.44}$$

with $\eta_{ch,i} = \eta\left(\dot{\gamma}_{ch}, T_{m,i}\right)$ for a shear-thinning melt. For the channel depth H we used an average value H_{av}, which was calculated as the cross-sectional area of the screw channels divided by the arc length at the barrel diameter D_B over which the channels extend (A_{scr} is the cross-sectional area of one screw, see Appendix B):

$$H_{av} = \frac{D_B^{\ 2}\cdot\frac{\pi}{4} - A_{scr} - \alpha\cdot\frac{D}{2}\cdot h\cdot n_F}{\frac{D_B}{2}\cdot(4\psi+\alpha)\cdot n_F} \tag{4.45}$$

We estimated the mean viscous dissipation based on this concept (Eqs. 4.31, 4.33 - 4.38, 4.43 - 4.45) for conveying elements. In the case of kneading elements, we adopted the

equations to account for an additional contribution to the viscous dissipation rate, caused by the gaps in the offset region between the kneading discs (i.e., the shaded region in Figure 4.9a and b). Thus, Eq. 4.34 for kneading elements changes to the following:

$$\dot{q}_{diss,circ,i} = \frac{\dot{q}_{diss,ga,i} \cdot \varepsilon_{ga} + \dot{q}_{diss,off,i} \cdot \varepsilon_{off} + \dot{q}_{diss,ch,i} \cdot \varepsilon_{ch} \cdot f_i}{\varepsilon_{ga} + \varepsilon_{off} + \varepsilon_{ch} \cdot f_i} \tag{4.46}$$

where $\dot{q}_{diss,off,i}$ is the viscous dissipation rate in the offset region and ε_{off} the average volume fraction of the offset region during one revolution. Similar to the gap region, we assumed that the offset gaps are always completely filled, including the case of partially filled elements. The offset distance slightly reduces the volume fraction of the gap region for kneading elements:

$$\varepsilon_{ga} = \frac{\alpha \cdot D \cdot n_F \cdot h \cdot L_D \cdot n_D}{A_{cr} \cdot L} \quad \dot{m}_{fb,i} = \rho_i \cdot K_{fb,i} \cdot n \cdot f_i \cdot A_{cr} \cdot D \tag{4.47}$$

where L_D is the length of a single disc and n_D the number of kneading discs. L is the total length of the kneading element, L_{off} the distance of the offset gaps (see Figure 4.9c):

$$L = L_D \cdot n_D + L_{off} \cdot (n_D - 1) \tag{4.48}$$

For the average volume fraction of the offset region during a revolution, we developed the following heuristic approximation (where κ is the offset angle of the element):

$$\varepsilon_{off} = \frac{\alpha \cdot D \cdot (D - C_L) \cdot L_{off} \cdot (n_D - 1)}{2 \cdot A_{cr} \cdot L} \cdot \frac{\psi \cdot n_F}{2 \cdot \pi} \cdot \left| \frac{\kappa}{90°} \right| \tag{4.49}$$

The first fraction of Eq. 4.49 describes the volume fraction for full overlap of the adjacent discs of a 90° kneading element (see shaded area in Figure 4.9a). However, the overlap is present only for a short period during the whole revolution, accounted for by the second fraction of Eq. 4.49 *($\psi \cdot n_F / 2\pi$)*. The third fraction $|\kappa/90°|$ interpolates for offset angles different from 90°: For a (theoretical) 0° offset angle there occurs no overlap during the revolution; for a 45° kneading block occurs approximately 50% of the overlap compared to a 90° offset angle (see Figure 4.9a and b).

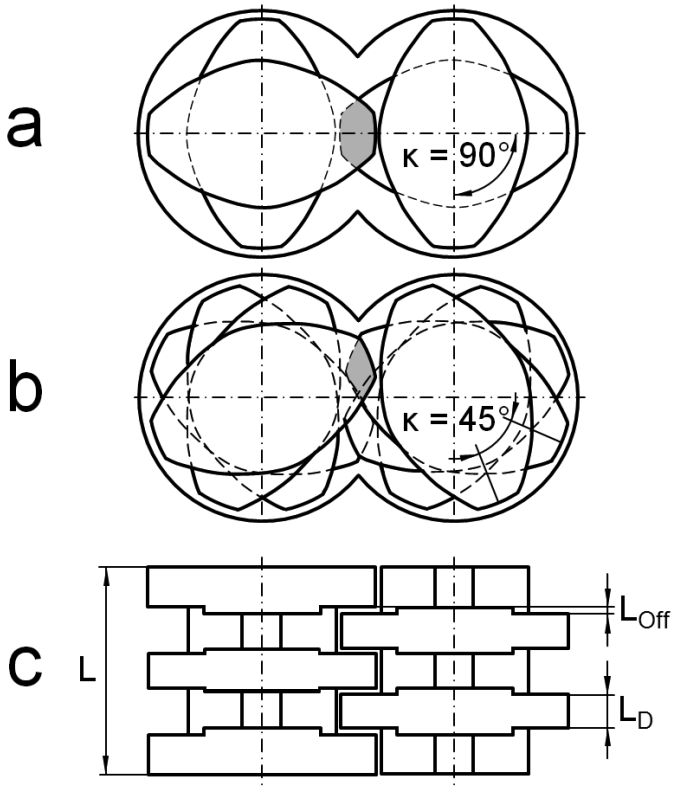

Figure 4.9: Overlap area in the offset region of kneading elements for (a) 90° offset angle and (b) 45° offset angle, (c) geometrical parameters for a kneading element with 5 discs: length L, disc length L_D, offset distance L_{Off}.

The channel regions include the remaining volume (similarly to Eq. 4.36):

$$\varepsilon_{ch} = 1 - \varepsilon_{ga} - \varepsilon_{off} \tag{4.50}$$

The viscous dissipation rate in the offset region is calculated assuming a linear velocity profile in the gap, similarly to Eq. 4.37:

$$\dot{q}_{diss,off,i} = \eta_{off,i} \cdot \dot{\gamma}_{off}^{\,2} \tag{4.51}$$

with $\eta_{off,i} = \eta\left(\dot{\gamma}_{off}, T_{m,i}\right)$ for a shear-thinning melt. The shear rate in the offset gaps $\dot{\gamma}_{off}$ is the relative circumferential velocity between both screws per gap distance L_{off}, similarly to Eq. 4.38:

$$\dot{\gamma}_{ga} = \frac{2C_L \cdot \pi \cdot n}{L_{off}} \tag{4.52}$$

4.2.8 Heat Transfer Coefficients

Three different HTCs are required in the energy balances (Eqs. 4.24 – 4.30), i.e., the HTC between melt and barrel α_b, melt and screws α_s and between barrel and the environment α_e. The HTC between melt and barrel is crucial, since it determines how far the melt temperature exceeds the barrel temperature due to dissipation. This also directly determines the melt viscosity and impacts the axial pressure gradient.

Pawlowski[30] showed, that the heat transfer between barrel and melt depends on screw speed and throughput. However, the throughput dependency is often neglected, specifically in the case of low throughputs, as typically encountered in the case of pharmaceutical extrusion. According to the experimental work of Guo and Chung[34], the Nusselt number for heat transfer to the barrel can be expressed as $Nu = C \cdot Re^{0.5} \cdot Pr^{0.33}$. White et al.[35] showed analytically for a co-rotating twin-screw extruder, that $Nu \sim (Re \cdot Pr)^{1/3}$, which is similar to the experimentally determined dependence $Nu \sim Re^{0.28} \cdot Pr^{0.33}$ reported by Todd[29,35,54]. Thus, we used a similar power-law correlation to calculate the HTC between melt and barrel α_b:

$$\alpha_b = \frac{Nu \cdot \lambda_m}{D} \tag{4.53}$$

$$Nu = C \cdot Re^k \cdot Pr^{0.33} \tag{4.54}$$

where Pr is the Prandtl number of the melt and the Reynolds number Re is based on screw speed n, screw diameter D and density and viscosity of the melt ρ and η:

$$Re = \frac{n \cdot D^2 \cdot \rho}{\eta} \tag{4.55}$$

Our previous work[51] yielded experimental data for the screw speed dependency of the melt temperature for a typical non-Newtonian polymer used in pharmaceutics (Soluplus®), and we found that these measurements are not well-described with the Nusselt correlations mentioned above. Thus, we fitted the exponent k and the coefficient C from our measured data (k = 0.838, C = 26.8), for a detailed description see below.

For the heat transfer between melt and screw, we used the same value as between melt and barrel $\alpha_s = \alpha_b$. This may be an approximation; however the screw temperature is expected to be similar to the melt temperature since the screws are only in contact with melt in the considered section. Thus, the heat transfer between melt and screws is not dominant in the energy balance.

The HTC between barrel and environment is not crucial for the conditions inside the barrel, since the barrel temperature is usually controlled, i.e., kept constant. Thus, the heat transfer to the environment is only of interest, if the required heating or cooling power of the barrel should be calculated. The overall HTC for the barrel can be estimated via a Nusselt number correlation for free convection around a horizontal cylinder, which is given for example in the VDI Heat Atlas[55].

4.2.9 Gap Temperature

The proposed 1D model does not resolve radial or circumferential gradients and thus, accounts for an average melt temperature over the cross-section of the twin-screw. However, in reality, the temperature is distributed over the cross direction due to the local differences of the viscous dissipation rate in gap and channel regions. Specifically, in gap regions, the circumferential shear rate (Eq. 4.38) is strongly increased compared to channel regions (typically more than 20-fold). Thus, the viscous dissipation rate, scaling with the square of the shear rate, is orders of magnitude higher in the gap region.[53] Thus, the temperature is typically higher in the gap, depending on the material and the operating conditions. Evidently, computationally more intensive 3D methods are required to solve the temperature field accurately. However, in practical applications an estimation of the gap temperature can be sufficient to determine if temperature peaks are critical, for example, in terms of thermal degradation. Therefore, we estimated the gap temperature based on the viscous dissipation rate in the gaps (Eq. 4.37), using a simple energy balance, consisting of the amount of dissipation in the gap and the throughput through the gap, which experiences the average temperature increase ΔT^{ga}:

$$\dot{q}_{diss,ga} \cdot V_{ga} = \rho \cdot \dot{V}_{ga} \cdot c_p \cdot \Delta T^{ga} \tag{4.56}$$

The volume of the gap region in a screw section of the length L can be expressed as $V_{ga} = ½ \cdot \alpha \cdot D \cdot h \cdot L$ (see Figure 4.7). The corresponding throughput is $\dot{V}_{ga} = \dot{\gamma}_{ga} \cdot h/2 \cdot h \cdot L$ which is based on the average velocity in the shear flow $\dot{\gamma}_{ga} \cdot h/2$. Substituting these in Eq. 4.56 yields for the average temperature increase:

$$\Delta T^{ga} = \frac{\dot{q}_{diss,ga}}{\rho \cdot c_P} \cdot \frac{\alpha \cdot D}{\dot{\gamma}_{ga} \cdot h} \tag{4.57}$$

with $\dot{\gamma}_{ga}$ from Eq. 4.38. For α see Appendix B. The actual gap temperature T^{ga} in element i is then

$$T_i^{ga} = T_i^m + \Delta T_i^{ga} \tag{4.58}$$

According to Kohlgrüber et al.[52], another equation for the temperature increase in the gap results from consideration of the temperature field in the boundary layer of a Newtonian fluid. In contrast to the average gap temperature Eq. 4.58, this describes the maximum temperature increase, which is the case directly at the screw surface, where the residence time in the gap is the highest. Moreover, the theoretical limit case of an adiabatic wall was presumed, which leads to the maximum possible gap temperature:

$$\Delta T^{ga,max} = 1.43 \cdot \eta \cdot \left(\frac{\left(\alpha \cdot D/2 \cdot \dot{\gamma}_{ga}{}^2\right)^2}{\lambda \cdot \left(\rho \cdot c_P\right)^2} \right)^{1/3} \tag{4.59}$$

$$T_i^{ga,max} = T_i^m + \Delta T_i^{ga,max} \tag{4.60}$$

4.2.10 Screw Driving Power and Torque

The screw driving power was calculated via a summation of the required power input in each numerical element:

$$P_{screw} = \sum_{i=1}^{N} P_{screw,i} \tag{4.61}$$

Two mechanisms contribute to the screw driving power, i.e., the pumping power $P_{pump,i}$, which is required to convey the melt against increasing pressure, and the dissipated power $\dot{Q}_{diss,i}$, which represents the amount of power transferred into heat:

$$P_{screw,i} = P_{pump,i} + \dot{Q}_{diss,i} \tag{4.62}$$

The pumping power was calculated as throughput times pressure difference between adjacent elements, which yields positive values when the pressure increases in the conveying direction (i.e., conveying against backpressure) and negative values when the pressure decreases in the conveying direction (i.e., the pressure supports the flow in conveying direction, the case for non-conveying elements and backward conveying elements):

$$P_{pump,i} = \dot{V}_i \cdot \Delta p_i \tag{4.63}$$

The required screw torque is the screw driving power divided by the angular speed:

$$T_{Screw} = \frac{P_{Screw}}{2\pi n} \tag{4.64}$$

Note, that the screw driving power and the torque are calculated for both screws together, i.e., the torque of each screw is half of the one specified by Eq. 4.64.

4.3 Material Properties

The required material properties in the proposed model are density, viscosity, thermal conductivity and heat capacity. For our experimental studies, the pharmaceutical-grade matrix material Soluplus® was used, which is a polyvinyl caprolactam-polyvinyl acetate-polyethylene glycol graft copolymer specifically designed for HME. Detailed information is provided by the manufacturer.[56]

4.3.1 Density

We described the density measurements in detail in our previous work.[51] The measured data were fitted with the Menges model, which describes the density ρ [kg/m³] depending on pressure p and temperature T:

$$\rho = \left(\frac{K_1}{p + K_4} + \frac{K_2 \cdot T}{p + K_3} \right)^{-1} \tag{4.65}$$

The parameters ($K_1 - K_4$) established through the measurements are provided in Table 4.2 for temperatures above and below the glass transition temperature T_g, which is described by $T_g = 72.7 + 2.90 \cdot 10^{-7} \cdot p$ (T_g in [°C], depending on pressure p in [Pa]).

Table 4.2: Menges model parameters.

	$T < T_g$	$T > T_g$
K_1 [Pa m³/kg]	$2.97 \cdot 10^6$	$2.95 \cdot 10^6$
K_2 [Pa m³/kg K]	35.5	116
K_3 [Pa]	$1.67 \cdot 10^8$	$2.61 \cdot 10^8$
K_4 [Pa]	$3.43 \cdot 10^9$	$3.48 \cdot 10^9$

4.3.2 Melt Viscosity

The viscosity measurements were also described in our previous work.[51] For the shear-thinning melt viscosity we used the temperature-dependent Carreau model, see also Rauwendaal[57] (with zero-shear-rate viscosity η_0, critical shear rate $\dot{\gamma}_{crit}$, and Carreau index m, given in Table 4.3):

$$\eta(\dot{\gamma}, T) = \frac{\eta_0 \cdot a_T}{\left(1 + \frac{|\dot{\gamma}| \cdot a_T}{\dot{\gamma}_{crit}} \right)^m} \tag{4.66}$$

The temperature shift factor a_T was described by the Williams-Landel-Ferry (WLF) equation (with temperature T and reference temperature T_r, for the parameters see Table 4.3):

$$a_T = \exp\left[\frac{-C_1 \cdot (T - T_r)}{C_2 + T - T_r} \right] \tag{4.67}$$

Table 4.3: Viscosity parameters.

η_0	3000 Pa·s
$\dot{\gamma}_{crit}$	5.79 s^{-1}
m	0.395
T_r	170 °C
C_1	10.7
C_2	135 °C

4.3.3 Thermal Conductivity

The thermal conductivity of Soluplus® was measured between 20 and 220°C using a thermal conductivity measurement device, type K-System II (Advanced CAE Technology Inc., Ithaca, USA) according to ASTM D5930-09. A linear function was fitted (T in [°C], λ in [W/mK]):

$$\lambda = 0.156 + 4.70 \cdot 10^{-4} \cdot T \tag{4.68}$$

4.3.4 Heat Capacity

The heat capacity function of Soluplus® was determined from data provided by the manufacturer[56] (T in [°C], c_p in [J/kgK]):

$$c_p = 1527 + 4.07 \cdot T \tag{4.69}$$

4.4 Determination of Heat Transfer

In a completely filled screw section, the dissipated heat is mainly removed by the barrel, i.e., the heat transfer to the barrel has to balance the viscous dissipation, which is proportional to the melt viscosity and the screw speed squared (see Eqs. 4.37, 4.38, 4.43, 4.44):

$$\eta \cdot n^2 \sim \alpha_b \cdot A_{bm} \cdot \left(T_m - T_b\right) \tag{4.70}$$

The barrel surface area A_{bm} is constant, and thus can be canceled out. Expressing the HTC in Eq. 4.70 α_b via the Nusselt number Nu (Eq. 4.53) leads to the following (where the right-hand side was nondimensionalized with the screw diameter D):

$$Nu = \frac{\alpha_b \cdot D}{\lambda_m} \sim \frac{\eta \cdot n^2 \cdot D^2}{\lambda_m \cdot (T_m - T_b)} \tag{4.71}$$

Using the power law correlation Eq. 4.54 we obtain:

$$\frac{Nu}{C \cdot \mathrm{Pr}^{0.33}} = \mathrm{Re}^k \sim \frac{\eta \cdot (n \cdot D)^2}{\lambda_m \cdot (T_m - T_b) \cdot \mathrm{Pr}^{0.33}} \tag{4.72}$$

Eq. 4.72 correlates screw speed and melt temperature, i.e., for given data of screw speed and melt temperature the exponent k can be determined. In our previous work,[51] we measured melt temperature versus screw speed for different types of screw elements using a Coperion ZSK 18 extruder with a specifically constructed melt temperature probe mounted directly at the end of the screws, which was extending into the melt flow and was thermally isolated from the barrel. The measured melt temperature was between 10 and 20 °C higher (depending on the screw speed) than the barrel temperature of 180 °C, but not significantly different among the investigated screw elements (conveying elements as well as kneading elements). The measured data are shown in Table 4.4, where the ± values represent the standard deviation of the variation among the investigated screw elements.

Table 4.4: Measured melt temperature and standard deviation (±) vs. screw speed.

n [min^{-1}]	T_m [°C]
60	193.5 ± 1.6
120	197.2 ± 1.7
180	200.9 ± 1.3

Using these data in Eq. 4.72 and fitting the exponent k, the resulting k is between 0.75 and 0.86, depending on how the viscosity value is calculated, i.e., using the gap shear rate (Eq. 4.38) or the channel shear rate (Eq. 4.44) in the Carreau model (Eq. 4.66). This is

obviously different from the *Nu* correlations reported in the literature,[29,34,35,54] where *k* was between 0.28 and 0.5.

In order to determine the coefficient *C* in Eq. 4.54, we replaced the proportionality in Eq. 4.72 by calculating the viscous dissipation rate from Eqs. 4.31, 4.34 – 4.38 and 4.43 – 4.45. However, we neglected the contribution from the pressure-driven flow Eq. 4.33, since the throughput dependency of the measured melt temperature was almost vanishing, i.e., we calculated the viscous dissipation rate purely from the circumferential shear rates:

$$\left(\eta_{Ga}\cdot\dot{\gamma}_{Ga}^{\,2}\cdot\varepsilon_{Ga}+4\cdot\eta_{Ch}\cdot\dot{\gamma}_{Ch}^{\,2}\cdot\varepsilon_{Ch}\right)\cdot A_{cr}\cdot L\approx\alpha_{bm}\cdot A_{bm}\cdot\left(T_m-T_b\right) \tag{4.73}$$

From this, the HTC α_b and the Nusselt number *Nu* can be expressed as

$$Nu=\frac{\alpha_b\cdot D}{\lambda_m}\approx\frac{\left(\eta_{Ga}\cdot\dot{\gamma}_{Ga}^{\,2}\cdot\varepsilon_{Ga}+4\cdot\eta_{Ch}\cdot\dot{\gamma}_{Ch}^{\,2}\cdot\varepsilon_{Ch}\right)\cdot A_{cr}\cdot D}{\lambda_m\cdot L_{bm}\cdot\left(T_m-T_b\right)} \tag{4.74}$$

where the ratio A_{bm}/L is the circumference of the barrel hole L_{bm}. We calculated the Nusselt number (from Eq. 4.74) and the Reynolds number (from Eq. 4.55) for the data shown in Table 4.4, where we used the Carreau model (Eq. 4.66) with the channel shear rate (Eq. 4.44) for the viscosity value in Eq. 4.55.

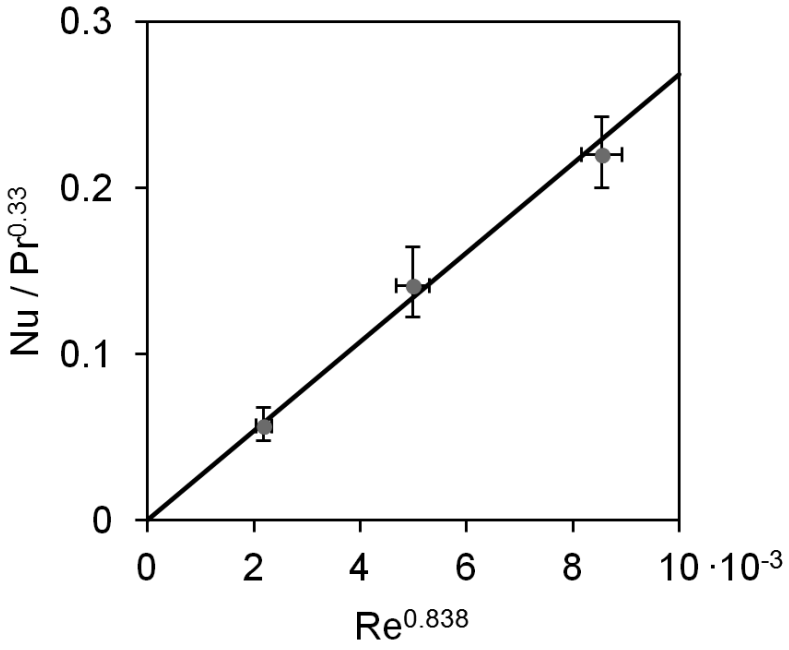

Figure 4.10: Fit of the power law $Nu = C \cdot Re^k \cdot Pr^{0.33}$ based on experimental data.

The resulting data $Nu/Pr^{0.33}$ versus Re are shown in Figure 4.10, together with the fitted power law according to:

$$\frac{Nu}{\mathrm{Pr}^{0.33}} = C \cdot \mathrm{Re}^{k} \tag{4.75}$$

This yielded the following correlation, which we used for the results presented below:

$$Nu = 26.8 \cdot Re^{0.838} \cdot Pr^{0.33} \tag{4.76}$$

4.5 Numerical Solution

The proposed model consists of transient equations for the filling ratios, temperatures and species mass fraction of the numerical elements along the twin-screw. Thus, unsteady simulations are possible. However, for practical applications the steady state is usually of interest, which was achieved by solving the transient equations, starting from a defined initial state, until the steady state was reached.

For partially filled numerical elements (filling ratio $f_i < 1$), the balance equations for mass (Eq. 4.5), species mass fraction (Eq. 4.23) and thermal energy (Eqs. 4.24, 4.28 and 4.30) constitute a system of ODEs (i.e., five time-dependent ODEs for each numerical element) which was solved in MATLAB® R2009a (The Mathworks, Inc.) using the "ode15s" built-in solver.

From Eq. 4.5, the time derivative of the filling ratio df_i/dt can be directly calculated (using the mass flow rates Eqs. 4.1 and 4.2).

Eq. 4.23 allows the calculation of the time derivative of the species mass fraction dw_i/dt in the following way (note that mass fraction w_i and filling ratio f_i are both time-dependent, while the time-dependency of the density ρ_i was neglected):

$$\frac{dw_i}{dt} = \frac{1}{\rho_i \cdot V_i \cdot f_i}\left(\sum_{i-1 \to i} \dot{m} \cdot w_{i-1} + \sum_{i+1 \to i} \dot{m} \cdot w_{i+1} - \left(\sum_{i \to i-1} \dot{m} + \sum_{i \to i+1} \dot{m} \right) \cdot w_i \right) - \frac{w_i}{f_i} \cdot \frac{df_i}{dt} \tag{4.77}$$

where the sums of the flow rates to/from the adjacent elements are known from the mass balance.

Similarly, from Eq. 4.24, the time derivate of the melt temperature dT_i^m/dt can be calculated:

$$\frac{dT_i^m}{dt} = \frac{\sum_{i-1\to i}\dot{m}\cdot c_{p,i-1}^m\cdot T_{i-1}^m + \sum_{i+1\to i}\dot{m}\cdot c_{p,i+1}^m\cdot T_{i+1}^m - \left(\sum_{i\to i-1}\dot{m} + \sum_{i\to i+1}\dot{m}\right)\cdot c_{p,i}^m\cdot T_i^m + \dot{Q}_{bm,i} + \dot{Q}_{sm,i}}{\rho_i\cdot V_i\cdot f_i\cdot c_{p,i}^m} + \frac{\dot{q}_{Diss,i}}{\rho_i\cdot c_{p,i}^m} - \frac{T_i^m}{f_i}\cdot\frac{df_i}{dt} \tag{4.78}$$

where the calculation of the source terms is described in the sections above in detail. The thermal energy balances for the barrel (Eq. 4.28) and the screws (Eq. 4.30) allow calculation of the time derivatives of barrel temperature dT_i^b/dt and screw temperature dT_i^s/dt directly.

For completely filled numerical elements (f_i = 1), the mass balance is described by Eq. 4.4, which simplifies the problem to four ODEs (Eqs. 4.23, 4.24, 4.28 and 4.30) and one algebraic equation (Eq. 4.4) for each numerical element. Substituting the mass flow rates Eq. 4.1 and Eq. 4.2 in the mass balance of a completely filled element Eq. 4.4 yields:

$$\begin{aligned}&\rho_{i-1}\cdot K_{f,i-1}\cdot n\cdot f_{i-1}\cdot A_{cr}\cdot D + \rho_{i+1}\cdot K_{b,i+1}\cdot n\cdot f_{i+1}\cdot A_{cr}\cdot D - \frac{D^4}{K_{p,i-1}}\cdot\frac{\rho_{i-1}}{\eta_{i-1}}\cdot\frac{p_i - p_{i-1}}{\Delta x_{i-1}}\\ &= \rho_i\cdot K_{f,i}\cdot n\cdot f_i\cdot A_{cr}\cdot D + \rho_i\cdot K_{b,i}\cdot n\cdot f_i\cdot A_{cr}\cdot D - \frac{D^4}{K_{p,i}}\cdot\frac{\rho_i}{\eta_i}\cdot\frac{p_{i+1} - p_i}{\Delta x_i}\end{aligned} \tag{4.79}$$

which constitutes a linear, algebraic system of equations for the pressure p_i of all adjacent numerical elements which are completely filled (as also shown by Choulak et al.[48]). This system was solved via matrix inversion in each step of the built-in ODE solver. Using the resulting pressure values p_i and mass flow rates the species mass balance (Eq. 4.77), and the thermal energy balances (Eqs. 4.78, 4.28 and 4.30) were solved similarly to partially filled elements.

To obtain an RTD, we set the species mass fraction w_i initially to zero, and changed it to a finite value at the feed w_0 after steady state was reached. The time course of the species mass fraction at the die w_{N+1} was the step response $F(t)$, normalized to one:

$$F(t) = \frac{w_{N+1}(t)}{w_0} \tag{4.80}$$

The RTD *E(t)* was obtained as time derivative of the step response *F(t)*:

$$E(t) = \frac{dF(t)}{dt} \tag{4.81}$$

4.6 Results and Discussion

Typically, polymer melts in HME show a shear-thinning and temperature-dependent viscosity. This is accounted for in our model. However, a model based on physical principles must also generate reasonable results for simplified cases. Therefore, before addressing a case with complex material behavior, we present results for the simplified situation of a constant-viscosity material, i.e., a temperature-independent Newtonian fluid. Here, the flow field is decoupled from the thermal energy equation, i.e., the actual value of the local temperature does not impact the flow. Results for this theoretical scenario were shown by Bierdel[53] using CFD. We compared our model results to that reference data.

4.6.1 Test Case: Newtonian Fluid

The CFD results of Bierdel[53] show the axial pressure gradient versus throughput (the so-called pressure characteristic) and the screw driving power versus throughput (power characteristic) in dimensionless form for a Newtonian fluid in a completely filled twin-screw conveying element with screw diameter 60 mm (shaded Graphs (a) and (d) in Figure 4.11). To provide insights into the different contributions of the screw driving power, we divided it into pumping power and dissipated power in the following way.

The pumping power is defined as volumetric throughput times pressure difference $P_{pump} = \dot{V} \cdot \Delta p$, which could be directly obtained by multiplying Graph (a) with the dimensionless throughput, yielding Graph (b):

$$\frac{P_{pump}}{\eta (nD)^2 \Delta x} = \frac{\dot{V}}{nD^3} \cdot \frac{\Delta p \cdot D}{\eta \cdot n \cdot \Delta x} \tag{4.82}$$

The dissipated power (Graph c) was obtained by subtracting the (b) pumping power from the (d) driving power:

$$\frac{\dot{Q}_{diss}}{\eta(nD)^2\Delta x} = \frac{P_{screw}}{\eta(nD)^2\Delta x} - \frac{P_{pump}}{\eta(nD)^2\Delta x} \tag{4.83}$$

We parameterized our model with the geometrical parameters of the investigated screw element as shown by Bierdel[53] and summarized in Table 4.5. In addition to the geometrical parameters, the screw parameters A_1 and A_2 (i.e., the corresponding K_f and K_p according to Eqs. 4.9 and 4.10) are a required input for our model. Since A_1 and A_2 are the axis intercepts of the dimensionless pressure characteristic, they were obtained from the CFD results of Bierdel[53] for this specific screw element (see Table 4.5). For the material properties and screw speed, see Table 4.5.

Table 4.5: Parameters used for the 60mm twin-screw.

Number of flights n_F	2
Outer screw diameter D	60 mm
Screw core diameter D_C	38 mm
Barrel diameter D_B	61 mm
Centerline distance C_L	50 mm
Pitch T_s	120 mm
Screw parameter A_1	0.510
Screw parameter A_2	1520
Density	1000 kg/m³
Viscosity	1000 Pas
Speed	95 min^{-1}

We used a screw length of 1200 mm followed by a die element. Thus, our results include a completely filled screw section at the die, while the remaining part is partially filled. Along the screws we used $N = 30$ numerical elements. This gave a sufficient resolution.

To analyze the model of this screw element in all possible operation states (i.e., conveying, overrun and backward pumping screws), we varied the throughput in a wide range of 50 – 800 kg/h. The value of 800 kg/h already exceeded the throughput of the element at 95 rpm (i.e., overrun screw). This is usually not achieved in practical applications for conveying elements with a large pitch. We also simulated the corresponding left-handed element with a throughput of 50 – 200 kg/h, to show that the curves extend continuously to the backward pumping conditions.[53] We did not vary screw speed, viscosity and density since the dimensionless pressure and power characteristic are independent of these variations for a constant viscosity. Since our model is based on the dimensionless pressure characteristic (Eq. 4.6), this is trivially fulfilled.

We evaluated the axial pressure gradient $\Delta p_i/\Delta x_i$, the pumping power $P_{pump,i}$ (Eq. 4.63), the dissipated power $\dot{Q}_{diss,i} = \dot{q}_{diss,i} \cdot V_i$ (Eq. 4.31) and the screw driving power $P_{screw,i}$ (Eq. 4.62) for a numerical element i in the completely filled section (in the considered case of a constant viscosity, those parameters are equal for all numerical elements in the completely filled section). We also evaluated the same parameters in the partially filled section, however, the pumping power is always zero there and thus, the screw driving power equals the dissipated power (Eq. 4.62). Reference results were not available for the partially filled section, since the 3D simulation of partially filled twin-screws is still a challenging (and most unresolved) task.

The results of our model are shown in Figure 4.11 (symbols) compared to the corresponding results of Bierdel[53] (solid, grey lines). For a clear representation we plotted dashed lines through our model results, which are linear fits in the case of (a) pressure characteristic and power characteristic for (d) completely filled and (e) partially filled screws, whereas the dashed lines for (b) pumping power and the (c) dissipated power were calculated from the linear fits (a) and (d) by Eqs. 4.82 and 4.83.

When the throughput equals the inherent throughput ($\dot{V}/nD^3 = A_1$), the completely filled screws do not generate pressure, but purely convey the melt. If a flow resistance exists downstream (e.g., the die), a pressure gradient is generated to overcome the downstream resistance. When conveying against backpressure, the screws achieve a throughput lower than the inherent throughput, since the pressure drives a flow backwards along the screw

channels and through the gaps, superposing the inherently conveyed throughput. This operation state is called “conveying screw”. The pumping power, which is the effective power invested in conveying against pressure, is zero for $\dot{V} = 0$ (where the screws do not achieve throughput, i.e., conveying against a closed die) and for the inherent throughput ($\dot{V} / nD^3 = A_1$, where no axial pressure gradient exists). Between those states the pumping power yields positive values, since the screws provide this power for conveying against increasing pressure. The pumping power versus throughput yields a parabolic curve, because it is the product of throughput and axial pressure gradient. The dissipated power shows a minimum at the inherent throughput, where the axial pressure profile is flat and no pressure-driven flow in axial direction is established. At this point, our model accounts purely for the circumferential shear rates to calculate the viscous dissipation rate. With increasing backpressure, the dissipated power increases due to additional shear rates caused by the pressure-driven flow in axial direction. This amount increases with the square of the axial pressure gradient (Eq. 4.33), thus yielding a parabola with the negative curvature of the pumping power. Finally, the sum of pumping power and dissipated power, which is the entire screw driving power, is a linear function over the throughput.

The highest pressure gradients are achieved for backward conveying elements (sometimes called “left-handed”) whose conveying effect has to be overcome by the pressure-driven flow. This operation state is called “backward pumping screw” and can be shown in the region of negative throughputs, since the throughput is negative with respect to the conveying direction of the element. Then its pressure characteristic is represented by the same line used for the corresponding forward conveying element. The dissipated power increases extremely for this case due to the strong pressure-driven flow. However, the pumping power is negative, since the flow is driven by the pressure, not by the screws.

The third operation state is called “overrun screw” and occurs for throughputs higher than the inherent throughput. These conditions are of less practical significance and can be achieved only for elements with a very low inherent throughput. Then, the throughput is higher than the inherent throughput of the considered screw element and the pressure decreases in conveying direction, i.e., the pressure-driven flow achieves the throughput together with the conveying effect.

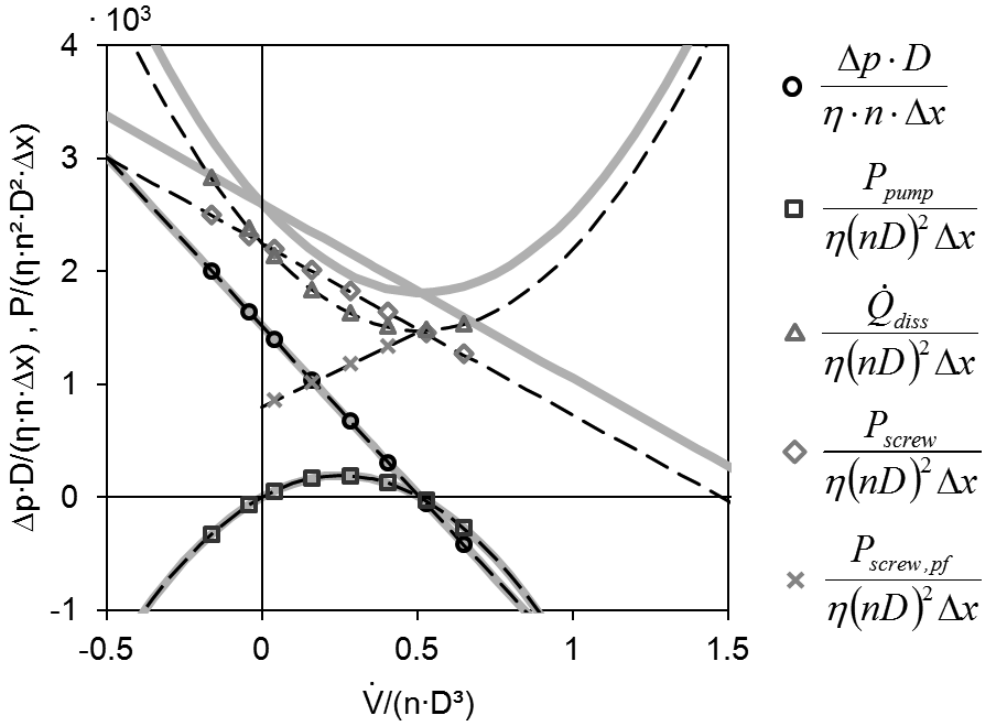

Figure 4.11: Results simulated with the 1D model (symbols and dashed lines) compared to the corresponding curves based on CFD simulations from Bierdel[53] (solid, grey lines) in dimensionless form for (○) pressure gradient, (□) pumping power, (△) dissipated power and screw driving power for the (◇) completely filled and (×) partially filled screw element versus throughput.

The partially filled state only exists under the conveying screw conditions, i.e., between zero throughput and the inherent throughput and is established when the screws convey without backpressure. Then, a filling ratio of the screws between zero and one is achieved, depending on throughput and screw speed, i.e., the filling ratio is zero for a throughput of zero and one for the inherent throughput. The pumping power is zero in the partially filled state, since no pressure is generated. Thus, the entire screw driving power is dissipated here. The linear driving power versus throughput results from the assumptions, that the throughput of the partially filled screws scales linearly with the filling ratio (Eq. 4.1), and that the volume-specific viscous dissipation rate in the screw channels is constant for increasing filling ratio (thus the dissipated power in the channels scales linearly with the filling ratio, Eq. 4.34). At a throughput of zero, the driving power approaches a value larger than zero, since the gaps are still filled and cause a torque, even when the empty screws rotate. The inherent throughput connects the partially filled state with the completely filled state, since it can be achieved by a partially filled screw with a filling

ratio approaching one, as well as by a completely filled screw with a pressure gradient approaching zero.

The pressure characteristic and pumping power versus throughput results of our model were necessarily identical to the CFD results of Bierdel[53], since the parameters A_1 and A_2 were obtained from there. This was, therefore, not a prediction of our model, rather a required input. However, both curves were exactly defined by only two input parameters for the considered screw element. The dissipated power and the driving power were calculated based on the underlying pressure characteristic and the geometry, without using any additional empirical input parameters. The resulting dissipated power and driving power of our model slightly underestimated the corresponding CFD results. The linear decrease of the driving power with increasing throughput and the curvature of the dissipated power over throughput were identical to the CFD results, which was also a consequence of the inferred values of A_1 and A_2. Evidently, the approach used to calculate the viscous dissipation rate is a simplification. However, in addition to providing quantitatively excellent agreement of the resulting power characteristic with the CFD results, it also accounts for the underlying physical phenomena in a qualitatively correct way.

4.6.2 Non-Newtonian Fluid

Having demonstrated that our model yields good quantitative results for a constant viscosity material, we simulated experiments reported in our previous work.[51] In contrast to the constant viscosity case, here there is an interaction with the material properties due to the temperature and shear-rate dependent viscosity here.

As described previously in detail,[51] we experimentally determined the pressure characteristics of six different screw elements with Soluplus® using a ZSK 18 extruder from Coperion (Germany) with a nominal screw diameter of 18 mm. We measured the axial pressure gradient $\Delta p/\Delta x$ in a completely filled screw section close to the die using two pressure probes and the corresponding melt temperature T_m using a temperature probe located in the clearance volume between screws and die, thermally isolated from the barrel. The screw elements investigated were two conveying screw elements termed “24/24” and “16/16” with different pitches of 24 and 16 mm, respectively, two kneading elements “KB

45/5/8" and "KB 45/5/8 LH" (45° offset angle, 5 discs, 8 mm length, right- and left-handed), a kneading element "KB 90/5/8" and a kneading element "KB 45/5/16". All elements are depicted in Figure 4.13. We varied the screw speed from 60 – 180 rpm and the throughput from 0.5 – 4 kg/h for conveying elements and 0.5 – 2 kg/h for kneading elements. From this data, we evaluated the screw parameters A_1 and A_2 (and A_0 for the non-conveying element KB 90/5/8) for the investigated screw elements using the temperature- and shear rate-dependent properties of Soluplus®.

We parameterized our model with the dimensions of a ZSK 18 extruder given in Table 4.6 (the values were measured and differ from manufacturer's data due to wear). The parameters A_0, A_1 and A_2 used for the screw elements investigated are given in Table 4.7 as obtained from the experiments. The required disc length of the kneading elements is also given there.

Table 4.6: Parameters of the used ZSK 18 extruder.

Number of flights n_F	2
Outer screw diameter D	17.8 mm
Screw core diameter D_C	11.6 mm
Barrel diameter D_B	18.3 mm
Centerline distance C_L	15 mm

Table 4.7: Screw parameters for the investigated screw elements.

Screw Element	A_1	A_2	Disc Length L_D
24/24	0.359	767	-
16/16	0.226	809	-
KB 45/5/8	0.155	259	1.1 mm
KB 45/5/16	0.145	218	2.55 mm
KB 90/5/8	$A_0 = 1214$		1.1 mm

For the simulations, we considered a 360 mm long screw section (see Figure 4.12) to achieve a partially filled screw at the inlet and a completely filled screw section at the die. We used N = 36 numerical elements. The element of interest was located between the pressure sensors (PI), the remaining elements were conveying elements with a pitch of 24 mm. We varied the die diameter in order to obtain a constant length of the completely filled screw section (approximately 100 mm back from the die as in Figure 4.12), analogous to the die valve used in the experiments. In the simulations, we evaluated the pressure difference at the positions of the pressure sensors (PI), and the melt temperature at the end of the screws (TI), as in the experiments. The barrel temperature was 180 °C in experiments and simulations.

Example results of filling ratio, pressure and temperatures along the twin-screw are shown in Figure 4.12 for the 24/24 element with 60 rpm and 1kg/h. The filling ratio showed a completely filled section about 100 mm back from the die, where the pressure showed a nearly constant gradient towards the screw end, while ambient pressure values were obtained in the partially filled section.

In the partially filled section, the melt temperature T_m reached an approximately constant level of ca. 188 °C. The difference of ca. 8 °C to the barrel temperature is the effect of dissipated power, which is removed by conduction to the barrel walls. In the completely filled section (x > 260mm), the melt temperature was significantly higher due to the increased amount of dissipation, while the surface area of the barrel, over which the heat had to be removed, remained the same. At the interface to the completely filled section, the melt temperature increased abruptly, due to the increased dissipation and the intensive backflow there, which is a multiple of the throughput in this case. The gap temperatures shown (average gap temperature T^{ga}, Eq. 4.58 and maximum gap temperature $T^{ga,max}$, Eq. 4.60) were about 1 °C and 2 °C, respectively, higher than the (bulk) melt temperature T_m.

This is quite moderate and seems to be negligible. However, the gap between screws and barrel of the ZSK 18 extruder was comparatively wide (0.25 mm, i.e., 1.4 % of the screw diameter). Depending on the manufacturer and the degree of wear, the relative gap size can also be the half of that or even less. Due to the square dependency of the viscous dissipation rate on the shear rate this can easily cause a four-fold energy dissipation in the

gaps and consequently higher gap temperatures. Similarly, increasing screw speed, which was 60 rpm in the case shown, increases the gap shear rate and, for example, led to a maximum gap temperature of ca. 4 °C higher than the bulk temperature at 180 rpm in our simulations. Moreover, the viscous dissipation rate scales linearly with the viscosity, which was in the range of 300 – 800 Pas in the shown case (shear-rate and temperature dependent). Viscosities up to some 1000 Pas are typical in HME (depending on the excipients used and the barrel temperature), which would strongly increase the gap temperature. Thus, gap temperatures can easily reach 20 °C more than the bulk melt temperature and even higher (an example is also given in Bierdel[53]), which may cause serious thermal degradation issues.

The calculated screw temperature was similar to the melt temperature, due to the intense contact of the screws with the surrounding melt. However, the screws are typically constructed of steel, thus support heat transfer due to conduction in axial direction from hot spots (e.g., the completely filled section in our example) to cooler sections (the partially filled section here).

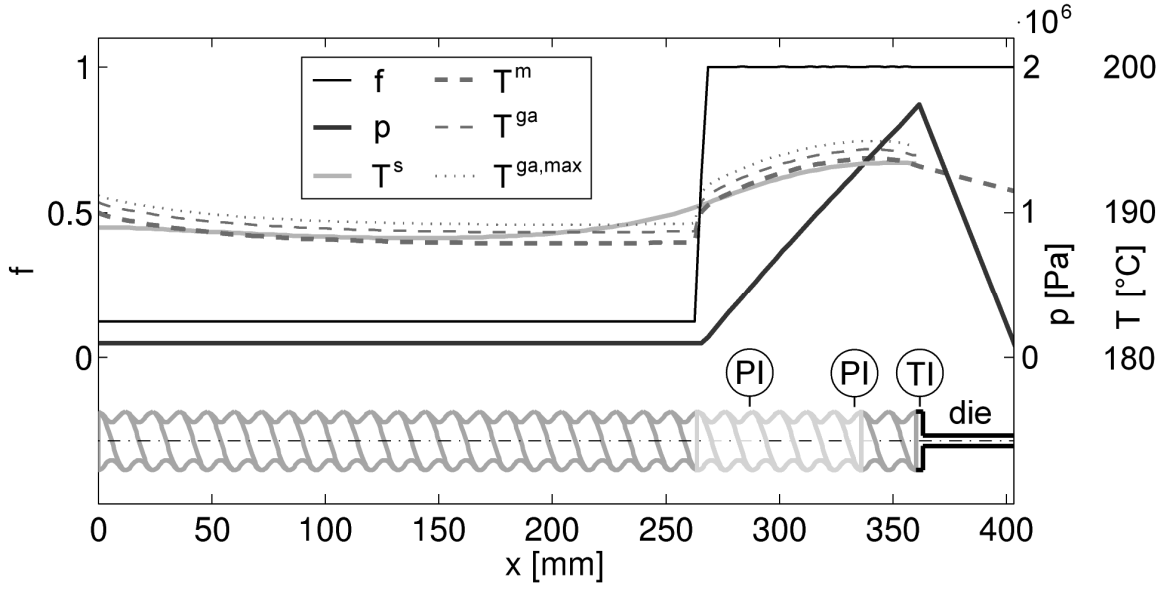

Figure 4.12: Typical profile as predicted by the 1D model for 60 rpm, 1kg/h and barrel temperature of 180°C. Shown are filling ratio *f*, (absolute) pressure *p*, screw temperature T^s, melt temperature T^m, gap temperature T^{ga} and maximum gap temperature $T^{ga,max}$. The element of interest is highlighted (here element 24/24, between x = 264 – 336 mm). The remaining elements are 24/24 conveying elements (grey). PI indicates pressure sensors, TI the temperature sensor.

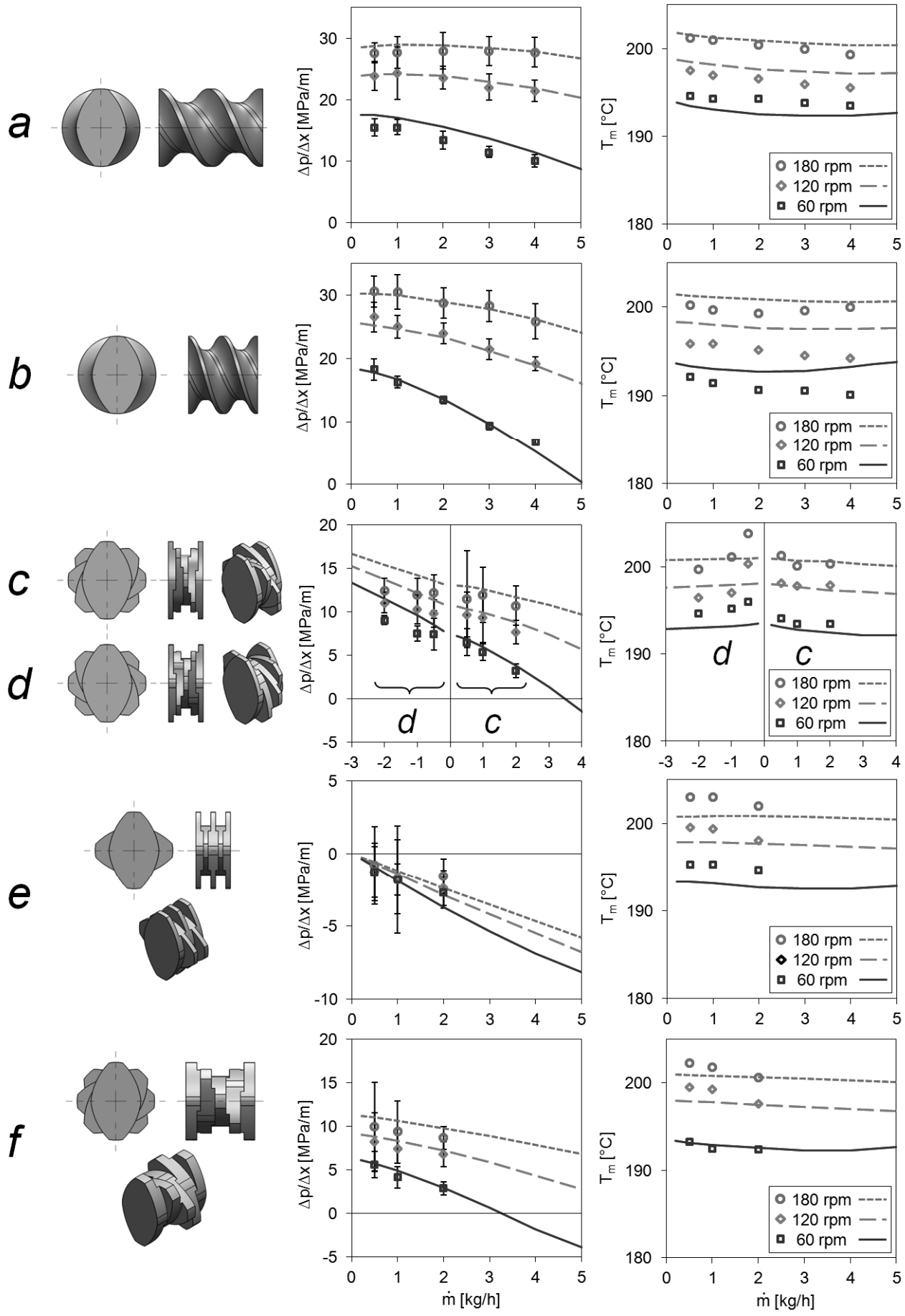

Figure 4.13: Comparison of experimental data (symbols) and corresponding simulation results (lines) for axial pressure gradient and melt temperature for six different screw elements: (a) 24/24, (b) 16/16, (c) KB 45/5/8, (d) KB 45/5/8 LH, (e) KB 90/5/8, (f) KB 45/5/16.

Beyond the presented insights into the flow of completely filled and partially filled screw elements, we used the data shown in Figure 4.12 to evaluate the axial pressure gradient $\Delta p/\Delta x$ in the completely filled screw section (i.e., pressure difference of the sensors PI divided by their distance) and the melt temperature T_m at the screw end (sensor TI). These data are shown in Figure 4.13a for all investigated cases of the 24/24 element (i.e., variable screw speed and throughput), together with the corresponding experimental data. Figure 4.13b – f show the analogous results for the screw elements 16/16, KB 45/5/8, KB 45/5/8 LH, KB 90/5/8 and KB 45/5/16, respectively. Note, that we used the empirical screw parameters A_0, A_1 and A_2, determined from the measurements in our previous work,[51] as input for the presented simulation results. Similarly, the coefficients of the used heat transfer correlation (Eq. 4.76) were determined from these measurements (see sections above). Thus, the agreement of the simulation results with the experimental data is good, which demonstrates that the proposed model yields reasonable results if the screw parameters and the underlying heat transfer correlation are appropriate.

The experimentally determined parameters A_1 were in good agreement with the proposed estimation Eq. 4.11[52] for conveying elements, i.e., A_1 can be predicted for conveying elements independently of experimental data. However, for the A_1-parameters of the kneading elements, and the A_2-parameters such estimation rules do not exist, and CFD simulations or experiments are required to determine these parameters for a given screw element geometry. Also, the heat transfer correlation for other extruders would require a numerical analysis via non-isothermal CFD simulations.

The results of the pressure gradient versus throughput in Figure 4.13 illustrate the different conveying behavior of various screw elements. The intercept of the curves with the x-axis (does not occur in most plots in the shown parameter range) indicates the inherent throughput at the considered screw speed, i.e., the throughput which is achieved when conveying without backpressure. With increasing pressure gradient the throughput decreases due to the pressure-driven backflow. The pressure gradient also increases with increasing screw speed, as well as the inherent throughput.

It is obvious, that the inherent throughput of the conveying elements (24/24 and 16/16) is approximately proportional to the pitch (e.g., at 60 rpm ca. 8kg/h and 5kg/h for 24/24 and

16/16, respectively). This is also indicated by the A_1 parameters, which represent the dimensionless inherent throughput. For the kneading elements the inherent throughput is lower due to their geometry, even zero for the KB 90/5/8 which does not actively convey since its offset angle of 90° leads to a neutral conveying behavior.

The pressure gradient of the left-handed element KB 45/5/8 LH is expected to be the extension of the corresponding right-handed KB 45/5/8 element to the backward-pumping conditions (i.e., negative throughput), since the left-handed element is the mirror-inverted copy of the right-handed element and is physically equivalent. Thus, the model prediction for both elements extend the Graphs of the KB 45/5/8 in the direction of negative throughputs; however, the experimental results yielded lower pressure gradients. The reason for this behavior is currently not clear and would require more detailed numerical studies via CFD or refined experiments.

The melt temperature depends mainly on the screw speed and weakly on the throughput. It reaches a similar level for all screw elements investigated. The experimental results showed more variation among the different screw elements than the simulation results, specifically the measured temperatures for the 16/16 element were relatively low compared to the 24/24 element and the temperatures for the KB 90/5/8 were relatively high. High-precision experiments (which are difficult in extruders) should be performed in the future as we noticed similar deviations in repeated experiments.

The qualitative trend of the melt temperature versus throughput for the conveying elements (e.g., for the 16/16 element) shows, that for throughputs close to zero the melt temperature decreases with throughput. This is caused by decreased dissipation due to decreased backflow and also decreased residence time in the completely filled screw section. However, close to the inherent throughput, where the backflow vanishes, the temperature increases with increasing throughput, which is caused by the similar temperature in the partially filled section (whose filling ratio was close to one, then) compared to the completely filled screw section.

For the KB 45/5/8 LH, the measured melt temperature shows a significant increase for decreasing throughput, which is not observed in the model results. This appears to be an effect of residence time (i.e., higher temperature with higher residence time at lower

throughput). However, if this was the case, similar behavior would be expected for the other elements. Moreover, the viscosity of Soluplus® and, consequently, the dissipated power decreases strongly with increasing temperature, i.e., the material temperature is quite stable for a given screw speed, as shown by the model results. Thus, the cause for the deviation in temperature behavior in the case of KB 45/5/8 LH elements is not clear. However, the model results for the temperature are mostly in good agreement with the measurements and the deviations are within a few degrees. Thus, we are confident that the proposed model can be a versatile tool for the design, optimization and control of HME.

4.6.3 Residence Time Distribution

Detailed experimental results regarding the RTD are available in the literature, e.g., Puaux et al.[44]. We studied those experiments to validate our model results. It should be noted that although the experiments considered the entire extrusion process including melting, our model assumed all the material to be molten. Puaux et al. used a Clextral BC 21 fully intermeshing co-rotating twin-screw extruder. The parameters of the screw geometry are given in Table 4.8, the entire screw length was 900 mm.

Table 4.8: Parameters of the Clextral BC 21 extruder.

Number of flights n_F	2
Outer screw diameter D	25 mm
Screw core diameter D_C	16 mm
Barrel diameter D_B	25.5 mm
Centerline distance C_L	21 mm

The screws were configured using conveying elements only, right-handed and left-handed (termed “Profile B”[44]). Thus, we could predict the A_1 parameter using Eq. 4.11. For the A_2 parameter we interpolated from our measured data (given in Table 4.7) using the pitch to diameter ratio T_s/D. This is possible since these data are dimensionless and independent of the extruder size (assuming geometrical similarity). The resulting screw parameters are given in Table 4.9 and the screw configuration is shown in Figure 4.14 (where the left-handed element is highlighted in black).

Table 4.9: Used screw configuration and screw parameters.

Type	Length [mm]	Pitch [mm]	A_1	A_2
right-handed	50	16	0.197	832
right-handed	50	25	0.308	798
right-handed	100	33	0.406	768
left-handed	50	25	0.308	798
right-handed	150	16	0.197	832
right-handed	200	25	0.398	798
right-handed	300	33	0.406	768

The material was a low-density polyethylene (LDPE), for which we assumed a density of 920 kg/m³. The rheological parameters of the LDPE were not available, thus we considered a simplified scenario with a constant viscosity of 500 Pas. It is known from the literature, that the influence of the rheology on the RTD of co-rotating twin-screws is often negligible (see Gao et al.[42], Elkouss et al.[58], Amedu et al.[47]). Thus, we did not expect an influence of this simplification on the resulting RTD. With that, the flow rates are decoupled from the temperature profile and thus, the RTD is independent of the barrel temperatures, thermal conductivity and heat capacity of the melt. Although, this is not the case in reality, our model results confirmed that the rheology has a negligible impact on the RTD. Clearly, the material temperature and pressure profile is strongly influenced by the rheology, but the RTD is mainly determined by the mass flow rates along the screws, which are more a consequence of the screw geometry rather than the rheology of the melt.

For the results presented in the previous sections we used a rather coarse axial resolution (around 60% of the screw diameter D) which had low impact on the resulting profiles of pressure, filling ratio and temperature. In contrast, for the RTD the axial resolution is crucial, i.e., the finer the resolution, the more accurate the resulting RTD. Thus, we decreased the axial resolution to 3 mm here (i.e., 0.12D), which led to a total number of N = 303 numerical elements. Further refinement was limited by the low computational efficiency of MATLAB® (using a compiled language would significantly increase the computational efficiency). However, a comparison of the axial resolution of 3 mm (N =

303) to 6 mm (N = 151) yielded comparable results for the RTD, i.e., a resolution in the order of 10% of the screw diameter is sufficiently fine.

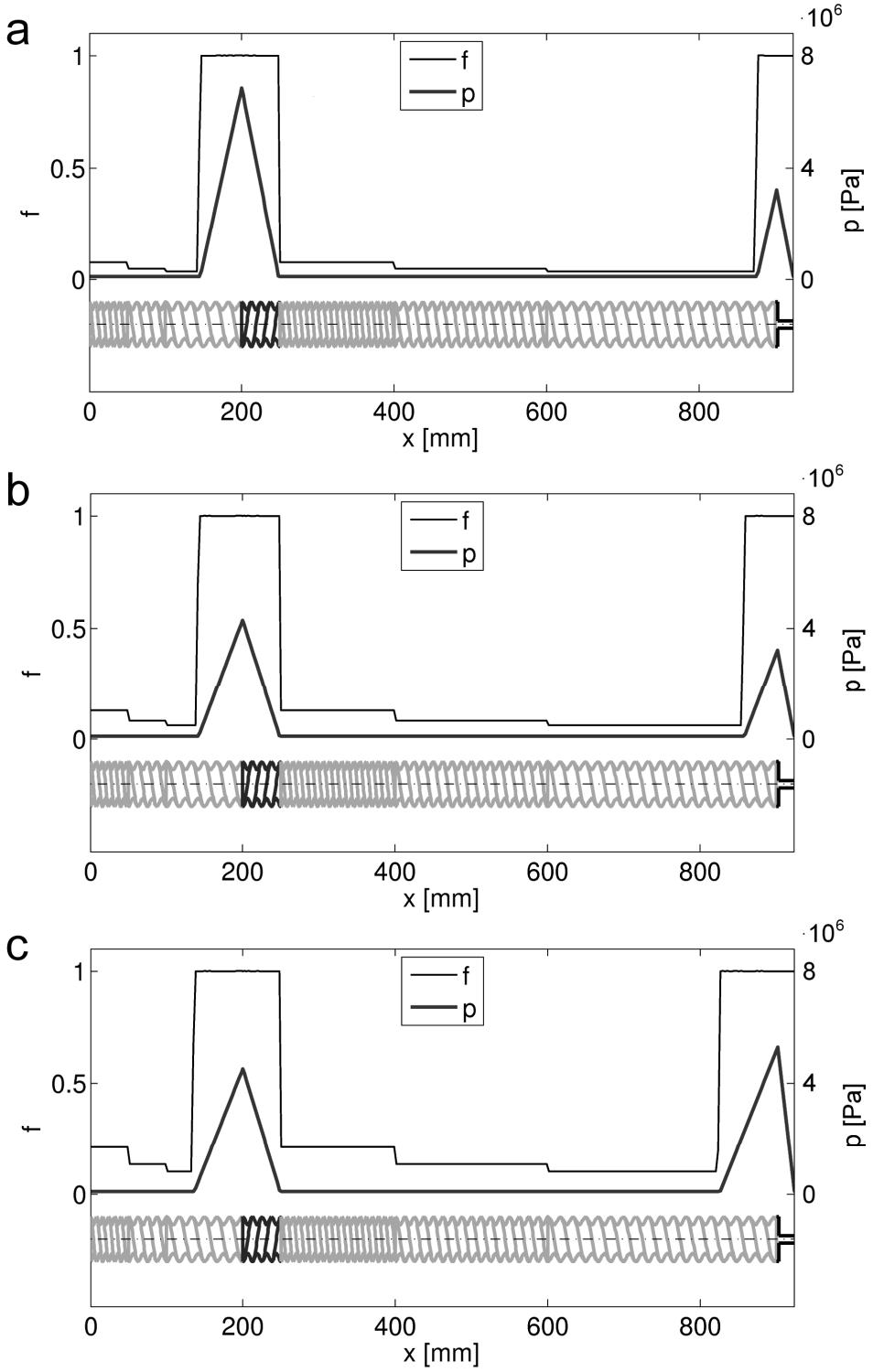

Figure 4.14: Typical filling ratio and pressure profiles for (a) 500 rpm and 6.5 kg/h, (b) 300 rpm and 6.5 kg/h, and (c) 300 rpm and 10.8 kg/h.

We simulated the RTD for the cases described above, i.e., variable screw speed (200 – 500 rpm) at a throughput of 6.5 kg/h, and for variable throughput (3.8 – 10.8 kg/h) at a screw speed of 300 rpm. The resulting profiles of the filling ratio and pressure along the screws are shown in Figure 4.14 for three cases. We did not show the corresponding melt temperature profiles due to the simplification used.

The profiles of pressure and filling ratio in Figure 4.14 are qualitatively similar. The cases mainly differ in terms of completely-filled screw length, peak pressure and filling ratio in the partially filled sections. In all cases, the left-handed element caused a completely filled section, since it had to be overflown by pressure. The peak pressure occured at the transition from the right-handed element (acting as pressure generator) to the left-handed element (acting as pressure consumer). In the experiments this section was used to melt the material, supported by high energy dissipation, mixing and a significant residence time due to the high filling ratio. A similar situation appeared at the die; here the generated pressure was consumed by the die flow and the peak pressure was located at the end of the screws. In the partially filled sections, the pressure had ambient values, while the filling ratio varied corresponding to the pitch. The filling ratio in the partially filled sections was highest in case c (high throughput and low screw speed) and lowest in case a (low throughput and high screw speed), since a higher throughput and a lower screw speed both require a higher filling ratio in partially filled screws.

The length of the back pressure at the die was also greatest in case c and lowest in case a, since the increased throughput (case c) caused an increased die pressure drop, whereas the increased screw speed (case a) led to an increased axial pressure gradient in the completely filled section, i.e., a shorter back pressure at the die.

For a constant throughput (cases a and b), the completely filled length at the left-handed element was constant, because the increased screw speed (case a) caused an increased axial pressure gradient for right and left-handed elements in the same proportion, i.e., the peak pressure was increased, but the completely filled length remained constant. For the increased throughput (case c), this completely filled length was slightly increased, since the left-handed element required an increased axial pressure gradient to achieve the increased throughput (i.e., a higher peak pressure), whereas the right-handed element exhibited a

decreased axial pressure gradient, and consequently an increased completely filled length to achieve the peak pressure.

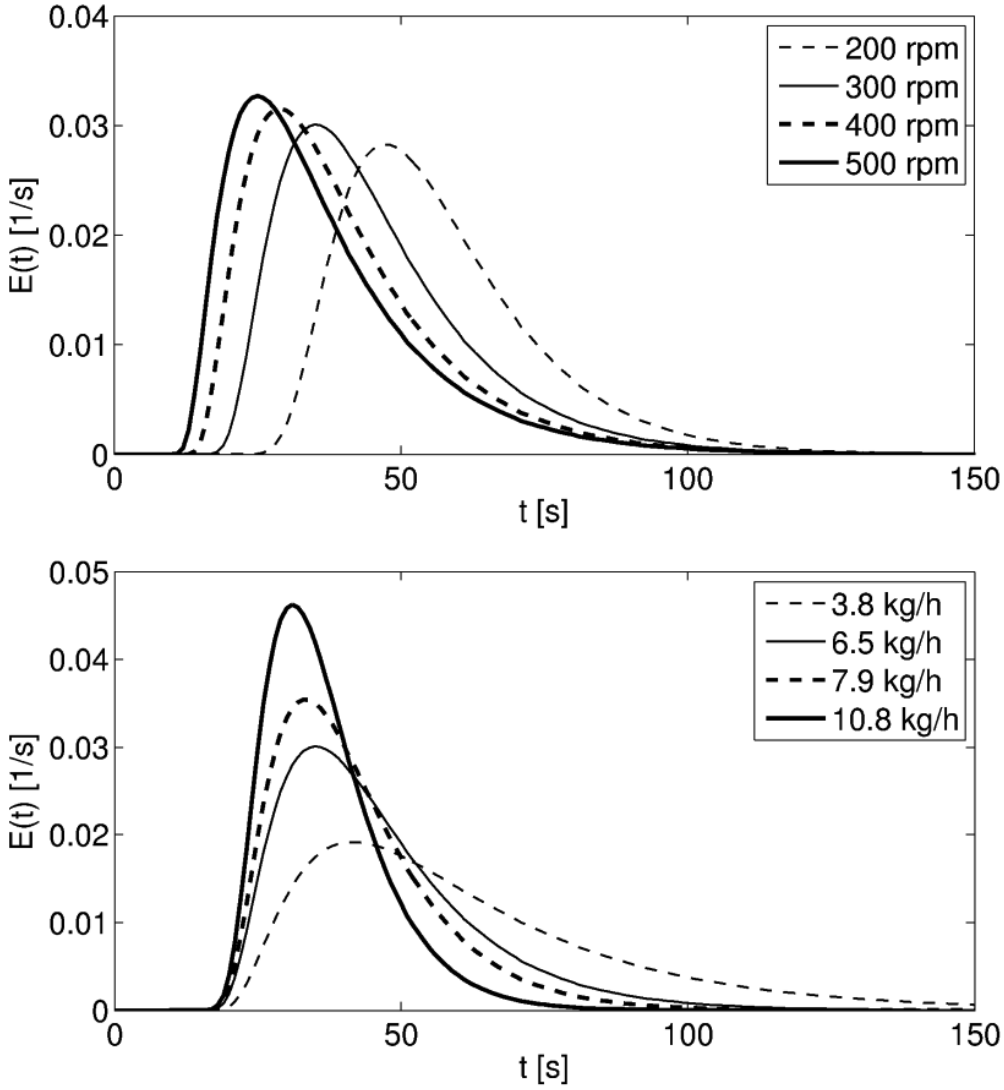

Figure 4.15: Simulation results for: (top) the RTD with 6.5 kg/h and variable screw speed and (bottom) 300 rpm and variable throughput.

The computed RTD curves for all considered cases are shown in Figure 4.15. From this figure it is obvious, that the screw speed had a different impact on the RTD compared to the throughput. For increasing screw speed and constant throughput (Figure 4.15 top), the mean residence time decreased, whereas the width of the RTD remained nearly constant. This can be explained by the decrease of the mean residence time in the partially filled sections with increasing screw speed, i.e., faster conveying due to the higher screw speed

($\tau \sim 1/n$). In contrast, the length of the completely filled sections (i.e., the material volume V contained there) was only slightly decreased due to the higher screw speed (see also Figure 4.14 a and b), and consequently the mean residence time in the completely filled sections remained nearly constant due to the constant throughput ($\tau \sim V/\dot{V}$). Note that axial mixing was mainly caused by completely filled screw sections, whose volume, throughput and mean residence time were nearly constant here. Thus, also the width of the RTD remained constant, although the screw speed was varied.

For constant screw speed and increasing throughput (Figure 4.15 bottom), both the mean residence time and the width of the RTD decreased, however, the left shoulder of the RTD occurred at nearly the same time. Here, the conveying velocity in partially filled sections was constant due to the constant screw speed. Thus, the mean residence time in partially filled sections remained nearly constant. However, the mean residence time in completely filled screw sections decreased with increasing throughput ($\tau \sim V/\dot{V}$, note that V increased only slightly with increasing throughput, see Figure 4.14 b and c). Due to the decreased mean residence time in completely filled sections also the variance, i.e., the width of the RTD decreased.

We calculated the mean residence time τ and its standard deviation σ for the presented results. The obtained values are shown in comparison to the experimental results of Puaux et al.[44] in Figure 4.16 as a function of the (top) screw speed and (bottom) throughput. Considering, that we approximated the extrusion process with a simplified model which accounted only for melt with a constant viscosity, the agreement of our results with the experiments was excellent. Specifically, the model yielded a quantitatively good estimation for the residence time in all cases considered and also the qualitative trends were in agreement for the screw speed variation. In the case of variation in throughput there appeared to be a difference in the qualitative trend with experimental data, although uncertainty due to the low number of experimental data points could not be excluded. Also, the negative curvature of the experimental values versus throughput is not in agreement with the above considerations ($\tau \sim 1/\dot{V}$). However, a deviation from those considerations could also be caused by effects in the solid conveying and melting zone, which were not covered by our model.

Although, the experimental RTDs were determined for the entire process including the intake and melting zone, we obtained good agreement with our metering model where the entire material was assumed to be molten. The shown results indicate that our model approximated the RTD of the entire process well, and that for this purpose the actual material rheology, and also heat capacity and thermal conductivity, were not required. The assumption of a constant viscosity was sufficient. Obviously, the axial mixing was mainly dominated by the conveying properties of the screw geometry and nearly independent of the material properties, at least for low Weissenberg numbers Wi < 1. If elastic effects become dominant, an influence on the RTD can be expected, as shown by Elkouss et al.[58]. However, we did not account for elastic effects in our model.

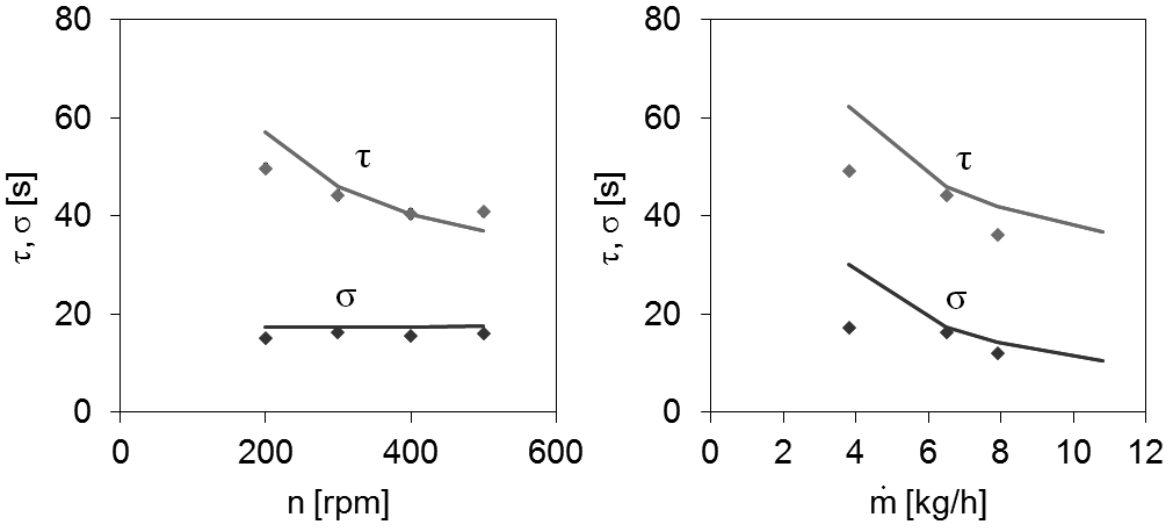

Figure 4.16: Mean residence time τ and standard deviation σ over (top) screw speed and (bottom) throughput for simulation results (lines) and experimental results of Puaux et al.[44] (symbols).

4.7 Summary and Conclusions

We presented a general and detailed 1D model of a co-rotating twin-screw extruder with focus on pharmaceutical HME. The model accounts – in a mechanistic way – for the mass transfer along the screws and the relevant heat transfer mechanisms. It yields 1D profiles for filling ratio, pressure and temperature of screws and melt in screw channels and gaps, which are difficult to access in experimental studies and depend strongly on the screw configuration used. In addition the maximum temperature in the gaps can be estimated. Furthermore, the model is capable of calculating screw driving power, torque and the RTD.

Based on geometrical parameters of the screw elements and two empirical parameters for each screw element (A_1 and A_2) the model can simulate arbitrary screw configurations, and thus, provides the opportunity to study different variants of screw configurations, i.e., to optimize the screw configuration. The model is applicable to Newtonian and non-Newtonian rheologies. Moreover, the impact of other process parameters, such as screw speed, throughput and barrel temperature, as well as material parameters, can be studied. Since 3D simulation of the entire extrusion processes is still problematic in terms of the model requirements and computational effort today, a 1D model is a highly useful alternative to spatially-resolved CFD and DEM simulations.

However, the full complexity of reality cannot be covered by such a simplified model. Thus, it is still limited in some aspects of practical application. Since we focused on the metering zone, the melting zone is still not included. Furthermore, calculations were made using properties of pure materials. In reality the material properties vary with the state of mixedness (e.g., plasticizers), which would require highly complex methods to capture and model the material behavior of mixtures of three or even more components. Despite that, simulations with mixing-independent material properties can provide useful insight into the general characteristics of the HME process and lead at least to qualitative agreement of overall trends.

In summary, the presented approach provides a good basis for further developments, for example, modeling of melting and devaporization, to achieve a comprehensive tool for the computer aided development, optimization and scale-up of entire extrusion processes, allowing a rational design of such processes in accordance with QbD requirements.

4.8 Abbreviations

1D	one-dimensional
3D	three-dimensional
CFD	computational fluid dynamics
DEM	discrete element method
HME	hot-melt extrusion
HTC	heat transfer coefficient
LDPE	low density poly-ethylene

ODE	ordinary differential equation
RTD	residence time distribution

4.9 Nomenclature

Latin symbols

A_0	screw parameter for non-conveying elements [-]
A_1, A_2	screw parameters for conveying elements [-]
A_3	empirical shear rate parameter [-]
A_b, A_s	cross-section area of barrel and screws [m²]
A_{bm}, A_{sm}	heat exchange area barrel/melt and screws/melt [m²]
A_e	barrel/environment surface area [m²]
A_{cr}	free cross-section area of the twin-screw [m²]
$A_{s,ch}$	screw channel surface area [m²]
$A_{s,tip}$	screw tip surface area [m²]
A_{surf}	total screw surface area [m²]
a_T	temperature shift factor (Carreau model, WLF equation) [-]
C	coefficient in the Nusselt correlation [-]
C_1 , C_2	parameters of the WLF equation [-, °C]
C_L	centerline distance [m]
c_p^b , c_p^m , c_p^s	heat capacity of the barrel, melt, screws [J/kgK]
D	outer screw diameter [m]
D_B	barrel diameter [m]
D_C	screw core diameter [m]
d	die diameter [m]
$E(t)$	pulse response (RTD density function) [s^{-1}]
$F(t)$	step response (cumulative RTD) [-]
f	filling ratio [-]
H	channel depth [m]
h	gap distance [m]
K_1, K_2, K_3, K_4	parameters of the Menges model [Pam³/kg, Pam³/kgK, Pa, Pa]
K_b, K_f	screw conveying parameter [-]
K_p	screw pressure parameter [-]

k	Reynolds exponent in the Nusselt correlation [-]
L_{Die}	die length [m]
L_D	disc length of kneading elements [m]
L_{off}	offset length of kneading elements [m]
m	Carreau index [-]
m_b , m_s	mass of barrel and screws [kg]
$\dot{m}$	mass flow rate [kg/s]
$\dot{m}_f$, $\dot{m}_b$	forward or backward screw-driven mass flow rate [kg/s]
$\dot{m}_p$	pressure-driven mass flow rate [kg/s]
N	number of numerical elements [-]
Nu	Nusselt number [-]
n	screw speed [s^{-1}]
n_F	number of flights [-]
n_D	kneading element disc number [-]
P_{heat}	barrel heating/cooling power [W]
P_{pump}	pumping power [W]
P_{screw}	screw driving power [W]
Pr	Prandtl number [-]
p	pressure [Pa]
$\dot{Q}$	heat flux [W]
$\dot{Q}_e$	heat loss to the environment [W]
$\dot{Q}_{bm}$, $\dot{Q}_{sm}$	heat fluxes barrel/melt and screws/melt [W]
$\dot{q}$	volume-specific heat source [W/m³]
Re	Reynolds number [-]
T	temperature [°C]
T^e,	environment temperature [°C]
T^b, T^m, T^s	temperature of barrel, melt, screws [°C]
ΔT_{ga}	temperature increase in the gap [°C]
T_r	reference temperature (WLF equation) [°C]
T_s	screw pitch [m]

T_{screw}	screw torque [Nm]
T_{trans}	transition temperature (Menges model) [°C]
t	time [s]
V	volume [m³]
$\dot{V}$	volumetric throughput [m³/s]
$\dot{V}^*$	dimensionless volumetric throughput [-]
v	specific volume [m³/kg]
w	species mass fraction [-]
x	axial coordinate [m]

Greek symbols

α	tip angle [°]
α_b, α_s	HTC barrel/melt and screws/melt [W/m²K]
$\alpha_e,$	HTC barrel/environment [W/m²K]
$\dot{\gamma}$	shear rate [s^{-1}]
$\dot{\gamma}_{crit}$	critical shear rate (Carreau model) [s^{-1}]
$\dot{\gamma}_r$	representative shear rate [s^{-1}]
$\dot{\gamma}_W$	wall shear rate [s^{-1}]
ε	volume fraction [-]
η	dynamic viscosity [Pas]
η_o	zero-shear-rate viscosity (Carreau model) [Pas]
η_r	representative viscosity [Pas]
κ	kneading element offset angle [°]
$\lambda_b, \lambda_m, \lambda_s$	thermal conductivity of the barrel, melt, screws [W/mK]
ρ	density [kg/m³]
σ	standard deviation of the residence time [s]
τ	mean residence time [s]
τ_W	wall shear stress [Pa]
ψ	angle in the screw cross-section [°]

Subscripts

ax	axial
ch	channel
circ	circumferential
diss	viscous dissipation
ga	gap
i	element i
off	offset

4.10 References

(1) Kohlgrüber, K. *Co-Rotating Twin-Screw Extruders*; Carl Hanser Publishers: Munich, 2008.

(2) Kleinebudde, P. Pharmazeutisches Produktdesign: Gezielte Freisetzung von Wirkstoffen durch unterschiedliche Extrusionstechniken. *Chemie Ing. Tech.* **2011**, *83*, 589–597.

(3) Breitenbach, J. Melt Extrusion: From Process to Drug Delivery Technology. *Eur. J. Pharm. Biopharm.* **2002**, *54*, 107–117.

(4) Repka, M. A.; Gutta, K.; Prodduturi, S.; Munjal, M.; Stodghill, S. P. Characterization of Cellulosic Hot-Melt Extruded Films Containing Lidocaine. *Eur. J. Pharm. Biopharm.* **2005**, *59*, 189–196.

(5) Ghebre-Sellassie, I.; Martin, C. *Pharmaceutical Extrusion Technology*; Marcel Dekker Inc.: New York, 2003.

(6) Ishikawa, T. 3-D Non-Isothermal Flow Field Analysis and Mixing Performance Evaluation of Kneading Blocks in a Co-Rotating Twin Srew Extruder. *Polym. Eng. Sci.* **2001**, *41*, 840–849.

(7) Bertrand, F.; Thibault, F.; Delamare, L.; Tanguy, P. A. Adaptive Finite Element Simulations of Fluid Flow in Twin-Screw Extruders. *Comput. Chem. Eng.* **2003**, *27*, 491–500.

(8) Barrera, M. A.; Vega, J. F.; Martínez-Salazar, J. Three-Dimensional Modelling of Flow Curves in Co-Rotating Twin-Screw Extruder Elements. *J. Mater. Process. Technol.* **2008**, *197*, 221–224.

(9) Potente, H.; Többen, W. H. Improved Design of Shearing Sections with New Calculation Models Based on 3D Finite-Element Simulations. *Macromol. Mater. Eng.* **2002**, *287*, 808–814.

(10) Ficarella, A.; Milanese, M.; Laforgia, D. Numerical Study of the Extrusion Process in Cereals Production: Part I. Fluid-Dynamic Analysis of the Extrusion System. *J. Food Eng.* **2006**, *73*, 103–111.

(11) Rodríguez, E. O. Numerical Simulations of Reactive Extrusion in Twin Screw Extruders, Waterloo, Canada, 2009.

(12) Sarhangi Fard, A.; Hulsen, M. A.; Meijer, H. E. H.; Famili, N. M. H.; Anderson, P. D. Adaptive Non-Conformal Mesh Refinement and Extended Finite Element Method for Viscous Flow inside Complex Moving Geometries. *Int. J. Numer. methods fluids* **2012**, *68*, 1031–1052.

(13) Sarhangi Fard, A.; Hulsen, M. A.; Meijer, H. E. H.; Famili, N. M. H.; Anderson, P. D. Tools to Simulate Distributive Mixing in Twin-Screw Extruders. *Macromol. Theory Simulations* **2012**, *21*, 217–240.

(14) Sarhangi Fard, A.; Anderson, P. D. Simulation of Distributive Mixing inside Mixing Elements of Co-Rotating Twin-Screw Extruders. *Comput. Fluids* **2013**, *87*, 79–91.

(15) Hétu, J.-F.; Ilinca, F. Immersed Boundary Finite Elements for 3D Flow Simulations in Twin-Screw Extruders. *Comput. Fluids* **2013**, *87*, 2–11.

(16) Rathod, M. L.; Kokini, J. L. Effect of Mixer Geometry and Operating Conditions on Mixing Efficiency of a Non-Newtonian Fluid in a Twin Screw Mixer. *J. Food Eng.* **2013**, *118*, 256–265.

(17) Pokriefke, G. Numerische Analyse reibungsbehafteter Strömungen in teilgefüllten Extrudern, Universität der Bundeswehr Hamburg, 2005.

(18) Cleary, P. W.; Robinson, M. Understanding Viscous Fluid Transport and Mixing in a Twin Screw Extruder. In *8th International Conference on CFD in Oil & Gas, Metallurgical and Process Industries*; Trondheim, Norway, 2011.

(19) Carneiro, O. S.; Nóbrega, J. M.; Pinho, F. T.; Oliveira, P. J. Computer Aided Rheological Design of Extrusion Dies for Profiles. *J. Mater. Process. Technol.* **2001**, *114*, 75–86.

(20) Lin, Z.; Juchen, X.; Xinyun, W.; Guoan, H. Optimization of Die Profile for Improving Die Life in the Hot Extrusion Process. *J. Mater. Process. Technol.* **2003**, *142*, 659–664.

(21) Patil, P. D.; Feng, J. J.; Hatzikiriakos, S. G. Constitutive Modeling and Flow Simulation of Polytetrafluoroethylene (PTFE) Paste Extrusion. *J. Nonnewton. Fluid Mech.* **2006**, *139*, 44–53.

(22) Mitsoulis, E.; Hatzikiriakos, S. G. Steady Flow Simulations of Compressible PTFE Paste Extrusion under Severe Wall Slip. *J. Nonnewton. Fluid Mech.* **2009**, *157*, 26–33.

(23) Ardakani, H. A.; Mitsoulis, E.; Hatzikiriakos, S. G. Thixotropic Flow of Toothpaste through Extrusion Dies. *J. Nonnewton. Fluid Mech.* **2011**, *166*, 1262–1271.

(24) Radl, S.; Tritthart, T.; Khinast, J. G. A Novel Design for Hot-Melt Extrusion Pelletizers. *Chem. Eng. Sci.* **2010**, *65*, 1976–1988.

(25) Yacu, W. A. Modelling a Twin Screw Co-Rotating Extruder. *J. Food Eng.* **1985**, *8*, 1–21.

(26) Meijer, H. E. H.; Elemans, P. H. M. The Modeling of Continuous Mixers. Part I: The Corotating Twin-Screw Extruder. *Polym. Eng. Sci.* **1988**, *28*, 275–290.

(27) White, J. L.; Chen, Z. Simulation of Non-Isothermal Flow in Modular Co- Rotating Twin Screw Extrusion. *Polym. Eng. Sci.* **1994**, *34*, 229–237.

(28) Potente, H.; Hanhart, W. Design and Processing Optimization of Extruder Screws. *Polym. Eng. Sci.* **1994**, *3*, 937–945.

(29) Vergnes, B.; Della Valle, G.; Delamare, L. A Global Computer Software for Polymer Flows in Corotating Twin Screw Extruders. *Polym. Eng. Sci.* **1998**, *38*, 1781–1792.

(30) Pawlowski, J. *Transportvorgänge in Einwellen-Schnecken*; Otto Salle Verlag, Verlag Sauerländer: Aarau, Frankfurt am Main, Salzburg, 1990.

(31) Szydlowski, W.; White, J. L. An Improved Theory of Metering in an Intermeshing Corotating Twin-Screw Extruder. *Adv. Polym. Technol.* **1987**, *7*, 177–183.

(32) Potente, H.; Fornefeld, A.; Michel, P.; Wittemeier, R. Analyse und Berechnung der Strömungsvorgänge im zylindrischen Scherspalt von Plastifizieraggregaten. *Rheol. Acta* **1987**, *26*, 193–199.

(33) Wang, Y.; White, J. L. Non-Newtonian Flow Modelling in the Screw Regions of an Intermeshing Corotating Twin Screw Extruder. *J. Nonnewton. Fluid Mech.* **1989**, *32*, 19–38.

(34) Guo, Y.; Chung, C. I. Dependence of Melt Temperature on Screw Speed and Size in Extrusion. *Polym. Eng. Sci.* **1989**, *29*, 415–419.

(35) White, J. L.; Kim, E. K.; Keum, J. M.; Jung, H. C. Modeling Heat Transfer in Screw Extrusion With Special Application to Modular Self-Wiping Co-Rotating Twin-Screw Extrusion. *Polym. Eng. Sci.* **2001**, *41*, 1448–1455.

(36) Todd, D. B. Residence Time Distribution in Twin-Screw Extruders. *Polym. Eng. Sci.* **1975**, *15*, 437–443.

(37) Potente, H.; Koch, M. Residence Time Behavior in Grooved-Barrel Extruders. *Adv. Polym. Technol.* **1989**, *9*, 119–127.

(38) Chen, L.; Pan, Z.; Hu, G.-H. Residence Time Distribution in Screw Extruders. *AIChE J.* **1993**, *39*, 1455–1464.

(39) Oberlehner, J.; Cassagnau, P.; Michel, A. Local Residence Time Distribution Screw Extruder in a Twin. *Chem. Eng. Sci.* **1994**, *49*, 3897–3907.

(40) De Ruyck, H. Modelling of the Residence Time Distribution in a Twin Screw Extruder. *J. Food Eng.* **1997**, *32*, 375–390.

(41) Giudici, R.; Nascimento, C. A. O.; Beiler, I. C.; Scherbakoff, N. Transient Experiments and Mathematical Modeling of an Industrial Twin-Screw Extruder Reactor for Nylon-6,6 Polymerization. *Ind. Eng. Chem. Res.* **1997**, *36*, 3513–3519.

(42) Gao, J.; Walsh, G. C.; Bigio, D.; Briber, R. M.; Wetzel, M. D. Residence-Time Distribution Model for Twin-Screw Extruders. *Process Syst. Eng.* **1999**, *45*, 2541–2549.

(43) Prat, L.; Guiraud, P.; Rigal, L.; Gourdon, C. Two Phase Residence Time Distribution in a Modified Twin Screw Extruder. *Chem. Eng. Process.* **1999**, *38*, 73–83.

(44) Puaux, J. P.; Bozga, G.; Ainser, A. Residence Time Distribution in a Corotating Twin-Screw Extruder. *Chem. Eng. Sci.* **2000**, *55*, 1641–1651.

(45) Kumar, A.; Ganjyal, G. M.; Jones, D. D.; Hanna, M. A. Modeling Residence Time Distribution in a Twin-Screw Extruder as a Series of Ideal Steady-State Flow Reactors. *J. Food Eng.* **2008**, *84*, 441–448.

(46) Baron, R.; Vauchel, P.; Kaas, R.; Arhaliass, A.; Legrand, J. Dynamical Modelling of a Reactive Extrusion Process: Focus on Residence Time Distribution in a Fully Intermeshing Co-Rotating Twin-Screw Extruder and Application to an Alginate Extraction Process. *Chem. Eng. Sci.* **2010**, *65*, 3313–3321.

(47) Amedu, O. K.; Penlington, R.; Busawon, K.; Morgan, A. Application of Statistical Techniques and Mechanistic Modelling to the Mixing Process in Co-Rotating Twin-Screw Extruders. In *2013 AIChE Annual Meeting Conference Proceedings*; San Francisco, 2013.

(48) Choulak, S.; Couenne, F.; Le Gorrec, Y.; Jallut, C.; Cassagnau, P.; Michel, A. Generic Dynamic Model for Simulation and Control of Reactive Extrusion. *Ind. Eng. Chem. Res.* **2004**, *43*, 7373–7382.

(49) Zagal, A.; Vivaldo-Lima, E.; Manero, O. A Mathematical Model for the Reactive Extrusion of Methyl Methacrylate in a Co-Rotating Twin-Screw Extruder. *Ind. Eng. Chem. Res.* **2005**, *44*, 9805–9817.

(50) Puaux, J.-P.; Cassagnau, P.; Bozga, G.; Nagy, I. Modeling of Polyurethane Synthesis by Reactive Extrusion. *Chem. Eng. Process.* **2006**, *45*, 481–487.

(51) Eitzlmayr, A.; Khinast, J.; Hörl, G.; Koscher, G.; Reynolds, G.; Huang, Z.; Booth, J.; Shering, P. Experimental Characterization and Modeling of Twin-Screw Extruder Elements for Pharmaceutical Hot Melt Extrusion. *AIChE J.* **2013**, *59*, 4440–4450.

(52) Kohlgrüber, K.; Bierdel, M.; Conzen, C.; Hepperle, J.; Kirchhoff, J.; König, T.; Thiele, H. Optimierter Betrieb und Scale-up von Doppelschnecken-Extrudern. In *Seminar Handout*; Kohlgrüber, K., Ed.; VDI Wissensforum: Leverkusen, Germany, 2012.

(53) Bierdel, M. Computational Fluid Dynamics. In *Co-Rotating Twin-Screw Extruders*; Kohlgrüber, K., Ed.; Carl Hanser Publishers: Munich, 2008.

(54) Paul, E. L.; Atiemo-Obeng, V. A.; Kresta, S. M. *Handbook of Industrial Mixing*; John Wiley & Sons, Inc.: Hoboken, New Jersey, 2004.

(55) Gnielinkski, V.; Kabelac, S.; Kind, M.; Martin, H.; Mewes, D.; Schaber, K.; Stephan, P. *VDI-Wärmeatlas*; VDI, V. D. I.; GVC, V.-G. V. und C., Eds.; 10th ed.; Springer Verlag: Berlin, Heidelberg, 2006.

(56) Kolter, K.; Karl, M.; Gryczke, A. *Hot-Melt Extrusion with BASF Pharma Polymers Extrusion Compendium*; 2nd ed.; BASF: Ludwigshafen, 2012.

(57) Rauwendaal, C. *Polymer Extrusion*; 4th ed.; Hanser Publishers: Munich, 2001.

(58) Elkouss, P.; Bigio, D. I. Influence of Polymer Viscoelasticity on the Residence Distributions of Extruders. *AIChE J.* **2006**, *52*, 1451–1459.

"*There ought to be something very special about the boundary conditions of the universe, and what can be more special than that there is no boundary?*"

(Stephen Hawking)

5

A Novel Method for Modeling of Complex Wall Geometries in Smoothed Particle Hydrodynamics*

Smoothed particle hydrodynamics (SPH) has become increasingly important during recent decades. Its meshless nature, inherent representation of convective transport and ability to simulate free surface flows make SPH particularly promising with regard to simulations of industrial mixing devices for high-viscous fluids, which often have complex rotating geometries and partially filled regions (e.g., twin-screw extruders). However, incorporating the required geometries remains a challenge in SPH since the most obvious and most common ways to model solid walls are based on particles (i.e., boundary particles and ghost particles), which leads to complications with arbitrarily-curved wall surfaces. To overcome this problem, we developed a systematic method for determining an adequate interaction between SPH particles and a continuous wall surface based on the underlying SPH equations. We tested our new approach by using the open-source particle simulator "LIGGGHTS" and comparing the velocity profiles to analytical solutions and SPH simulations with boundary particles. Finally, we followed the evolution of a tracer in a twin-cam mixer during the rotation, which was experimentally and numerically studied by several other authors, and ascertained good agreement with our results. This supports the validity of our newly-developed wall interaction method, which constitutes a step forward in SPH simulations of complex geometries.

---

* This chapter is based on: Eitzlmayr, A.; Koscher, G.; Khinast, J. A Novel Method for Modeling of Complex Wall Geometries in Smoothed Particle Hydrodynamics. *Comput. Phys. Commun*. 2014, *185*, 10, 2436–2448.

5.1 Introduction

Smoothed particle hydrodynamics (SPH) is a Lagrangian, particle-based method that approximates the continuum equations of fluid mechanics based on an interpolation technique for spatially-disordered nodes. Originally developed for compressible flows, the Monaghan[1] approach exhibits an inherent compressibility also when applied to the incompressible flow of liquids. However, if the chosen speed of sound is sufficiently high, the density variability is negligible. Thus, real liquids are described as compressible using a low Mach number.[2] In contrast to the real speed of sound, a fictitious (smaller) value is typically used in SPH to avoid unreasonably low time steps.

In the field of computational fluid dynamics SPH is a rather new method that complements conventional mesh-based approaches, such as the finite volume method (FVM) and finite element method (FEM). Due to its meshless nature, SPH is well-suited for problems that involve moving and complex geometries and strong deformations of the fluid domain, as in the case of industrial mixing processes. At low Reynolds numbers, when turbulence does not support mixing, the mixer design is even more crucial for uniform and efficient mixing.[3] Such devices are typically used in the food, fine-chemicals, polymer and pharmaceutical industries. For example, extrusion processes, which are common in the polymer and food industries, are becoming increasingly interesting to pharmaceutical manufacturing (which is our field of interest). Simulation of these devices with SPH does not require sophisticated re-meshing techniques which are a prerequisite for mesh-based methods (e.g., Bertrand et al.[4], Barrera et al.[5], Bierdel[6]). Moreover, SPH implicitly accounts for the convective species transport,[1] which is also beneficial for the simulation of mixing processes.[3]

In contrast to mesh-based methods, SPH can inherently simulate free surface flows, which makes it suitable for simulating partially-filled mixing devices (e.g., twin-screw extruders). Robinson et al.[3] obtained SPH results for a simple twin-cam mixer at low Reynolds numbers and found them in good agreement with the experimental and FEM results of Avalosse and Crochet[7]. Moreover, Cleary and Robinson used SPH to simulate mixing in a twin-screw extruder[8] and in a helical ribbon mixer[9].

Despite the increasing use of SPH in the last decades, there is still no existing unique and comprehensive way of modeling boundaries in SPH. However, appropriate boundary modeling is essential, since – for example – modeling walls simply as flat, repulsive surfaces creates undesirable and unphysical effects due to missing neighbors outside of the wall. Thus, the simulation of complex geometries, typically required in technical applications, remains a challenge.

The most obvious way is to model walls consisting of particles. Frequently-used techniques for modeling solid walls in SPH include different types of boundary particles, ghost particles and normalizing conditions.[10] Akin to real boundaries consisting of atoms or molecules, boundary particles are fixed particles arranged along a wall that exert repulsive forces on fluid particles in the vicinity of the wall.[11] The boundary particles can interact with the adjacent fluid particles either differently from the interaction between fluid particles (e.g., Monaghan[10], Gomez-Gesteira et al.[11]), or in the same way as the fluid particles (sometimes termed as "fixed fluid particles", e.g., Dalrymple and Knio[12], Gomez-Gesteira and Dalrymple[13]). However, in the latter case several rows of boundary particles are required to represent a solid wall in order to guarantee a sufficient number of neighbors for fluid particles next to the wall. In contrast to boundary particles representing the wall, ghost particles are generated by mirroring fluid particles on the wall's surface. To achieve the no-slip condition, the opposite velocity direction of the corresponding fluid particle is assigned to each ghost particle (e.g., Takeda et al.[14], Randles and Liberski[15], Colagrossi and Landrini[16], De Leffe et al.[17] and Børve[18]). To model walls without additional particles, normalizing conditions have been developed that correct errors caused by the absence of neighbors opposite to the wall via normalization (e.g., Feldman and Bonet[19], Ferrand et al.[20]). For more details of SPH boundary methods see also González et al.[21] and Groenenboom et al.[22].

When applied to complex-shaped geometries, as it often is in the case in technical applications, the above particle-based boundary methods encounter several issues. A sophisticated procedure is required to set one or more layers of fixed boundary particles that are equally spaced along the arbitrarily-curved surface. Mirroring particles on the wall surface can be problematic on edges and corners,[23] yielding empty or overfilled regions on the concave or convex edges/corners, respectively. Furthermore, planar walls configured of

particles are structured, i.e., the repulsion and shear forces exerted on a fluid particle moving parallel to the wall are not constant.[24]

In technical applications, geometries are typically generated using CAD (Computer Aided Design) software and can easily be transformed into the *.stl file format (Surface Tessellation Language), which is commonly used to provide geometry data for simulations by approximating an arbitrarily-shaped surface via a tessellation consisting of small triangles (the so-called STL-mesh). In order to efficiently apply SPH to STL-meshes, a wall interaction without additional particles is required. One way to achieve this was described by Kruisbrink et al.,[24] who modeled the wall interaction based on normal and tangential forces acting on fluid particles in the vicinity of a continuous wall.

In our work, we defined the wall interaction systematically, based on the underlying SPH equations. In addition to normal and tangential wall forces, this leads to a wall contribution for the density of a fluid particle adjacent to the wall. In the same way, boundary conditions for other quantities (e.g., temperature) can be systematically determined.

In our work, we investigated the mathematical influence of the wall on adjacent fluid particles based on a wall setup consisting of boundary particles of the type “fixed fluid particles”. We compiled the obtained data into polynomials depending on the wall distance, which allows us to immediately calculate boundary contributions of a fluid particle with a given distance to the wall. The obtained polynomials were implemented into a SPH code to simulate complex geometries using STL-meshes.

5.2 Used SPH Formalism

Our approach is based on the weakly-compressible SPH method due to Monaghan,[2,25,26] where the continuity equation is approximated as follows (yielding the time evolution of the density of particle a, ρ_a , with b being the neighbors of a, including a):

$$\frac{d\rho_a}{dt} = \sum_b m_b \left(\vec{v}_a - \vec{v}_b\right) \cdot \vec{\nabla}_a W_{ab} \tag{5.1}$$

Here, m is the particle mass, $\vec{v}$ is the particle velocity and $\vec{\nabla}_a W_{ab}$ is the gradient of the kernel function W around particle b evaluated at the position of particle a. For simplicity

reasons, we abbreviated the kernel function $W(|\vec{r}_{ab}|, h)$ as W_{ab}, where $\vec{r}_{ab} = \vec{r}_a - \vec{r}_b$ is the distance vector between particles *a* and *b* and *h* is the smoothing length).

For liquids, the following equation of state is typically used, ρ_0 being the reference density at pressure $P = 0$:[2]

$$P = B\left[\left(\frac{\rho}{\rho_0}\right)^{\gamma} - 1\right] \tag{5.2}$$

The coefficient *B* can be calculated from the speed of sound *c* and the reference density ρ_0:

$$B = \frac{c^2 \rho_0}{\gamma} \tag{5.3}$$

The chosen speed of sound should be high enough to keep the density variability low in the case of liquids (typically $\Delta\rho/\rho_0 \leq 0.01$), yet as small as possible to enable larger time steps. The criteria to achieve this are described in, e.g., Morris et al.[27]:

$$c^2 \approx \frac{1}{\delta} max\left(V_0^{\,2}, \frac{\nu V_0}{L_0}, aL_0\right) \quad \text{with} \quad \delta = \frac{\Delta\rho}{\rho_0} \tag{5.4}$$

Here V_0 is the maximum fluid velocity, ν the kinematic fluid viscosity, L_0 a typical length scale and *a* a force per mass acting on the particles. The first criterion limits the compression due to kinetic energy and can also be expressed by the Mach number ($Ma^2 \leq \delta$, see also Monaghan[2]). The second and third criteria in Eq. 5.4 limit the compression due to viscous and mass forces.

As exponent γ in Eqs. 5.2 and 5.3, a value of 7 is typically used. However, since in the case of small density variations ($\rho \approx \rho_0$), the difference between $\gamma = 7$ and its linearization ($\gamma = 1$) disappears, we used $\gamma = 1$ for simplicity reasons. Note that the derivative of pressure *P* with respect to density ρ is defined only by the speed of sound and is not affected by γ, as can easily be shown by differentiating Eq. 5.2 and substituting *B* from Eq. 5.3:

$$\left.\frac{dP}{d\rho}\right|_{\rho=\rho_0} = \frac{B\gamma}{\rho_0}\left(\frac{\rho}{\rho_0}\right)^{\gamma-1} = c^2 \tag{5.5}$$

Due to the strong dependence of pressure on density in liquids under the weakly-compressible SPH method, small density errors, which accumulate over time when Eq. 5.1 is used for the density, can lead to strong oscillations in the pressure field. A common way to overcome this problem is to periodically apply a filter to the density field. We used the Shepard filter every 30 time steps (e.g., Gomez-Gesteira et al.[23]):

$$\rho_a^{new} = \frac{\sum_b m_b W_{ab}}{\sum_b \frac{m_b}{\rho_b} W_{ab}} \tag{5.6}$$

For the momentum equation, which essentially yields the acceleration of each particle, the following form was suggested by Monaghan[26] that includes interaction forces due to pressure P, an artificial viscosity term Π_{ab} and tensile correction $R(f_{ab})^4$:

$$\frac{d\vec{v}_a}{dt} = -\sum_b m_b\left(\frac{P_a}{{\rho_a}^2} + \frac{P_b}{{\rho_b}^2} + \Pi_{ab} + R\left(f_{ab}\right)^4\right)\vec{\nabla}_a W_{ab} \tag{5.7}$$

The artificial viscosity model for Π_{ab} (for details see Monaghan[2,25], Gomez-Gesteira et al.[23]) conserves linear and angular momentum exactly, which may be important, especially for high Reynolds numbers. However, for low Reynolds number flows (as considered in our study) better results can be obtained by using the viscosity model of Morris et al.[27], whose drawback of inexact angular momentum conservation is of less importance here, and which leads to the following modification of the momentum equation:

$$\frac{d\vec{v}_a}{dt} = -\sum_b m_b\left(\frac{P_a}{{\rho_a}^2} + \frac{P_b}{{\rho_b}^2} + R\left(f_{ab}\right)^4\right)\vec{\nabla}_a W_{ab} + \sum_b \frac{m_b\left(\mu_a + \mu_b\right)}{\rho_a \rho_b}\left(\frac{1}{|\vec{r}_{ab}|}\frac{\partial W_{ab}}{\partial r_a}\right)\vec{v}_{ab} \tag{5.8}$$

The tensile correction according to Monaghan[26] was used to avoid the unphysical clustering of SPH particles in regions with negative pressure:

$$R = R_a + R_b \tag{5.9}$$

with

$$R_{a,b} = \begin{cases} \dfrac{\varepsilon \left| P_{a,b} \right|}{{\rho_{a,b}}^2} & (P_{a,b} < 0) \\ 0 & (\text{otherwise}) \end{cases} \tag{5.10}$$

$$f_{ab} = \frac{W_{ab}}{W(\Delta x, h)} \tag{5.11}$$

For parameter ε the value 0.2 is commonly used. For the kernel function W, we employed the cubic-spline kernel, defined in one, two or three dimensions as follows:[25,26]

$$W\left(|\vec{r}_{ab}|, h\right) = \frac{\sigma}{h^d} \begin{cases} 1 - \dfrac{3}{2}\left(\dfrac{|\vec{r}_{ab}|}{h}\right)^2 + \dfrac{3}{4}\left(\dfrac{|\vec{r}_{ab}|}{h}\right)^3 & 0 \le \dfrac{|\vec{r}_{ab}|}{h} < 1 \\ \dfrac{1}{4}\left(2 - \dfrac{|\vec{r}_{ab}|}{h}\right)^3 & 1 \le \dfrac{|\vec{r}_{ab}|}{h} < 2 \\ 0 & 2 \le \dfrac{|\vec{r}_{ab}|}{h} \end{cases} \tag{5.12}$$

Here, d is the number of spatial dimensions (1, 2 or 3) and σ is a constant with the values of $2/3$, $10/(7\pi)$ and $1/\pi$ in 1D, 2D or 3D, respectively. It has been suggested to use a smoothing length of 1.2 to 1.3 times the initial particle spacing Δx on a cubic lattice (see Monaghan[1], Liu and Liu[28]). Here, we used the 1.2-fold spacing, which leads to a number of approximately 57 neighbors within a sphere of the radius 2h in 3D:

$$h = 1.2\Delta x \tag{5.13}$$

The smoothing length, which represents the spatial resolution of the simulation, is strongly linked to the time step which is required for stability. Morris et al.[27] showed the following criteria (c being the speed of sound, a a mass force and ν the kinematic fluid viscosity):

$$\Delta t \le min\left(0.25\frac{h}{c}, 0.25\sqrt{\frac{h}{a}}, 0.125\frac{h^2}{\nu}\right) \tag{5.14}$$

The first constraint in Eq. 5.14 is a Courant-Friedrichs-Lewy (CFL) condition, and the second and third ones are limitations due to mass forces and viscous forces. For more details concerning the fundamentals of SPH please refer to the literature, e.g., Monaghan[1,2,25,26], Liu and Liu[28], Price[29], Gomez-Gesteira et al.[23].

5.3 Wall Interaction

To determine the interaction of a single fluid particle with a solid wall, we created a setup of boundary particles representing a planar wall parallel to the *x*-*y* plane (see Figure 5.1). The boundary particles are essentially treated as fluid particles, only with suppressed movement (i.e., the type "fixed fluid particles"). We placed a single fluid particle in the vicinity of the wall, moved it along the wall and determined the contributions of the boundary particles to the SPH interaction terms of that fluid particle. In order to obtain generally applicable results, the mathematical derivation below was required.

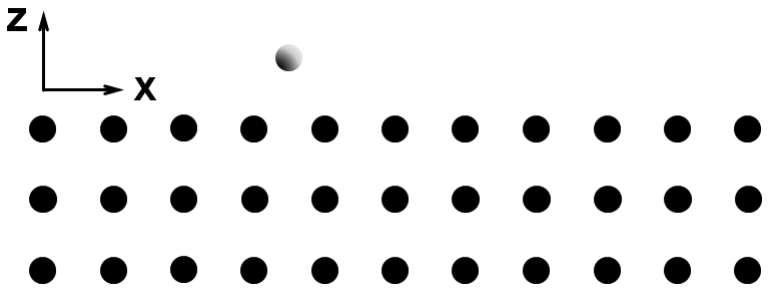

Figure 5.1: Planar wall consisting of boundary particles (shown in black, 11 rows in the y-direction) together with a single fluid particle (shown in white).

For the continuity equation (Eq. 5.1) of the single fluid particle *a* we obtained the following expression when the velocity of the boundary particles (BP) was set to zero (i.e., using the fluid particle velocity relative to the wall), assuming the same mass for all particles $m_a = m_b$:

$$\left.\frac{d\rho_a}{dt}\right|_{BP} = m_a \sum_{b \in BP} \vec{v}_a \cdot \vec{\nabla}_a W_{ab} \tag{5.15}$$

The velocity vector of the fluid particle can be split into parallel (v_x) and normal (v_z) components (the v_y component is 0):

$$\left.\frac{d\rho_a}{dt}\right|_{BP} = m_a \sum_{b\in BP} \begin{pmatrix} v_x \\ 0 \\ v_z \end{pmatrix} \cdot \begin{pmatrix} \partial W_{ab}/\partial x \\ \partial W_{ab}/\partial y \\ \partial W_{ab}/\partial z \end{pmatrix} = m_a \sum_{b\in BP} v_{a,x} \frac{\partial W_{ab}}{\partial x} + m_a \sum_{b\in BP} v_{a,z} \frac{\partial W_{ab}}{\partial z} \tag{5.16}$$

Considering that the kernel is an even function (i.e., its gradient is odd), the first term of Eq. 5.16 must be dropped. It can also be argued that the density of the fluid particle is not affected by the boundary particles when the movement is parallel to the wall. The remaining part can be transformed in order to obtain a dimensionless expression that we denoted as $F_{\nabla W}$ (dimensionless boundary contribution for the continuity equation), where the velocity $v_{a,z}$ is perpendicular to the wall and positive for a particle approaching the wall:

$$\left.\frac{d\rho_a}{dt}\right|_{BP} = m_a v_{a,z} \frac{1}{h^4} F_{\nabla W} \quad \text{with} \quad F_{\nabla W} = h^4 \sum_{b\in BP} \frac{\partial W_{ab}}{\partial z} \tag{5.17}$$

Considering the structure of the kernel function Eq. 5.12 (i.e., W depends only on the ratio $|\vec{r}_{ab}|/h$ and is proportional to $1/h^3$ in 3D) shows that the chosen dimensionless form of $F_{\nabla W} = \sum_{b\in BP} \partial\left(h^3 W\right)/\partial\left(z/h\right)$ contains only dimensionless distances. Thus, it is constant for a constant ratio of $h/\Delta x$ (Eq. 5.13). Therefore, this formulation is independent of the chosen size of the setup (i.e., the particle spacing Δx), which is also valid for the analogous dimensionless terms obtained below.

We used the same approach for the momentum equation. Considering the pressure terms in Eq. 5.8 and assuming that the pressure and density of the boundary particles P_b and ρ_b are equal to the pressure and density of the fluid particle P_a and ρ_a, we obtain:

$$\left.\frac{d\vec{v}_a}{dt}\right|_{BP} = -m_a \sum_{b\in BP} \left(2 \frac{P_a}{\rho_a^{\,2}} \right) \vec{\nabla}_a W_{ab} \tag{5.18}$$

By splitting the kernel gradient into components, we established that the components parallel to the wall need to be dropped due to the odd gradient function. It can also be argued that the pressure of the boundary particles acts as a repulsive force and does not influence a velocity component parallel to the wall:

$$\left.\frac{d\vec{v}_a}{dt}\right|_{BP} = -m_a \frac{2P_a}{\rho_a^2} \begin{pmatrix} \sum_{b\in BP} \partial W_{ab}/\partial x \\ \sum_{b\in BP} \partial W_{ab}/\partial y \\ \sum_{b\in BP} \partial W_{ab}/\partial z \end{pmatrix} = -m_a \frac{2P_a}{\rho_a^2} \begin{pmatrix} 0 \\ 0 \\ \sum_{b\in BP} \partial W_{ab}/\partial z \end{pmatrix} \tag{5.19}$$

The remaining part refers to the normal (z) component of the fluid particle velocity $v_{a,z}$ and can be written as (obtaining the expression $F_{\nabla W}$ again):

$$\left.\frac{dv_{a,z}}{dt}\right|_{BP} = -m_a \frac{2P_a}{\rho_a^2} \frac{1}{h^4} F_{\nabla W} \tag{5.20}$$

To obtain the boundary contribution for the Morris model, we proceeded analogously. Assuming equal values of m, ρ and μ for boundary and fluid particles, we obtain the following expression for the viscous forces in the Morris model (Eq. 5.8):

$$\left.\frac{d\vec{v}_a}{dt}\right|_{BP} = \frac{m_a 2\mu_a \vec{v}_{a,tan}}{\rho_a^2} \sum_{b\in BP} \left(\frac{1}{|\vec{r}_{ab}|} \frac{\partial W_{ab}}{\partial r_a} \right) \tag{5.21}$$

Since viscous wall forces should act only in the direction tangential to the wall, we used the tangential component of the particle velocity $\vec{v}_{a,tan}$ instead of the particle velocity $\vec{v}_a$ (which is practically the same for particles in the vicinity of the wall, where the flow perpendicular to the wall is negligible). Eq. 5.21 can be written in the following way in order to obtain a dimensionless expression, which we called $F_{\nabla W/r}$ (dimensionless boundary contribution for the Morris model):

$$\left.\frac{d\vec{v}_a}{dt}\right|_{BP} = -\frac{m_a 2\mu_a \vec{v}_{a,\tan}}{\rho_a^2 h^5} F_{\nabla W/r} \quad \text{with} \quad F_{\nabla W/r} = -h^5 \sum_{b\in BP} \left(\frac{1}{|\vec{r}_{ab}|} \frac{\partial W_{ab}}{\partial r_a} \right) \tag{5.22}$$

The remaining term in the momentum equation (Eq. 5.8) is the tensile correction according to Monaghan[26], which prevents the clustering of fluid particles in the case of negative pressure and yields significant contributions only when the distance between two adjacent particles is considerably small compared to the typical distance. Since we used a repulsive potential (shown in detail later) to prevent the penetration of the wall, no wall interaction

for the tensile correction was required as the essential conditions at the wall (no-penetration and no-slip) were achieved rather by repulsion, pressure and viscous forces.

From the particle setup in Figure 5.1, we determined the values of $F_{\nabla W}$ and $F_{\nabla W/r}$ as follows: we moved the fluid particle along the wall (i.e., in the *x*-direction) at a defined wall distance *z*. During the movement, we recorded the mass-specific force of the fluid particle *a*, exerted by the boundary particles. Due to the non-uniform structure of the wall composed of boundary particles, the force showed a marginal fluctuation along *x* (in the order of 1%) which was averaged. In order to determine pressure and viscous forces separately, we first set the viscosity of all particles $\mu = 0$ (viscous forces vanished). From the force normal to the wall ($dv_{a,z}/dt$) we calculated the dimensionless expression $F_{\nabla W}$ as follows (obtained from Eq. 5.20):

$$F_{\nabla W} = -\frac{\rho_a^{\,2} h^4}{2 P_a m_a} \frac{dv_{a,z}}{dt} \tag{5.23}$$

Then, we set the pressure of all particles $P = 0$ (pressure forces vanished) and determined the tangential force ($dv_{a,x}/dt$). This was converted into the dimensionless expression $F_{\nabla W/r}$ as follows (obtained from Eq. 5.22):

$$F_{\nabla W/r} = -\frac{\rho_a^{\,2} h^5}{2 \mu_a m_a v_{a,x}} \frac{dv_{a,x}}{dt} \tag{5.24}$$

These measurements were performed for different wall distances *z*. The results of $F_{\nabla W}$ and $F_{\nabla W/r}$ versus the dimensionless wall distance $z^* = z/h$ are shown in Figure 5.2. As expected, they decrease with the increasing distance to the wall and reach zero approximately at $z^* = 1.5$. We fitted the following polynomials to these data (also shown in Figure 5.2):

$$F_{\nabla W}\left(z^*\right) = \begin{cases} -0.607\left(z^*\right)^4 + 2.59\left(z^*\right)^3 - 3.09\left(z^*\right)^2 - 0.059 z^* + 1.37 & \left(z^* < 1.45\right) \\ 0 \quad \left(\text{otherwise}\right) \end{cases} \tag{5.25}$$

$$F_{\nabla W/r}(z^*) = \begin{cases} -0.571(z^*)^4 + 1.413(z^*)^3 + 0.622(z^*)^2 - 3.92z^* + 2.59 & (z^* < 1.43) \\ 0 \quad (\text{otherwise}) \end{cases} \tag{5.26}$$

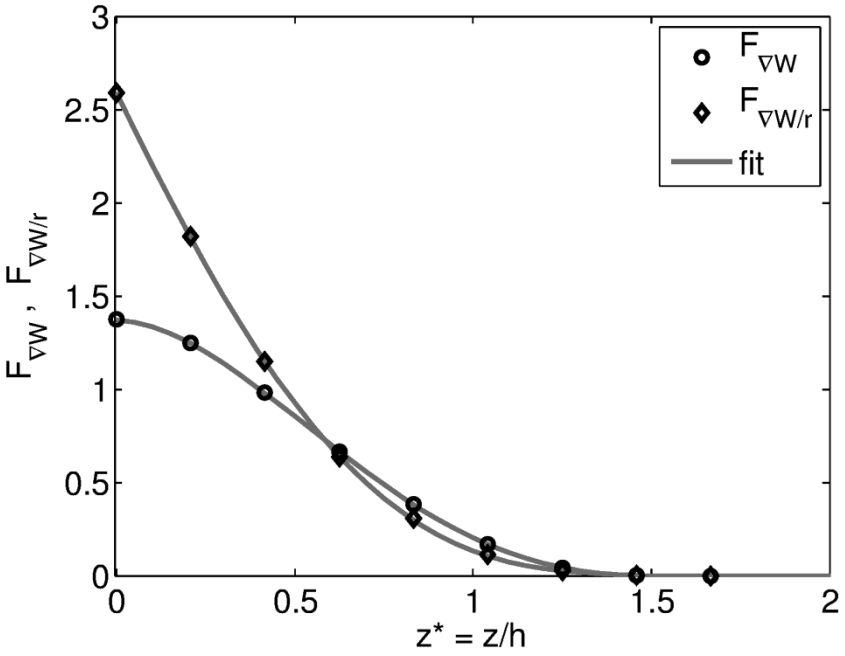

Figure 5.2: Measured dimensionless boundary contributions (symbols) and fitted polynomials (lines).

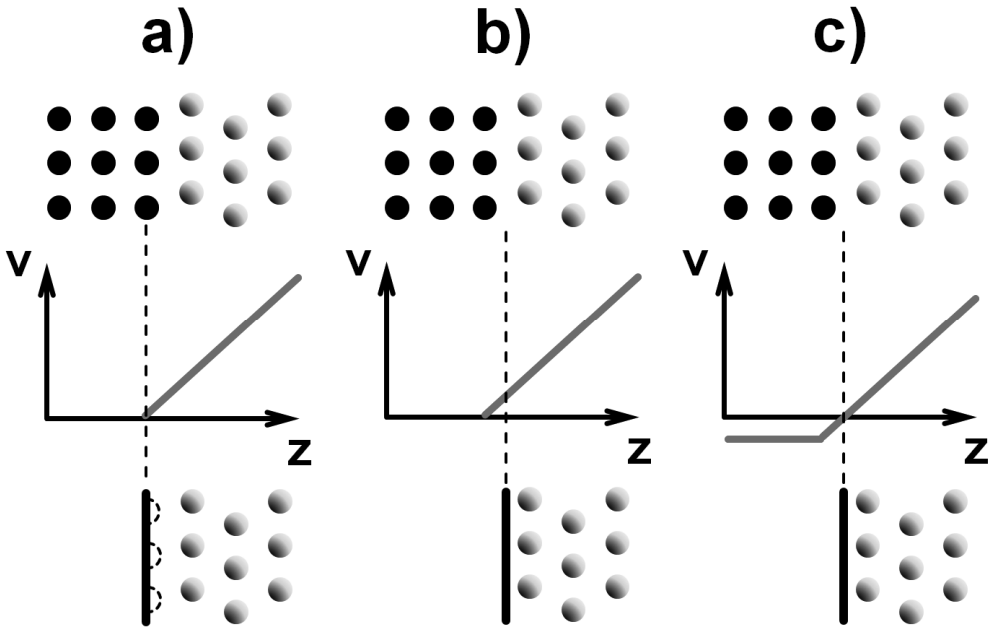

Figure 5.3: Three scenarios (a,b,c) for the wall position with regard to the no-slip condition, the top row shows boundary particles (black) and fluid particles (white), the middle row the corresponding tangential velocity profiles, and the bottom row the corresponding representation as continuous walls.

In Figure 5.3 various scenarios are depicted how the position of the wall surface ($z^* = 0$) can be chosen. In Figure 5.3a the wall surface coincides with the wall particles, yielding a zero velocity at the wall (as it should be). However, as can be seen in the corresponding bottom schematic, a significant part of the space adjacent to the wall is particle free. In Figure 5.3b the wall surface is located in between boundary particles and the first layer of fluid particles. Here the space is filled, but the velocity is not exactly zero at the wall. To achieve the exact no-slip condition while filling the space with particles we chose the scenario depicted in Figure 5.3c, where we assigned a velocity to the boundary particles such that the average at the wall is zero. This assigned velocity of the boundary particles $\vec{v}_{BP}$ is calculated assuming a linear profile of the tangential velocity as shown in Figure 5.4. The corrected tangential velocity is the sum of the original tangential velocity $\vec{v}_{a,tan}$ and $\vec{v}_{BP}$ (where Δx is the particle spacing):

$$\vec{v}_{a,tan}^{corr} = \vec{v}_{a,tan}\left(1+\frac{\Delta x}{2z}\right) \tag{5.27}$$

To apply this, we replaced the tangential velocity $\vec{v}_{a,tan}$ in Eq. 5.22 by the corrected tangential velocity $\vec{v}_{a,tan}^{corr}$ from Eq. 5.27, yielding:

$$\left.\frac{d\vec{v}_a}{dt}\right|_{BP} = -\frac{m_a 2\mu_a \vec{v}_{a,\tan}}{{\rho_a}^2 h^5}\left(1+\frac{\Delta x}{2z}\right)F_{\nabla W/r} \tag{5.28}$$

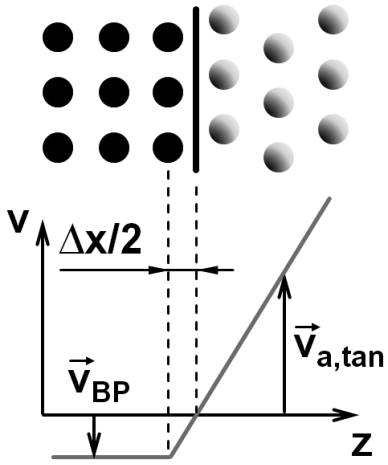

Figure 5.4: Imitated velocity of the boundary particles to enforce the no-slip condition exactly.

The above used assumption, i.e., equal mass of the boundary particles compared to the considered fluid particles, implies no restriction for the applicability of the obtained dimensionless boundary contributions (i.e., the polynomials Eqs. 5.25 and 5.26), since each summation contribution in the underlying Eqs. 5.1 and 5.8 is weighted with the mass of the contributing particle. Thus, using a lower mass and a correspondingly lower spacing of the boundary particles (i.e., to maintain the correct density) would result in proportionally higher magnitudes of the dimensionless boundary contributions (Eqs. 5.25 and 5.26) due to the increased number of boundary particles per volume. Since the values of the dimensionless boundary contributions are weighted with the mass of the boundary particles, the finally obtained boundary contributions (Eqs. 5.17, 5.20 and 5.28) are independent of the presumed boundary particle mass (and the corresponding boundary resolution). This is reasonable, considering that the boundary resolution is actually not existing when the developed wall interaction is applied instead of boundary particles.

Similarly, the effect of the presumed smoothing length $h = 1.2\Delta x$ (Eq. 5.13) can be considered. Increasing the smoothing length h by a factor ξ ($h = 1.2\xi\,\Delta x$) would lead to the same situation as the refinement of the boundary particle spacing Δx by factor $1/\xi$ (i.e., yielding the ξ^3-fold number of boundary particles in 3D). In the latter case, the dimensionless boundary contributions $F_{\nabla W}$ and $F_{\nabla W/r}$ (Eqs. 5.17 and 5.22) would have the ξ^3-fold number of summation contributions. However, the values of each contribution remained the same due to the unchanged geometry and smoothing length (i.e., identical values at the same boundary particle positions, and similar values for positions in between due to the refinement). Thus, increasing the ratio $h/\Delta x = 1.2$ by factor ξ, yields the ξ^3-fold values for the dimensionless boundary contributions. Based on that, $F_{\nabla W}$ and $F_{\nabla W/r}$ (and the analogous expressions in the Appendix A) can be applied for different ratios $h/\Delta x$ when weighted with the prefactor ξ^3, i.e., when the following expressions $\widetilde{F}_{\nabla W}$ and $\widetilde{F}_{\nabla W/r}$ are used instead of $F_{\nabla W}$ and $F_{\nabla W/r}$ in Eqs. 5.17, 5.20 and 5.28 (while $F_{\nabla W}$ and $F_{\nabla W/r}$ are still obtained from the fitted polynomials Eqs. 5.25 and 5.26):

$$\widetilde{F}_{\nabla W}\left(z^*\right) = \left(\frac{h}{1.2\Delta x}\right)^3 F_{\nabla W}\left(z^*\right) \tag{5.29}$$

$$\widetilde{F}_{\nabla W/r}\left(z^*\right)=\left(\frac{h}{1.2\Delta x}\right)^3 F_{\nabla W/r}\left(z^*\right) \tag{5.30}$$

The assumption in Eq. 5.21, i.e., equal viscosity of the boundary particles compared to the considered fluid particles, is trivial, since we considered a Newtonian fluid. However, even for a variable viscosity (e.g., shear rate or temperature dependence) this assumption would be adequate, since the viscosity is a fluid property rather than a wall property. As we developed the wall interaction based on the interaction between fluid particles, the wall exerts the same type of forces than the fluid, thus requires a viscosity value, which must be equal to the fluid viscosity adjacent to the wall.

However, the assumptions in Eq. 5.18 of equal density and pressure for the boundary particles compared to the considered fluid particle clearly differ from the situation when directly using boundary particles. In the latter case, the boundary particles show a lower density variation (and consequently a lower pressure variation) than the adjacent fluid particles due to the incompressibility of the (fixed) boundary particles (i.e., a density and pressure variation of the boundary can only be caused by the influence of adjacent fluid particles). Consequently, in the case of a strongly compressed fluid the boundary fails to provide the required counter pressure and the fluid particles penetrate the wall. Due to our assumptions, the boundary always acts with the same pressure as the considered fluid particle, which is expected to reduce the penetrability of the wall. However, even when using the same pressure for the boundary as for the considered fluid particle, penetration can happen due to a higher number of particles per volume in the compressed fluid compared to the incompressible boundary, and thus, more force contributions from the fluid which push fluid particles into the boundary. We actually found this problem in cases, where strong compression was exerted by parts of a moving geometry (with boundary particles as well as our developed wall interaction method). For that reason, we additionally used a repulsive force, which acts on short wall distances, where fluid particles usually should not stay, and increases inversely proportional to the wall distance. This can be physically interpreted as the impenetrability of a solid wall, which causes strong repulsion on microscopic ranges. We used the following repulsive force model,

similarly to Monaghan[2] (given as scalar, for the direction of the repulsive force we used the wall normal vector):

$$F_{rep}(z)=\begin{cases} D\left(\frac{z_0}{z}-1\right) & (z \le z_0) \\ 0 & (z > z_0) \end{cases} \tag{5.31}$$

Here z_0 is the range of the potential, i.e., fluid particles are kept approximately at this distance, depending on the actual values of the exerted forces. To be consistent with our other considerations, a half-particle spacing $\Delta x/2$ was used for z_0. The parameter D determines the magnitude of the repulsive forces.

5.4 Results and Discussion

We implemented our novel wall interaction method in the open-source particle code "LIGGGHTS" (www.liggghts.com)[30], which is a modularly-organized particle simulator that incorporates SPH and other particle-based simulation approaches. For the time integration, the SPH module of LIGGGHTS employs the often-used second-order Verlet algorithm, as described, e.g., by Monaghan[1].

In our simulations, rather than using boundary particles, we represented the walls as a set of triangles imported from an STL-mesh. To distinguish them from boundary particles, we termed the continuous walls "STL-walls." For particles in the vicinity of the STL-wall, the required dimensionless boundary contributions were calculated by the determined polynomials Eqs. 5.25 and 5.26 using the closest distance of the considered fluid particle to the wall surface (i.e., the distance perpendicular to the closest triangle or the distance to an edge or corner). These were converted into the physical boundary contributions by Eqs. 5.17, 5.20 and 5.28. As only the closest distance to the wall surface determines the interaction, the size and shape of the wall triangles is not critical for the results.

To validate the results, we considered four cases in detail, each with boundary particles and STL-walls for comparison purposes (for an overview, see Table 5.1). Case 1 represents the shear flow in a channel between two parallel walls (see Figure 5.5), one steady and one moving in the x-direction (so-called Couette flow). Similarly, case 2 describes the

pressure-driven flow between two parallel, steady walls (Poiseuille flow). The cases 3 and 4 are analogous to 1 and 2, however, including a ridge which extends into the flow from one channel wall (see Figure 5.7).

Table 5.1: Case parameters (Setup I: Figure 5.5, Setup II: Figure 5.10).

Case	Setup	V_0 [m/s]	a_x [m/s²]	*Re*
1	I	0.1	0	1.00
2	I	0	10	0.41
3	II	0.1	0	0.60
4	II	0	10	0.12

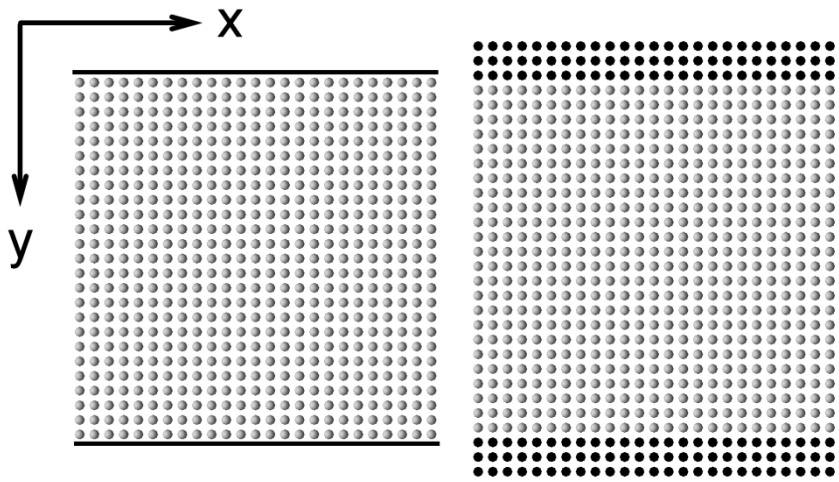

Figure 5.5: Particle setup I with boundary particles (right) and STL-walls (left).

In cases 1 and 2, we used the particle setup I shown in Figure 5.5 with boundary particles (right) and STL-walls (left). The setup extended over 5 particles in the *z*-direction, and the boundaries in the *x*- and *z*-directions were periodic. The channel width was $H = 5$ mm both for boundary particles and STL-walls, and the particle spacing was $\Delta x = 0.2$ mm. Due to the different arrangement of the particles adjacent to the wall surface, this resulted in 25 particles across the channel for the STL-walls and 24 for the boundary particles. The smoothing length was $h = 0.24$ mm (according to Eq. 5.13), the fluid density was $\rho = 1000$ kg/m³, the viscosity was $\mu = 0.5$ Pas, and the speed of sound $c = 10$ m/s was found to

satisfy the criteria of Eq. 5.4. Based on these parameters, a time step of $1 \cdot 10^{-6}$s was used (Eq. 5.14).

In case 1 we used a velocity of V_0 = 0.1 m/s in the x-direction at the lower wall (Couette flow), resulting in a Reynolds number of 1. The transient development of the flow was compared to the analytical solution (where ν is the kinematic viscosity):[31]

$$v(y,t) = V_0 \sum_{n=0}^{\infty} \left[\operatorname{erfc}\left(2n\eta_h + \eta\right) + \operatorname{erfc}\left(2(n+1)\eta_h - \eta\right) \right] \tag{5.32}$$

with $\eta = \dfrac{y}{2\sqrt{\nu t}}$ and $\eta_h = \dfrac{H}{2\sqrt{\nu t}}$

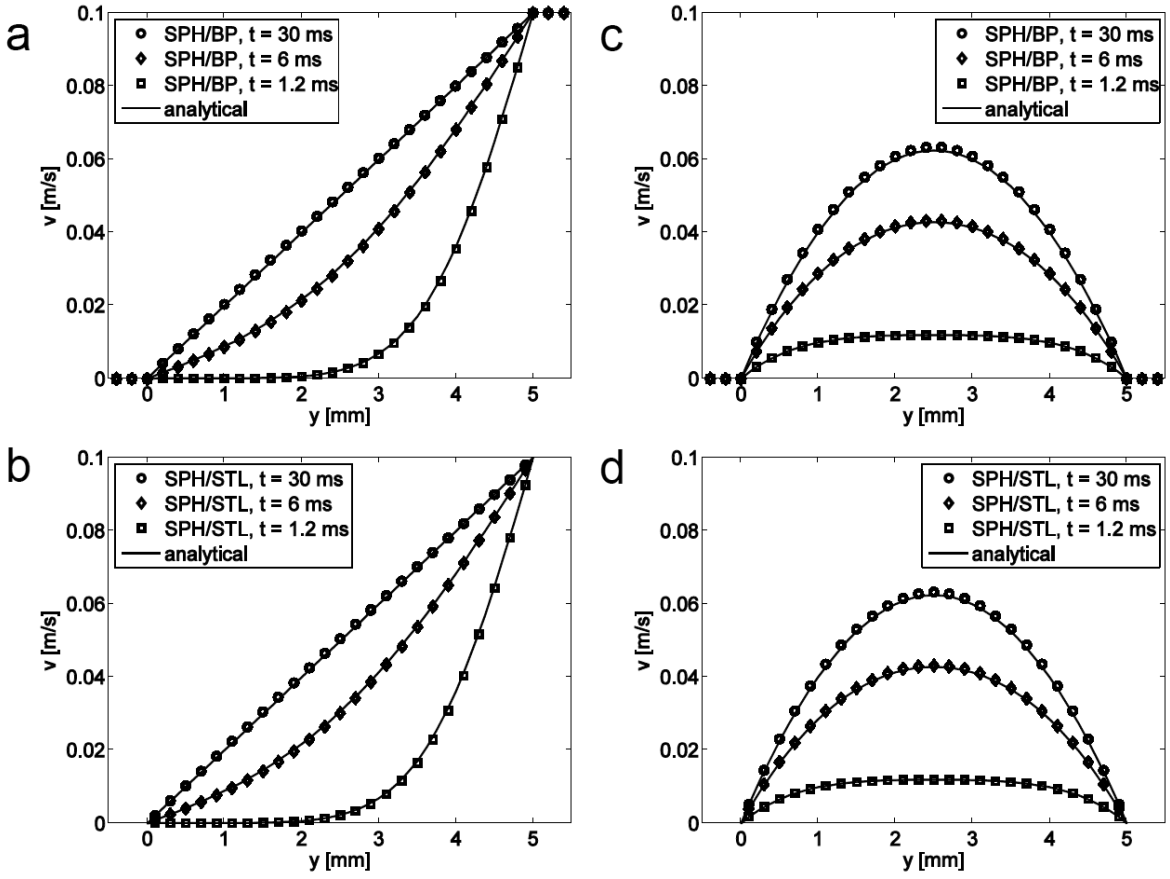

Figure 5.6: Velocity profiles of the transient flow obtained from SPH (symbols) compared to the analytical solution (lines) for a) Couette flow (case 1) with boundary particles, b) Couette flow (case 1) with STL-walls, c) Poiseuille flow (case 2) with boundary particles, d) Poiseuille flow (case 2) with STL-walls using the cubic spline kernel (Eq. 5.12).

The results for case 1 are shown in Figure 5.6a for the boundary particles and in Figure 5.6b for the STL-walls at three times (1.2 ms, 6 ms and 30 ms) after the lower plate began to move, the last one being the steady-state solution. The symbols indicate the actual particle velocities versus the *y*-coordinate (which were constant along the *x* and *z*-coordinates). The SPH results were in good agreement with the analytical solution for the boundary particles and STL-walls. Clearly, the proposed wall interaction for the STL-walls led to the same results as the boundary particles.

Using the same setup, we simulated the transient Poiseuille flow driven by a body force in the *x*-direction of a_x = 10 m/s² (case 2), and compared the results to the following analytical solution:[27]

$$v(y,t) = \frac{a_x}{2\nu} y(y-H) + \sum_{n=0}^{\infty} \frac{4a_x H^2}{\nu\pi^3(2n+1)^3} sin\left(\frac{\pi y}{H}(2n+1)\right) exp\left(-\frac{(2n+1)^2\pi^2\nu}{H^2}t\right) \qquad (5.33)$$

The resulting velocity profiles are shown in Figure 5.6c for the boundary particles and Figure 5.6d for the STL-walls for 1.2 ms, 6 ms and 30 ms after the movement began (30 ms being the steady-state solution). Analogous to case 1, the symbols indicate the actual particle velocities versus the *y*-coordinate, which were independent of the *x* and *z*-coordinates. The obtained Reynolds number was 0.41, using the average velocity in the channel. Similarly to the Couette flow case, the SPH results were in excellent agreement with the analytical solution. In this instance, the SPH velocity profiles were slightly larger compared to the analytical solution, which was also reported by Morris et al.[27]. However, the profiles obtained with boundary particles and STL-walls were not significantly different.

Our new wall interaction method was developed for a planar wall. We recorded information regarding the wall's contributions as polynomial fits that depended on the distance to the wall, which meant that applying them to arbitrarily-shaped surfaces with edges and corners would be a simplification. In the most extreme case a particle in the vicinity of an edge would have the same boundary contributions as a particle in the vicinity of a planar wall at equal distance to the wall/edge, which is not the case for boundary particles. To determine if this simplification leads to significant errors, we considered two

cases that were similar to cases 1 and 2 but with a ridge extending into the channel. This setup II is shown in Figure 5.7 for the boundary particles (right) and the STL-walls (left). We used periodic boundaries in the *x* and *z*-directions and the same parameters (i.e., particle spacing, smoothing length, fluid density and viscosity) as in cases 1 and 2.

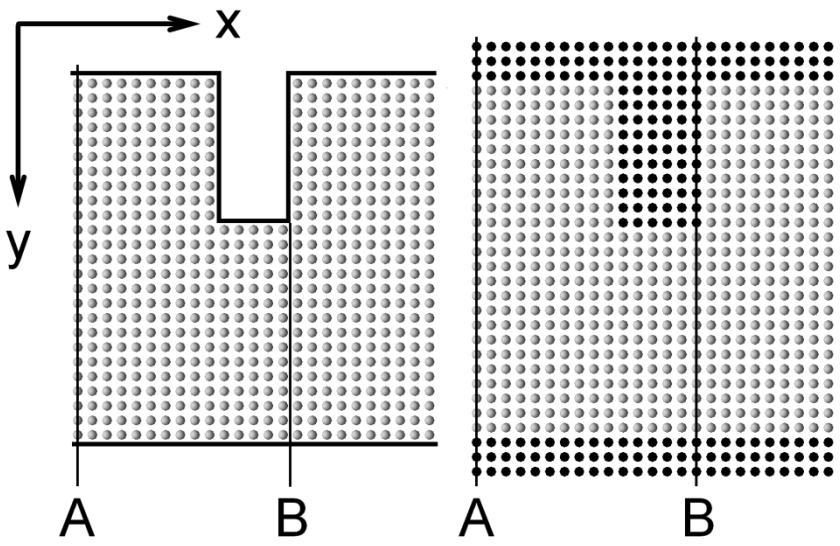

Figure 5.7: Particle setup II for the channel flow, including a ridge, for boundary particles (right) and STL-walls (left). At cross-sections A and B we determined velocity profiles.

In case 3 a velocity of 0.1 m/s was used for the lower wall and the transient flow similar to the Couette flow was simulated. Defining the Reynolds number with the channel width at the bottleneck (3 mm), Re = 0.6 was obtained. We determined the velocity profiles in cross-sections A and B at 0.6 ms, 3 ms and 15 ms after the movement of the lower wall began (15 ms being the steady-state solution) and compared the results for the boundary particles and the STL-walls (see Figure 5.8a and Figure 5.8b). For the lack of an analytical solution, both cases are compared directly now. For cases 3 and 4, the shown profiles indicate the actual velocities of the particles next to the cross-sections A and B (which were constant along the *z*-coordinate).

For the Poiseuille flow, in case 4 we simulated setup II with a body force of 10 m/s² in the *x*- direction and showed the velocity profiles in cross-sections A and B in Figure 5.8c and Figure 5.8d for the boundary particles and STL-walls (for 0.6 ms, 3 ms and 15 ms). A Reynolds number of 0.12 resulted, using the channel width at the bottleneck (3mm) and the

corresponding average velocity. The results confirmed that the edges created negligible errors when the STL-walls were used.

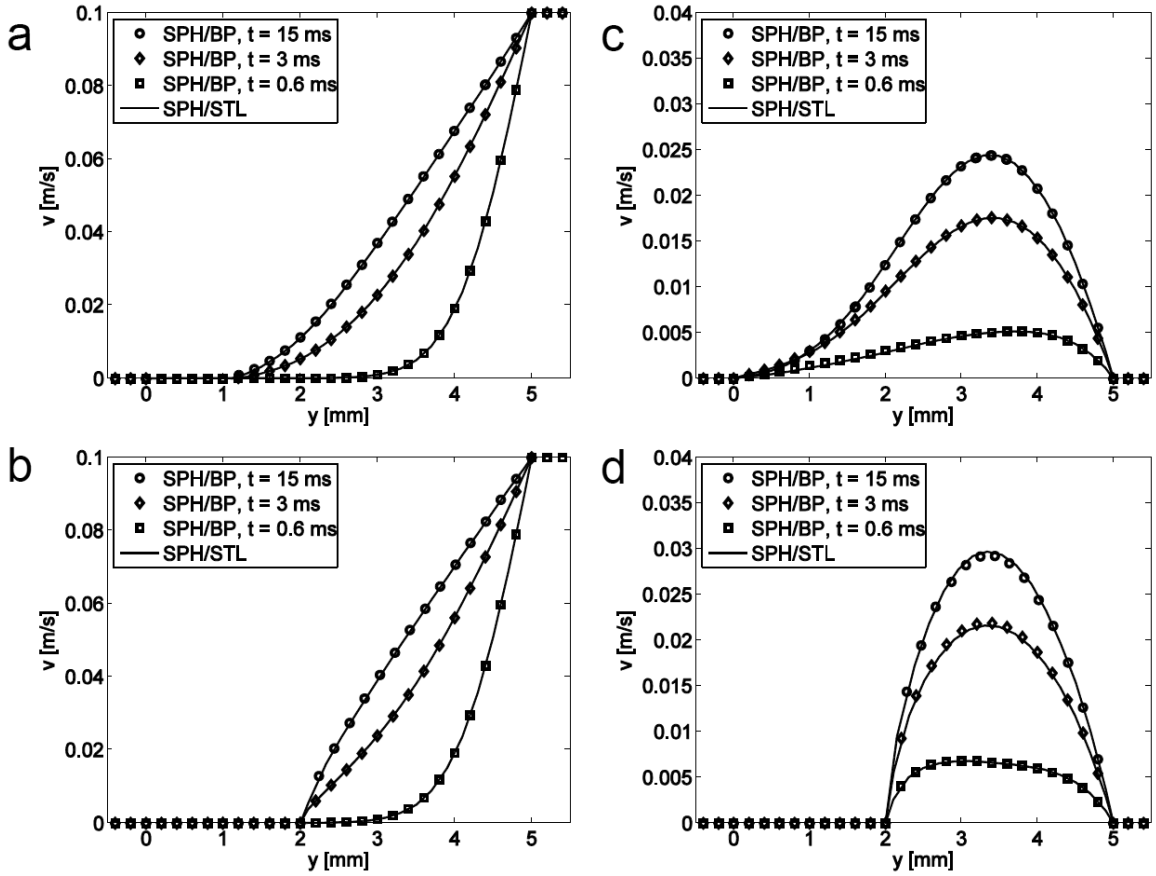

Figure 5.8: Velocity profiles for the transient flow obtained from SPH with boundary particles (symbols) and STL-walls (lines) for a) case 3, cross-section A, b) case 3, cross-section B, c) case 4, cross-section A, d) case 4, cross-section B.

For the results above we used the smoothing length $h = 1.2\Delta x$, which was presumed for the development of the dimensionless boundary contributions. However, we argued that these can also be applied to a different ratio $h/\Delta x$. Thus, we simulated the test cases 1 and 2 again with $h = 1.5\Delta x$, correcting the polynomials as proposed in Eqs. 5.29 and 5.30. The resulting velocity profiles after 1.2 ms, 6 ms and 30 ms are shown in Figure 5.9 compared to the analytical solution. The excellent agreement shows that our proposed way of applying the polynomials to a different smoothing length is correct.

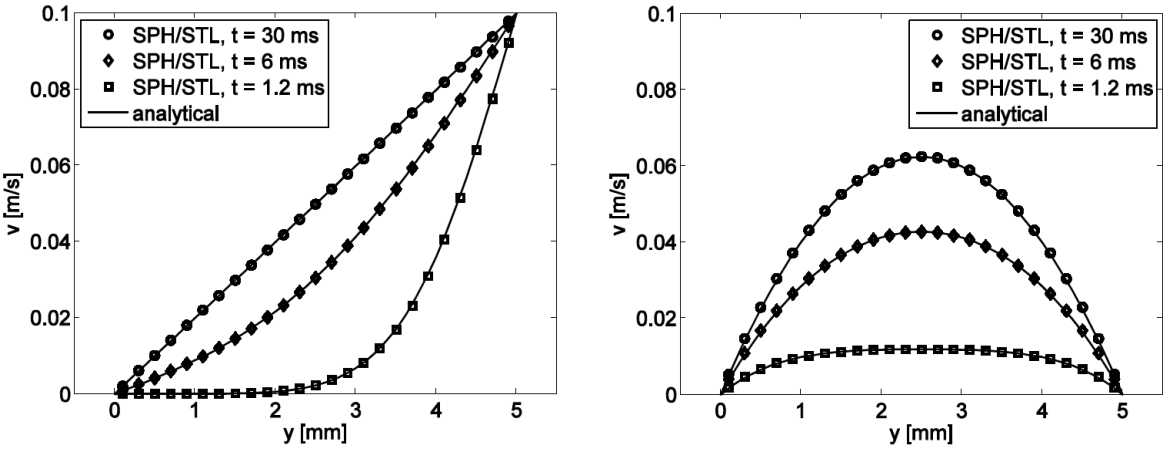

Figure 5.9: Velocity profiles of the transient flow obtained from SPH with STL-walls (symbols) compared to the analytical solution (lines) with a smoothing length $h = 1.5\Delta x$ for the Couette flow (case 1, left) and the Poiseuille flow (case 2, right).

As presented in detail above, the dimensionless wall contributions have been developed based on the cubic spline kernel. For the application of other kernel functions, the wall contributions have to be determined in an analogous way. However, since most kernel functions have a similar shape, we expect that the application of our developed polynomials to simulations with other kernel functions could be a reasonable approximation (depending on the considered kernel function). To test our conjecture we simulated the test cases 1 and 2 also with a fifth order Wendland kernel[11] and a spiky kernel of third order[32]:

$$W\left(|\vec{r}_{ab}|,h\right)=\frac{21}{16^2\pi h^3}\begin{cases}\left(2-\dfrac{|\vec{r}_{ab}|}{h}\right)^4\left(2\dfrac{|\vec{r}_{ab}|}{h}+1\right) & 0\le\dfrac{|\vec{r}_{ab}|}{h}<2\\ 0 & 2\le\dfrac{|\vec{r}_{ab}|}{h}\end{cases} \tag{5.34}$$

$$W\left(|\vec{r}_{ab}|,h\right)=\frac{15}{64\pi h^3}\begin{cases}\left(2-\dfrac{|\vec{r}_{ab}|}{h}\right)^3 & 0\le\dfrac{|\vec{r}_{ab}|}{h}<2\\ 0 & 2\le\dfrac{|\vec{r}_{ab}|}{h}\end{cases} \tag{5.35}$$

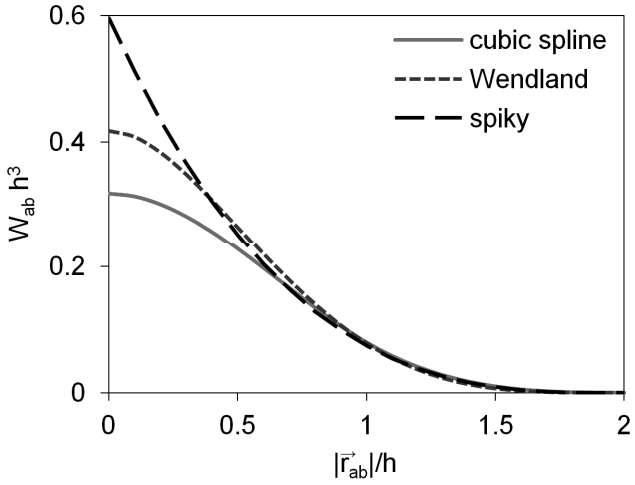

Figure 5.10: Plots of the used kernel functions (cubic spline kernel Eq. 5.12, Wendland kernel Eq. 5.32, spiky kernel Eq. 5.33).

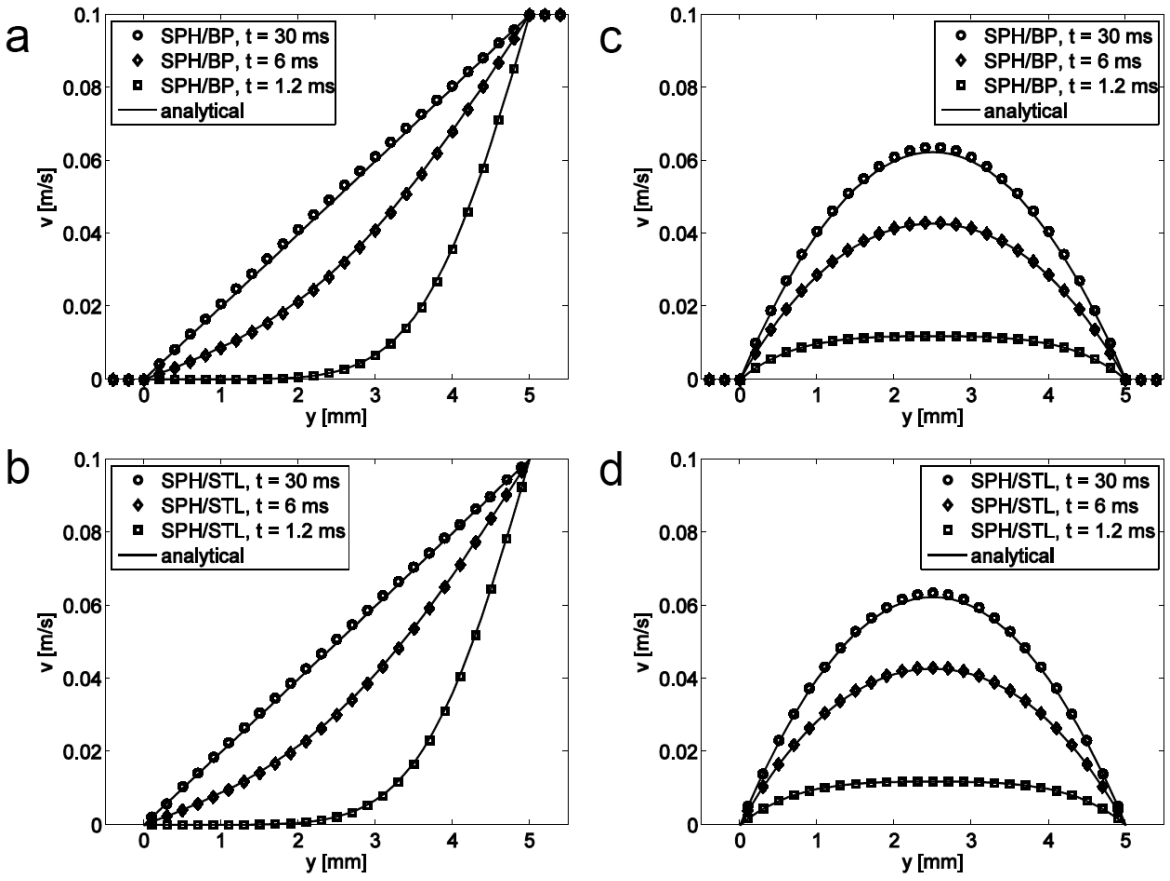

Figure 5.11: Velocity profiles of the transient flow obtained from SPH (symbols) compared to the analytical solution (lines) for a) Couette flow (case 1) with boundary particles, b) Couette flow (case 1) with STL-walls, c) Poiseuille flow (case 2) with boundary particles, d) Poiseuille flow (case 2) with STL-walls using the Wendland kernel (Eq. 5.32).

All kernel functions are illustrated in Figure 5.10. The resulting velocity profiles for the Wendland kernel are shown in Figure 5.11 and for the spiky kernel in Figure 5.12. The impact of the changed kernel is very small in both cases. For the Wendland kernel the velocity profiles show a good agreement with the analytical solution, while for the spiky kernel the velocity is slightly overestimated in case of the Poiseuille flow (case 2), and small disturbances are obvious in the Couette flow profiles (case 1) near the walls.

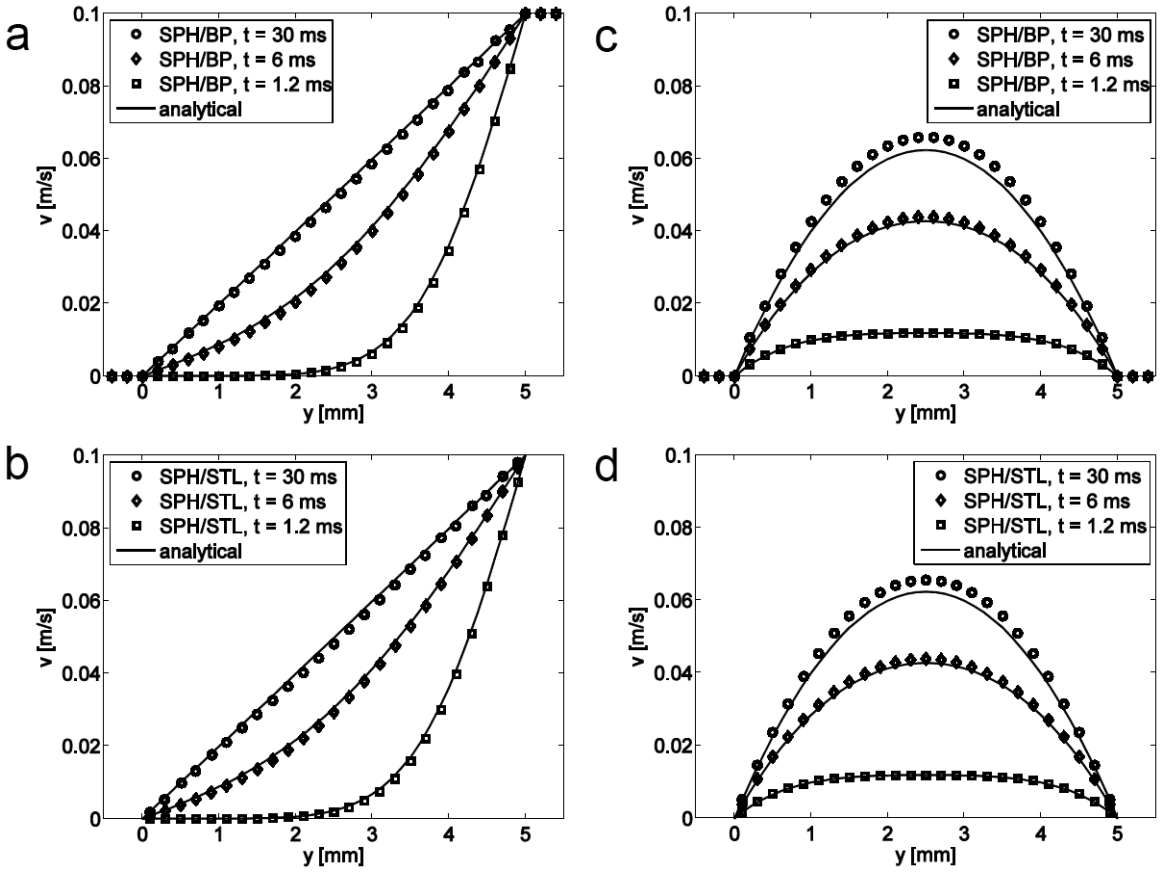

Figure 5.12: Velocity profiles of the transient flow obtained from SPH (symbols) compared to the analytical solution (lines) for a) Couette flow (case 1) with boundary particles, b) Couette flow (case 1) with STL-walls, c) Poiseuille flow (case 2) with boundary particles, d) Poiseuille flow (case 2) with STL-walls using the spiky kernel (Eq. 5.33).

Interestingly, these deviations occur for STL-walls as well as for boundary particles. Clearly, in the case of boundary particles the respective kernel was used for both, fluid and boundary particles. Thus, the disturbances are not caused by the applied STL-wall interaction. However, the spiky kernel itself seems to be the reason for the observed

deviations. Hence, reasonable results can be expected for the application of our method to other kernel functions, at least if they have a shape similar to the shown functions.

To test if the proposed method could be applied to more complex cases, we simulated the mixing experiments of Avalosse and Crochet[7] for a co-rotating twin-cam mixer in two geometries: first, with two circular cams and, second, with two triangular cams, each with counter-clockwise rotation of n = 0.5 rpm (see Figure 5.13). A Newtonian fluid with a density of ρ = 1500 kg/m³ and a viscosity of μ = 50 Pas was used, yielding a Reynolds number of $9 \cdot 10^{-4}$ (based on the barrel diameter D = 60 mm: $Re = nD^2\rho/\mu$). To visualize the mixing effect caused by the rotation of the cams, a color tracer that initially formed a rectangular pattern was inserted into the transparent fluid (see the initial configurations in Figure 5.14 and Figure 5.15, top left).

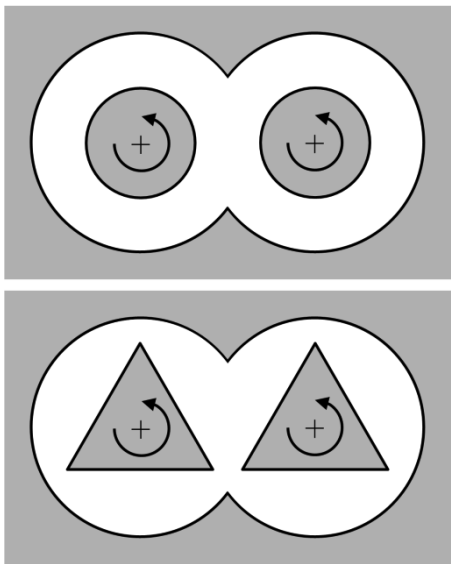

Figure 5.13: Schematic of the twin-cam mixer with circular cams (top) and triangular cams (bottom).

We simulated both experiments using SPH (with the STL-walls) and the proposed wall interaction method. Since this is a 2D problem and our approach involved a 3D smoothing kernel, to guarantee a sufficient number of neighbors in all directions we chose the thickness of 2 particles and periodic boundaries in the normal direction. The smoothing length was 0.3 mm and the initial particle spacing was 0.25 mm, resulting in the total of about 125.000 particles in both cases. For time-step purposes, we set the viscosity a factor of 10^{-4} lower than in the experiment (0.005 Pas, yielding a Reynolds number of 9), since

the flow field does not depend on the viscosity value in the Stokes regime (i.e., when inertia forces are negligible). Although the limit of the Stokes regime is not exactly known in this case, Pawlowski[33] found experimentally that for another type of rotor-stator mixer (a single screw extruder) it was above Re = 40 (using the analogous definition). We assumed Re = 9 to be in the Stokes regime in our case, which was supported by the results of Robinson et al.[3] who reported no distinguishable effects on the results when simulating the twin-cam mixer with SPH at Reynolds numbers of up to Re = 9. We established that a speed of sound c = 0.05 m/s was sufficient for Eq. 5.4 and used a time step of $1 \cdot 10^{-3}$ s (according to Eq. 5.14).

Snapshots of our simulation of the circular cams are shown in Figure 5.14 (0 – 4 revolutions). It was in good agreement with the experimental and FEM results of Avalosse and Crochet[7]. Snapshots of the triangular cams are shown in Figure 5.15 (0 – 5/3 revolutions). Again, they agreed well with the experimental and FEM results of Avalosse and Crochet[7], the FEM results of Bertrand et al.[4] and the SPH results of Robinson et al.[3] who used the boundary particle method, yet with a different implementation.

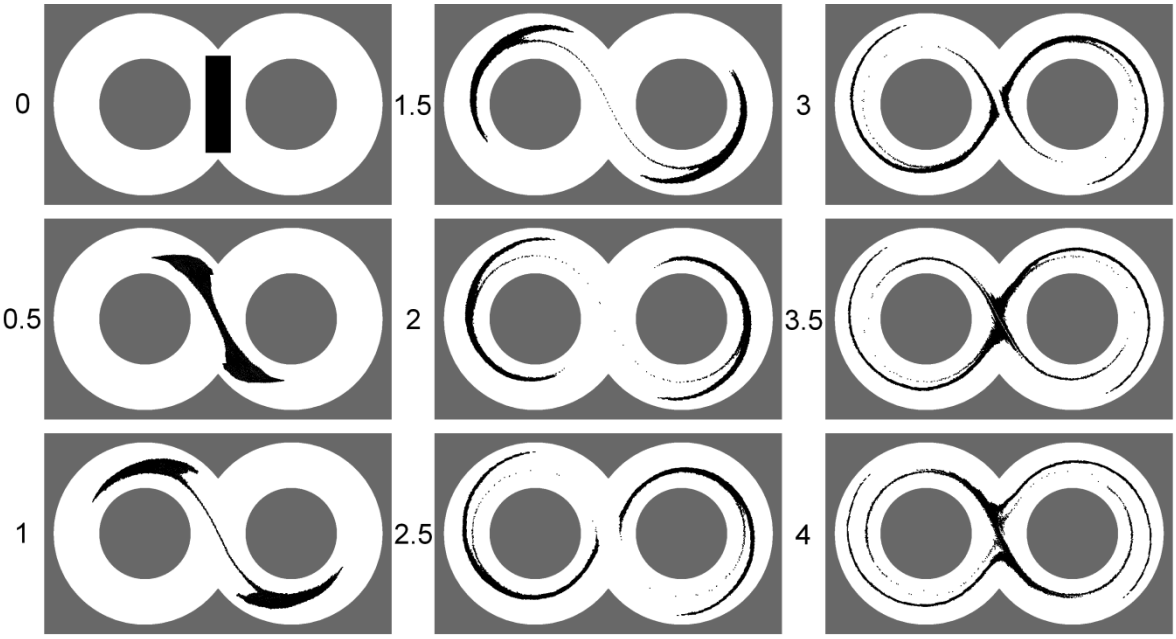

Figure 5.14: Snapshots of the tracer during the counter-clockwise rotation of the circular mixing cams for 0 – 4 revolutions.

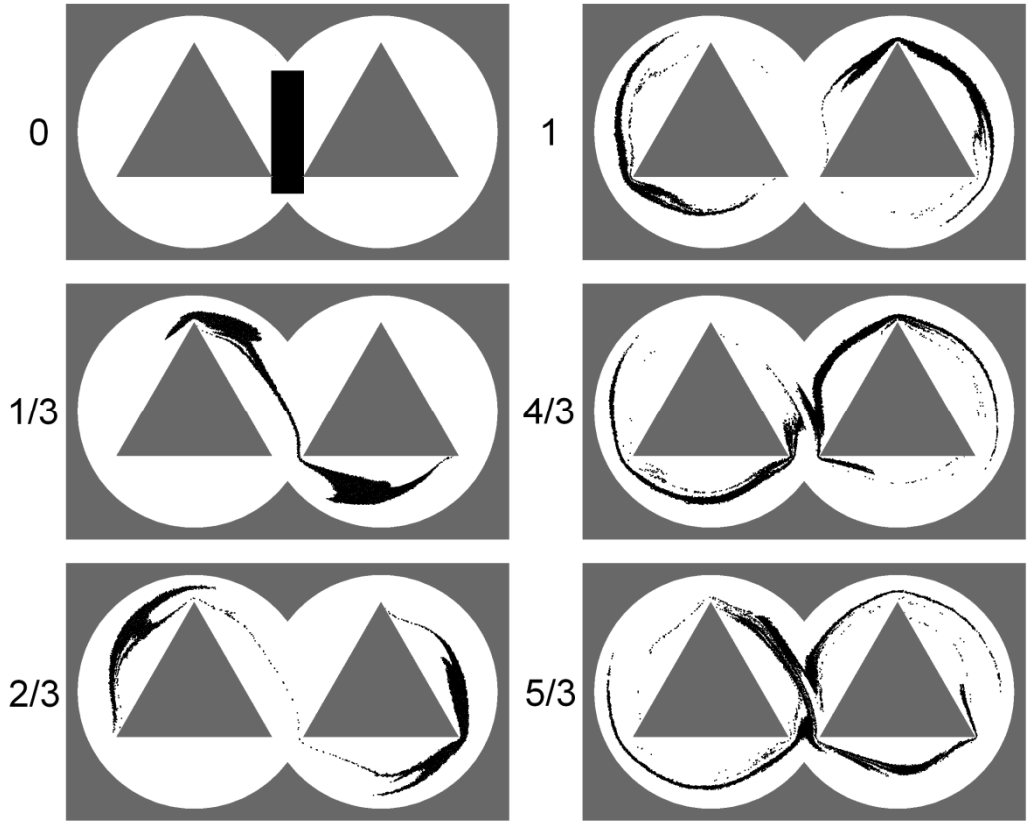

Figure 5.15: Snapshots of the tracer during the counter-clockwise rotation of the triangular mixing cams for 0 – 5/3 revolutions.

5.5 Summary and Conclusions

This work presents a novel method of modeling solid wall boundary conditions for laminar flow in SPH without additional particles, which is suitable for complex wall geometries imported from CAD programs (e.g., in the STL-format). Using the boundary particle method, we determined the contributions of boundary particles to a single fluid particle in the vicinity of a planar wall by moving the fluid particle along the wall and recording the forces exerted on it. This information was compiled into polynomial fits of the boundary contributions based on the wall distance in a dimensionless form. These expressions are independent of problem-specific parameters in order to allow for a general applicability using arbitrary parameter values, such as density, viscosity, and resolution. We ensured the exact no-slip condition at the wall and added repulsive forces to completely avoid wall penetration. With the obtained polynomials, we could immediately calculate the boundary contributions of fluid particles based on their distance from the wall, without having to

account for the complicated arrangement between boundary particles in the complex wall geometry or to mirror ghost particles over walls, including edges and corners.

To validate the new method, we applied unsteady velocity profiles for the channel flow driven by pressure (the Poiseuille flow) and the drag of a moving wall (the Couette flow). Both of the flows were investigated using boundary particles and STL-walls for laminar conditions, and each one was in good agreement with the corresponding analytical solution. To account for the effect that edges have on the flow field for our developed wall interaction, we added a ridge extending into the channel. The results for the boundary particles and STL-walls were in good agreement, indicating that errors around edges failed to significantly affect the entire flow field.

To test a more complex case, we applied our method to simulate the laminar flow in a twin-cam mixer according to the experiments of Avalosse and Crochet[7]. The resulting time-evolution of the mixing pattern was in good agreement with the experimental and numerical results of Avalosse and Crochet[7], Bertrand et al.[4] and Robinson et al[3].

The proposed method could be used to efficiently treat complex-shaped STL-surfaces in SPH. It shows correct results for laminar flow along planar walls and around edges. Although the method was developed for a constant ratio of smoothing length to initial particle spacing, we showed how it can be correctly applied to different smoothing lengths. Thus, it is applicable for simulations with variable resolution and smoothing length.

Moreover, the shown polynomials were developed for the underlying set of SPH equations and the kernel function (i.e., the SPH formulation of Monaghan including the continuity equation for the density, the Morris viscosity model and the cubic spline kernel). Additionally to that, we provided the respective polynomials for the density summation equation and the artificial viscosity model in the Appendix A. For other models the polynomials can be determined in a similar way – if required (i.e., the obtained dimensionless expressions appear more than once, e.g., we found the dimensionless expression of the continuity equation equally in the pressure term of the momentum equation). For other kernel functions, analogous polynomials can be determined in the same manner. However, as we showed for two different kernel functions, the errors due to

the provided polynomials based on the cubic spline kernel were vanishing. For any other kernels, the applicability can be easily investigated with the shown test cases. Nevertheless, the cubic spline kernel is one of the most frequently used kernels, and in many application cases a variation of the kernel function is of minor significance.

5.6 Abbreviations

1D	one-dimensional
2D	two-dimensional
3D	three-dimensional
BP	boundary particles
FEM	finite element method
FVM	finite volume method
SPH	smoothed particle hydrodynamics
STL	surface tessellation language

5.7 Nomenclature

Latin symbols

B	parameter in the equation of state [Pa]
c	speed of sound [m/s]
D	parameter for the repulsive wall force [N]
d	number of spatial dimensions [-]
f_{ab}	parameter used in the tensile correction [-]
$F_{\nabla W}$	dimensionless boundary contribution for continuity equation and pressure term [-]
$\widetilde{F}_{\nabla W}$	dimensionless boundary contribution for continuity equation and pressure term, generalized for variable smoothing length [-]
$F_{\nabla W/r}$	dimensionless boundary contribution for the viscous term [-]
$\widetilde{F}_{\nabla W/r}$	dimensionless boundary contribution for the viscous term, generalized for variable smoothing length [-]
F_{rep}	repulsive wall force [N]
h	smoothing length [m]

m_a	mass of particle *a* [kg]
P_a	pressure of particle *a* [Pa]
$\vec{r}_a$	position of particle *a* [m]
R	parameter used in the tensile correction [$m^5/kg\ s^2$]
Re	Reynolds number [-]
$\vec{v}_a$	velocity of particle *a* [m/s]
$v_{a,\tan}$	velocity component tangential to the wall [m/s]
$v_{a,\tan}^{corr}$	corrected velocity component tangential to the wall [m/s]
$W_{ab} = W\left(\lvert\vec{r}_{ab}\rvert, h\right)$	kernel function evaluated for particles *a* and *b* [m^{-3}]
z	wall distance [m]
$z^* = z/h$	dimensionless wall distance [-]
z_0	interaction length of the repulsive wall force [m]

Greek symbols

γ	exponent in the equation of state [-]
Δx	particle spacing [m]
μ_a	viscosity of particle *a* [Pas]
Π_{ab}	artificial viscosity term [$m^5/kg\ s^2$]
ρ_a	density of particle *a* [kg/m^3]
ρ_0	reference density in the equation of state [kg/m^3]
σ	normalization parameter in the kernel function [-]

5.8 References

(1) Monaghan, J. J. Smoothed Particle Hydrodynamics. *Reports Prog. Phys.* **2005**, *68*, 1703–1759.

(2) Monaghan, J. J. Simulating Free Surface Flows with SPH. *J. Comput. Phys.* **1994**, *110*, 339–406.

(3) Robinson, M.; Cleary, P.; Monaghan, J. Analysis of Mixing in a Twin Cam Mixer Using Smoothed Particle Hydrodynamics. *AIChE J.* **2008**, *54*, 1987–1998.

(4) Bertrand, F.; Thibault, F.; Delamare, L.; Tanguy, P. A. Adaptive Finite Element Simulations of Fluid Flow in Twin-Screw Extruders. *Comput. Chem. Eng.* **2003**, *27*, 491–500.

(5) Barrera, M. A.; Vega, J. F.; Martínez-Salazar, J. Three-Dimensional Modelling of Flow Curves in Co-Rotating Twin-Screw Extruder Elements. *J. Mater. Process. Technol.* **2008**, *197*, 221–224.

(6) Bierdel, M. Computational Fluid Dynamics. In *Co-Rotating Twin-Screw Extruders*; Kohlgrüber, K., Ed.; Carl Hanser Publishers: Munich, 2008.

(7) Avalosse, T.; Crochet, M. J. Finite-Element Simulation of Mixing: 1. Two-Dimensional Flow in Periodic Geometry. *AIChE J.* **1997**, *43*, 577–587.

(8) Cleary, P. W.; Robinson, M. Understanding Viscous Fluid Transport and Mixing in a Twin-Screw Extruder. In *8th International Conference on CFD in Oil & Gas, Metallurgical and Process Industries*; Trondheim, Norway, 2011.

(9) Robinson, M.; Cleary, P. W. Flow and Mixing Performance in Helical Ribbon Mixers. *Chem. Eng. Sci.* **2012**, *84*, 382–398.

(10) Monaghan, J. J.; Kajtar, J. B. SPH Particle Boundary Forces for Arbitrary Boundaries. *Comput. Phys. Commun.* **2009**, *180*, 1811–1820.

(11) Gomez-Gesteira, M.; Rogers, B. D.; Dalrymple, R. A.; Crespo, A. J. C.; Narayanaswamy, M. *User Guide for the SPHysics Code*; 2010.

(12) Dalrymple, R. A.; Knio, O. SPH Modelling of Water Waves. *Coast. Dyn.* **2001**, 779–787.

(13) M. Gómez-Gesteira; Dalrymple, R. A. Using a Three-Dimensional Smoothed Particle Hydrodynamics Method for Wave Impact on a Tall Structure. *J. Waterw. Port, Coast. Ocean Eng.* **2004**, *130*, 63–69.

(14) Takeda, H.; Miyama, S. M.; Sekiya, M. Numerical Simulation of Viscous Flow by Smoothed Particle Hydrodynamics. *Prog. Theor. Phys.* **1994**, *92*, 939–960.

(15) Randles, P. W.; Libersky, L. D. Smoothed Particle Hydrodynamics : Some Recent Improvements and Applications. *Comput. Methods Appl. Mech. Eng.* **1996**, *139*, 375–408.

(16) Colagrossi, A.; Landrini, M. Numerical Simulation of Interfacial Flows by Smoothed Particle Hydrodynamics. *J. Comput. Phys.* **2003**, *191*, 448–475.

(17) De Leffe, M.; Le Touzé, D.; Alessandrini, B. A Modified No-Slip Condition in Weakly-Compressible SPH. In *6th International SPHERIC Workshop*; Rung, T.; Ulrich, C., Eds.; Schriftenreihe Schiffbau: Hamburg, 2011; pp. 291–297.

(18) Børve, S. Generalized Ghost Particle Method for Handling Boundaries. In *6th International SPHERIC Workshop*; Rung, T.; Ulrich, C., Eds.; Schriftenreihe Schiffbau: Hamburg, 2011; pp. 313–320.

(19) Feldman, J.; Bonet, J. Dynamic Refinement and Boundary Contact Forces in SPH with Applications in Fluid Flow Problems. *Int. J. Numer. Methods Eng.* **2007**, *72*, 295–324.

(20) Ferrand, M.; Violeau, D.; Rogers, B. D.; Laurence, D. Consistent Wall Boundary Treatment for Laminar and Turbulent Flows in SPH. In *6th International SPHERIC Workshop*; Rung, T.; Ulrich, C., Eds.; Schriftenreihe Schiffbau: Hamburg, 2011; pp. 275–282.

(21) González, L. M.; Souto-Iglesias, A.; Macià, F.; Colagrossi, A.; Antuono, M. On the No-Slip Boundary Condition Enforcement in SPH Methods. In *6th International SPHERIC Workshop*; Rung, T.; Ulrich, C., Eds.; Schriftenreihe Schiffbau: Hamburg, 2011; pp. 283–290.

(22) Groenenboom, P. H. L. A Unified View of SPH Wall Boundary Conditions and Particle Motion Correction Methods. In *6th International SPHERIC Workshop*; Rung, T.; Ulrich, C., Eds.; Schriftenreihe Schiffbau: Hamburg, 2011; pp. 305–312.

(23) Gomez-Gesteira, M.; Rogers, B. D.; Dalrymple, R. A.; Crespo, A. J. C. Numerical Simulation of Interfacial Flows by Smoothed Particle Hydrodynamics. *J. Hydraul. Res.* **2010**, *48*, 6–27.

(24) Kruisbrink, A. C. H.; Pearce, F. R.; Yue, T.; Cliffe, K. A.; H. P. Morvan. *SPH Concepts for Continuous Wall and Pressure Boundaries*; Rung, T.; Ulrich, C., Eds.; Schriftenreihe Schiffbau: Hamburg, 2011; pp. 298–304.

(25) Monaghan, J. J. Smoothed Particle Hydrodynamics. *Annu. Rev. Astron. Astrophys.* **1992**, *30*, 543–574.

(26) Monaghan, J. J. SPH without a Tensile Instability. *J. Comput. Phys.* **2000**, *159*, 290–311.

(27) Morris, J. P.; Fox, P. J.; Zhu, Y. Modeling Low Reynolds Number Incompressible Flows Using SPH. *J. Comput. Phys.* **1997**, *136*, 214–226.

(28) Liu, G.-R.; Liu, M. B. *Smoothed Particle Hydrodynamics: A Meshfree Particle Method*; Liu, G.-R.; Liu, M. B., Eds.; World Scientific Publishing Co. Pte. Ltd.: Singapore, 2003.

(29) Price, D. J. Smoothed Particle Hydrodynamics and Magnetohydrodynamics. *J. Comput. Phys.* **2012**, *231*, 759–794.

(30) Kloss, C.; Goniva, C.; Hager, A.; Amberger, S.; Pirker, S. Models, Algorithms and Validation for Opensource DEM and CFD-DEM. *Prog. Comput. Fluid Dyn. An Int. J.* **2012**, *12*, 140–152.

(31) Pozorski, J.; Wawrenczuk, A. SPH Computation of Incompressible Viscous Flows. *J. Theor. Appl. Mech.* **2002**, *40*, 917–937.

(32) Müller, M.; Charypar, D.; Gross, M. Particle-Based Fluid Simulation for Interactive Applications. In *Proceedings of the 2003 ACM SIGGRAPH/Eurographics symposium on computer animation (SCA '03)*; Aire-la-Ville, Switzerland, 2003; pp. 154–159.

(33) Pawlowski, J. *Transportvorgänge in Einwellen-Schnecken*; Otto Salle Verlag, Verlag Sauerländer: Aarau, Frankfurt am Main, Salzburg, 1990.

"*Once we accept our limits, we go beyond them.*"

(Albert Einstein)

Co-Rotating Twin-Screw Extruders: Detailed Analysis of Conveying Elements Based on SPH. Part 1: Hydrodynamics*

Due to the complex geometry of the rotating screws and, typically, free surface flows in partially filled screw sections, first principles simulations of the flow in co-rotating intermeshing twin-screw extruders using the well-established, mesh-based CFD (computational fluid dynamics) approaches are highly challenging. These issues can be resolved via the smoothed particle hydrodynamics (SPH) method thanks to its meshless nature and the inherent capability to simulate free surface flows. In our previous work, we developed a novel method for modeling the boundary conditions with complex wall geometries, under which SPH could be efficiently applied to complex surfaces of typical screw geometries of extruders. In this work, we employed SPH and our boundary method to study the flow in a conveying element in detail. To address unresolved clearances, we developed a new model that is coupled to SPH and can correctly account for the flow through unresolved clearances. A validation of our approach using CFD data from the literature for a completely filled conveying element indicated excellent agreement. Consequently, we studied the flow in a partially filled conveying element and obtained results for the flow rate, the power input and the axial force with variable filling ratio. A detailed analysis of the corresponding mixing phenomena is presented in Part 2. Our results show that the proposed method is a comprehensive approach to study the flow in different types of screw elements in detail, providing an excellent basis for further development of simplified models of entire extrusion processes.

---

* This chapter is based on: Eitzlmayr, A.; Khinast, J. Co-Rotating Twin-Screw Extruders: Detailed Analysis of Conveying Elements Based on Smoothed Particle Hydrodynamics. Part 1: Hydrodynamics. Submitted to *Chem. Eng. Sci*.

6.1 Introduction

Developed in the 1940s and 1950s, intermeshing extruders have been widely used in different industries for many decades, for example, to manufacture polymers, chemicals and foodstuffs. The most common type of extrusion devices is the co-rotating, intermeshing twin screw extruder. Its advantages include good mixing performance, self-cleaning screws, short residence time and good product quality. Single-screw extruders are primarily used for melting and pressure build-up and do not have superior mixing properties. Other types of extruders, such as counter-rotating twin-screw, multi-screw or ram extruders, are designed for more specialized applications.[1]

In recent years, extrusion has become increasingly attractive to the pharmaceutical industry with regard to manufacturing of solid drug products.[2] Depending on the materials involved, there are several types of pharmaceutical extrusion processes, such as hot-melt extrusion (HME), hot-melt granulation, wet extrusion and solid lipid extrusion.[3] HME is particularly promising for pharmaceutical applications in terms of increasing the bioavailability of poorly soluble drug molecules and forming solid solutions and amorphous solid dispersions.[4,5] Moreover, since HME is solvent-free, it does not involve costs associated with the solvent, separation, recovery and disposal. Due to its variety of individual screw elements (e.g., conveying elements, kneading elements and mixing elements), the typical modular screw design of co-rotating, intermeshing twin-screw extruders offers almost unlimited options with regard to the actual screw configuration design. Although this allows high operational flexibility, developing an appropriate screw configuration to accommodate the actual process requirements is highly challenging and normally requires extensive experience and/or experimental and empirical work.

In experiments, an extruder is essentially a black box, and accurate measurements of process variables such as the filling ratio and melt temperature are difficult to achieve. Modeling and simulation methods can provide an understanding of the complex flow and mixing phenomena associated with the interaction between the rotating screw geometry, material properties and operation conditions, potentially leading to effective scale-up approaches.

However, extruders are highly complex, witnessed by the fact that no fully resolved first principles simulations of entire twin-screw extruders have been reported to date. There are several reasons: First, free surface flows, which are difficult to model, occur in the partially filled screw sections. Second, the flow behavior of the processed material mixtures is typically complex, mostly non-Newtonian, which requires an extensive amount of measurements for a complete description of the macroscopic properties of the material mixtures. Third, extruders are highly non-isothermal, requiring the coupling between mass, momentum and energy balances. Fourth, due to the small gap between the screws and between the screws and the barrel, the flow needs to be highly resolved. Moreover, a fully resolved simulation of the transition from the granular to the molten state is currently infeasible.

Several simulation approaches for twin-screw extruders exist today, which are mainly divided into one-dimensional (1D) and three-dimensional (3D) methods. The computationally less expensive 1D approach yields an approximate description of the process variables along the screw axes (e.g., filling ratio, pressure, temperature) while neglecting their distributions in radial and azimuthal direction. Here, the flow around the screw geometry is not fully resolved, thus, the 1D approach depends on simplified models (based on first principles), which account for the impact of the actual screw geometry by correlating integral properties of the flow field, for example the flow rate, the axial pressure gradient or the power input. This usually involves empirical parameters which are characteristic for the considered screw element geometries, and have to be determined by fully resolved simulations or experiments. Since the averaging over the cross section involves also the spatial distribution of material properties, e.g., the viscosity, the characteristic screw parameters can also depend on the considered material. However, this simplified method often yields sufficiently accurate predictions that contribute to process understanding and significantly reduce experimental effort. Due to its comparably low computational expense, it is still the only way to develop a simulation of the entire extrusion process. For more detailed information about 1D modeling, please refer to the literature.[6–17]

For first principles simulations of the flow in co-rotating twin-screw extruders, mainly mesh-based CFD (computational fluid dynamics) methods, such as the FEM (finite

element method) and FVM (finite volume method), have been used.[18–34] However, simulating free surface flows in partially filled screw sections remains extremely challenging. To address this issue, Pokriefke[35], for example, used FVM with an Eulerian multiphase model and applied a sophisticated mesh refinement at the free surfaces.

Being mesh-free, the smoothed particle hydrodynamics (SPH) method may be used to simulate partially filled extruders: achieving partial filling requires the same effort as complete filling and mixing phenomena can be observed by tracking tracer particles without additional modeling work. Cleary and Robinson[36] applied SPH to study mixing in a co-rotating twin-screw extruder using boundary particles to model the screw and barrel surfaces.

In this work, we applied SPH to study the hydrodynamics (Part 1) and mixing (Part 2) in a conveying element of a co-rotating twin-screw extruder in completely- and partially-filled states. For the boundary conditions at the wall surfaces, we used a new approach proposed in our previous work[37]. Instead of the classical method of modeling walls in SPH based on particles (e.g., boundary particles and ghost particles), we determined polynomial fits to calculate the interaction of a solid wall with adjacent fluid particles directly from the distances between the wall and the fluid particles. This can be efficiently applied to complex geometries in the *.stl format (surface tessellation language) generated by commonly used CAD (computer aided design) software and, thus, allows a practicable pre-processing strategy for complex geometries in SPH simulations.

6.2 Dimensionless Groups

Pawlowski[38] introduced dimensionless groups to describe the flow in screw machines and, specifically, single-screw extruders. Kohlgrüber[1] applied them to twin-screw extruders based on the assumption that the relevant flow parameters of a completely filled screw element were the barrel diameter D as the measure of the length scale, the fluid viscosity η, the fluid density ρ, the screw speed n, the achieved flow rate $\dot{V}$, the axial pressure drop Δp over the considered length L, the screw driving power P and the axial force F exerted on the screws. By means of dimensional analysis, these nine parameters can be reduced to six dimensionless groups. One of them is the simplex L/D, which is usually neglected by considering an infinitely extended system ($L/D \rightarrow \infty$). The remaining five dimensionless

groups are the Reynolds number $Re = nD^2\rho/\eta$, the dimensionless flow rate $\dot{V}/nD^3$, which can be viewed as throughput per screw revolution (using the screw speed n) relative to the volume of the extruder (represented by the cubed barrel diameter D), the dimensionless axial pressure drop $\Delta pD/\eta nL$ (based on viscosity η and the axial length L), the dimensionless driving power $P/\eta n^2 D^2 L$ and the dimensionless axial force $F/\eta nDL$.

As shown theoretically and experimentally,[38,1] the flow in a completely filled screw element (single- or twin-screw) can be described via correlations of the dimensionless groups: the so-called pressure characteristic $\Delta pD/\eta nL = f_A(Re, \dot{V}/nD^3)$, the power characteristic $P/\eta n^2 D^2 L = f_B(Re, \dot{V}/nD^3)$ and the axial force characteristic $F/\eta nDL = f_C(Re, \dot{V}/nD^3)$. For creeping flows ($Re \rightarrow 0$), which usually occur in extruders due to the high viscosities, the dependency on the Reynolds number vanishes. Thus, for the specific case of a Newtonian temperature-independent fluid under the creeping flow conditions these correlations are characteristic for the geometry of the considered screw element in the dimensionless form (as they do not depend on the length scale, viscosity and screw speed). Moreover, in this case, the correlations are linear due to the linearity of the Stokes equations valid for creeping flows. Then they can be described by the axis intercepts of the power characteristic (A_1, A_2), pressure characteristic (B_1, B_2) and axial force characteristic (C_1, C_2)[38,1]:

$$\frac{\Delta pD}{\eta nL} = A_2 \cdot \left(1 - \frac{1}{A_1}\frac{\dot{V}}{nD^3}\right) \tag{6.1}$$

$$\frac{P}{\eta n^2 D^2 L} = B_2 \cdot \left(1 - \frac{1}{B_1}\frac{\dot{V}}{nD^3}\right) \tag{6.2}$$

$$\frac{F}{\eta nDL} = C_2 \cdot \left(1 - \frac{1}{C_1}\frac{\dot{V}}{nD^3}\right) \tag{6.3}$$

Specifically, parameter A_1 represents the dimensionless flow rate in a completely filled screw element without backpressure, which is termed “inherent conveying capacity”. Similarly, the parameters B_1 and C_1 are the dimensionless flow rates at zero driving power and zero axial force, which are less relevant for practical applications. The parameters A_2,

B_2 and C_2 represent the dimensionless pressure drop, driving power and axial force at zero flow rate, i.e., when conveying against a closed die.

6.3 Reference Case and Geometry

To validate the results of the SPH simulation, we used the results of FVM simulations of a two-flighted conveying element of a co-rotating twin-screw extruder in the completely filled state reported by Bierdel[23], who specifically described the pressure characteristic (Eq. 6.1) and the power characteristic (Eq. 6.2) of this element. The geometry is illustrated in Figure 6.1. The outer screw diameter is D_o = 60 mm, the inner screw diameter is D_i = 38 mm, the centerline distance is C = 50 mm and the barrel diameter is D = 61 mm (thus, the clearance distances are 0.5 mm between the screw and the barrel and 1 mm between the screws). The pitch is T_S = 120 mm, the length is half of the pitch (L = 60 mm) and periodic boundaries were applied in the z-direction.

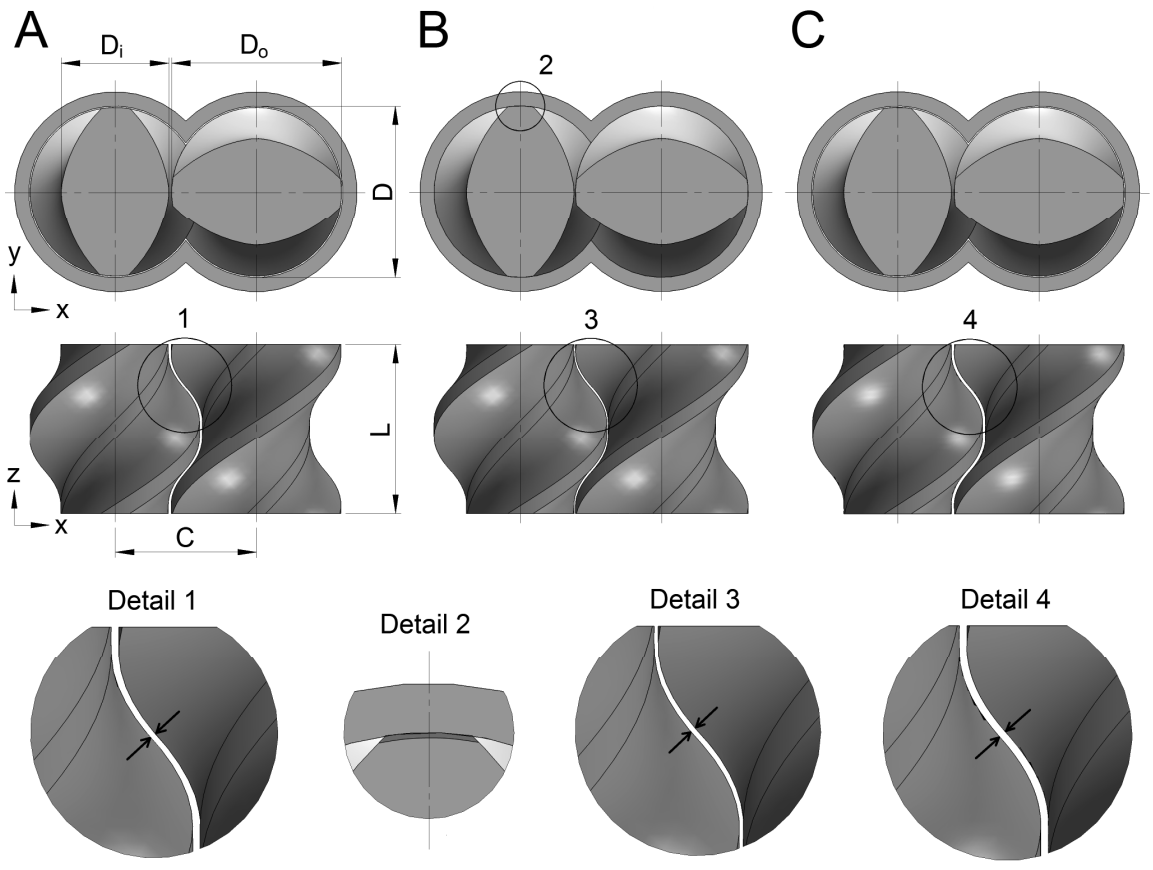

Figure 6.1: Geometry of the two-flighted conveying element and details of the clearances.

From these data, we modeled the screw geometry using the software SolidWorks according to the definition of the cross section profile of closely intermeshing twin-screw extruders.[1,39,40] However, since only the fully wiped geometry (i.e., without clearances) is exactly defined by the underlying kinematic principles, additional strategies are required to construct the clearances. Since this specific detail was not obvious from the reference[23], we used the simplest method and generated the clearances by increasing the centerline distance and the barrel diameter, i.e., by constructing the fully-wiped profile with a centerline distance C = 49 mm and a barrel diameter D = 60 mm, subsequently shifting the screws in the radial direction by 1 mm and increasing the barrel diameter by 1 mm to achieve the clearances. The resulting geometry A is shown in Figure 6.1.

To import the geometry into the simulation software LIGGGTHS, we converted the screw and barrel geometry into the *.stl format with the open-source tool GMSH (http://geuz.org/gmsh/), approximating the spatially curved surfaces with small triangles (see Figure 6.2).

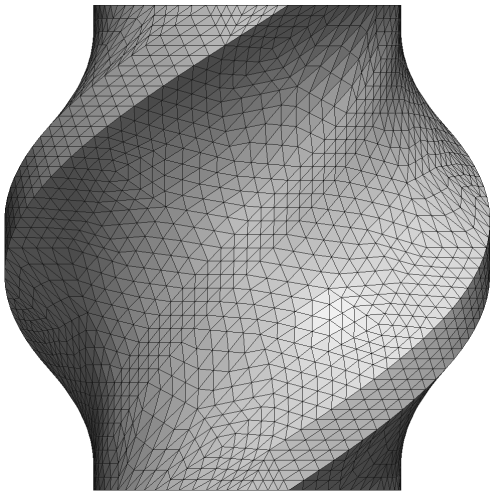

Figure 6.2: STL surface mesh of the screw element.

In order to investigate the effect of the clearances on the simulation results, we performed simulations in a modified geometry, with closed clearances between the screws and the barrel, i.e., the outer screw diameter D_o was equal to the barrel diameter D. For that purpose, we extended the screw flights of geometry A by 0.5 mm, as shown by the dark shaded area in Figure 6.1, Detail 2. This yielded the geometry B. Detail 3 in Figure 6.1 illustrates that the clearance between the screws is halved compared to Detail 1.

However, we later learned from personal communication that Bierdel[23] used a different method to create the clearances, the so-called "surface-equidistant method" constructing the fully-wiped profile with the final values of C = 50 mm and D = 61 mm and, subsequently, offsetting the surface of the screw element by 0.5 mm perpendicularly to the surface.

A screw geometry based on the surface-equidistant method yields a constant clearance distance in the intermeshing region, i.e., avoids tighter clearances between the screws at small pitches (and the corresponding high shear conditions). Clearly, this has advantages, particularly with regard to sensitive materials. However, in contrast to other methods[1], the resulting cross section profile depends on the pitch of the screw element, leading to a slight mismatch at the interface of various screw elements. As such, the extruder manufacturers typically do not use the surface-equidistant method.

Geometry C, resulting from the surface equidistant method and shown in Figure 6.1, was almost equal to geometry A, with the identical main dimensions D, C, D_o and D_i. However, the surface- equidistant method yielded a slightly different cross-sectional profile of geometry C, and the clearances between the screws were slightly increased in some regions compared to geometry A (illustrated in Figure 6.1, Details 1 and 4). Therefore, we repeated two of our simulations with geometry C to determine how this affected the agreement with the data of Bierdel[23].

6.4 Computational Approach

6.4.1 Smoothed Particle Hydrodynamics (SPH)

The SPH method is a Lagrangian particle method, where the fluid is discretized into small mass points (so-called particles). The flow is represented by the movement of those particles, which is calculated based on interaction forces approximating the continuity and momentum equations. We used the weakly compressible SPH method according to Monaghan[41–44], calculating the density via the discretized continuity equation:

$$\frac{d\rho_a}{dt} = \sum_b m_b \left(\vec{v}_a - \vec{v}_b\right) \cdot \vec{\nabla}_a W_{ab} \tag{6.4}$$

where m is the particle mass, $\vec{v}$ is the particle velocity and $\vec{\nabla}_a W_{ab}$ is the gradient of the kernel function W around particle b evaluated at in the position of particle a. For the momentum equation, we used the form proposed by Morris et. al[45] for low-Reynolds-number flows. In addition, we applied the tensile correction $R(f_{ab})^4$ of Monaghan[43] to avoid the unphysical clustering of fluid particles at low pressures that may occur at free surfaces:

$$\frac{d\vec{v}_a}{dt} = -\sum_b m_b \left(\frac{p_a}{\rho_a^2} + \frac{p_b}{\rho_b^2} + R(f_{ab})^4 \right) \vec{\nabla}_a W_{ab} + \sum_b \frac{m_b(\eta_a + \eta_b)}{\rho_a \rho_b} \left(\frac{1}{|\vec{r}_{ab}|} \frac{\partial W_{ab}}{\partial r_{ab}} \right) \vec{v}_{ab} + \vec{a} \tag{6.5}$$

where p is the pressure, η the dynamic viscosity, $\vec{r}_{ab} = \vec{r}_a - \vec{r}_b$ is the distance vector between particles a and b, $\vec{v}_{ab} = \vec{v}_a - \vec{v}_b$ is the relative velocity and $\vec{a}$ is a body force (e.g., gravity). The tensile correction $R(f_{ab})^4$ is an artificial term, which is required to avoid the unphysical clustering of fluid particles at low pressures that may occur at free surfaces. All other terms in Eq. 5 represent physical forces, i.e., the pressure forces, viscous forces and body forces. The factor f_{ab} of the tensile correction is defined as:

$$f_{ab} = \frac{W_{ab}}{W(\Delta x, h)} \tag{6.6}$$

The factor R consists of two contributions, one for each of the considered fluid particles a and b:

$$R = R_a + R_b \tag{6.7}$$

where R_a is calculated by:

$$R_a = \begin{cases} \dfrac{\varepsilon |p_a|}{\rho_a^2} & (p_a < 0) \\ 0 & (\text{otherwise}) \end{cases} \tag{6.8}$$

R_b is obtained analogous to R_a by replacing a with b, the parameter ε is commonly set to 0.2. If both pressures p_a and p_b are positive, Monaghan[43] recommends to calculate R as follows:

$$R = 0.01\left(\frac{p_a}{\rho_a^2} + \frac{p_b}{\rho_b^2}\right) \tag{6.9}$$

Similarly to our previous work,[37] we used the following linear form for the equation of state to approximate an incompressible fluid:

$$p = c^2(\rho - \rho_0) + p_0 \tag{6.10}$$

where c is the speed of sound in the fluid, ρ_0 is the reference density and p_0 is a background pressure[46]. The chosen speed of sound had to be high enough to keep the density variability low in the case of liquids (typically $\delta = \Delta\rho/\rho_0 \leq 0.01$). The criteria to achieve this are described in Morris et al.[45]:

$$c^2 \geq \frac{1}{\delta}\max\left(V_0^2, \frac{\nu V_0}{L_0}, aL_0\right) \tag{6.11}$$

where V_0 is the maximum fluid velocity, ν is the kinematic fluid viscosity, L_0 is a relevant length scale and a is a body force acting on the particles. The first criterion limits the compression due to kinetic energy and can also be expressed by the Mach number ($Ma^2 \leq \delta$, see also Monaghan[42]). The second and third criteria in Eq. 6.11 limit the compression due to the viscous and body forces.

We filtered the density field every 30th time steps using the Shepard correction (e.g., Gomez-Gesteira et al.[47]), which is a common way of avoiding unphysical oscillations in the pressure field caused by small density errors that typically accumulate over time due to Eq. 6.4:

$$\rho_a^{new} = \frac{\sum_b m_b W_{ab}}{\sum_b \frac{m_b}{\rho_b} W_{ab}} \tag{6.12}$$

For the kernel function W, we employed the cubic-spline kernel defined as follows:[43]

$$W\left(|\vec{r}_{ab}|,h\right)=\frac{1}{\pi h^3}\begin{cases}1-\frac{3}{2}\left(\frac{|\vec{r}_{ab}|}{h}\right)^2+\frac{3}{4}\left(\frac{|\vec{r}_{ab}|}{h}\right)^3 & 0\le\frac{|\vec{r}_{ab}|}{h}<1\\ \frac{1}{4}\left(2-\frac{|\vec{r}_{ab}|}{h}\right)^3 & 1\le\frac{|\vec{r}_{ab}|}{h}<2\\ 0 & 2\le\frac{|\vec{r}_{ab}|}{h}\end{cases} \tag{6.13}$$

The smoothing length h was set to 1.2 times particle spacing Δx ($h = 1.2\Delta x$), resulting in a number of approximately 57 neighbors within a sphere of radius $2h$, as recommended.[44,48] Since the particle spacing develops dynamically during a simulation, we used its initial value to determine the smoothing length, at which the particles were regularly arranged on a cubic lattice. Considering that in a weakly compressible flow the density (i.e., mass per volume) is almost constant, there can be no significant changes of the average particle spacing during a simulation.

The following criteria were shown by Morris et al.[45] to determine the required time step, which is crucial for stability (c being the speed of sound, a the body force and ν the kinematic fluid viscosity):

$$\Delta t \le \min\left(0.25\frac{h}{c}, 0.125\frac{h^2}{\nu}, 0.25\sqrt{\frac{h}{a}}\right) \tag{6.14}$$

The first constraint in Eq. 6.14 is a Courant-Friedrichs-Lewy (CFL) condition, and the second and third ones are due to the viscous forces and body forces. Another criterion shown by Monaghan[49] considers the CFL condition and the viscous limitation together (simplified for liquids):

$$\Delta t \le \frac{0.3h}{c(1+1.2\alpha)} \tag{6.15}$$

where α is the artificial viscosity, which can be calculated from the kinematic viscosity by $\alpha = 10\nu/hc$.[44] Note that the limit of Eq. 6.15 for $\alpha \to 0$ is $\Delta t \le 0.3\ h/c$, while in the case of $\alpha \to \infty$ after substituting α by $10\nu/hc$ it is $\Delta t \le 0.025\ h^2/\nu$. These are qualitatively equivalent to the first and second criteria in Eq. 6.14.

For more details concerning the fundamentals of SPH, please refer to the literature (e.g., Monaghan[41–44], Liu and Liu[48], Price[50], Gomez-Gesteira et al.[47]). The numerical studies were conducted using the open-source particle simulator LIGGGHTS.[51]

6.4.2 Wall Boundary Conditions

There is still no unique way of modeling solid walls in SPH. Commonly used techniques include boundary particles, fixed fluid particles, ghost particles and normalizing conditions.[52] Boundaries consisting of particles are problematic for complex geometries, since the creation of a regular arrangement of boundary particles along arbitrarily curved walls would require a sophisticated procedure. Moreover, technical geometries are usually available in file formats that approximate the curved surfaces by a tessellation consisting of triangles (e.g., the STL format), and a direct use of these commonly used geometry formats would be much simpler than a preprocessing required to set boundary particles. Ghost particles, which are fluid particles mirrored over wall surfaces, lead to complications at edges and corners. Normalizing conditions are involved and computationally expensive in 3D.

However, proper wall modeling is essential in SPH, since for particles in the vicinity of the walls the number of neighbors is not complete, which causes unphysical effects. Due to the drawbacks of the existing methods for complex geometries, we developed a novel wall interaction method, which accounts for the contributions of the wall to the continuity and momentum equations of a single fluid particle, depending on the distance of the fluid particle from the wall surface. This was presented in detail in our previous work,[37] where we used a solid wall consisting of fixed fluid particles (representing the missing neighbors) to investigate their impact on a single, moving fluid particle. The results, transformed into a dimensionless and general form, were fitted by polynomials, which allow the efficient calculation of the wall interaction terms using the distance of the fluid particle from the wall surface, without requiring any additional particles to represent the wall. For more details please refer to our previous work.[37]

In addition to these wall contributions to the continuity and momentum equation of the fluid particles, a repulsive force was required to prevent the penetration of fluid particles into the walls in regions with strong fluid compression. For the detailed reasons, please

refer to our previous work.[37] Similar as shown there, we used the following repulsion model, which was proposed by Monaghan with $\alpha = 4$, $\beta = 2$[42] and $\alpha = 1/2$, $\beta = -1/2$[53]:

$$F_{rep}(r) = \begin{cases} C_{rep} \cdot \left[\left(\frac{r_0}{r} \right)^{\alpha} - \left(\frac{r_0}{r} \right)^{\beta} \right] & (r \le r_0) \\ 0 & (r > r_0) \end{cases} \tag{6.16}$$

where r is the normal distance to the wall and r_0 is the range of the potential. We established that the computationally less expensive exponents $\alpha = 1$, $\beta = 0$ not only worked well in our case, but also allowed larger time steps than $\alpha = 4$, $\beta = 2$. Thus, we used Eq. 6.16 with $\alpha = 1$, $\beta = 0$. For consistency with previous considerations,[37] a half-particle spacing was used for the range of the repulsion force $r_0 = \Delta x/2$.

6.4.3 Clearance Flow

Modeling

An intrinsic characteristic of the SPH method (without using variable resolution schemes) is that the resolution in the entire flow field is constant. The resolution used in this work equals one layer of fluid particles in the clearances, i.e., the average particle spacing was equal to the clearance distance (0.5 mm). Thus, the clearance flow is not fully resolved. Even in this case, about 10^6 SPH particles are required to fill the entire volume with the associated computational costs. A resolution refinement by factor ξ would lead to a ξ^3-fold increase in the number of particles in 3D and, together with the corresponding time step refinement, approximately to a ξ^4-fold increase in the computational expense (i.e., a refinement by factor $\xi = 5$ would lead to a 125- and about 625-fold increase in the number of particles and the computational expense, respectively).

Even applying a variable resolution SPH scheme (i.e., a local refinement by splitting and merging of particles[54,55]) cannot solve that problem efficiently. Since the volume fraction of the clearances was about 2% for the considered geometry, the local refinement would still lead to an increase by a factor of $0.02 \cdot \xi^4$ in the computational expense (e.g., a refinement by factor $\xi = 5$ would require a 12-fold increase in the computational expense). The reason for this extreme ratio is that the refinement in SPH occurs equally in all directions, while it is required only in the cross-direction of the clearances. Under mesh-

based CFD methods, stretched cells, which resolve the cross direction finer than the longitudinal direction, are used in such cases. This has no equivalent in SPH.

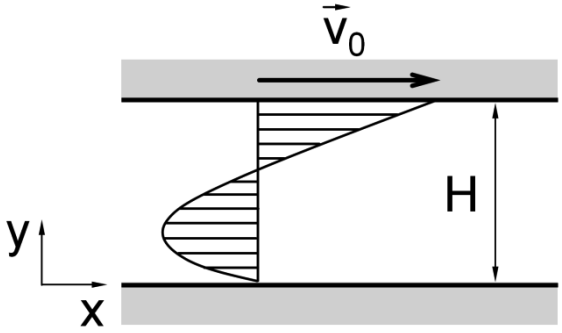

Figure 6.3: Velocity profile in a channel between two parallel walls.

To overcome this challenge, we proposed a model based on the analytical solution of the Newtonian flow between two parallel walls, which appropriately accounts for the flow rate and the wall shear forces in unresolved clearances. The steady and developed flow between two parallel walls in 3D (with distance H and relative velocity $\vec{v}_0$, as illustrated in Figure 6.3) at a constant viscosity η with a pressure gradient $\vec{\nabla} p$ can be easily derived from the Navier-Stokes equations. This yields the following velocity profile, which is the superposition of a linear drag flow profile over a pressure-driven, parabolic velocity profile:

$$\vec{v}(y) = \vec{v}_0 \frac{y}{H} - \frac{H^2}{2\eta} \vec{\nabla} p \left(1 - \frac{y}{H}\right) \frac{y}{H} \tag{6.17}$$

Note that the vectors in Eq. 6.17 are parallel to the walls since the velocity component normal to the walls is strictly zero. Since this velocity profile is a parabola, it is completely defined by 3 velocity vectors (i.e., the velocity of a single fluid particle in the clearance and the known wall velocities). As such, the pressure gradient $\vec{\nabla} p$ can be calculated using Eq. 6.17 with the values of the relative wall velocity $\vec{v}_0$ and the particle velocity $\vec{v}(y)$ at the position y:

$$\vec{\nabla} p = \frac{2\eta}{(H - y)y} \left(\vec{v}_0 \frac{y}{H} - \vec{v}(y) \right) \tag{6.18}$$

To apply this to a fluid particle "a" in the clearance (illustrated in Figure 6.4), we considered the general case of both walls moving. In this case, the velocities of fluid particle $\vec{v}_a$ and upper wall $\vec{v}_{W,2}$ can be formulated relative to the lower wall velocity $\vec{v}_{W,1}$:

$$\vec{v}_{a,rel} = \vec{v}_a - \vec{v}_{W,1} \tag{6.19}$$

$$\vec{v}_{W,rel} = \vec{v}_{W,2} - \vec{v}_{W,1} \tag{6.20}$$

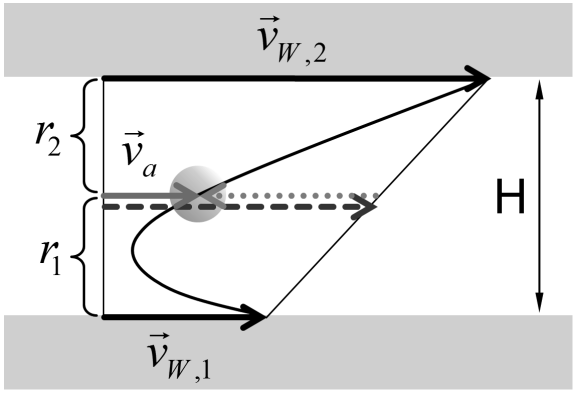

Figure 6.4: Single fluid particle in a clearance with the velocity vectors of both walls and the particle. The dashed (blue) and dotted (magenta) arrows show the drag flow contribution and the pressure-driven contribution of the flow, respectively. The distances r_1 and r_2 are the wall distances of the particle.

Substituting $\vec{v}(y) = \vec{v}_{a,rel}$, $\vec{v}_0 = \vec{v}_{W,rel}$, $y = r_1$ and $H = r_1 + r_2$ in Eq. 6.18 yields:

$$\vec{\nabla} p = \frac{2\eta}{r_1 r_2}\left(\vec{v}_{W,rel}\frac{r_1}{r_1 + r_2} - \vec{v}_{a,rel}\right) \tag{6.21}$$

which is a measure of the curvature of the velocity profile at the position of the considered fluid particle in the clearance and can be used to calculate the corresponding wall shear stresses. To that end, the velocity gradients on both walls can be obtained from Eq. 6.17 by differentiation:

$$\left.\frac{d\vec{v}}{dy}\right|_{y=0} = \frac{\vec{v}_0}{H} - \frac{H}{2\eta}\vec{\nabla} p \tag{6.22}$$

$$\left.\frac{d\vec{v}}{dy}\right|_{y=H} = \frac{\vec{v}_0}{H} + \frac{H}{2\eta}\vec{\nabla}p\,\frac{\Delta pD}{\eta nL} = A_2 \cdot \left(1 - \frac{1}{A_1}\frac{\dot{V}}{nD^3}\right) \tag{6.23}$$

Multiplication with viscosity η and substitution of $\vec{v}_0 = \vec{v}_{W,rel}$ and $H = r_1 + r_2$ yield the wall shear stresses of the lower and upper walls:

$$\vec{\tau}_{W,1} = \eta\frac{\vec{v}_{W,rel}}{r_1 + r_2} - \frac{r_1 + r_2}{2}\vec{\nabla}p \tag{6.24}$$

$$\vec{\tau}_{W,2} = \eta\frac{\vec{v}_{W,rel}}{r_1 + r_2} + \frac{r_1 + r_2}{2}\vec{\nabla}p \tag{6.25}$$

To calculate the corresponding wall forces, the shear stresses are multiplied by the wall contact area. This is obtained as the fluid particle volume divided by the clearance distance (i.e., considering the volume uniformly distributed across the clearance):

$$A_{contact} = \frac{m_p}{\rho_p(r_1 + r_2)} \tag{6.26}$$

With that, the wall forces of the lower wall $\vec{F}_{W,1}$ and upper wall $\vec{F}_{W,2}$ exerted on the considered fluid particle are:

$$\vec{F}_{W,1} = -\vec{\tau}_{W,1}A_{contact} \tag{6.27}$$

$$\vec{F}_{W,2} = \vec{\tau}_{W,2}A_{contact} \tag{6.28}$$

This allows to calculate the wall shear forces in an unresolved clearance, which requires substituting the Morris viscosity model with Eqs. 6.19 – 6.21 and 6.24 – 6.28 in the momentum equation (Eq. 6.5):

$$\frac{d\vec{v}_a}{dt} = -\sum_b m_b\left(\frac{p_a}{\rho_a^{\,2}} + \frac{p_b}{\rho_b^{\,2}} + R(f_{ab})^4\right)\vec{\nabla}_a W_{ab} + \frac{\vec{F}_{W,1} + \vec{F}_{W,2}}{m_a} + \vec{a} \tag{6.29}$$

However, calculating the pressure forces this way would yield too little pressure gradient contributions due to the incomplete neighbor count at positions within the clearance.

Although the used wall interaction was developed to compensate the lack of neighbors in the vicinity of the walls, it fails in terms of the pressure gradients, since the wall reflects uniform pressure and does not contribute to any tangential pressure gradients. This deficiency vanishes in resolved flows since the pressure gradient is calculated correctly for all particles with a complete neighbor count (i.e., inside the fluid). However, in the most extreme case with only one layer of fluid particles across the clearance, all particles have an incomplete neighbor count and tangential pressure gradients are not correctly represented. Grenier et al.[56] showed, that the kernel gradient can be renormalized with the factor $\Sigma(m_b/\rho_b)W_{ab}$, which yields the value of 1 for a complete neighbor count (inside the fluid) and values < 1 for an incomplete neighbor count (at boundaries). The more complex matrix renormalization proposed by Bonet and Lok[57] would additionally guarantee the first order consistency, i.e., the exact evaluation of the gradient of a linear field. However, the use of this technique is computationally more expensive because it requires the evaluation of nine additional neighbor summations in 3D, compared to only one summation for the scalar factor $\Sigma(m_b/\rho_b)W_{ab}$. As we found, that also the latter could reproduce pressure gradients sufficiently accurate for technical applications (see the validation cases below), we used this for the renormalization of the pressure gradient in the clearance regions. With that, the modified momentum equation for the unresolved clearance is:

$$\frac{d\vec{v}_a}{dt} = -\frac{\sum_b m_b \left(\frac{p_a}{\rho_a^{\,2}} + \frac{p_b}{\rho_b^{\,2}} + R(f_{ab})^4 \right) \vec{\nabla}_a W_{ab}}{\sum_b \frac{m_b}{\rho_b} W_{ab}} + \frac{\vec{F}_{W,1} + \vec{F}_{W,2}}{m_a} + \vec{a} \tag{6.30}$$

Although all forces are appropriately calculated in Eq. 6.30, the resulting flow rate through the clearance is typically incorrect since the entire fluid in the clearance moves together with the resulting particle velocities. For example, if the applied resolution is equal to the clearance distance H (yielding a single layer of fluid particles in the clearance), a pure Poiseuille flow causes the entire fluid in the clearance to move with the maximum velocity, while slower velocities adjacent to the walls are not accounted for.

In order to achieve a particle velocity equal to the equivalent average velocity of the flow rate (and, thus, the correct flow rate through the clearance), we introduced an appropriate velocity correction factor that was determined as follows: A pure drag flow (linear profile)

does not require a velocity correction since the particle velocity is equal to the average velocity (assuming the particles are located in the center of the clearance, which is the case due to the wall symmetry). The maximum velocity of a purely pressure-driven flow (parabolic profile) is 1.5 times higher than the average velocity, i.e., without the correction the flow rate would be overestimated by 50%. Thus, the pressure-driven contribution of the superposed flow profile (see Figure 6.4, dotted arrow) has to be corrected accordingly. Since in Eq. 6.21, exactly this pressure-driven contribution of the velocity is stated in brackets (i.e., the difference of the actual particle velocity and the drag flow contribution), we added multiplication with the velocity correction f_{corr} (which is 1.5 for one layer of particles in the clearance):

$$\vec{\nabla}p = \frac{2\eta}{r_1 r_2}\left(\vec{v}_{W,rel}\frac{r_1}{r_1+r_2} - \vec{v}_{a,rel}\right) f_{corr} \tag{6.31}$$

As such, the f_{corr}-fold value of the pressure-driven contribution of the particle velocity is used to calculate the pressure gradient and the corresponding wall shear forces, which means that in a steady state the obtained particle velocity is equal to the flow-rate-equivalent average velocity.

Since this model should also properly account for the flow if the clearance contains more than one layer of fluid particles, the dependency of the velocity correction factor on the number of particle layers in the clearance must be considered. The number of particle layers can be calculated as the clearance distance divided by the fluid particle spacing $N = (r_1 + r_2)/\Delta x$. For a number of N particles layers, the average velocity of the particles $v_{av,P}(N)$ can be calculated as

$$v_{av,P}(N) = \frac{1}{N}\sum_{i=1}^{N} v(y) \tag{6.32}$$

where $v(y)$ is the velocity of the particle in position y in the cross direction (see Figure 6.5). The parabolic function $v(y)$ for a pure Poiseuille flow in 2D can be obtained from Eq. 6.17:

$$\frac{v(y)}{v_{av}} = 6\left(1 - \frac{y}{H}\right)\frac{y}{H} \tag{6.33}$$

where v_{av} is the average velocity of the parabola, illustrated by a dashed line in Figure 6.5.

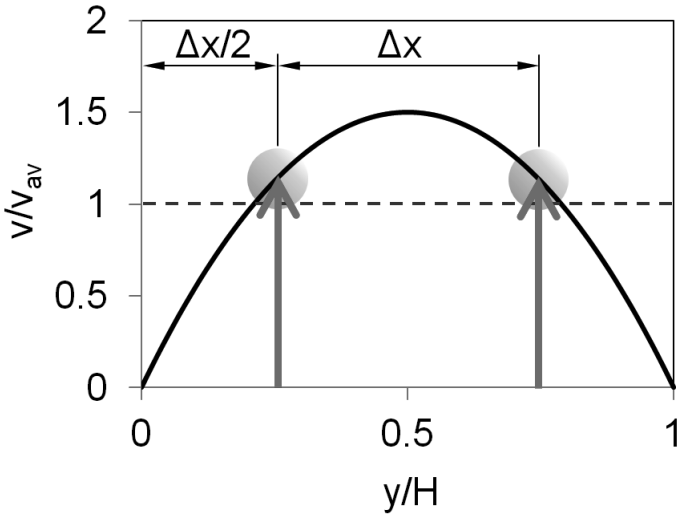

Figure 6.5: Parabolic velocity profile in a pressure-driven clearance flow with, e.g., two layers of fluid particles representing the flow ($N = 2$). The dashed (blue) line shows the flow-rate-equivalent average velocity of the parabola v_{av}, the (red) arrows illustrate the particle velocity vectors (without the velocity correction factor) and Δx is the particle spacing.

Substituting Eq. 6.33 in Eq. 6.32 and calculating the particle position of particle i as $y = \Delta x/2 + (i-1)\Delta x$ (as illustrated in Figure 6.5) using $\Delta x /H = 1/N$ yields:

$$\frac{v_{av,P}}{v_{av}} = \frac{6}{N}\sum_{i=1}^{N}\left(1-\frac{y}{H}\right)\frac{y}{H} = \frac{6}{N^2}\sum_{i=1}^{N}\left[\left(i-\frac{1}{2}\right)-\frac{1}{N}\left(i-\frac{1}{2}\right)^2\right] \tag{6.34}$$

Eq. 6.34 can be evaluated for a given N. For $N = 1$, 2, 3, 4 and 5, it yields the values 1.5, 1.125, 1.05556, 1.03125 and 1.02, respectively. These numbers actually represent the velocity correction factor f_{corr}, i.e., the ratio between the (uncorrected) average particle velocity and the average velocity of the parabolic profile. Clearly, f_{corr} approaches 1 for large N's: at higher resolution, the flow rate represented by the particles converges with the integral of the parabolic profile. Moreover, the number of particle layers does not have to be a natural number since the fluid particles can also fill a given clearance distance via a disordered arrangement. Thus, a continuous function to fit the discrete summation Eq. 6.34 was required. We established that the following function reproduces the values of Eq. 6.34 exactly:

$$f_{corr} = 1 + \frac{1}{2}\left(\frac{1}{N}\right)^2 = 1 + \frac{1}{2}\left(\frac{\Delta x}{r_1 + r_2}\right)^2 \tag{6.35}$$

Substituting Eqs. 6.19 – 6.21 in 6.24 and 6.25, Eqs. 6.24 – 6.26 in 6.27 and 6.28 and Eqs. 6.27 and 6.28 in Eq. 6.30 yields the following momentum equation in the clearance:

$$\frac{d\vec{v}_a}{dt} = -\frac{\sum_b m_b \left(\frac{p_a}{\rho_a^2} + \frac{p_b}{\rho_b^2} + R(f_{ab})^4\right)\vec{\nabla}_a W_{ab}}{\sum_b \frac{m_b}{\rho_b} W_{ab}} + \frac{2\eta_a}{r_2 \rho_a}\left(\frac{\vec{v}_{W,2} - \vec{v}_{W,1}}{r_1 + r_2} - \frac{\vec{v}_a - \vec{v}_{W,1}}{r_1}\right) \cdot f_{corr} + \vec{a} \tag{6.36}$$

The criteria below were established in order to substitute the SPH momentum equation Eq. 6.5 with the clearance model Eq. 6.36:

- the considered particle is in contact with two walls (the barrel and screw walls). This model was not applied to the clearance between the screws where the walls are non-parallel and the flow is more complex than assumed for the derivation of the model. However, the volume fraction of the fluid inside the clearance between the screws is much lower than that between the screws and the barrel.

- the sum of the wall distances $r_1 + r_2$ is smaller than a predefined clearance distance parameter (to avoid using the clearance model in resolved regions with two adjacent walls).

Validation of the Clearance Model

The newly developed clearance model (Eq. 6.36) was incorporated in the open-source software LIGGGHTS and various tests based on a setup of an unresolved clearance flow between two parallel walls with open periodic boundaries in the remaining directions (Figure 6.6a) were conducted. We studied a Couette flow, a Poiseuille flow and a superposition of both. A pressure gradient along the clearance was not applied, since the pressure on the corresponding periodic boundaries must be equal. As such, we used a body force a_x in the x-direction to achieve the Poiseuille flow.

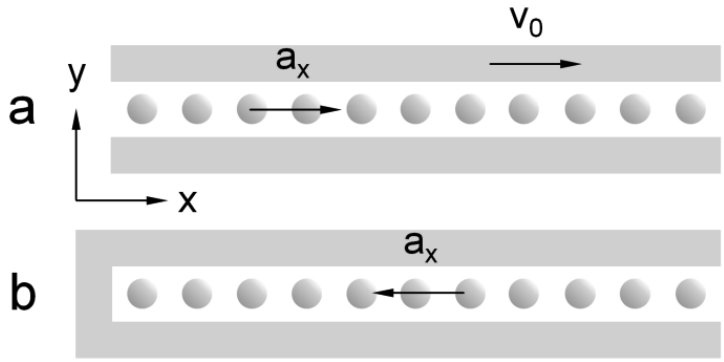

Figure 6.6: Setup for the test cases with one layer of fluid particles across the clearance, (a) with open periodic boundaries in the x-direction and (b) one closed boundary in the x-direction. The extension in the z-direction was 5 layers of fluid particles, also with open periodic boundaries.

First, we considered the Couette flow using the setup shown in Figure 6.6a, i.e., a pure drag flow between two walls forming a 0.5 mm-wide clearance with a relative wall velocity of v_0 = 0.1 m/s. The density was 1000 kg/m³ and the viscosity was 1 Pas, yielding a Reynolds number of 0.05. The smoothing length varied: we started at h = 0.6 mm and refined it to h = 0.3 mm, h = 0.2 mm and h = 0.12 mm. In each case, the initial particle spacing was $\Delta x = h / 1.2$. This yielded 1, 2, 3 and 5 layers of fluid particles per clearance distance, respectively (see Table 6.1). We simulated the unsteady Couette flow, beginning with a stationary fluid at t = 0. The resulting particle velocities after 0.02 ms and 0.2 ms (which was the steady state) are specified in Figure 6.7, left column (the shown particle velocities were equal for all particles in the clearance due to the periodicity). The data were then compared with the exact velocity profiles (unsteady and steady) calculated from a series solution:[58]

$$v(y,t) = v_0 \cdot \sum_{n=0}^{\infty} \left[\operatorname{erfc}\left(2 \cdot n \cdot \eta_h + \eta\right) + \operatorname{erfc}\left(2 \cdot (n+1) \cdot \eta_h - \eta\right) \right] \tag{6.37}$$

with $\eta = \dfrac{y}{2\sqrt{\nu \cdot t}}$ and $\eta_h = \dfrac{H}{2\sqrt{\nu \cdot t}}$

The resulting average velocities in the clearance for the unsteady and steady states after 0.02 ms are shown in Table 6.2 together with the corresponding relative error compared to the series solution (Eq. 6.37). Since the model is based on the steady state analytical

solution, the relative errors vanished in the steady state. In the unsteady state, the relative errors were below 3% for the Couette flow.

Table 6.1: Values of smoothing length h, initial particle spacing Δx and the resulting number of particle layers across the 0.5 mm clearance.

h [mm]	0.6	0.3	0.2	0.12
Δx [mm]	0.5	0.25	0.167	0.1
# of particle layers	1	2	3	5

Table 6.2: Average velocity and corresponding relative errors for the investigated cases.

# of particle layers	1	2	3	5
Couette flow				
v_{av} [m/s] (0.02 ms)	0.0308	0.0308	0.0316	0.0323
Rel. error (0.02 ms)	2.8%	2.8%	0.3%	1.9%
v_{av} [m/s] (steady state)	0.05	0.05	0.05	0.05
Rel. error (steady state)	0.0%	0.0%	0.0%	0.0%
Poiseuille flow				
v_{av} [m/s] (0.02 ms)	0.0128	0.0128	0.0126	0.0122
Rel. error (0.02 ms)	11.3%	11.3%	9.6%	6.1%
v_{av} [m/s] (steady state)	0.0208	0.0208	0.0208	0.0208
Rel. error (steady state)	0.0%	0.0%	0.0%	0.0%
Superposition				
v_{av} [m/s] (0.02 ms)	0.0180	0.0180	0.0191	0.0201
Rel. error (0.02 ms)	10.1%	10.1%	5.4%	0.5%
v_{av} [m/s] (steady state)	0.0292	0.0292	0.0292	0.0292
Rel. error (steady state)	0.0%	0.0%	0.0%	0.0%

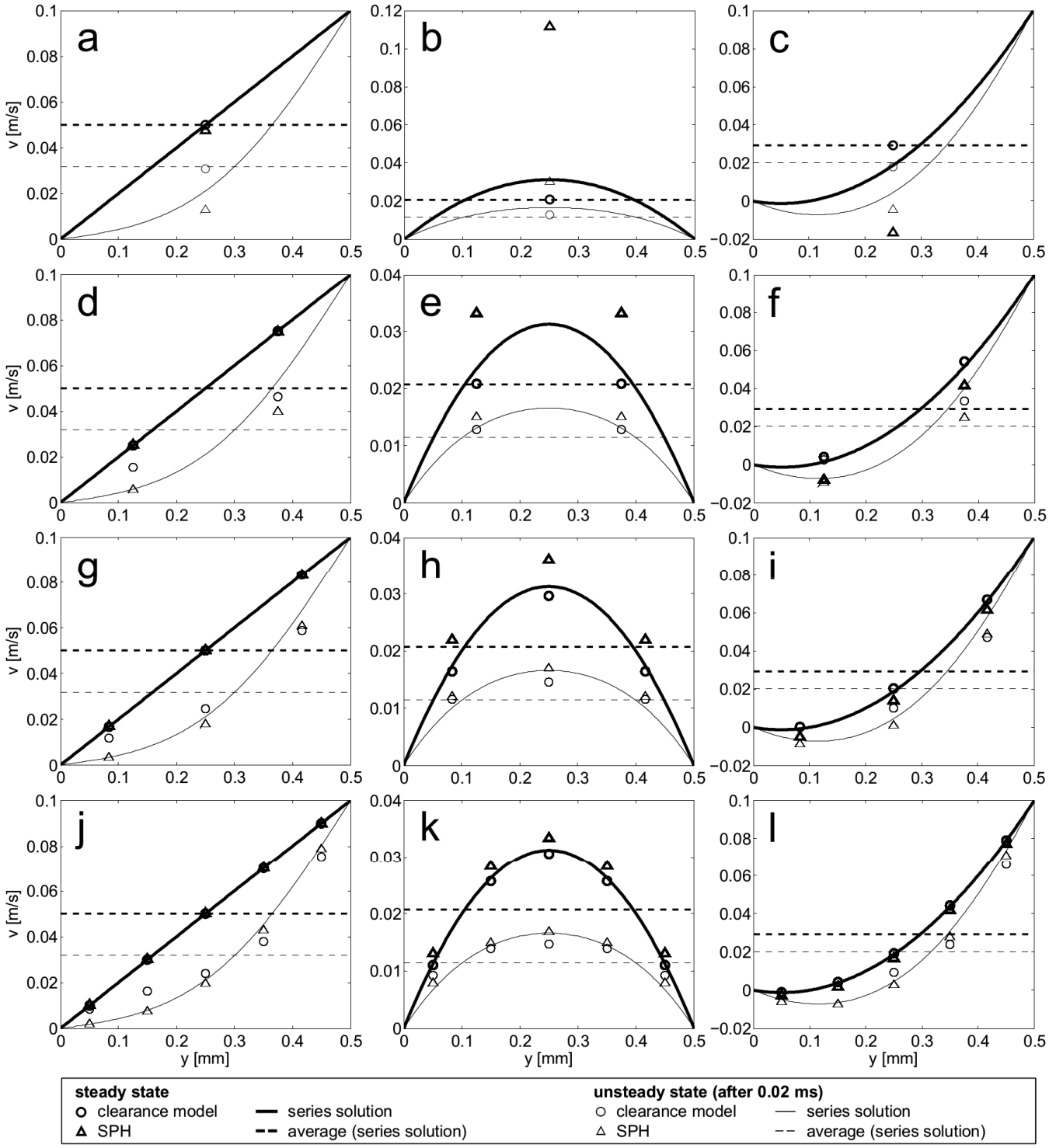

Figure 6.7: Velocity profiles in the clearance for the Couette flow (left column), the Poiseuille flow (middle column) and the superposition of the Couette and Poiseuille flows (right column) for different numbers of particle layers in the clearance (resolution): a – c for 1 layer, d – f for 2 layers, g – i for 3 layers and j – l for 5 layers.

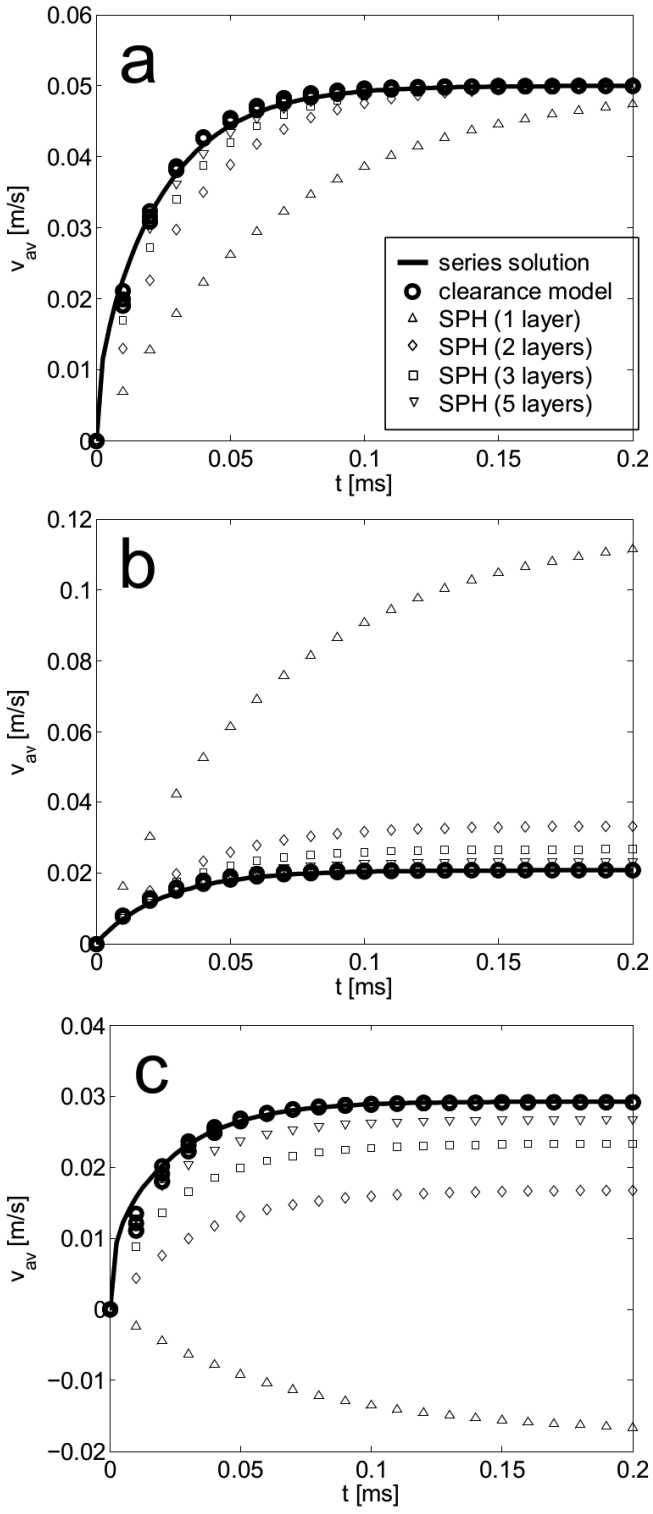

Figure 6.8: Flow-rate-equivalent average velocity v_{av} over time t for the (a) Couette flow, (b) Poiseuille flow and (c) superposition of the Couette and Poiseuille flows. The data for SPH are shown for various resolutions, yielding one, two, three and five layers of particles across the clearance. In the clearance model, these 4 lines almost overlapped.

Subsequently, to demonstrate the advantages of the new clearance model, we compared our data to the velocities predicted by the SPH method without the clearance model. In the case of one particle layer per clearance distance (Figure 6.7a), due to the linear velocity profile, the steady state velocities for both the clearance model and SPH yielded exactly the average velocity of the profile. However, after 0.02 ms the unsteady velocities varied significantly: the clearance model velocity was close to the average velocity of the exact profile (i.e., the flow rates agreed), but SPH yielded a significantly lower velocity. The situation was similar for two, three and five particle layers per clearance distance (Figure 6.7d, g and j): the steady state velocities always yielded the exact values for both the clearance model and SPH, while the unsteady profiles varied. However, with the increasing resolution refinement, the SPH velocities became more accurate (nearly exact for 5 particle layers, Figure 6.7j), while the clearance model velocities did not exactly match the series solution (which was not required, since the model was intended for the unresolved case).

Figure 6.8a shows the flow rate over time for all Couette flow cases. Clearly, the flow rate of SPH converged with the series solution for increasing resolution refinement, while it deviated significantly for the unresolved case with one layer of particles. In contrast, the flow rate in the clearance model was close to the series solution, regardless of the resolution. Clearly, for the unresolved Couette flow, the clearance model significantly improved the flow rate prediction, compared to SPH in the unsteady case.

For the second case (the Poiseuille flow), all parameters were identical to the Couette flow, except for the body force a_x = 1000 m/s². As before, we varied the resolution yielding one, two, three and five particle layers across the clearance. The resulting particle velocities are shown in Figure 6.7 (middle column) in comparison with the clearance model, SPH and the following series solution:[45]

$$v(y,t) = \frac{a_x}{2\nu} \cdot y(y-H) + \sum_{n=0}^{\infty} \frac{4a_x H^2}{\nu\pi^3 (2n+1)^3} \cdot \sin\left(\frac{\pi y}{H} \cdot (2n+1)\right) \cdot \exp\left(-\frac{(2n+1)^2 \pi^2 \nu}{H^2} \cdot t\right) \quad (6.38)$$

Numerical values for the obtained average velocities in the clearance and the corresponding relative errors are provided in Table 6.2. While they were in exact

agreement for the steady state, errors of up to 11% occurred in the unsteady state after 0.02 ms. In contrast to the Couette flow, the velocity profile was nonlinear and the steady state results for the clearance model and SPH did not match. In case of one particle layer in the clearance, the steady state SPH velocity was more than 5-fold that of the exact average velocity due to the lack of resolution, while the corresponding clearance model velocity was in agreement with the average velocity in the exact solution. The unsteady velocity after 0.02 ms was well approximated by the clearance model, but significantly overpredicted by SPH. Similarly to the Couette results, for the steady state both the clearance model and SPH results converged with the exact profile with the increasing resolution refinement. For the unsteady profile, in contrast to the clearance model results, the SPH results converged with the exact profile. The flow rate over time for the Poiseuille flow is shown in Figure 6.8b. For all of the investigated resolutions, the flow rate of the clearance model was close to the exact solution, while the SPH flow rate strongly deviated due to coarser resolution and was close to the exact value for 5 particle layers per clearance distance.

Finally, we superposed the Couette flow over the Poiseuille flow using a wall velocity of 0.1 m/s and a body force of -1000 m/s² (i.e., acting against the wall velocity). The other parameters were the same as above. The resulting velocity profiles and the flow rate over time are shown in Figure 6.7, right column, and Figure 6.8c, respectively. For the exact solution, we superposed the series solutions Eqs. 6.37 and 6.38. For 1 particle layer across the clearance, due to the strong deviation of the pressure-driven flow component, the SPH method even yielded a negative flow rate compared to the clearance model.

Since the above results did not address pressure forces, we studied the effect of body force a_x on the hydrostatic pressure in an unresolved clearance using the proposed clearance model (Eq. 6.36). To that end, we used a similar setup as before, but closed the clearance at one end in the x-direction (Figure 6.6b). We varied the resolution and applied the same values for the smoothing length and initial particle spacing as above (see Table 6.1). The body force was a_x = 10 m/s², the density 1000 kg/m³ and the viscosity 1 Pas. Figure 6.9 shows the resulting pressure of the fluid particles in the x-direction for the case involving one layer of fluid particles across the clearance (symbols). We fitted a linear function using these data (solid line in Figure 6.9) and listed the obtained pressure gradients *dp/dx* in

Table 6.3. The obtained results were close to the theoretical value of 10 000 Pa/m for all investigated cases, and the corresponding relative errors were below 1%, indicating that the proposed normalization factor for the pressure forces in Eq. 6.36 was correct.

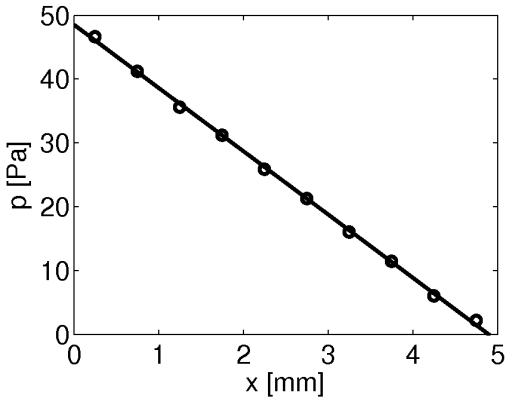

Figure 6.9: Hydrostatic pressure profile in a 0.5 mm wide clearance with one layer of fluid particles (symbols indicate the pressure of the fluid particles, the linear function is a fit).

Table 6.3: Obtained hydrostatic pressure gradient and corresponding relative error for the investigated cases.

# of particle layers	1	2	3	5
dp/dx [Pa/m]	9911	10079	9988	10032
Relative error	0.89%	0.79%	0.12%	0.32%

6.4.4 Simulation Parameters

In the FVM simulation reported by Bierdel[23] the density was ρ = 1000 kg/m³, the viscosity was η = 1000 Pas and the screw speed was n = 95 rpm, which yielded a Reynolds number of Re = 0.0059 (using the definition $Re = nD^2\rho/\eta$). Since the dimensionless parameters did not depend on viscosity and screw speed, their values did not have to be matched. A decrease in viscosity was essential for the time step and computational expense. Eq. 6.14 suggests that an upper limitation of the time step is inversely proportional to the viscosity ($\Delta t < 0.125\ h^2/\nu$). For the required number of time steps per screw revolution at high viscosities this means that:

$$(n\Delta t)^{-1} \sim \frac{\nu}{nh^2} = \frac{\eta}{nh^2\rho} = \left(\frac{D}{h}\right)^2 \frac{\eta}{nD^2\rho} = \left(\frac{D}{h}\right)^2 Re^{-1} \tag{6.39}$$

Eq. 6.39 shows that the number of time steps per screw revolution clearly depends on the smoothing length to diameter ratio h/D (i.e., the resolution) and is inversely proportional to the Reynolds number Re, which is a drawback when simulating highly viscous flows, as typical in extrusion. Optimization by choosing the involved parameters (screw speed, viscosity and length scale) is not possible. With the used method, the only way to reduce the computational expense is to increase the Reynolds number as much as possible.

Information on the creeping flow regime for twin-screw extruders is limited. Pawlowski[38] showed experimentally that for a single-screw extruder the pressure characteristic was independent from the Reynolds number up to $Re = 40$. We correctly assumed (see results below) that the limiting Reynolds number was similar for a twin-screw extruder and used the parameters that yielded a Reynolds number of $Re = 3.72$, which was one order of magnitude lower than the above value ($Re = 40$) and was expected to fulfill the conditions for the creeping flow regime. The screw speed and viscosity were $n = 60$ rpm and $\eta = 1$ Pas, and density was kept at the original value of 1000 kg/m³ (i.e, $\rho_0 = 1000$ kg/m³ in Eq. 6.10). Using these parameters, we simulated eight cases with a completely filled screw element (geometry A) and varied the axial pressure drop $dp/dz = 0$, 5, 10, 15, 20, 25, 30 and 35 kPa/m (Scenario 1 in Table 6.4). Similar as shown for the reference results,[23] we applied periodic boundaries in the axial direction. Although, inflow and outflow boundaries are possible with SPH,[59,60] periodic boundaries were more efficient in this case due to the periodicity of the geometry. Since the pressure must be equal at both periodic boundaries (i.e., zero pressure drop), we replaced the axial pressure drop dp/dz with the body force $a_z = dp/dz / \rho$, acting against the pumping and conveying direction ($a_z = 0$, 5, 10, 15, 20, 25, 30 and 35 m/s²). This superposed the pressure drop caused by the screw rotation with a hydrostatic pressure gradient, yielding a zero pressure drop together.

As discussed above, the spacing we chose was fine enough to allow the flow of fluid particles through the tightest clearances of the geometry with only one layer of fluid particles. In co-rotating twin-screws, the tightest clearance distance is typically between the screws and the barrel (depending on the method of creating the clearances, the tightest clearance may be between the screws, specifically for small pitches). In our case, since this distance was 0.5 mm, we set the initial particle spacing Δx to 0.5 mm and the smoothing length to 1.2 times of Δx ($h = 0.6$ mm). The initial particle positions were at the nodes of a

cubic lattice, with a distance of at least Δx /2 between the particle centers and the walls, since particles closer to the wall surface can blow up the simulation due to the wall repulsion (Eq. 6.16). This resulted in 981 278 fluid particles for the completely filled cases. The mass of the fluid particles was determined as the entire mass of the fluid (calculated from the geometry's free volume of 132 617 mm³) divided by the number of the particles.

Table 6.4: Simulation parameters.

Scen.	Geo.	n	η	Re	h	c	p_0	C_{rep}	ρ_{Init}	Δt	$(n\Delta t)^{-1}$
		[rpm]	[Pas]	-	[mm]	[m/s]	[Pa]	[mN]	[kg/m³]	[µs]	[10^3]
1, 2	A	60	1	3.72	0.6	15	500	2-3	1050	5	200
3	B	60	1	3.72	0.6	15	500	2-3	1050	5	200
4	A	60	2	1.86	0.6	15	500	3	1050	5	200
5	A	60	0.2	18.6	0.6	15	100	0.5	1050	10	100
6	A	150	1	9.30	0.6	15	500	2	1050	5	80
7	A	60	1	3.72	1.2	15	500	10	1120	5	200
8	A	60	1	3.72	0.6	7.5	0	25-100	1081	1-5	200-1000
9	C	60	1	3.72	0.6	15	500	3	1080	5	200

The particle initialization in a complex geometry is not trivial, since in general a regular initial arrangement of the particles does not exactly match the shape of the boundaries, which causes empty spaces between fluid and boundaries. This could be avoided by a recently proposed particle packing algorithm, which achieves a particle initialization that matches the shape of the geometry well.[61] Moreover, this strongly reduces the numerical noise caused by the particle rearrangement in the early stages of the simulation. However, in our work it was sufficient to initialize the particles on a regular lattice. In order to compensate the resulting empty spaces between fluid and boundaries, we set the initial density of the particles higher than the desired 1000 kg/m³, which caused a slight expansion of the weakly compressible fluid during the first time steps, sufficient to fill the entire volume. However, it was difficult to determine the initial density that would yield the average density of the fluid particles after expanding to be 1000 kg/m³. Although the

exact value of the density is unimportant for creeping flows, the equation of state for a weakly compressible fluid (Eq. 6.10) shows that pressure strongly depends on small density variations. Thus, pressure values could easily be negative, causing formation of partially filled regions, or too high, enhancing the time step limitation due to higher interaction forces. We iteratively established that an initial density of ρ_{Init} = 1050 kg/m³ was appropriate in this case and the resulting average density of the fluid was slightly above 1000 kg/m³ (within a range of 0.5%).

Moreover, we used a background pressure $p_0 > 0$ in the equation of state. Otherwise, the pressure values would be distributed around zero for the density distributed around ρ_0 = 1000 kg/m³, resulting in the formation of partially filled regions at negative pressure. A value of p_0 = 500 Pa was sufficient to keep the screw element completely filled.

For the speed of sound, we used the values recommended in Eq. 6.11. The maximum fluid velocity was estimated by the circumferential screw velocity $v_0 = D_o \pi n$ = 0.188 m/s (for 60 rpm). With δ = 0.01 (i.e., allowing approximately 1% density variation in the flow field), the first criterion of Eq. 6.11 yielded $c > 1.88$ m/s. For the length scale L_0 of the second criterion, the clearance distance (L_0 = 0.5 mm) was used since the highest shear rates and highest viscous forces were expected in the clearances. This yielded $c > 6.13$ m/s. To calculate the third criterion, we used the length of the screw element (L_0 = 60 mm) since the axial body force acted over this length, yielding $c > 14.49$ m/s². In the end, we set the speed of sound to c = 15 m/s, the limiting criterion being the (maximum) applied body force of 35 m/s².

Based on this, we calculated the required time step as shown in Eqs. 6.14 and 6.15. The CFL criterion in Eq. 6.14 yielded $\Delta t < 10$ µs, the second criterion yielded $\Delta t < 45$ µs due to the viscosity and the third criterion yielded $\Delta t < 1035$ µs due to the body force. Clearly, the body force did not limit the time step in this case. Eq. 6.15, which involves both, the CFL and viscosity criteria, yielded $\Delta t < 5.14$ µs (with $\alpha = 10\nu/hc = 1.11$). Since, according to Eq. 6.15, the effect of the viscosity was still present (1.2 α is in the same order of magnitude as 1), we used a time step of Δt = 5 µs, requiring a number of $2 \cdot 10^5$ steps per screw revolution at 60 rpm. A time step of 10 µs was not sufficient and led to unstable simulations.

While investigating the required time step, we established that stability strongly depended on the applied wall repulsion (Eq. 6.16). As mentioned above, the exponents $\alpha = 1$, $\beta = 0$ were beneficial, and the value of the parameter C_{rep} was crucial for stability. In order to rationally determine the value of C_{rep}, we considered the underlying interaction forces that have to be balanced by wall repulsion to avoid wall penetration. The viscous forces are irrelevant, since they act tangentially on the walls. In contrast, the pressure forces act perpendicularly to the walls, but are mainly balanced by the pressure term of the applied wall interaction. We established that increasing the pressure level (i.e., increasing background pressure p_0) required a higher repulsion parameter C_{rep} for stability. To that end, we estimated C_{rep} based on the comparison of wall repulsion and pressure forces due to the actual pressure p:

$$C_{rep} \sim \frac{m^2 p}{\rho^2 h^4} \tag{6.40}$$

The right hand side was derived from the momentum equation (Eq. 6.5), where the pressure term was proportional to mp/ρ^2, the kernel gradient scaled with h^{-4} and the particle mass m was multiplied to convert acceleration into the force. Since the particle mass m may be expressed as density ρ times volume and the particle volume is proportional to h^3, Eq. 6.40 can be simplified to $C_{rep} \sim h^2 p$. Our simulations confirmed that the following estimation yielded useful values for C_{rep}:

$$C_{rep} \approx 10 h^2 p \tag{6.41}$$

where p is an average value of the expected pressure distribution (e.g., p_0, if the density is distributed around ρ_0). From Eq. 6.41 we estimated the value of C_{rep} for the completely filled cases based on the background pressure p_0. Since the density was slightly above 1000 kg/m³ and, consequently, the obtained average pressure was higher than p_0, the chosen values for C_{rep} (shown in Table 6.4) were approximately 50% higher than recommended by Eq. 6.41. Nevertheless, the exact value of C_{rep} was less critical, rather the order of magnitude.

In order to investigate the extent to which our new clearance model improved the quantitative agreement, we repeated three cases of Scenario 1 without it (denoted as

Scenario 2), while using all other parameters as in Scenario 1. To demonstrate the effect of the clearances on the results, we repeated three simulations with geometry B (Figure 6.1), with the clearances between the screws and barrel completely closed (Scenario 3).

To show that the above modifications to viscosity and the screw speed had a vanishing effect on the results, we repeated one simulation according to Scenario 1 with varied viscosity (Scenario 4 with 2 Pas and Scenario 5 with 0.2 Pas) and a varied screw speed (Scenario 6 with 150 rpm). The corresponding changes to other parameters are stated in Table 6.4.

Furthermore, we repeated four simulations of Scenario 1 with a lower resolution (Scenario 7 with Δx = 1 mm, h = 1.2 mm) and less computational expense (112 148 particles) at the cost of the clearance flow, since the fluid particles were too large to pass through the clearances.

Scenario 8 involved simulations of the partially filled screw element (geometry A), where most parameters were the same as in Scenario 1. The body force was set to zero, since a partially filled element does not convey against pressure. Instead of that, we varied the filling ratio. For the initial particle positions, we separated the element into a completely filled section and an empty section according to the filling ratio in the axial direction, which was the simplest way to determine the filling ratio exactly. After the first screw revolution, the fluid was uniformly distributed in the axial direction, which is typical for partially filled conveying elements. The background pressure was set to zero. Although the initial expansion of the fluid was not required for the partially filled element, we applied it to achieve the same number of particles per volume as in the completely filled simulations. In contrast, the initial density ρ_{Init} was determined differently: in the partially filled case, where no compression of the fluid was possible, the expansion always achieved the average pressure of zero and the average density of 1000 kg/m³, regardless of the applied value of ρ_{Init}. Thus, we calculated the initial density for the partially filled simulations based on the particle mass and the initial particle spacing, which yielded ρ_{Init} = 1081 kg/m³.

Furthermore, since stability problems intensified with the decreasing filling ratio in the partially filled simulations, we changed the value of the speed of sound. We reduced c to 7.5 m/s in the partially filled element, which was reasonable in the absence of the body

force. Using that, we simulated the filling ratios of 1, 0.95, 0.9, 0.75 and 0.5. For lower filling ratios, we additionally had to decrease the time step to avoid stability problems (2.5 µs for filling ratios 0.25 and 0.1, and1 µs for filling ratio 0.05).

Eq. 6.41 was not suitable for determining the wall repulsion parameter C_{rep} for the partially filled element, where the fluid was not as compressed as in the completely filled state. Interestingly, we found that the required values of C_{rep} in the partially filled state were significantly larger than those in the completely filled state (C_{rep} was iteratively determined, see Table 6.4 for the obtained values). The reason for that, as well as for the increased stability problems at low filling ratios, is currently unclear, and more detailed investigations are required.

Finally, we repeated two simulations with Scenario 1 with geometry C (Figure 6.1) after we learned that our method for creating geometry A was different from the geometry used by Bierdel[23]. This led to Scenario 9, under which we calculated only 1 revolution to yield pressure drop and power to compare the results with Bierdel[23]. These simulations are not included in the mixing studies described below.

6.5 Results and Discussion

The simulations were performed at 32 Intel XEON cores (2.0 GHz) and 128 GB RAM. The required computation time for one screw revolution ($2 \cdot 10^5$ time steps) and 10^6 particles was ca. 40 h. This might be more than required for mesh-based CFD methods, which can save a lot by varying the spatial resolution. However, if also mixing should be investigated using tracer particles – see Part 2 of this work[62] – a high particle number is required also for CFD which eliminates this drawback.

Figure 6.10 illustrates the axial velocity and the pressure distribution over the cross-section of the completely filled screw element for variable backpressure (snapshots from simulations under Scenario 1). The angular position of the screws was chosen arbitrarily (9° off the vertical direction). The rotation was in the clockwise direction and the conveying direction was towards the observer.

Case a_z = 0 m/s² (top) showed only positive axial velocity values, clearly, the rotating screws conveyed all the material in the same direction (except negligible negative values in

the clearances between screws and barrel, where the pressure caused a slight backflow). This case represents inherent conveying, i.e., the resulting dimensionless flow rate is the A_1-parameter in Eq. 6.1. The highest axial velocity occurred in the nip region, where the screws intermeshed. In the screw channels, far from the nip region, the axial velocity was lower and reached zero at the wall surfaces due to the no-slip condition. The corresponding pressure profile showed the maximum values at the top of the nip region, where the fluid was compressed in a chamber of the geometry, and the minimum values in the back of the screw flights.

With the increasing backpressure (i.e., increasing a_z), the velocity maxima in the nip region remained similar due to the strong enforcement of the flow by the movement of the geometry in this region. However, in the screw channels, the axial velocity decreased with the increasing backpressure and reached negative values at 25 and 30 m/s², which represented a flow through the screw channels against the conveying direction driven by backpressure. Clearly, the flow rate (i.e., the integral of the axial velocity over the cross section area) decreased with the increasing backpressure and became negative between 20 and 25 m/s². The corresponding pressure profiles looked qualitatively similar to the case of 0 m/s², but showed increasing pressure variations in the cross-section as the backpressure increased.

Similar axial velocity profiles of the half-filled screw element (Scenario 8) at 6 snapshots during a ¼ revolution are shown in Figure 6.11 (representative for other filling ratios). The pressure distribution in the partially filled state is not shown, since it was similar to the completely filled state without backpressure. These snapshots were taken from the backside to clearly show the partial filling, thus the rotation is counter-clockwise here and the conveying direction away from the observer. Figure 6.12 shows a 3D view of the half-filled screw element. Specifically, the top view of Fig. 12 shows all particles, whereas in the bottom view the particles adhering to the barrel wall (i.e., with a velocity magnitude of almost zero) are suppressed in order to provide a better visibility of the free surfaces.

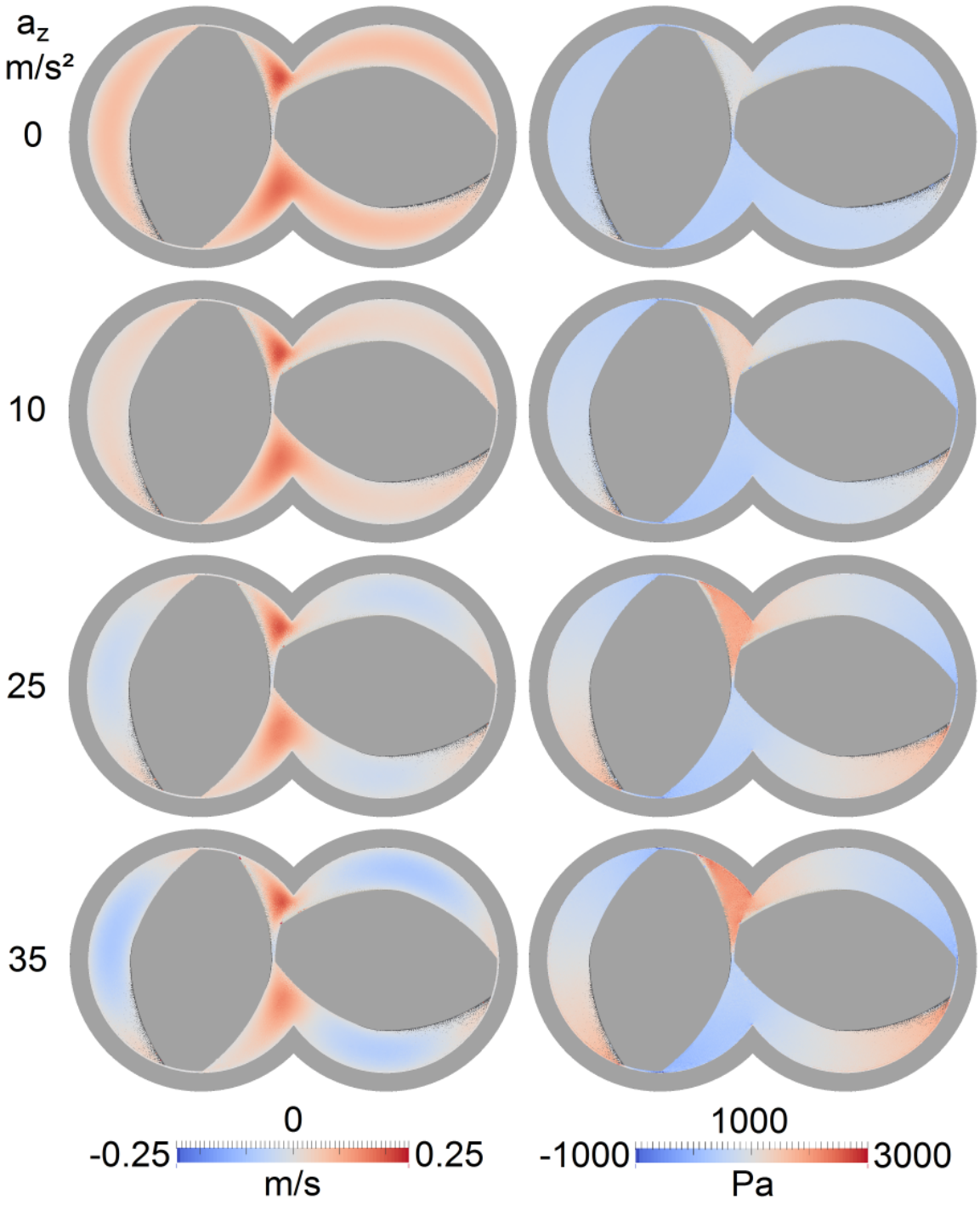

Figure 6.10: Snapshots of the axial velocity (left column) and pressure (right column) in the cross-section of the completely filled screw element (clockwise rotation) for variable axial body force a_z.

Figure 11 and Figure 12 demonstrate how the melt is distributed over the cross section in the partially filled two-flighted conveying element, i.e., located in three regions that are forced along the barrel wall by the screws (like a snow plough clearing the road). The

patterns observed in the empty regions were produced by fluid particles adhering to the screw and barrel surfaces, resulting from the flow through the clearances (in reality, this adhering material can form a thin film on the wall surfaces, at least in surface-wetting materials). As in the completely filled screw element, the maximum values of the axial velocity occurred in the nip region, while the channel regions had lower values. Negative values did not occur, similarly to the case a_z = 0 m/s² of the completely filled element (except slight backflow through the clearances). The latter represents the transition between the partially and completely filled states, since it results from a completely filled section with backpressure approaching zero and from a partially filled section with the filling ratio approaching 1.

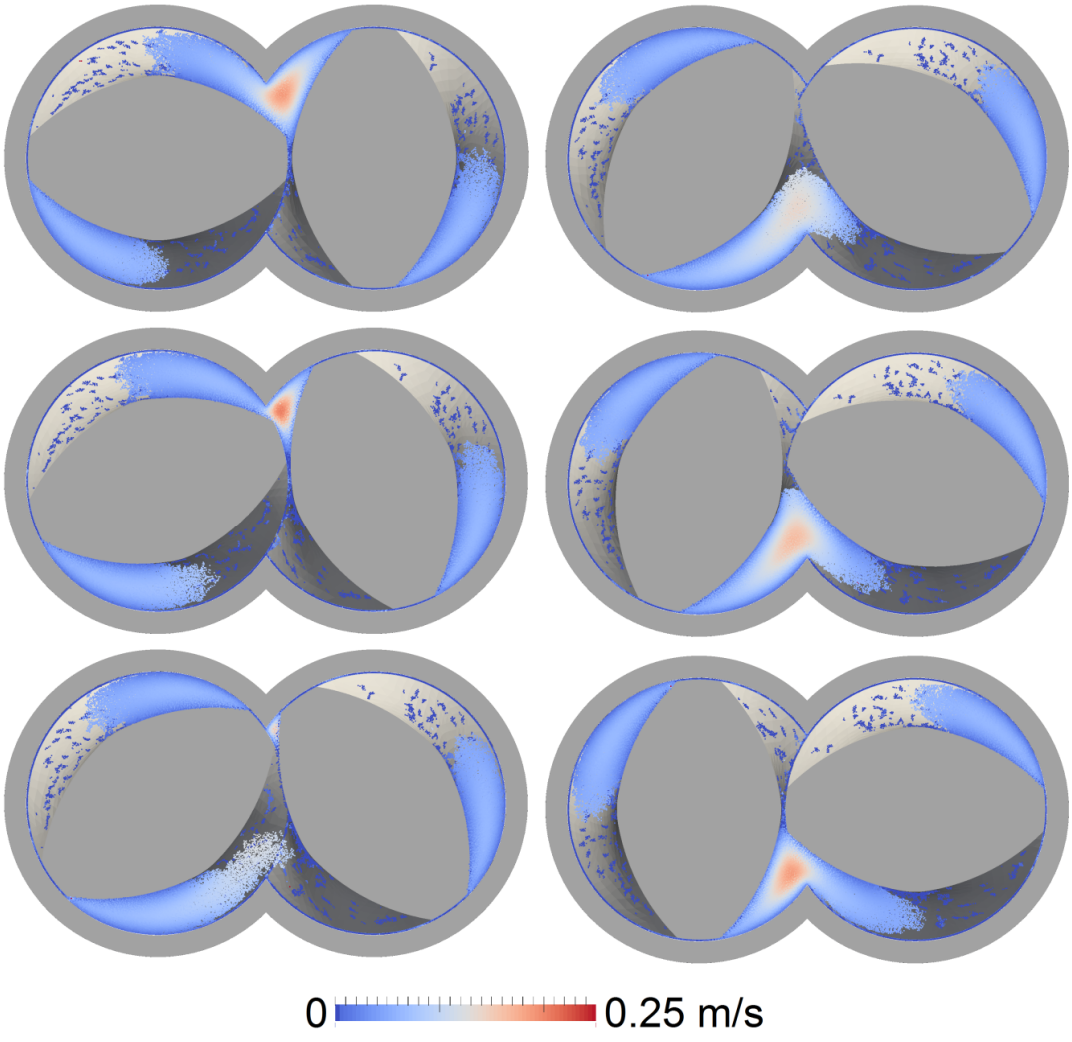

Figure 6.11: Snapshots of the axial velocity in the cross-section of the half-filled screw element during a ¼ revolution (counter-clockwise rotation).

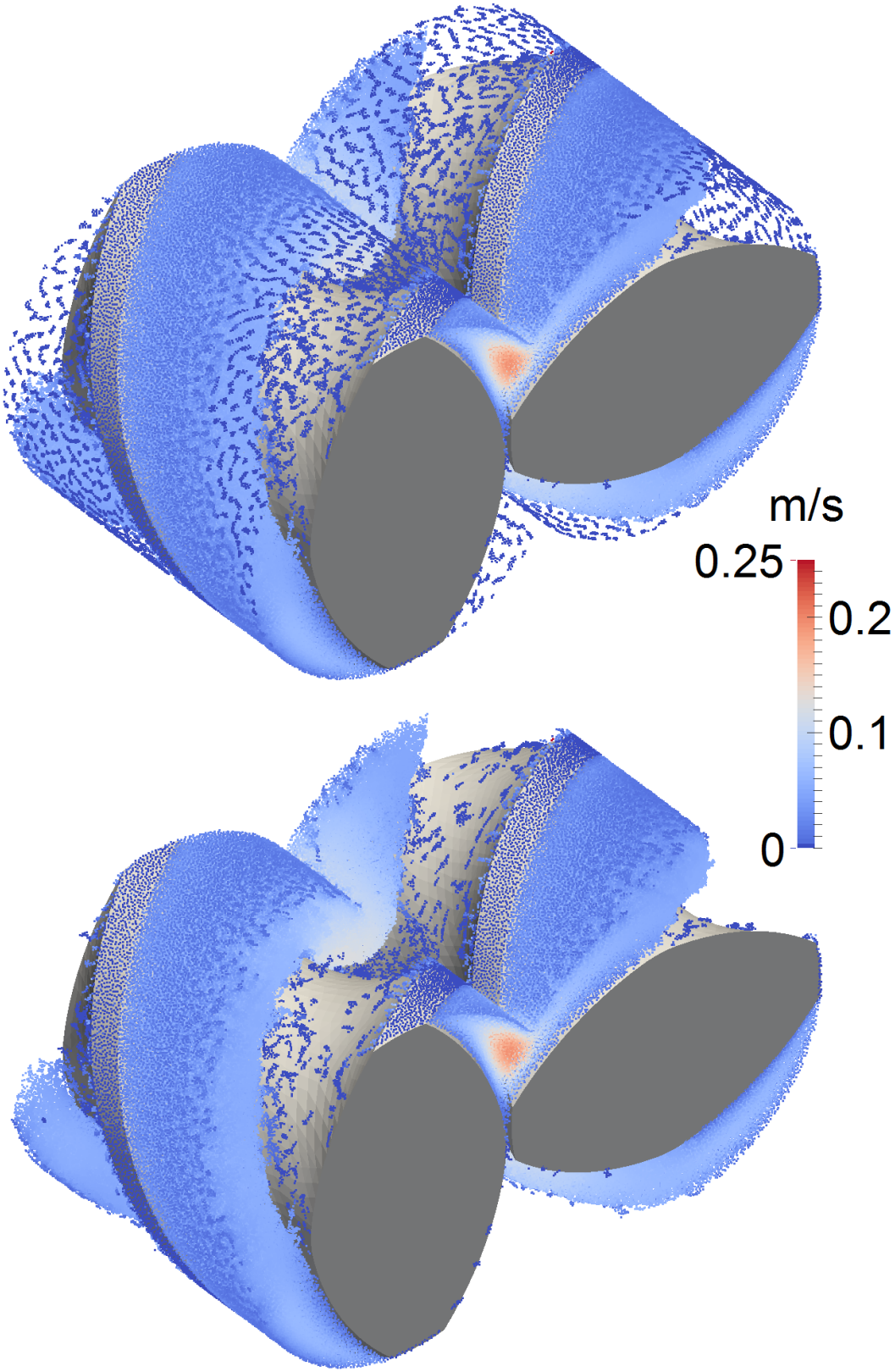

Figure 6.12: Snapshots of the half-filled screw element and axial velocity distribution (clockwise rotation). Top: including all particles, bottom: suppressing particles at the barrel wall.

The representation of the free surface (mainly obvious from Fig. 11) is not fully exact, which is related to the particle discretization. Irregularities at the scale of the particle spacing occurred probably due to the continuous fluid deformation and the related particle rearrangement. This could possibly be improved by including a surface tension model.

Quantitative results for pressure, power and axial force characteristic (see Eqs. 6.1 – 6.3) are shown in Figure 6.13, Figure 6.14 and Figure 6.15. The rotation torque and the axial force were computed from the interaction forces of each fluid particle with the STL meshes of the screws. Figure 6.13 shows the pressure characteristic results for all scenarios, except for the partially filled simulations (Scenario 8 with zero backpressure), compared to the FVM result of Bierdel[23]. All of the results are in good agreement and show the typical pressure characteristic of a completely filled conveying element, i.e., the inherent conveying capacity at the intercept with the abscissa and a decreasing flow rate with the increasing backpressure due to the backflow through the screw channels (as qualitatively discussed above for Figure 6.10).

The region of positive flow rate and positive backpressure is termed “conveying screw”[1] since the screw element actively conveys against the pressure drop. Operation states with negative back pressure and flow rates that are higher than the inherent conveying capacity are referred to as “overrun screw” since they are achieved via a pressure drop in the conveying direction, which supports the flow. This region is only relevant for screw elements with a comparably low inherent conveying capacity and not for a conveying element with a pitch as large as the one we investigated. However, the region of negative flow rates, or the “backward pumping screw,” is of practical relevance, since it represents a backward-conveying element (occasionally termed “left-handed”). Backward-conveying elements have the same shape as the corresponding forward-conveying elements but the inverted torsion. Due to the symmetry, a physically identical situation can be established by using the geometry of the forward conveying element and inverting the flow rate. As such, we yielded backward-conveying conditions with the geometry of the forward-conveying element by increasing the backpressure sufficiently to achieve a negative flow rate.

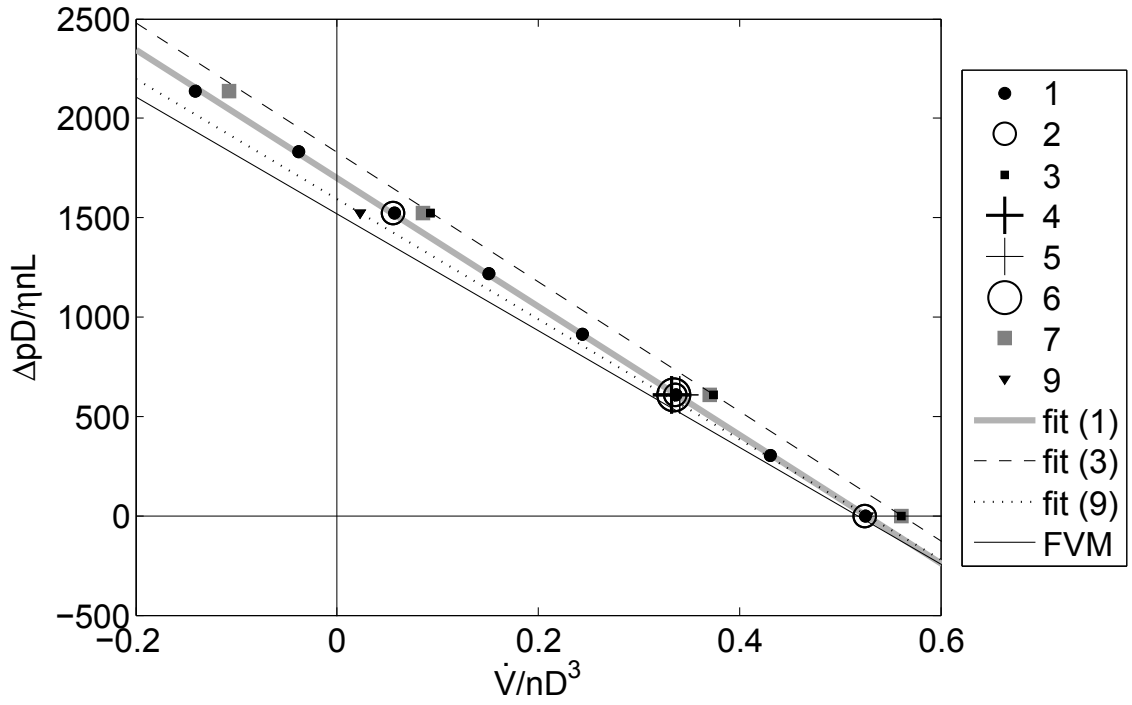

Figure 6.13: Pressure characteristic for the completely filled simulations (Scenarios 1 – 7 and 9) and linear fits for Scenarios 1, 3 and 9 compared with FVM data[23].

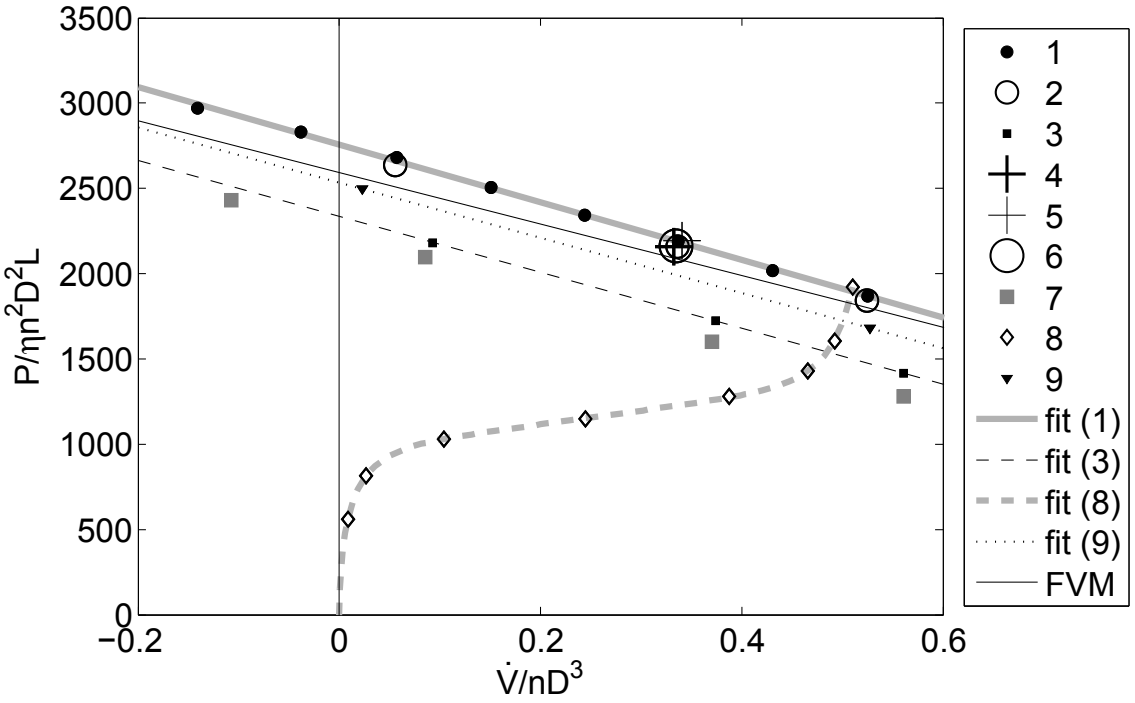

Figure 6.14: Power characteristic in the completely filled simulations (Scenarios 1 – 7 and 9) together with linear fits for Scenarios 1, 3 and 9 in comparison with FVM data[23]. Data points for Scenario 8 and the nonlinear fit represent the partially filled simulations.

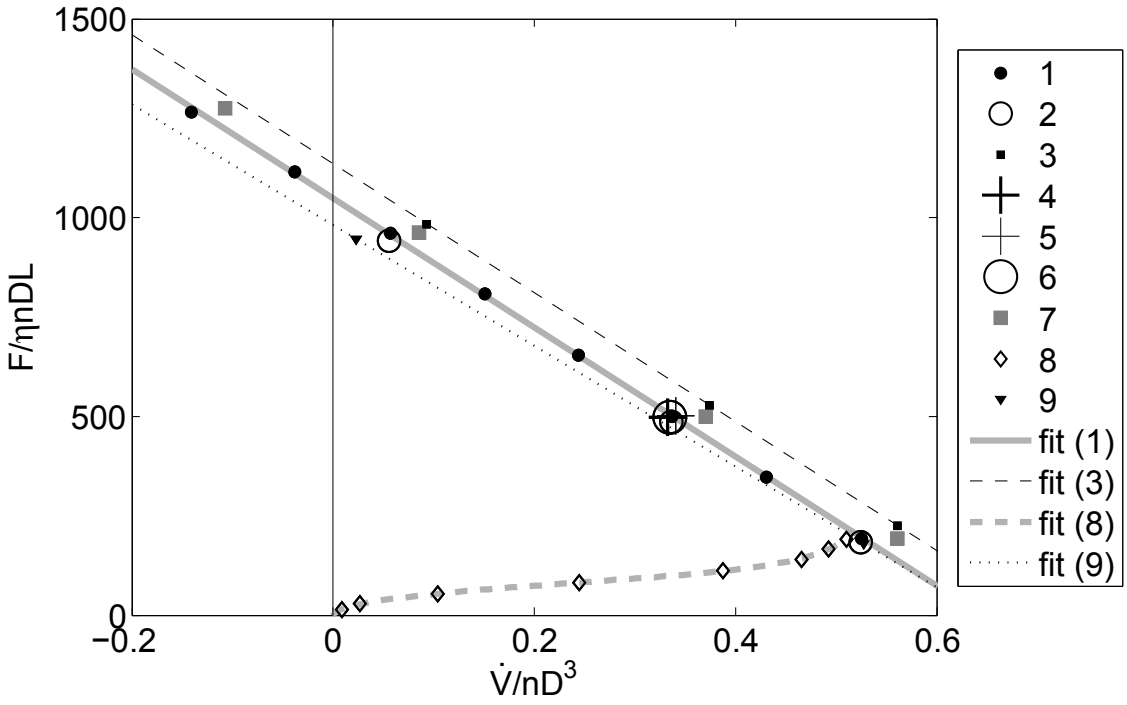

Figure 6.15: Axial force characteristic for the completely filled simulations (Scenarios 1 – 7 and 9) and linear fits for Scenarios 1, 3 and 9. Data points for Scenario 8 and the nonlinear fit represent the partially filled simulations.

Scenarios 1, 2, 4, 5 and 6 yielded the equivalent pressure characteristic, and Scenarios 3 and 7 deviated significantly. This is reasonable, since under Scenario 3 (geometry B with closed clearances) no backflow through the clearances occurred and, consequently, the achieved flow rate was higher than for geometry A. Although Scenario 7 also involved geometry A, the clearance flow was not present there due to the coarser resolution (1mm), which prevented fluid particles from passing the 0.5 mm clearances. As a result, Scenario 7 yielded a similar pressure characteristic as Scenario 3.

The coincidence of Scenarios 1, 4, 5 and 6 confirms the independency of the pressure characteristic on variations of viscosity and screw speed in the case of Newtonian, temperature-independent, creeping flow.

The similarities of Scenarios 1 (with the clearance model) and 2 (without the clearance model) show that our new clearance model has a vanishing effect on the pressure characteristic. The reason is the type of flow within the clearances between the screws and the barrel, which is the superposition of a drag flow (caused by the relative velocity) and a

pressure-driven flow (caused by the pressure difference between adjacent screw channels). The clearance flow is dominated by the drag flow, which was e.g. shown by Bierdel[23] and can be easily confirmed as follows: The pressure difference along the clearance in circumferential direction of about 2000 Pa (see Figure 6.10) and the viscosity of 1 Pas yield an average velocity of 0.0083 m/s in a 0.5 mm tight and ca. 5 mm long clearance (based on the analytical solution for the Poiseuille flow, see e.g., Eq. 6.17), whereas the circumferential velocity of 0.188 m/s at 60 rpm yields an average velocity of 0.094 m/s for the drag flow, which is about 10 times as much. As shown above, the SPH equations yield the exact velocity in unresolved clearances for the steady state in a pure Couette flow.

Together with the small volume of the clearances compared to the entire volume, the global variables show vanishing errors for the considered simplified scenario of a Newtonian, temperature-independent fluid. However, in further developments, which account for the local energy dissipation rate and local temperature of the fluid, significant errors can be expected without appropriate clearance modeling.

Although the SPH simulations for Scenarios 1 - 7 yielded good results, they deviated somewhat from the FVM results[23], especially in terms of pressure drop at zero flow rate that was about 12% higher in our simulations for geometry A. The main reason was the above-mentioned difference in the method for creating the clearances, which yielded the same main dimensions of the screw element but smaller clearance distances in some regions between the screws and a higher pressure drop in geometry A than in geometry C. When geometry C was generated via the same clearance formation method as the one described by Bierdel[23], the agreement of the pressure characteristic significantly improved (Scenario 9) and the remaining deviation of the axis intercepts A_1 and A_2 was below 5%. Clearly, numerical methods are never exact and the deviations may be caused by small errors of both methods. The values of the determined parameters A_1 and A_2 for the fits under Scenarios 1, 3 and 9 and the FVM results[23] are shown in Table 6.5.

The power characteristics shown in Figure 6.14 show analogous results: they were nearly identical for Scenarios 1, 2, 4, 5 and 6, but for Scenarios 3 and 7 yielded a significantly lower driving power due to the absence of clearance flow between the screws and barrel with correspondingly high power consumption. The power characteristic of geometry A

(Scenario 1) has higher power values than that of geometry C (Scenario 9) due to the smaller clearance distance between the screws. The obtained B_1 and B_2 parameter values are shown in Table 6.5. The deviation between Scenario 9 and the FVM results[23] was below 3% for the B_2 parameter and almost 10% for the B_1 parameter. With increasing backpressure, i.e., decreasing flow rate, the power of the completely filled element increased due to the pumping power required for conveying against a pressure gradient and the additional dissipation power of the pressure-driven backflow.

Table 6.5: Resulting screw parameters.

Scenario	1	3	8	9	FVM [23]
A_1	0.526	0.561	0.510	0.527	0.518
A_2	1699	1829	-	1594	1521
B_1	1.629	1.425	-	1.566	1.714
B_2	2756	2334	-	2535	2595
B_5	1866	1415	1921	1681	1812
C_1	0.645	0.700	-	0.646	-
C_2	1048	1135	-	980.8	-
C_5	193.4	225.4	191.7	179.7	-

Note, that for the partially filled element (Scenario 8) the flow rate is directly related to the filling ratio (this correlation is shown in detail in Fig. 16). With the decreasing flow rate (and filling ratio), a nonlinear decrease of the driving power was observed. The nonlinearity was especially significant above a filling ratio of 0.75 and below 0.25, which was possibly due to higher shear rates near the borders of the screw channels than in the center. The reason for the strong increase of the driving power at zero flow rate is the clearance flow. I.e., even when the screw is almost empty, the clearances between screws and barrel are filled, causing a significant power consumption due to the high shear rates there.

In contrast to the pressure characteristic, a power characteristic exists for the partially filled state (Scenario 8). The driving power in the partially filled state coincides with the

completely filled state at the inherent conveying, where the element is completely filled and operated without pressure drop. The driving power at that point is described via parameter B_5 as proposed by Kohlgrüber[63] (see Table 6.5). It is the maximum of the dimensionless driving power in the partially filled state, and can be calculated from the pressure characteristic of the completely filled element according to Eq. 6.2 using parameters A_1, B_1 and B_2 (i.e., $B_5 = B_2\ (1 - A_1/\ B_1)$). However, a small deviation between Scenarios 1 and 8 occurred (both for A_1 and B_5) due to the reduced speed of sound (7.5 m/s vs. 15 m/s) in the partially filled simulations (Scenario 8).

With the decreasing flow rate, a nonlinear decrease in the driving power was observed. The nonlinearity was especially significant above a filling ratio of 0.75 and below 0.25, which was possibly due to a lower channel depth and higher shear rates near the borders of the screw channels than in its center.

The axial force characteristics (Figure 6.15) showed similar trends. These data were not shown by Bierdel[23] since they are of less practical significance, and thus, no comparison to FVM data can be made. However, for the construction of the screw's axial bearings it is important to consider the axial forces. Clearly, in the completely filled element the axial force strongly depends on the backpressure, whereas in the partially filled screw element it decreases with the decreasing flow rate (and the decreasing filling ratio), similarly to the driving power. Table 6.5 shows the resulting parameters C_1, C_2 and C_5 (the latter is analogues to B_5 for the axial force characteristic and can be calculated from the axial force characteristic of the completely filled screw element acc. to Eq. 6.3 ($C_5 = C_2\ (1 - A_1/\ C_1)$).

Results for the partially filled screw element are shown in Figure 6.16 in detail. We normalized the flow rate, the power and the axial force between 0 and 1 to achieve a more general representation. To that end, we used the normalized flow rate proposed by Pawlowski[38]:

$$\Lambda = \frac{\dot{V}}{\dot{V}_{f=1}} = \frac{\dot{V}}{A_1 n D^3} \tag{6.42}$$

where $\dot{V}_{f=1}$ is the flow rate of the completely filled screw element operated without pressure drop (i.e., inherent conveying). Similarly, we described the normalized power Π_P and normalized axial force Π_F:

$$\Pi_P = \frac{P}{P_{f=1}} = \frac{P}{B_5 \eta n^2 D^2 L} \tag{6.43}$$

$$\Pi_F = \frac{F}{F_{f=1}} = \frac{F}{C_5 \eta n D L} \tag{6.44}$$

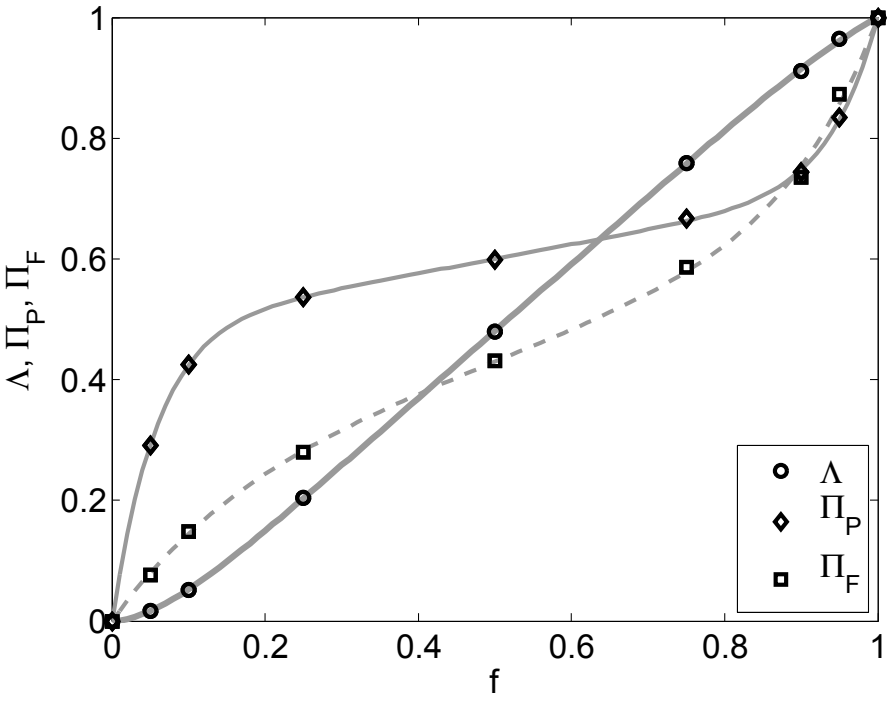

Figure 6.16: Simulation results and fits for normalized flow rate Λ, power Π_P and axial force Π_F versus filling ratio f.

Although the normalized flow rate was almost equal to the filling ratio (Figure 6.16), slight nonlinearities occurred at the filling ratios $f < 0.2$ and $f > 0.8$. Thus, the curves for power and axial force versus filling ratio looked slightly different to the corresponding curves in Figure 6.14 and Figure 6.15, where the abscissa showed the flow rate. Similar curves for the flow rate and the power versus filling ratio of a partially filled conveying element were also shown by Pokriefke[35], who used the FVM method with an Eulerian multiphase model. We applied the following mathematical functions to fit these data:

$$\Lambda = f - \alpha_0 (1-f)\left[1-(1-f)^{\phi_0}\right] + \alpha_1 f\left(1-f^{\phi_1}\right) \tag{6.45}$$

$$\Pi_P = f + \beta_0 (1-f)\left[1-(1-f)^{\chi_0}\right] - \beta_1 f\left(1-f^{\chi_1}\right) \tag{6.46}$$

$$\Pi_F = f + \gamma_0 (1-f)\left[1-(1-f)^{\psi_0}\right] - \gamma_1 f\left(1-f^{\psi_1}\right) \tag{6.47}$$

The values of the fitted parameters α, β, γ, ϕ, χ, ψ (index 0 and 1) are given in Table 6.6.

Table 6.6: Fitted parameters of the partially filled screw element (for index 0 and 1).

	0	1
α	0.0765	0.0373
β	0.480	0.280
γ	0.182	0.321
ϕ	13	11
χ	16	15
ψ	6	8

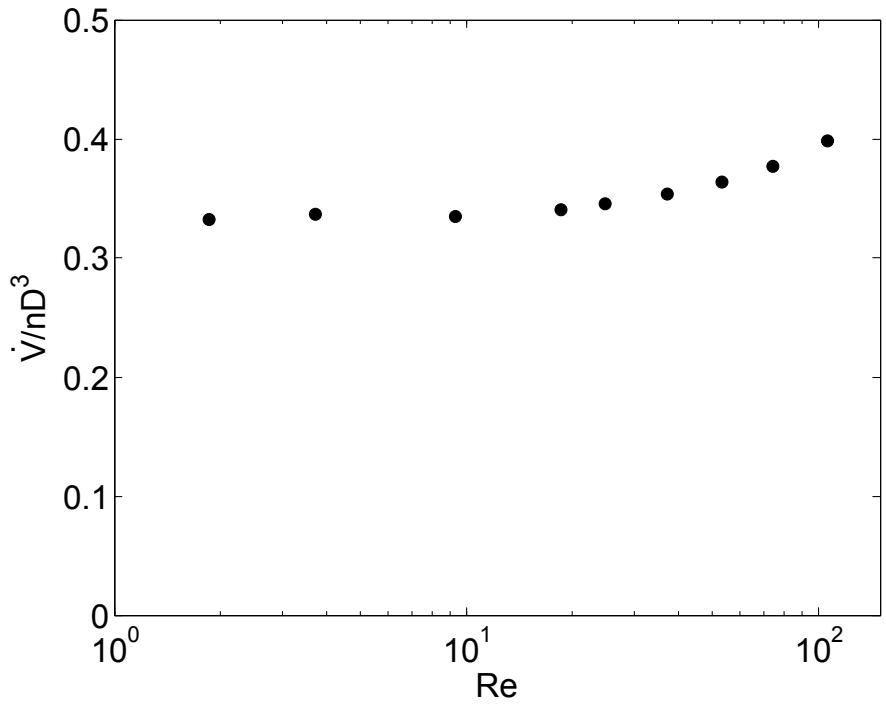

Figure 6.17: Dimensionless flow rate versus the Reynolds number.

In order to confirm that the resulting Reynolds number of 3.72 was in the creeping flow regime, additional simulations were performed that were identical to those of Scenarios 4 and 5 (Table 6.4) but with varying viscosity values down to 0.035 Pas, resulting in Re numbers as large as 106. The dimensionless flow rate versus the Reynolds number is shown in Figure 6.17 (together with the corresponding simulations for Scenarios 1, 4, 5 and 6). As can be seen the flow rate was constant for $Re \leq 10$, but deviated significantly for $Re > 10$. This agrees well with experimental observations of Pawlowski[38] who showed that at $Re \leq 40$ the pressure characteristic of a single-screw extruder did not depend on the Reynolds number.

6.6 Summary and Conclusions

In this work, we presented a new approach based on the SPH method for detailed flow simulations in complex geometries. We applied this to the simulation of a Newtonian, temperature-independent flow in a completely and partially filled conveying element of a co-rotating twin-screw extruder.

We developed a new model that accounts for the flow in unresolved clearances. The model was in exact agreement with the analytical solution for a Newtonian, developed steady-state flow and the deviations for unsteady flow were low. For the investigated conveying element, our results were in excellent agreement with the FVM results from the literature, demonstrating that our method accounts correctly for the flow field under the simplified scenario of a Newtonian, temperature-independent flow.

Several variations of parameters and geometry showed that the dimensionless results were robust with respect to viscosity, screw speed and resolution, whereas the clearance flow had significant impact on the results. However, without considering the local energy dissipation rate and the temperature inhomogeneity, the impact of the developed clearance model was low, i.e., the results of the simulations including the clearance model were almost the same compared to the simulations without the clearance model. Nevertheless, for future investigations including the temperature field significant errors can be expected in the local dissipation rate and temperature in clearances without appropriate clearance modeling or sufficient resolution.

As stated above, we applied our method to examine the flow in a partially filled screw element, which is a major advantage of the SPH method over mesh-based CFD. This is the first study that offers a detailed analysis of the flow field in a partially filled conveying element based on SPH.

Clearly, the chosen values for viscosity (1 Pas) and pressure gradient (0 – 35 kPa/m) are not typical for real extrusion processes. Also, the used screw speed (60 rpm) was relatively low, specifically when considering processes in the polymer industry. As explained in detail above, the only limitation for the computational expense is the Reynolds number. Thus, there is no limitation for the screw speed as long as the Reynolds number is not changed. Using the 10-fold screw speed and the 10-fold viscosity would not require more time steps per screw revolution, i.e., the computational expense per screw revolution would be the same with 600 rpm and 10 Pas. A further increase of the viscosity (and correspondingly the pressure gradient) up to typical values in the order of 1000 Pas (factor 100) would decrease the Reynolds number and increase the number of time steps per screw revolution by the same factor. Clearly, this would lead to inacceptable computation times. It can be expected that implicit SPH schemes would be beneficial and could significantly reduce the computation costs.[64–66] However, it can be easily obtained from the Stokes equations that in the creeping flow regime a variation of the viscosity (or a constant prefactor for a non-Newtonian viscosity function) would not change the velocity field. Only the pressure gradients would be changed by the same factor as the viscosity. This makes the question of higher viscosities unnecessary. In contrast, the thermal energy equation would be strongly affected by a changed viscosity value, thus the use of the unchanged (real) viscosity value would be required here. At first sight, the use of two different viscosity values (functions) for the momentum and energy equations seems to be a contradiction, however, the viscosity reduction factor required for the momentum equation can be considered as an internal numerical requirement of the method, which has theoretically no effect to the solution of the momentum equation (except the pressure values, which are not coupled to the energy equation for incompressible flow, and which could be easily scaled with the applied viscosity factor).

The assumed Newtonian, isothermal flow is not the case in real extrusion processes. As this is the first study, which applied SPH for the detailed and quantitative analysis of the

flow in a geometry typical for co-rotating twin-screw extruders, the focus was mainly on the complex screw geometry and the required boundary conditions. The obtained agreement of this simplified scenario with FVM data is a robust basis for further steps in this field. SPH models for non-Newtonian flow, thermal energy and viscoelasticity are existing and have to be included in future work.

The proposed method is a unique tool for further investigations of the flow in various types of screw elements, e.g. kneading and mixing elements. Its main advantages for co-rotating twin-screw extruders compared to mesh-based methods are: (i) SPH is mesh-free, (ii) it can easily account for free surface flows, and (iii) it facilitates the investigation of mixing by tracking tracer particles. In particular, as a Lagrangian method, SPH inherently accounts for convective mixing without numerical diffusion, as typically a drawback with mesh-based methods. A detailed analysis of the mixing phenomena is presented in Part 2[62]. Being the basis for refining empirical models of completely and partially filled screw elements, our results may lead to further improvement of more time-efficient 1D simulation tools for the study of the entire extrusion process. This can significantly facilitate design, optimization and scale-up of extrusion processes.

6.7 Abbreviations

1D	one-dimensional
3D	three-dimensional
CAD	computer aided design
CFL	Courant-Friedrichs-Lewy
FEM	finite element method
FVM	finite volume method
SPH	smoothed particle hydrodynamics
STL	surface tessellation language

6.8 Nomenclature

Latin symbols

A_1, A_2	axis intercepts of the pressure characteristic [-]
$A_{contact}$	wall contact area [m²]

a	mass specific body force [m/s²]
B_1, B_2	axis intercepts of the power characteristic [-]
B_5	dimensionless driving power at the inherent conveying [-]
C	centerline distance [m]
C_1, C_2	axis intercepts of the axial force characteristic [-]
C_5	dimensionless axial force at the inherent conveying [-]
C_{rep}	parameter for the repulsive wall force [N]
c	speed of sound [m/s]
D	barrel diameter [m]
D_i	inner screw diameter [m]
D_o	outer screw diameter [m]
f	filling ratio [-]
f_{ab}	parameter used in the tensile correction [-]
f_{corr}	velocity correction factor [-]
F	screw axial force [N]
F_{rep}	repulsive wall force [N]
H	clearance distance [m]
h	smoothing length [m]
L	length [m]
m	mass [kg]
N	number of revolutions [-]
n	screw speed [s^{-1}]
P	power [W]
p	pressure [Pa]
p_0	background pressure [Pa]
$\vec{r}$	particle position [m]
r	wall distance [m]
r_0	interaction length of the repulsive wall force [m]
R	parameter used in the tensile correction [m^5/kg s²]
Re	Reynolds number [-]
Δt	time step [s]
$\dot{V}$	flow rate [m³/s]

$\vec{v}$	velocity [m/s]
$W_{ab} = W\left(\lvert\vec{r}_{ab}\rvert, h\right)$	kernel function evaluated for particles *a* and *b* [m^{-3}]
Δx	particle spacing [m]

Greek symbols

α	artificial viscosity [-]
$\alpha_0, \alpha_1, \beta_0, \beta_1, \gamma_0, \gamma_1$	fitted parameters [-]
η	dynamic viscosity [Pas]
Λ	normalized flow rate [-]
ν	kinematic viscosity [m^2/s]
Π_F	normalized axial force [-]
Π_P	normalized driving power [-]
ρ	density [kg/m^3]
ρ_0	reference density in the equation of state [kg/m^3]
τ_W	wall shear stress [Pa]
$\phi_0, \phi_1, \chi_0, \chi_1, \psi_0, \psi_1$	fitted parameters [-]

6.9 References

(1) Kohlgrüber, K. *Co-Rotating Twin-Screw Extruders*; Carl Hanser Publishers: Munich, 2008.

(2) Ghebre-Sellassie, I.; Martin, C. *Pharmaceutical Extrusion Technology*; Marcel Dekker Inc.: New York, 2003.

(3) Kleinebudde, P. Pharmazeutisches Produktdesign: Gezielte Freisetzung von Wirkstoffen durch unterschiedliche Extrusionstechniken. *Chemie Ing. Tech.* **2011**, *83*, 589–597.

(4) Breitenbach, J. Melt Extrusion: From Process to Drug Delivery Technology. *Eur. J. Pharm. Biopharm.* **2002**, *54*, 107–117.

(5) Repka, M. A.; Gutta, K.; Prodduturi, S.; Munjal, M.; Stodghill, S. P. Characterization of Cellulosic Hot-Melt Extruded Films Containing Lidocaine. *Eur. J. Pharm. Biopharm.* **2005**, *59*, 189–196.

(6) White, J. L.; Chen, Z. Simulation of Non-Isothermal Flow in Modular Co- Rotating Twin Screw Extrusion. *Polym. Eng. Sci.* **1994**, *34*, 229–237.

(7) Potente, H.; Hanhart, W. Design and Processing Optimization of Extruder Screws. *Polym. Eng. Sci.* **1994**, *3*, 937–945.

(8) Vergnes, B.; Della Valle, G.; Delamare, L. A Global Computer Software for Polymer Flows in Corotating Twin Screw Extruders. *Polym. Eng. Sci.* **1998**, *38*, 1781–1792.

(9) Potente, H.; Bastian, M.; Flecke, J. Design of a Compounding Extruder by Means of the SIGMA Simulation Software. *Adv. Polym. Technol.* **1999**, *18*, 147–170.

(10) White, J. L.; Kim, E. K.; Keum, J. M.; Jung, H. C. Modeling Heat Transfer in Screw Extrusion With Special Application to Modular Self-Wiping Co-Rotating Twin-Screw Extrusion. *Polym. Eng. Sci.* **2001**, *41*, 1448–1455.

(11) Potente, H.; Kretschmer, K. Simulation and Evaluation of Compounding Processes. *Macromol. Mater. Eng.* **2002**, *287*, 758–772.

(12) Prat, L.; Guiraud, P.; Rigal, L.; Gourdon, C. A One Dimensional Model for the Prediction of Extraction Yields in a Two Phases Modified Twin-Screw Extruder. *Chem. Eng. Process.* **2002**, *41*, 743–751.

(13) Choulak, S.; Couenne, F.; Le Gorrec, Y.; Jallut, C.; Cassagnau, P.; Michel, A. Generic Dynamic Model for Simulation and Control of Reactive Extrusion. *Ind. Eng. Chem. Res.* **2004**, *43*, 7373–7382.

(14) Vergnes, B.; Berzin, F. Modeling of Reactive Systems in Twin-Screw Extrusion: Challenges and Applications. *Comptes Rendus Chim.* **2006**, *9*, 1409–1418.

(15) Bahloul, W.; Oddes, O.; Bounor-Legaré, V.; Mélis, F.; Cassagnau, P.; Vergnes, B. Reactive Extrusion Processing of Polypropylene/TiO2 Nanocomposites by In Situ Synthesis of the Nanofillers: Experiments and Modeling. *AIChE J.* **2011**, *57*, 2174–2184.

(16) Teixeira, C.; Gaspar-Cunha, A.; Covas, J. A. Flow and Heat Transfer Along the Length of a Co-Rotating Twin Screw Extruder. *Polym. Plast. Technol. Eng.* **2012**, *51*, 1567–1577.

(17) Eitzlmayr, A.; Koscher, G.; Reynolds, G.; Huang, Z.; Booth, J.; Shering, P.; Khinast, J. Mechanistic Modeling of Modular Co-Rotating Twin-Screw Extruders. *Int. J. Pharm.* **2014**, *474*, 157–176.

(18) Ishikawa, T. 3-D Non-Isothermal Flow Field Analysis and Mixing Performance Evaluation of Kneading Blocks in a Co-Rotating Twin Srew Extruder. *Polym. Eng. Sci.* **2001**, *41*, 840–849.

(19) Bertrand, F.; Thibault, F.; Delamare, L.; Tanguy, P. A. Adaptive Finite Element Simulations of Fluid Flow in Twin-Screw Extruders. *Comput. Chem. Eng.* **2003**, *27*, 491–500.

(20) Ficarella, A.; Milanese, M.; Laforgia, D. Numerical Study of the Extrusion Process in Cereals Production: Part I. Fluid-Dynamic Analysis of the Extrusion System. *J. Food Eng.* **2006**, *73*, 103–111.

(21) Ficarella, A.; Milanese, M.; Laforgia, D. Numerical Study of the Extrusion Process in Cereals Production: Part II. Analysis of Variance. *J. Food Eng.* **2006**, *72*, 179–188.

(22) Barrera, M. A.; Vega, J. F.; Martínez-Salazar, J. Three-Dimensional Modelling of Flow Curves in Co-Rotating Twin-Screw Extruder Elements. *J. Mater. Process. Technol.* **2008**, *197*, 221–224.

(23) Bierdel, M. Computational Fluid Dynamics. In *Co-Rotating Twin-Screw Extruders*; Kohlgrüber, K., Ed.; Carl Hanser Publishers: Munich, 2008.

(24) Conzen, C. Numerische und experimentelle Untersuchungen zu Transportvorgängen in Schneckenmaschinen, Universität Kassel, 2008.

(25) Rodríguez, E. O. Numerical Simulations of Reactive Extrusion in Twin Screw Extruders, Waterloo, Canada, 2009.

(26) Haghayeghi, R.; Khalajzadeh, V.; Farahani, M. F.; Bahai, H. Experimental and CFD Investigation on the Solidification Process in a Co-Rotating Twin Screw Melt Conditioner. *J. Mater. Process. Technol.* **2010**, *210*, 1464–1471.

(27) Vyakaranam, K. V.; Ashokan, B. K.; Kokini, J. L. Evaluation of Effect of Paddle Element Stagger Angle on the Local Velocity Profiles in a Twin-Screw Continuous Mixer with Viscous Flow Using Finite Element Method Simulations. *J. Food Eng.* **2012**, *108*, 585–599.

(28) Sarhangi Fard, A.; Hulsen, M. A.; Meijer, H. E. H.; Famili, N. M. H.; Anderson, P. D. Adaptive Non-Conformal Mesh Refinement and Extended Finite Element Method for Viscous Flow inside Complex Moving Geometries. *Int. J. Numer. methods fluids* **2012**, *68*, 1031–1052.

(29) Sarhangi Fard, A.; Hulsen, M. A.; Meijer, H. E. H.; Famili, N. M. H.; Anderson, P. D. Tools to Simulate Distributive Mixing in Twin-Screw Extruders. *Macromol. Theory Simulations* **2012**, *21*, 217–240.

(30) Sarhangi Fard, A.; Anderson, P. D. Simulation of Distributive Mixing inside Mixing Elements of Co-Rotating Twin-Screw Extruders. *Comput. Fluids* **2013**, *87*, 79–91.

(31) Hétu, J.-F.; Ilinca, F. Immersed Boundary Finite Elements for 3D Flow Simulations in Twin-Screw Extruders. *Comput. Fluids* **2013**, *87*, 2–11.

(32) Rathod, M. L.; Kokini, J. L. Effect of Mixer Geometry and Operating Conditions on Mixing Efficiency of a Non-Newtonian Fluid in a Twin Screw Mixer. *J. Food Eng.* **2013**, *118*, 256–265.

(33) Sobhani, H.; Anderson, P. D.; Meijer, H. H. E.; Ghoreishy, M. H. R.; Razavi-Nouri, M. Non-Isothermal Modeling of a Non-Newtonian Fluid Flow in a Twin Screw Extruder Using the Fictitious Domain Method. *Macromol. Theory Simulations* **2013**, *22*, 462–474.

(34) Durin, A.; De Micheli, P.; Nguyen, H.-C.; David, C.; Valette, R.; Vergnes, B. Comparison between 1D and 3D Approaches for Twin-Screw Extrusion Simulation. *Int. Polym. Process.* **2014**, *29*, 641–648.

(35) Pokriefke, G. Numerische Analyse reibungsbehafteter Strömungen in teilgefüllten Extrudern, Universität der Bundeswehr Hamburg, 2005.

(36) Cleary, P. W.; Robinson, M. Understanding Viscous Fluid Transport and Mixing in a Twin-Screw Extruder. In *8th International Conference on CFD in Oil & Gas, Metallurgical and Process Industries*; Trondheim, Norway, 2011.

(37) Eitzlmayr, A.; Koscher, G.; Khinast, J. A Novel Method for Modeling of Complex Wall Geometries in Smoothed Particle Hydrodynamics. *Comput. Phys. Commun.* **2014**, *185*, 2436–2448.

(38) Pawlowski, J. *Die Ähnlichkeitstheorie in der physikalisch-technischen Forschung*; Springer Publishers: Berlin/Heidelberg, Germany, 1971.

(39) Booy, M. L. Geometry of Fully Wiped Twin-Screw Equipment. *Polym. Eng. Sci.* **1978**, *18*, 973–984.

(40) Rauwendaal, C. *Polymer Extrusion*; 4th ed.; Hanser Publishers: Munich, 2001.

(41) Monaghan, J. J. Smoothed Particle Hydrodynamics. *Annu. Rev. Astron. Astrophys.* **1992**, *30*, 543–574.

(42) Monaghan, J. J. Simulating Free Surface Flows with SPH. *J. Comput. Phys.* **1994**, *110*, 339–406.

(43) Monaghan, J. J. SPH without a Tensile Instability. *J. Comput. Phys.* **2000**, *159*, 290–311.

(44) Monaghan, J. J. Smoothed Particle Hydrodynamics. *Reports Prog. Phys.* **2005**, *68*, 1703–1759.

(45) Morris, J. P.; Fox, P. J.; Zhu, Y. Modeling Low Reynolds Number Incompressible Flows Using SPH. *J. Comput. Phys.* **1997**, *136*, 214–226.

(46) Adami, S.; Hu, X. Y.; Adams, N. A. A Transport-Velocity Formulation for Smoothed Particle Hydrodynamics. *J. Comput. Phys.* **2013**, *241*, 292–307.

(47) Gomez-Gesteira, M.; Rogers, B. D.; Dalrymple, R. A.; Crespo, A. J. C. Numerical Simulation of Interfacial Flows by Smoothed Particle Hydrodynamics. *J. Hydraul. Res.* **2010**, *48*, 6–27.

(48) Liu, G.-R.; Liu, M. B. *Smoothed Particle Hydrodynamics: A Meshfree Particle Method*; Liu, G.-R.; Liu, M. B., Eds.; World Scientific Publishing Co. Pte. Ltd.: Singapore, 2003.

(49) Monaghan, J. J. On the Problem of Penetration in Particle Methods. *J. Comput. Phys.* **1989**, *82*, 1–15.

(50) Price, D. J. Smoothed Particle Hydrodynamics and Magnetohydrodynamics. *J. Comput. Phys.* **2012**, *231*, 759–794.

(51) Kloss, C.; Goniva, C.; Hager, A.; Amberger, S.; Pirker, S. Models, Algorithms and Validation for Opensource DEM and CFD-DEM. *Prog. Comput. Fluid Dyn. An Int. J.* **2012**, *12*, 140–152.

(52) Monaghan, J. J.; Kajtar, J. B. SPH Particle Boundary Forces for Arbitrary Boundaries. *Comput. Phys. Commun.* **2009**, *180*, 1811–1820.

(53) Monaghan, J. J.; Kos, A. Solitary Waves on a Cretan Beach. *J. Waterw. Port, Coast. Ocean Eng.* **1999**, *125*, 145–154.

(54) Feldman, J.; Bonet, J. Dynamic Refinement and Boundary Contact Forces in SPH with Applications in Fluid Flow Problems. *Int. J. Numer. Methods Eng.* **2007**, *72*, 295–324.

(55) Vacondio, R.; Rogers, B. D.; Stansby, P. K.; Mignosa, P.; Feldman, J. Variable Resolution for SPH: A Dynamic Particle Coalescing and Splitting Scheme. *Comput. Methods Appl. Mech. Eng.* **2013**, *256*, 132–148.

(56) Grenier, N.; Antuono, M.; Colagrossi, A.; Le Touzé, D.; Alessandrini, B. An Hamiltonian Interface SPH Formulation for Multi-Fluid and Free Surface Flows. *J. Comput. Phys.* **2009**, *228*, 8380–8393.

(57) Bonet, J.; Lok, T.-S. L. Variational and Momentum Preservation Aspects of Smooth Particle Hydrodynamic Formulations. *Comput. Methods Appl. Mech. Eng.* **1999**, *180*, 97–115.

(58) Pozorski, J.; Wawrenczuk, A. SPH Computation of Incompressible Viscous Flows. *J. Theor. Appl. Mech.* **2002**, *40*, 917–937.

(59) Kruisbrink, A. C. H.; Pearce, F. R.; Yue, T.; Cliffe, K. A.; H. P. Morvan. *SPH Concepts for Continuous Wall and Pressure Boundaries*; Rung, T.; Ulrich, C., Eds.; Schriftenreihe Schiffbau: Hamburg, 2011; pp. 298–304.

(60) Mahmood, O.; Kassiotis, C.; Violeau, D.; Ferrand, M.; Denis, C. Effect of Wall Boundary Treatment in SPH for Modelling Turbulent Flows with Inlet/outlet. In *6th International SPHERIC Workshop*; Rung, T.; Ulrich, C., Eds.; Schriftenreihe Schiffbau: Hamburg, 2011; pp. 333–339.

(61) Colagrossi, A.; Bouscasse, B.; Antuono, M.; Marrone, S. Particle Packing Algorithm for SPH Schemes. *Comput. Phys. Commun.* **2012**, *183*, 1641–1653.

(62) Eitzlmayr, A.; Khinast, J. Co-Rotating Twin-Screw Extruders: Detailed Analysis of Conveying Elements Based on Smoothed Particle Hydrodynamics. Part 2: Mixing. Submitted to *Chem. Eng. Sci.*

(63) Kohlgrüber, K.; Bierdel, M.; Conzen, C.; Hepperle, J.; Kirchhoff, J.; König, T.; Thiele, H. Optimierter Betrieb und Scale-up von Doppelschnecken-Extrudern. In *Seminar Handout*; VDI Wissensforum: Leverkusen, Germany, 2012.

(64) Cummins, S. J.; Rudman, M. An SPH Projection Method. *J. Comput. Phys.* **1999**, *152*, 584–607.

(65) Shao, S.; Lo, E. Y. M. Incompressible SPH Method for Simulating Newtonian and Non-Newtonian Flows with a Free Surface. *Adv. Water Resour.* **2003**, *26*, 787–800.

(66) Ihmsen, M.; Cornelis, J.; Solenthaler, B.; Horvath, C.; Teschner, M. Implicit Incompressible SPH. *IEEE Trans. Vis. Comput. Graph.* **2014**, *20*, 426–435.

"*Disorder increases with time because we measure time in the direction in which disorder increases.*"

(Stephen Hawking)

7

Co-Rotating Twin-Screw Extruders: Detailed Analysis of Conveying Elements Based on SPH. Part 2: Mixing*

A novel approach for the simulation of the flow in co-rotating twin-screw extruders based on smoothed particle hydrodynamics (SPH) was presented in Part 1. Specifically, we showed detailed results for the flow field in a completely filled conveying element, which are in excellent agreement with data from the literature obtained with computational fluid dynamics (CFD). Moreover, we studied the flow in the partially filled conveying element, facilitated by the inherent capabilities of SPH for modeling free surface flows. In Part 2, we show a detailed analysis of the mixing effects based on the presented SPH simulations. We studied the mixing using tracer particles for the completely and partially filled states, evaluated the time evolution of the intensity of segregation and fitted kinetic laws in order to determine mixing rates. We conducted this separately for overall mixing and axial mixing and analyzed the contributions of axial and cross mixing to the overall mixing rates. We showed these results for various operation states and finally, presented a case study highlighting the effect of the residence time on mixing together with the determined mixing rates per screw revolution. This confirms that SPH is a very promising tool for the investigation of mixing in complex geometries in both, completely filled and partially filled states. The presented results provide an excellent basis for the further improvement of simplified models of entire extrusion processes, including a quantification of mixing.

---

* This chapter is based on: Eitzlmayr, A.; Khinast, J. Co-Rotating Twin-Screw Extruders: Detailed Analysis of Conveying Elements Based on Smoothed Particle Hydrodynamics. Part 2: Mixing. Submitted to *Chem. Eng. Sci*.

7.1 Introduction

In Part 1[1], we presented the use of the smoothed particle hydrodynamics method (SPH[2–4]) for the simulation of the flow in co-rotating twin-screw extruders, which are widely used in different industries and increasingly attract interest in the pharmaceutical manufacturing.[5–9] We presented detailed results for the flow field in a completely filled conveying element with variable backpressure, which was also studied by Bierdel[10] using the finite volume method (FVM). We obtained excellent agreement with these data for the flow rate and the power input. Even more, we presented data for the flow in the partially filled conveying element with variable filling ratio. Since the simulation of partially filled extruders is problematic with well established, mesh-based computational fluid dynamics methods (CFD), comparable data are rare for this case. However, the trends of our results are in agreement with data shown by Pokriefke[11], who used FVM with an Eulerian multiphase method to simulate the flow in a partially filled twin-screw.

In Part 2 of this work, we present a detailed analysis of the extruder screw elements with regard to mixing. Numerical studies of mixing in extruders are mostly based on the tracking of tracer particles.[12–17] However, results obtained with tracer particles typically depend on the used initial configuration of the tracer, and a more general quantification of mixing would be desirable. Dispersion coefficients are tracer-independent quantities of the flow field and could be used to quantify dispersive mixing, however, their evaluation requires a rigorous distinction between convective and dispersive transport, which is a challenge for the complex flow in co-rotating twin-screws. Yang and Manas-Zloczower[18] proposed a parameter termed “mixing index”, which indicates the local type of flow on a scale between 0 and 1, where 0 indicates pure rotational flow, 0.5 pure shear flow and 1 pure elongational flow. This can be qualitatively correlated to the mixing and was used to study mixing in co-rotating twin-screw extruders.[18–20] Similarly, the so-called finite-time Lyapunov exponents can be used for the quantification of the local stretching of fluid elements and for the detection of attracting and repelling manifolds.[21,22] Although, these parameters are well suited to analyze the spatial distribution of the mixing, they do not allow the quantification of resulting product properties.

Since the achievement of certain product properties is usually the target in applications, we followed the mostly used approach and analyzed mixing based on tracer particles.

Specifically, we evaluated the intensity of segregation on a grid of cubed cells and tracked its time evolution during several screw revolutions. Subsequently, we fitted exponential functions through these data in order to determine the mixing kinetics, which might be used to predict mixing in simplified models of extrusion processes.[23,24]

7.2 Evaluation of Mixing

The current mixing study is based on the simulations presented in Part 1, which were conducted using the open-source particle simulator LIGGGHTS.[25] Since the SPH fluid elements represent Lagrangian particles, we employed them as tracer particles by marking them at a defined time. This was done after 0.5 revolutions, which was sufficient to obtain a developed flow. Initially, the tracer was a slice extending over a half of the cross-section and a third of the axial length (see Figure 7.1, top). This configuration was chosen in order to indicate cross mixing and axial mixing in combination, as it also occurs in reality. Clearly, to describe the mixing of this tracer completely, requires tracking until a homegeneous mixture is achieved. However, this was not possible due to the computational expense. Thus, we conducted the simulations during five revolutions, which was sufficient to fit kinetic laws. Snapshots of tracer positions during the revolutions are illustrated in Figure 7.1 for an exemplary case.

In order to quantify the mixing process, we used a grid of cubed cells (cell size 2 mm and volume 8 mm³, see Figure 7.2 top) and calculated the amount of tracer particles in each cell and its standard deviation. To correctly evaluate the standard deviation, a constant sample size is required. This was unattainable due to inevitable variations in the particle count per cell (e.g., caused by density variations, cells being divided by the walls and not completely filled or due to particles located at the cell interfaces and being divided by the interfaces). The average particle count inside each cell was calculated from the entire volume of 132,617 mm³ and the total particle count of 981,278, yielding 59.2 per cell. To approximate a constant sample size, we did not consider cells with less than 57 and more than 61 particles and only used cells with a particle count between 57 and 61 (i.e., with a variation of the sample size of about +/– 3%). As a result, approximately 50% of all particles were considered to calculate the standard deviation in the completely filled cases.

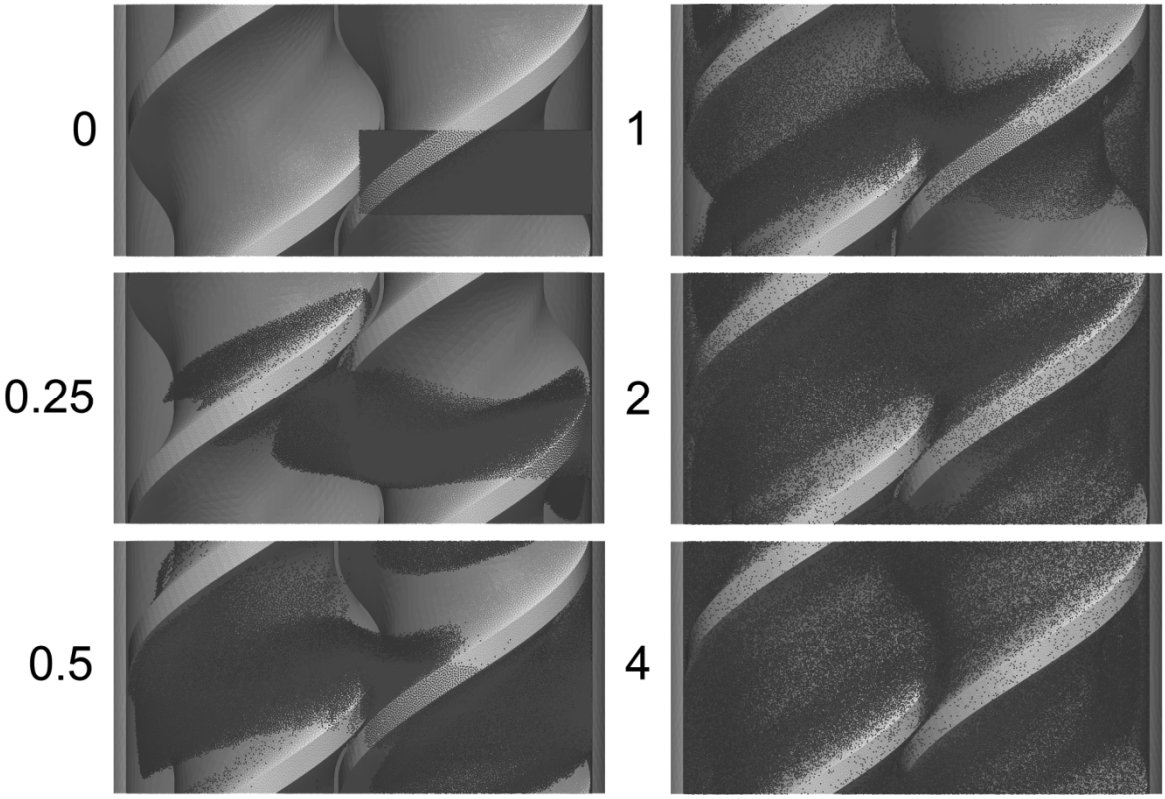

Figure 7.1: Snapshots of the tracer particle positions for Scenario 1 (a_z = 25 m/s², corresponding to $\dot{V}/nD^3$ = 0.057, see Part 1 for more details). The conveying direction was towards the top. The time from top to bottom: 0, 0.25, 0.5, 1, 2 and 4 revolutions.

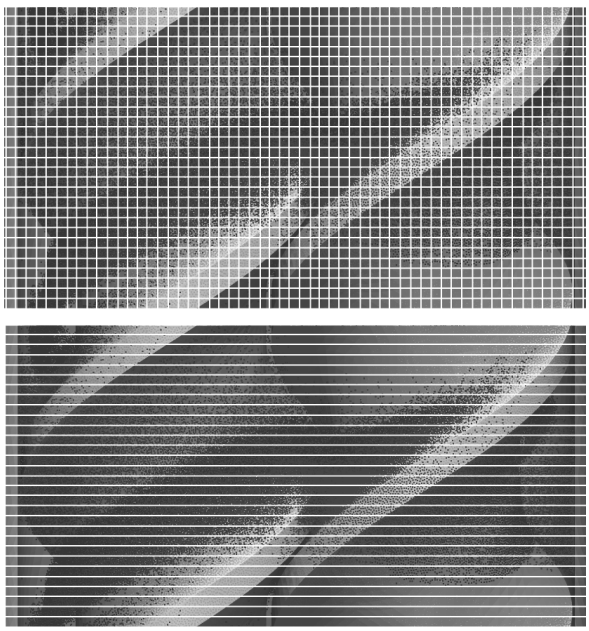

Figure 7.2: Grids used for the mixing evaluation: cubed cells of 2 mm size (top), slices 2 mm thick (bottom).

We normalized the standard deviation σ of the tracer content to give the intensity of segregation S (where N_{tracer} is the number of tracer particles and N_{total} the total particle number):

$$S = \frac{\sigma}{\sqrt{\frac{N_{tracer}}{N_{total}} \cdot \left(1 - \frac{N_{tracer}}{N_{total}}\right)}} \tag{7.1}$$

Figure 7.3 shows the time evolution of S for an exemplary case (a_z = 10 m/s²). In order to consider axial mixing separately, we applied the same procedure to cross-sectional slices (2 mm thick, see Figure 7.2 bottom) in the axial direction (i.e., one slice unified all cells in the same axial position). Since the cross sectional areas of the screws and barrel are constant in the axial direction and each slice contained the same amount of fluid volume, we considered all slices in this case. This yielded a similar time evolution of the segregation intensity S_{ax} (Figure 7.3) but only starting at around 0.6 rather than 1 since initially the tracer did not extend over the entire cross section (i.e., the initial state was not fully segregated). In all cases, the time evolution of S_{ax} was less regular than that of S, possibly due to a lower number of samples (30 slices vs. about 8000 cubed cells).

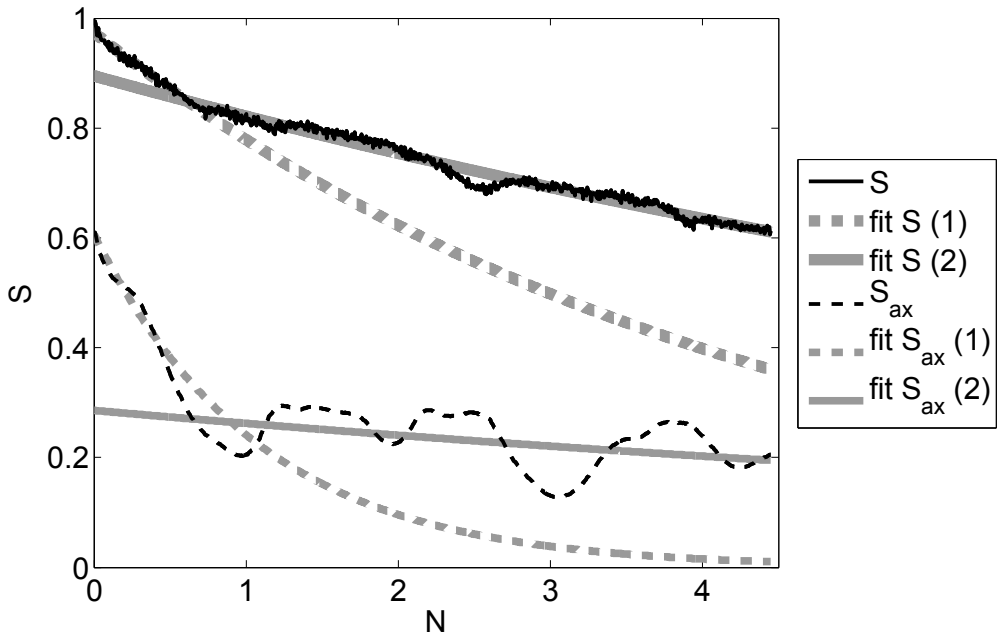

Figure 7.3: Intensity of segregation versus the number of revolutions evaluated through cubed cells (S) and cross-sectional slices (S_{ax}).

For both S and S_{ax} a pronounced inflection point after almost one revolution can be observed. This is due to the limited axial extension of the domain and the periodic boundary conditions in the axial direction, i.e., when the convective flow in the axial direction transported the tracer once through the entire domain it was coarsely distributed and the axial convection did not further support mixing. This is also illustrated in Figure 7.1: After 0.5 revolutions some of the tracer already crossed the periodic boundary and after 1 revolution the tracer was distributed along the axial direction. The further decrease in S_{ax} over time was obviously much slower than that during the first half revolution. The difference in the mixing rates was less pronounced for S since it involved not only axial but also cross mixing. A similar effect did not occur in the cross-sectional direction with no periodic boundaries to affect mixing in this case.

In order to determine mixing kinetics for the various mechanisms, we fitted exponential decay functions in each section of the determined evolutions curves (Figure 7.3):

$$S = S_0 e^{-kN} \tag{7.2}$$

$$S_{ax} = S_{ax,0} e^{-k_{ax} N} \tag{7.3}$$

7.3 Results and Discussion

The resulting values for the mixing rates before (k_1 and $k_{ax,1}$) and after (k_2 and $k_{ax,2}$) the inflection point are shown in Figure 7.4 and Figure 7.5 versus the dimensionless flow rate for the completely filled simulations (Scenarios 1 – 7). For the partially filled simulations (Scenario 8), the analogous mixing rates are shown in Figure 7.6 and Figure 7.7 versus the normalized flow rate Λ. For a detailed presentation of the Scenarios 1 – 8 see Part 1.

Mixing variations due different simulation parameters for Scenarios 1 – 7 were insignificant and almost no systematic difference was observed. Moreover, the mixing phenomena were well reproduced by the coarser resolution of 1 mm without the clearance flow (Scenario 7), which required much less computational expense compared to the resolution of 0.5 mm.

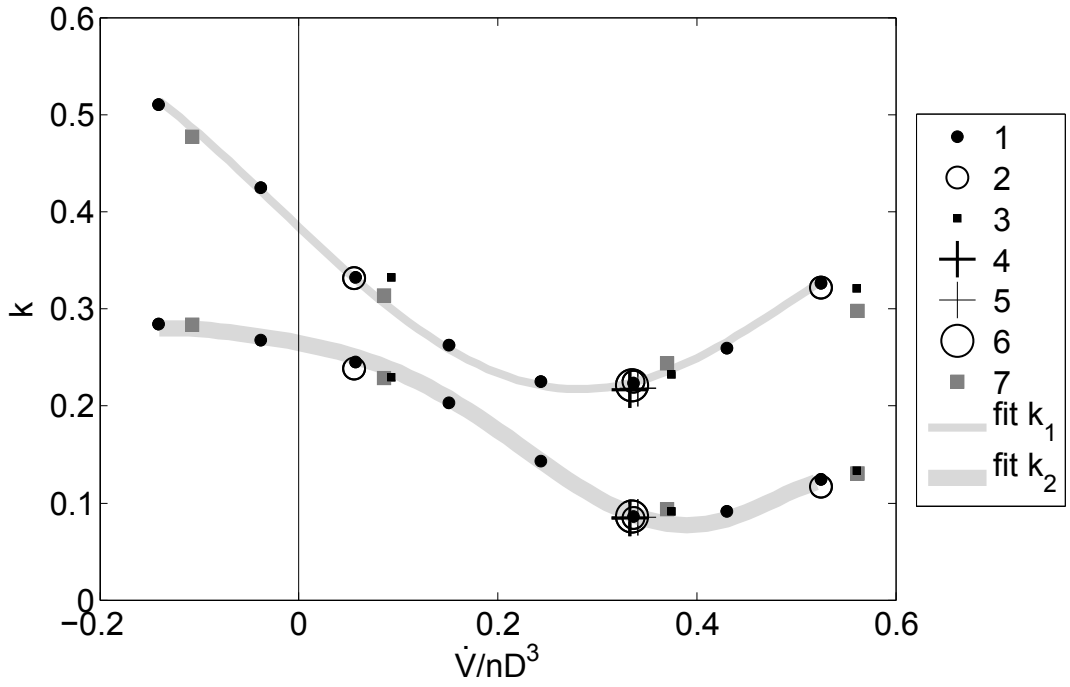

Figure 7.4: Mixing rates k_1 and k_2 (determined on cubed cells) versus the dimensionless flow rate in the completely filled state.

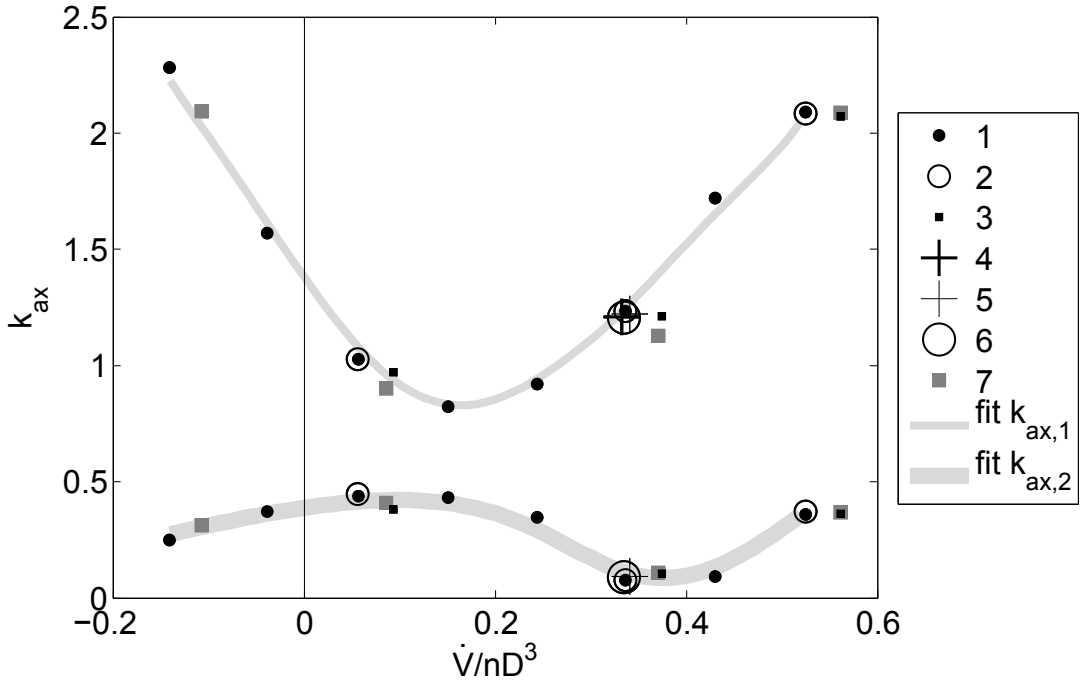

Figure 7.5: Mixing rates $k_{ax,1}$ and $k_{ax,2}$ (determined on the cross-sectional slices) versus the dimensionless flow rate in the completely filled state.

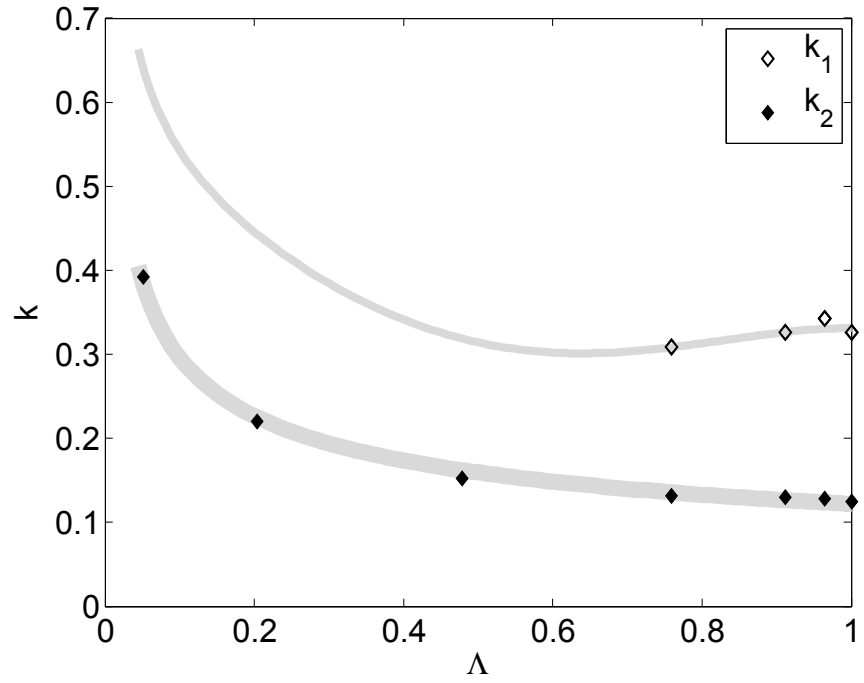

Figure 7.6: Mixing rates k_1 and k_2 (determined on cubed cells) versus the normalized flow rate Λ in the partially filled state.

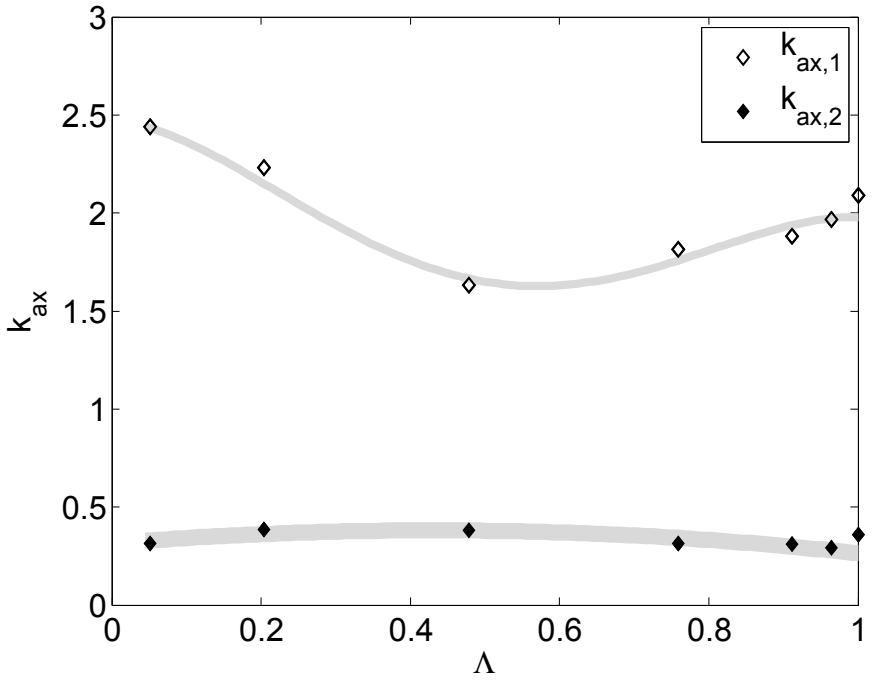

Figure 7.7: Mixing rates $k_{ax,1}$ and $k_{ax,2}$ (determined on the cross-sectional slices) versus the normalized flow rate Λ in the partially filled state.

In the partially filled state (Scenario 8), for filling ratios below $f = 0.75$ the first phase and the inflection point could not be identified due to increasing irregularities in the time evolution of S with decreasing filling ratio. This is possibly due to an insufficiently low number of sample cells since at low filling ratios most cells were only partially filled in the partially filled screw element and not considered when evaluating S. Thus, data points for k_1 are not shown below $f = 0.75$ (corresponding to $\Lambda \approx 0.75$) in Figure 7.6. The reason why we showed a fit for the missing k_1 data is explained below. This was not the case for the axial mixing rate $\underline{k_{ax}}$ (see Figure 7.7) since we took all cross-sectional slices into account (assuming that the fluid was uniformly distributed along the axial direction).

Clearly, the mixing rates k and k_{ax} are quantitatively not comparable since the considered sample sizes for S and S_{ax} varied significantly (i.e., each cubed cell contained the average particle number of 59 and the cross-sectional slices about 32000 at $f = 1$). However, the differences $k_1 - k_2$ and $k_{ax,1} - k_{ax,2}$ versus the flow rate yielded qualitatively similar curves, which supported the above suggestion that these differences occurred for the same reason, i.e., due to axial convection. Figure 7.8 shows both curves for the completely filled state (Scenario 1) and the partially filled state (Scenario 8), where we adjusted the axial mixing rates k_{ax} by a linear factor in order to collapse the curves. The adjusted axial mixing rates were named k_{ax}^{c}:

$$k_{ax}^{c} = \frac{k_{ax}}{\kappa} \tag{7.4}$$

The conversion factor κ, which was determined from the average of the k and k_{ax} values, was 8.32 and 8.20 in the completely and partially filled states, respectively. We fitted polynomials using the data shown in Figure 7.8. Clearly, the curves in the completely and partially filled cases converged with the vanishing pressure drop and as the filling ratio approached one (i.e., inherent conveying). Based on that, we developed the fits for k_1, k_2, $k_{ax,1}$ and $k_{ax,2}$ shown in Figure 7.4, Figure 7.5, Figure 7.6 and Figure 7.7, i.e., one curve of k_1 and k_2 was fitted and the other was calculated based on the fits for $k_1 - k_2$ and $k_{ax,1} - k_{ax,2}$ (for mathematical functions see the Appendix C). This is why the fit of k_1 for the partially filled state (Figure 7.6) is shown in the region $\Lambda < 0.75$ where no data points were available (i.e., k_2 was fitted and k_1 obtained from the fits of k_2 and $k_1 - k_2$).

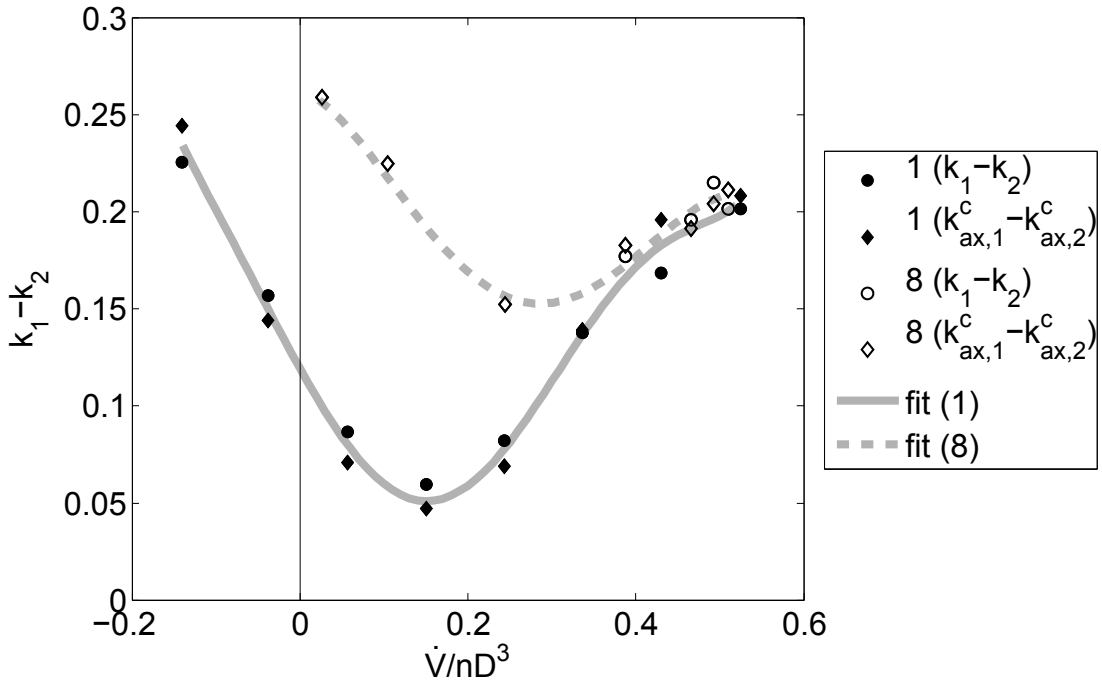

Figure 7.8: Mixing rates $k_1 - k_2$ and $\boldsymbol{k^c_{ax,1} - k^c_{ax,2}}$ versus the dimensionless flow rate in the completely filled state (Scenario 1) and the partially filled state (Scenario 8).

Figure 7.9 shows how different effects contributed to overall mixing. For a more compact representation, the resulting fits for the completely and partially filled states are shown together, specifically the overall mixing rates k_1 and k_2 and the difference $k_2 - k^c_{ax,2}$. The top curves for both states represent k_1, which is the overall mixing rate that includes all mixing mechanisms. The middle curves show k_2, which is similar to k_1 but without mixing via axial convection and thus, reflects cross mixing and axial dispersion. Similarly, $k_{ax,1}$ includes both axial mixing mechanisms, i.e., axial convection and axial dispersion. Since the difference between $k_{ax,1}$ and $k_{ax,2}$ is axial convection, $k_{ax,2}$ reflects axial dispersion. The difference $k_2 - k^c_{ax,2}$ represented by the lower curves in Figure 7.9 can be interpreted as the effect of cross mixing, which could not be further analyzed based on these data.

For practical considerations, the mixing rate k_2 is the most relevant one (i.e., the thick lines in Figure 7.9) since extruders are typically used for mixing continuous material streams, where the effect of axial convection on mixing vanishes in the same manner as it does in our simulations (after the inflection point in the evolutions of S and S_{ax}).

In the completely filled state, the mixing rate k_2 was the lowest at $\dot{V}/nD^3 \approx 0.4$ (i.e., about 75% of the inherent conveying capacity), which was caused by low axial dispersion and reduced cross mixing. Axial dispersion obviously collapsed since the axial velocity in the screw channels decreased due to backpressure and became more uniform compared to conveying without backpressure (see the results presented in Part 1). The respective flow rate $\dot{V}/nD^3 \approx 0.4$ is of less practical significance since extruders are typically operated in the range of $\dot{V}/nD^3 < 0.2$ (in pharmaceutical applications mostly < 0.1).

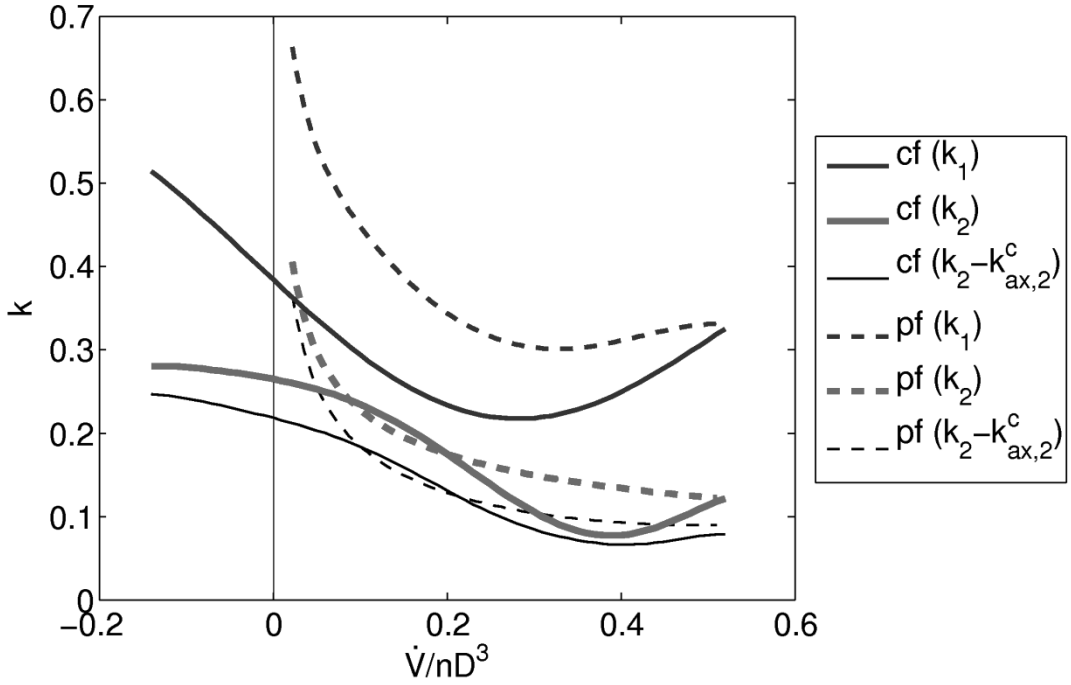

Figure 7.9: Fitted curves for the mixing rates k_1, k_2 and $k_2 - \boldsymbol{k_{ax,2}^c}$ versus the dimensionless flow rate in the completely filled state "cf" (Scenario 1) and the partially filled state "pf" (Scenario 8).

With the increasing backpressure and the decreasing flow rate, cross mixing and axial dispersion increased and reached maximum values in the region of negative flow rates (i.e., backward conveying elements). The reason could be increased backflow along the channels with increased backpressure, which affects both axial and cross mixing since the trajectories along the channels were extended in both, the axial and the cross directions. Interestingly, axial dispersion was the highest at $\dot{V}/nD^3 \approx 0.1$ and decreased slightly at flow rates around and below zero (see $k_{ax,2}$ in Figure 7.5).

However, the rate of axial convection mixing (i.e., the difference $k_1 - k_2$) was the lowest at $\dot{V}/nD^3 \approx 0.15$, which corresponds to zero flow rates in the screw channels (as presented in Part 1). Axial convection increased mixing significantly with increasing flow rate in the screw channels. The corresponding curves for complete and partial filling converged during inherent conveying (neglecting fitting inaccuracies), i.e., during changeover of the complete and partial fillings at $\dot{V}/nD^3 \approx 0.52$. As the filling ratio and the flow rate decreased, the mixing rates in the partially filled screw element mainly increased (except a slight decrease in mixing via axial convection) due to the increased cross mixing. In contrast, axial dispersion remained nearly constant over the entire range of the filling ratios and flow rates (see $k_{ax,2}$ in Figure 7.7). The increase in cross mixing with the decreasing filling ratio can be explained by the increase in the relative amount of material flowing through the clearances in the circumferential direction. This dramatically enhances cross mixing below $f = 0.1$. The effect of axial convection on mixing (see Figure 7.8) varied less depending on the flow rate in the partially filled state than in the completely filled state, possibly due to the absence of backflow in the partially filled state. The minimum axial convection mixing rate $k_{ax,1} - k_{ax,2}$ occurred at approximately 50% of the inherent conveying capacity (i.e., $f \approx 0.5$), however, this has fewer practical implications since axial convection is of minor significance for applications.

Interestingly, the mixing rates in the partially filled state were mostly higher than those in the completely filled state (see Figure 7.9), especially at low filling ratios $f < 0.1$. However, note that the mixing rates k and k_{ax} are defined as a relative change in the intensity of segregation per screw revolution, as the derivative of Eq. 7.2 implies (the same applies for Eq. 7.3):

$$k = -\frac{1}{S}\frac{dS}{dN} \tag{7.5}$$

Thus, the effect of residence time was not incorporated into the mixing rates k and k_{ax}, although this constitutes an important difference for the completely and partially filled screw sections. To demonstrate the effect residence time, we estimated the mixing effect versus the flow rate in the completely and partially filled screw sections for a given length

of the screw section. Based on the length L, the free cross section area A_{cr}, the filling ratio f and the flow rate $\dot{V}$ the average residence time τ can be estimated as:

$$\tau = \frac{f A_{cr} L}{\dot{V}} \tag{7.6}$$

Together with the screw speed n, the number of screw revolutions during time τ is $N = n\tau$. Substituting this in Eq. 7.2 for an initially unmixed state ($S_0 = 1$) yields:

$$S = \exp\left(-\frac{k n f A_{cr} L}{\dot{V}}\right) \tag{7.7}$$

Clearly, this is only an estimate since it fails to account for the distribution of residence time. However, it includes the main influences and reflects at least qualitative trends. Based on Eq. 7.7, we estimated S for the completely filled and partially screw sections using the fits for the practically relevant mixing rate k_2 (as show in Figure 7.9).

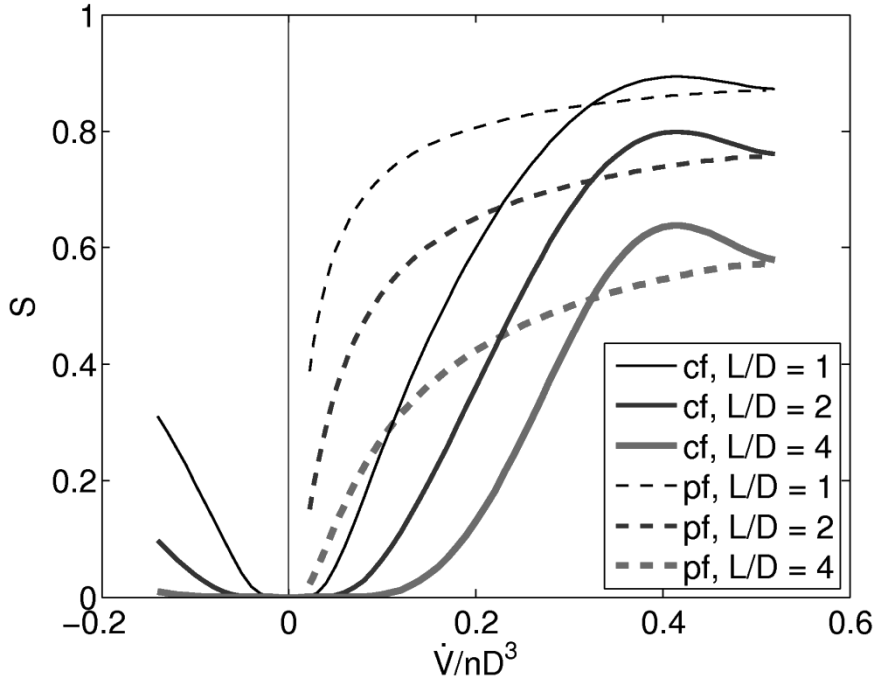

Figure 7.10: Intensity of segregation S versus the dimensionless flow rate determined from the fit for the mixing rate k_2 in a screw section with a given length-to-diameter ratio L/D (cf … completely filled, pf … partially filled).

The results are shown in Figure 7.10 versus the flow rate for various length-to-diameter ratios L/D of the considered screw section. In contrast to the results for the mixing rates, due to longer residence time mixing is more effective in the completely filled screw sections than in the partially filled screw sections. In all cases, the best mixing occurs at flow rates around zero due to an increase in the residence time caused by a decrease in the flow rate. At flow rates of almost zero the intensity of segregation for the partially filled screw sections converged to zero, i.e., at filling ratios close to zero suitable mixing occurred even in the partially filled screw section due to a high relative amount of the clearance flow. Similar trends were described in experimental results for a single-screw extruder.[26,27]

These trends suggest that the lowest possible dimensionless flow rates result in good mixing. However, besides higher investment costs that are required to achieve a lower flow rate for a given production rate in larger extruders, the specific mechanical energy consumption (SMEC, i.e., the energy required to rotate the screws in kWh per kg material) increases significantly as the residence time and the mixing performance increase. This is illustrated in Figure 7.11 which shows the ratio between the dimensionless driving power and the dimensionless flow rate (yielding the SMEC in dimensionless form, $PD/\dot{V}\eta nL$) versus the flow rate for Scenarios 1 and 8 for the complete and partial fillings, respectively. With the decreasing flow rate, i.e., with the increasing residence time, the SMEC increased dramatically. However, in the practically relevant operation range of $\dot{V}/nD^3 < 0.1 - 0.2$, the specific energy consumption was always much lower for the partial filling than for the complete one, which indicates that a partially filled section is suitable for the thermal relaxation of a material after a completely filled mixing zone. Clearly, mixing of highly-viscous materials requires energy. The better the mixing performance, the higher the SMEC, as Figure 7.10 and Figure 7.11 show. In practical applications, to avoid excessive energy input and stress to the material (especially in the pharmaceutical manufacturing that typically involves sensitive materials), it is very important to design the processes in such a way that residence time and mixing are sufficient but not overstated.

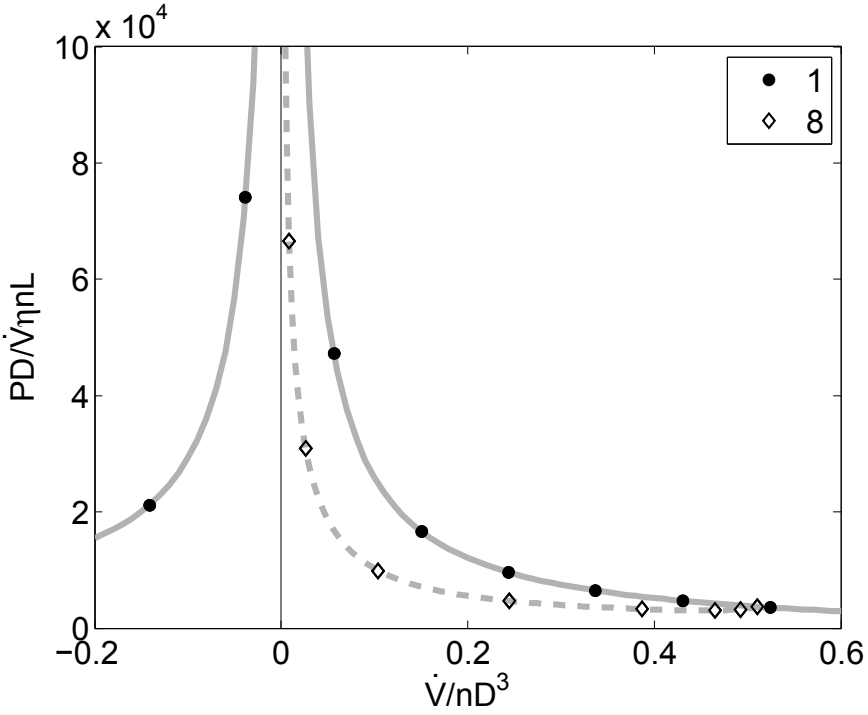

Figure 7.11: Specific mechanical energy consumption (SMEC) in the dimensionless form over the dimensionless flow rate for Scenario 1 (completely filled) and Scenario 8 (partially filled).

7.4 Summary and Conclusions

In this study, we present a detailed investigation of the mixing phenomena in a conveying element of a co-rotating twin-screw extruder in completely and partially filled states based on the SPH simulations presented in Part 1. We tracked tracer particles during several revolutions and evaluated the time evolution of the intensity of segregation using two different grids, indicating overall mixing and pure axial mixing. Based on that, we fitted kinetic laws and analyzed the contributions of axial and cross mixing to the overall mixing rate in various operation states.

Finally, we showed the importance of residence time along with the mixing rates per screw revolution: due to a higher residence time, the mixing performance was higher in the completely filled screw sections than in the partially filled screw sections, and the mixing performance increased with the decreasing flow rate. However, better mixing due to a higher residence time led to an increased specific mechanical energy consumption, meaning that in practice it is essential to find a compromise between good mixing and low energy input, especially with regard to sensitive materials.

This work also underlines the potential of the SPH method for the simulation of flow and mixing in co-rotating twin-screw extruders and demonstrates that results in excellent agreement with CFD data from the literature can be achieved. Thus, the presented approach is a robust tool for further investigations of flow and mixing in other screw element geometries. Clearly, the studied conveying element is only one type of screw elements among a variety of different geometries available for practical applications, e.g., conveying elements with various pitch-to-diameter ratios, kneading elements with different disc sizes and stagger angles, and specific mixing elements. This will reported in future communications.

Furthermore, our work provides a basis for refining empirical models of completely and partially filled screw elements. Our results may lead to an improvement of (more time-efficient) one-dimensional (1D) simulation tools for numerical studies of the entire extrusion process, facilitating the design, optimization and scale-up of extrusion processes.

7.5 Abbreviations

1D	one-dimensional
FVM	finite volume method
SMEC	specific mechanical energy consumption
SPH	smoothed particle hydrodynamics

7.6 Nomenclature

Latin symbols

A_{cr}	free cross section area [m²]
a_z	mass specific body force in the z direction [m/s²]
D	barrel diameter [m]
f	filling ratio [-]
k	mixing rate, related to S [-]
k_{ax}	mixing rate, related to S_{ax} [-]
k^c_{ax}	mixing rate k_{ax}, converted by the factor κ [-]
L	length [m]
N	number of revolutions [-]

n	screw speed [s^{-1}]
P	power [W]
S	intensity of segregation, indicating overall mixing [-]
S_{ax}	intensity of segregation, indicating pure axial mixing [-]
$\dot{V}$	flow rate [m^3/s]

Greek symbols

η	dynamic viscosity [Pas]
κ	conversion factor for the mixing rates [-]
Λ	normalized flow rate [-]
σ	standard deviation of the tracer content [-]
τ	mean residence time [s]

7.7 References

(1) Eitzlmayr, A.; Khinast, J. Co-Rotating Twin-Screw Extruders: Detailed Analysis of Conveying Elements Based on Smoothed Particle Hydrodynamics. Part 1: Hydrodynamics. Submitted to *Chem. Eng. Sci.*

(2) Monaghan, J. J. Simulating Free Surface Flows with SPH. *J. Comput. Phys.* **1994**, *110*, 339–406.

(3) Monaghan, J. J. SPH without a Tensile Instability. *J. Comput. Phys.* **2000**, *159*, 290–311.

(4) Monaghan, J. J. Smoothed Particle Hydrodynamics. *Reports Prog. Phys.* **2005**, *68*, 1703–1759.

(5) Breitenbach, J. Melt Extrusion: From Process to Drug Delivery Technology. *Eur. J. Pharm. Biopharm.* **2002**, *54*, 107–117.

(6) Ghebre-Sellassie, I.; Martin, C. *Pharmaceutical Extrusion Technology*; Marcel Dekker Inc.: New York, 2003.

(7) Kleinebudde, P. Pharmazeutisches Produktdesign: Gezielte Freisetzung von Wirkstoffen durch unterschiedliche Extrusionstechniken. *Chemie Ing. Tech.* **2011**, *83*, 589–597.

(8) Douroumis, D. *Hot-Melt Extrusion: Pharmaceutical Applications*; John Wiley & Sons, Ltd.: Chichester, 2012.

(9) Repka, M. A.; Langley, N.; DiNunzio, J. *Melt Extrusion - Materials, Technology and Drug Product Design*; Springer: New York, Heidelberg, Dordrecht, London, 2013.

(10) Bierdel, M. Computational Fluid Dynamics. In *Co-Rotating Twin-Screw Extruders*; Kohlgrüber, K., Ed.; Carl Hanser Publishers: Munich, 2008.

(11) Pokriefke, G. Numerische Analyse reibungsbehafteter Strömungen in teilgefüllten Extrudern, Universität der Bundeswehr Hamburg, 2005.

(12) Kalyon, D. M.; Gotsis, A. D.; Yilmazer, U.; Gogos, C. G.; Sangani, H.; Aral, B.; Tsenoglou, C. Development of Experimental Techniques and Simulation Methods To Analyze Mixing in Co-Rotating Twin Screw Extrusion. *Adv. Polym. Technol.* **1988**, *8*, 337–353.

(13) Ishikawa, T. 3-D Non-Isothermal Flow Field Analysis and Mixing Performance Evaluation of Kneading Blocks in a Co-Rotating Twin Srew Extruder. *Polym. Eng. Sci.* **2001**, *41*, 840–849.

(14) Rodríguez, E. O. Numerical Simulations of Reactive Extrusion in Twin Screw Extruders, Waterloo, Canada, 2009.

(15) Cleary, P. W.; Robinson, M. Understanding Viscous Fluid Transport and Mixing in a Twin Screw Extruder. In *8th International Conference on CFD in Oil & Gas, Metallurgical and Process Industries*; Trondheim, Norway, 2011.

(16) Sarhangi Fard, A.; Hulsen, M. A.; Meijer, H. E. H.; Famili, N. M. H.; Anderson, P. D. Tools to Simulate Distributive Mixing in Twin-Screw Extruders. *Macromol. Theory Simulations* **2012**, *21*, 217–240.

(17) Sarhangi Fard, A.; Anderson, P. D. Simulation of Distributive Mixing inside Mixing Elements of Co-Rotating Twin-Screw Extruders. *Comput. Fluids* **2013**, *87*, 79–91.

(18) Yang, H.-H.; Manas-Zloczower, I. Flow Field Analysis of the Kneading Disc Region in a Co-Rotating Twin Screw Extruder. *Polym. Eng. Sci.* **1992**, *32*, 1411–1417.

(19) Zhu, X. Z.; Wang, G.; He, Y. D. Numerical Simulation of Temperature and Mixing Performances of Tri-Screw Extruders with Non-Isothermal Modeling. *Res. J. Appl. Sci. Eng. Technol.* **2013**, *5*, 3393–3401.

(20) Rathod, M. L.; Kokini, J. L. Effect of Mixer Geometry and Operating Conditions on Mixing Efficiency of a Non-Newtonian Fluid in a Twin Screw Mixer. *J. Food Eng.* **2013**, *118*, 256–265.

(21) Robinson, M.; Cleary, P.; Monaghan, J. Analysis of Mixing in a Twin Cam Mixer Using Smoothed Particle Hydrodynamics. *AIChE J.* **2008**, *54*, 1987–1998.

(22) Robinson, M.; Cleary, P. W. Flow and Mixing Performance in Helical Ribbon Mixers. *Chem. Eng. Sci.* **2012**, *84*, 382–398.

(23) Eitzlmayr, A.; Khinast, J.; Hörl, G.; Koscher, G.; Reynolds, G.; Huang, Z.; Booth, J.; Shering, P. Experimental Characterization and Modeling of Twin-Screw Extruder Elements for Pharmaceutical Hot Melt Extrusion. *AIChE J.* **2013**, *59*, 4440–4450.

(24) Eitzlmayr, A.; Koscher, G.; Reynolds, G.; Huang, Z.; Booth, J.; Shering, P.; Khinast, J. Mechanistic Modeling of Modular Co-Rotating Twin-Screw Extruders. *Int. J. Pharm.* **2014**, *474*, 157–176.

(25) Kloss, C.; Goniva, C.; Hager, A.; Amberger, S.; Pirker, S. Models, Algorithms and Validation for Opensource DEM and CFD-DEM. *Prog. Comput. Fluid Dyn. An Int. J.* **2012**, *12*, 140–152.

(26) Pawlowski, J. *Die Ähnlichkeitstheorie in der physikalisch-technischen Forschung*; Springer Publishers: Berlin/Heidelberg, Germany, 1971.

(27) Kohlgrüber, K. *Co-Rotating Twin-Screw Extruders*; Carl Hanser Publishers: Munich, 2008.

"*You can know the name of a bird in all languages of the world, but when you're finished, you'll know absolutely nothing whatever about the bird… So let's take the bird and see what it's doing – that's what counts.*"

(Richard Feynman)

8

Investigation of Flow and Mixing in Typical Screw Elements of Co-Rotating Twin-Screw Extruders via SPH*

The modular screw design of co-rotating twin-screw extruders offers high operational flexibility, however, it also leads to challenges regarding the design of appropriate screw configurations. Modeling and simulation methods can be used to gain deeper insights into the flow and mixing phenomena of different screw element geometries. Due to its meshless nature, the smoothed particle hydrodynamics method (SPH) provides high potential for the simulation of free surface flows and mixing inside co-rotating twin-screw extruders. Based on our recent developments concerning boundary conditions at complex wall geometries and the flow through tight clearances, we studied flow and mixing inside five different screw elements typically used in practical applications. Our results show the differences among the investigated geometries with respect to the pressure characteristic for the completely filled state, the dependency of the flow rate on the filling ratio in the partially filled state and the power characteristic. Moreover, a detailed mixing analysis based on tracer particles is included, which shows mixing rates versus the flow rate for the completely filled elements. All results are dimensionless, thus, independent of the length scale and scale-up relevant. Beyond increased understanding of flow and mixing in these screw elements, our data provide important input information for simplified models of extruders, which are still of interest in industrial applications due to their low computational expense, and can significantly contribute to the efficient design, optimization and scale-up of extruders.

---

* This chapter is based on: Eitzlmayr, A.; Matić, J.; Khinast, J. Investigation of Flow and Mixing in Typical Screw Elements of Co-Rotating Twin-Screw Extruders via SPH, to be submitted.

8.1 Introduction

Co-rotating intermeshing twin-screw extruders have been widely used in different industries for many decades, for example, in the polymer, chemical and food industries. Its major advantages are the good mixing performance, the self-cleaning screws, the short residence time and the high flexibility due to the modular screw design. This particularly attracted the interest of the pharmaceutical industry in recent years for the manufacturing of solid drug products.[1] Depending on the materials involved, there are several types of pharmaceutical extrusion processes, such as hot-melt extrusion (HME), hot-melt granulation, wet extrusion and solid lipid extrusion.[2] HME is solvent-free and does not involve costs associated with the solvent separation, recovery and disposal. HME is a promising tool for increasing the bioavailability of poorly soluble drug molecules and forming solid solutions and amorphous solid dispersions.[3,4]

The modular screw design and the variety of individual screw elements available for practical applications provide almost unlimited options for the design of the screw configuration. However, this high operational flexibility leads to particular challenges in the design and optimization of the actual screw configuration in order to accommodate the actual process requirements. This normally requires extensive experience and empirical effort.

However, experimental investigations of extruders are limited, since process variables as the filling ratio and the melt temperature are difficult to measure. Modeling and simulation methods can provide an understanding of the complex flow and mixing phenomena associated with the interaction between the rotating screw geometry, material properties and operation conditions, and can lead to powerful approaches supporting the design, optimization and scale-up of extruders.

Nevertheless, the high complexity of extrusion processes requires model simplifications, and comprehensive first principles simulations of entire extrusion processes are still not achieved. Co-rotating twin-screw extruders are partially filled and the free surface flows are difficult to model. The tight clearances need to be sufficiently resolved, since they impact the entire flow field due to the high shear rates and the associated energy dissipation. The processed materials are usually complex, mostly non-Newtonian, which

requires an extensive amount of measurements for a sufficient description of their properties. The non-isothermal conditions in extruders lead to additional complications, since the mass, momentum and energy balances are coupled then. The transition from the granular to the molten state is even more complex and currently infeasible.

Today's modeling approaches are mainly divided into one-dimensional (1D) and three-dimensional (3D) methods. The computationally cheap 1D approach yields an approximate description of the process variables along the screw axes (e.g., filling ratio, pressure, temperature), however, does not account for their distributions over the cross section. The underlying models typically involve empirical parameters which have to be determined by 3D models or experiments. Despite of the strong simplifications, this approach often yields sufficiently accurate predictions that contribute to the process understanding and significantly reduce the experimental effort. Used in industrial applications due to its low computational expense, the 1D approach is still the only way to develop an efficient simulation of the entire extrusion process. For more detailed information about 1D modeling, please refer to the literature and our previous work.[5,6]

First principles simulations of the flow in co-rotating twin-screw extruders were mainly conducted with mesh-based CFD (computational fluid dynamics) methods, such as the FEM (finite element method) and FVM (finite volume method).[7–18] However, simulating free surface flows in partially filled screw sections remains extremely challenging with mesh-based CFD. For example, Pokriefke[19] used the FVM with an Eulerian multiphase model and applied a sophisticated mesh refinement at the free surfaces.

Beyond the conventional, mesh-based CFD methods, the smoothed particle hydrodynamics (SPH) method provides high potential for this particular challenge, since it is a mesh-free particle method, and does not require any additional modeling effort for free surface flows. Moreover, mixing phenomena can be easily observed by tracking of tracer particles. Cleary and Robinson[20] applied SPH to study mixing in a co-rotating twin-screw extruder using boundary particles to model the screw and barrel surfaces.

In our previous work[21,22], we proposed to use SPH for the simulation of partially filled extruders. In order to facilitate an efficient processing of the complex screw geometry, we developed a new wall interaction method, consisting of polynomials that compute the

interaction of a fluid particle with a wall surface depending on the distance from the wall[23]. This can be applied to complex surfaces in the *.stl format, which can easily be generated with well-known CAD (computer aided design) programs. Moreover, the flow through the tight clearances of extruders cannot be resolved without unfeasibly high computational expense. Even variable resolution schemes[24,25] cannot sufficiently improve this situation. Thus, we developed a model that accounts for the flow through unresolved clearances appropriately. SPH results based on these developments for a conveying element of a co-rotating twin-screw extruder were in excellent agreement with CFD data from the literature.[21]

In this work, we applied our approach to study the flow field and mixing in five typical screw elements used for co-rotating intermeshing twin-screw extruders. Specifically, we chose two conveying elements, a mixing element and two kneading elements. For the fluid we applied the scenario of a Newtonian fluid. Clearly, in reality the materials are typically more complex, mostly non-Newtonian and the results can be expected to depend more less on the actual material properties. However, we did not focus on any specific material, and for the simplest case of a Newtonian fluid the results can be expected to reflect mainly the effects of the screw elements, without any influence of nonlinear material properties. Moreover, for a Newtonian fluid under creeping flow conditions the results in dimensionless form are independent of the actual values of fluid viscosity, screw speed and length scale.[26,27]

8.2 Geometry

The geometry of the screw elements investigated in this work is based on a MICRO 27 co-rotating twin-screw extruder from Leistritz Extrusionstechnik GmbH (Nürnberg, Germany) with an outer screw diameter of 27 mm.

Numerous screw element types are available for co-rotating twin-screw extruders in practical applications, mostly conveying elements of various pitches, kneading elements with different stagger angles and disc thicknesses as well as specific mixing elements[27,28]. For this study, we chose five of the typical geometries from the elements available for the MICRO 27, namely two conveying elements with pitches 15 and 30 mm, two kneading elements with stagger angles 30° and 90° and a mixing element, whose geometry was

derived from the 15 mm conveying element by cutting through the screw flights in the axial direction to support mixing. These elements are illustrated in Figure 8.1. In the manufacturer's nomenclature they are called "GFA-2-15-30", "GFA-2-30-30", "GFM-2-15-30", "KB5-2-30-30" and "KB5-2-30-90", respectively. For simplicity, and since we slightly modified the geometry (see below), we termed the investigated screw elements "C15", "C30", "M15", "K30" and "K90", where "C" means conveying element, "M" mixing element and "K" kneading element.

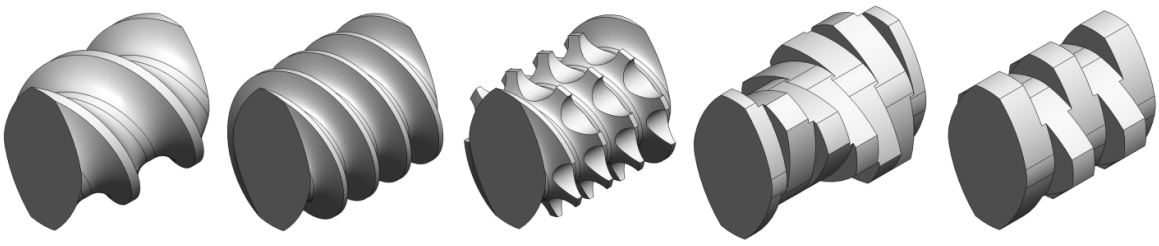

Figure 8.1: Geometry of the investigated screw elements (from left to right: C30, C15, M15, K30, K90).

The elements C15, C30, M15 and K90 are 30 mm long, which is the standard length of screw elements of the MICRO 27 extruder. In reality, the K30 element has the same length and consists of five kneading discs, where the orientation of the first and the last disc is not the same. This would be in conflict with periodic boundaries in the axial direction. Thus, we added one disc in order to enable the use of periodic boundaries, yielding a length of 36 mm for the K30 element (as shown in Figure 8.1).

The geometry of the element K90 is symmetrical with respect to a cross-sectional plane, thus it does not prefer any conveying direction and is therefore a non-conveying element. This is not the case for the elements C15, C30, M15 and K30, consequently, they have a certain conveying activity when rotating and exist in two different variants, forward conveying and backward conveying (often termed „right-handed" and „left-handed", respectively). Basically, we used the right-handed variants (i.e., conveying in the forward direction). The operation states of the corresponding left-handed elements were obtained with the right-handed geometries by inverting the direction of the flow rate, which is physically equivalent to the situation of the left-handed element.

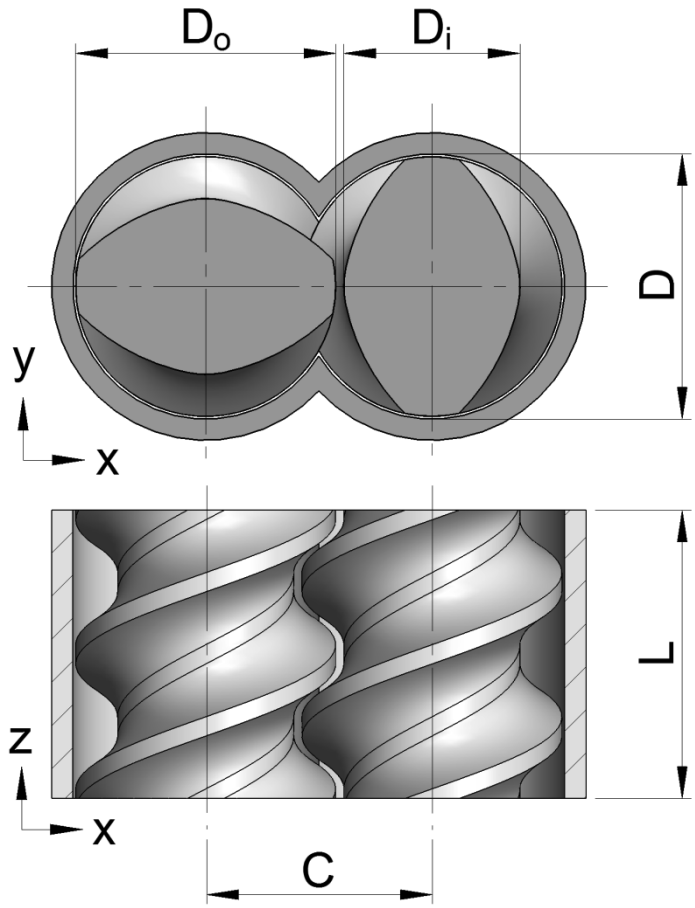

Figure 8.2: Simulation setup and main dimensions of the screw geometry, for example with the C30 element.

Table 8.1: Dimensions of the used screw geometry.

Barrel diameter D	27.6 (27.4) mm
Outer screw diameter D_o	27.0 mm
Inner screw diameter D_i	18.3 mm
Centerline Distance C	23.5 mm

A sketch of the setup used for the conducted simulations is illustrated in Figure 8.2, for example for the C30 element. It consists of a pair of screw elements within a barrel section. In the z-direction, we used periodic boundaries, i.e., fluid particles leaving the domain via a z-boundary simultaneously enter at the opposite z-boundary. Therefore the identical cross section is required for both z-boundaries, which was the reason for the above described modification of the K30 element. The main geometrical dimensions of the MICRO 27

screw profile are also illustrated in Figure 8.2 (outer and inner screw diameter D_o and D_i, barrel diameter D, centerline distance C and length L) and the values used for our simulations are given in Table 8.1.

Slight modifications of the real geometrical dimensions were required for the following reasons.

The resolution required to correctly account for the flow through the tight clearances between screws and barrel (see Figure 8.2) leads to unfeasibly high computation costs. Thus, we proposed a clearance model,[21] which accounts for the flow in unresolved clearances properly. With that, the particle spacing can be set equal to the tightest clearance distance, i.e., a single fluid particle can pass through the tightest clearance.

Even in this case, the particle number required to fill a 30 mm long screw element of the MICRO 27 extruder would be around 10^7, and the corresponding computation costs would be too high to allow a sufficient investigation of mixing in the relevant operation states. Thus we increased the barrel diameter to 27.6 mm, yielding clearances of 0.3 mm between screws and barrel. With the corresponding particle spacing of 0.3 mm a number of about $5 \cdot 10^5$ particles was required to fill a 30 mm long screw section. In addition, we increased the centerline distance to 23.5 mm in order to avoid clearances < 0.3 mm between the screws (which occurred for conveying elements with small pitches).

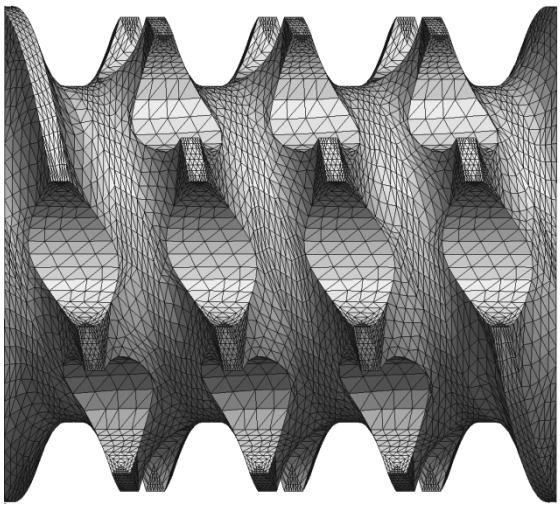

Figure 8.3: Used STL mesh for the M15 element.

In order to estimate the effect on the results, we repeated one case with a barrel diameter of 27.4 mm (which is still larger than the real value), yielding 0.2 mm clearances and ca. $1.8 \cdot 10^6$ particles.

The geometries were created with the software SolidWorks and transformed into the required *.stl format by the open-source software gmesh (http://geuz.org/gmsh/). For example, the used STL mesh for the M15 element is shown in Figure 8.3.

8.3 Computational Approach

For the simulations presented in this paper the weakly compressible SPH method according to Monaghan[29,30] including the Morris model for the viscous forces[31] was applied. For the kernel function we employed the cubic spline kernel. For the boundary conditions at the complex wall surfaces, we applied our new approach[23], which calculates the wall interaction of fluid particles with polynomials depending on the wall distance. For more details about the used method, please refer to our previous work.[21]

Additionally, we developed a novel density correction for the simulation of the completely filled screw elements for the following reason: Without this density correction, we observed a drift of the average density (averaged over all particles) in a completely filled geometry during the time. However, in a completely filled geometry, where the volume as well as the mass of the inserted fluid is strictly constant, also the average density has to remain constant, i.e., the observed drift is unphysical. Whether the density decreased or increased during time depended on the actual screw element geometry. Specifically, for the conveying elements the density (and consequently the pressure) decreased slightly during time, which resulted in the formation of partially filled zones in regions of too low pressure. On the contrast, for the kneading elements, density and pressure increased slightly during time, which was less critical since the completely filled state was not affected by the increasing pressure values. There was no systematic rule observed in this behavior, and the reason is still not clear. However, the used continuity equation does not account for the absolute level of the density, since it calculates the density time derivative. This is sensitive to any errors (also e.g., numerical errors from the discrete time integration), since there is no mechanism which ensures that the absolute density level remains correct.

In order to avoid this sensitivity, we developed the following correction, which uses the actual average density ρ_{av} (i.e., the density averaged over all fluid particles) and the reference density of the fluid ρ_0 (i.e., the desired average value of the density) and yields a corrective density time derivative:

$$\left(\frac{d\rho}{dt}\right)_{corr} = \frac{\rho_0 - \rho_{av}}{\tau_{corr}} \tag{8.1}$$

The time constant τ_{corr} was set to 0.1 s. This corrective density time derivative was applied to every fluid particle equally, i.e., it corrected only the level of the density, while the density gradients were not affected. With that, the average density could be kept close to the reference density, without any drift during time.

Beyond the model used in our previous work,[21,22] we extended the evaluation of mixing and calculated a parameter termed "mixing index", which was proposed by Manas-Zloczower[32] and indicates the local type of flow on a scale between 0 and 1, where 0 indicates pure rotational flow, 0.5 pure shear flow and 1 pure elongational flow. This parameter is defined as:

$$\zeta = \frac{\|\mathbf{D}\|}{\|\mathbf{D}\| + \|\mathbf{W}\|} \tag{8.2}$$

where $\|\mathbf{D}\|$ and $\|\mathbf{W}\|$ are the magnitudes of the rate-of-strain tensor **D** and the vorticity tensor **W**, which were calculated as follows:[33,34]

$$\|\mathbf{D}\| = \sqrt{2\mathbf{D} : \mathbf{D}} \tag{8.3}$$

Analogously for $\|\mathbf{W}\|$. The tensors **D** and **W** were calculated from the velocity gradient tensor **L** by:

$$\mathbf{D} = \frac{1}{2}\left(\mathbf{L} + \mathbf{L}^T\right) \tag{8.4}$$

$$\mathbf{W} = \frac{1}{2}\left(\mathbf{L} - \mathbf{L}^T\right) \tag{8.5}$$

The components of **L** for a fluid particle *a* were calculated by applying the discrete SPH kernel approximation, e.g., shown by Amini et al.[35], where *b* are the neighbor particles:

$$\mathbf{L}_{ij,a} = \left(\frac{\partial v_i}{\partial x_j} \right)_a = \sum_b \frac{m_b}{\rho_b} (v_{i,b} - v_{i,a}) \frac{\partial W_{ab}}{\partial x_j} \tag{8.6}$$

Here, v_i is the velocity component i, x_j the spatial coordinate j, m_b and ρ_b the mass and density of particle b, respectively, $v_{i,a}$ and $v_{i,b}$ the velocity components i of particles a and b and W_{ab} the kernel function evaluated for particles a and b.

The numerical studies were conducted using the open-source particle simulator LIGGGHTS.[36]

8.4 Parameters

Extruders are usually used for high-viscous materials (in the order of 10^2 – 10^3 Pas), which leads to Reynolds numbers of nearly zero ($Re \ll 1$), known as creeping flow conditions. Pawlowski[26] showed that the dimensionless results for flow rate, pressure generation and power input are independent of the Reynolds number for a Newtonian fluid under creeping flow conditions. This was confirmed in our previous work,[21,22] where we also found that creeping flow in co-rotating twin-screw extruders occurred for Reynolds numbers below 10 (based on the definition $Re = n \cdot D^2 \rho / \eta$, where n is the screw speed, D the barrel diameter, ρ the density and η the viscosity). This is of specific interest for SPH simulations, where the required time step is inversely proportional to the viscosity (at least when the viscous time step criterion is limiting). As we also showed,[21] this yields an inverse dependency of the number of time steps per screw revolution on the Reynolds number. Therefore it is beneficial for the computational costs to use a Reynolds number at the limit of the creeping flow regime.

Based on that, we chose the screw speed to be n = 150 rpm and the viscosity η = 0.2 Pas, which yields Re = 9.5. The density was ρ = 1000 kg/m³. As discussed above, the particle spacing was set equal to the tightest clearance distance, i.e., Δx = 0.3 mm. For the smoothing length, we used $h = 1.2\Delta x$, which is a commonly used value.[37,38]

In order to vary the operation state of the completely filled screw elements, the axial pressure rise had to be varied. However, the pressure could not be different at the periodic z-boundaries, thus, pressure rises were not possible in the direction where periodic boundaries were applied. To overcome this, we used an acceleration a_z in the axial direction (like the gravity), which led to a hydrostatic pressure profile. Thus, the flow had to establish a pressure rise that compensated the hydrostatic pressure, yielding a zero pressure rise in total. This allowed to control the axial pressure rise by the applied value of the acceleration a_z. The obtained pressure rise can be calculated by:

$$\frac{\Delta p}{L} = a_z \cdot \rho \tag{8.7}$$

The appropriated values for a_z depended on the actual geometry of the screw elements, which had different pressure generation capabilities. We started from a_z = 0 for each element, which represents conveying without backpressure, where the resulting flow rate is the so-called inherent conveying capacity. Variations of a_z were chosen in order to achieve flow rates in the practically relevant operation range of twin-screw extruders. The used ranges of a_z for each screw element are given in Table 8.2.

The speed of sound was determined based on the criteria proposed by Morris et al.[31]:

$$c^2 \geq \frac{1}{\delta} \max\left(V_0^{\,2}, \frac{\nu V_0}{L_0}, a L_0 \right) \tag{8.8}$$

Where $\delta = \Delta\rho/\rho_0$ is the maximum allowed relative variation of the density (mostly assumed δ = 0.01), V_0 is the maximum fluid velocity, ν is the kinematic viscosity of the fluid, L_0 is a relevant length scale and a is an acceleration acting on the particles. Based on these criteria, we determined the speed of sound to be c = 10 m/s, which was limited by the third criterion in Eq. 8.2. Here, a was the applied acceleration in the axial direction a_z and for L_0 we used the half pitch in case of the conveying elements, otherwise the entire element length of 30 mm. Only, for the M15 element we chose c = 5 m/s, since it required comparably low values of a_z to vary the flow rate. Although, the values of a_z were similarly small for the K90 element, it required c = 10 m/s to keep the density variation

low. This was caused by the strong compression exerted by the kneading effect. The used values of c are given in Table 8.2.

Table 8.2: Simulation parameters (completely filled state).

Element	a_z	c	Δt	$(n\Delta t)^{-1}$	V	N_{total}	ρ_{Init}	p_0	C_{rep}
	[m/s²]	[m/s]	[µs]	[10^3]	[ml]	[10^3]	[kg/m³]	[Pa]	[mN]
C15	0 – 200	10	2	200	12.53	466	1170	1000	2
C30	0 – 80	10	2	200	12.53	464	1100	1000	2
M15	-3.33 – 10	5	4	100	15.17	556	1100	300	0.5
K30	0 – 30	10	2	200	15.65	576	1080	1000	2
K90	0 – 10	10	2	200	13.28	489	1090	1000	3

With that, we calculated the required time step by the following criterion shown by Monaghan[39], which was in good agreement with the experiences of our previous work[21]:

$$\Delta t \leq \frac{0.3h}{c(1+1.2\alpha)} \tag{8.9}$$

where $\alpha = 10\eta/\rho hc$ is the artificial viscosity.[37] This yielded $\Delta t < 4.63$ µs (and $\Delta t < 5.89$ µs for the M15 element). To guarantee sufficient stability, we used $\Delta t = 2$ µs and $\Delta t = 4$ µs (i.e., $2 \cdot 10^5$ and $1 \cdot 10^5$ steps per revolution, respectively). These values are summarized in Table 8.2.

The required number of fluid particles N_{total} was calculated from the fluid volume V (given in Table 8.2), defined by the geometry and the desired particle spacing Δx, assuming a cubic lattice ($N_{total} = V/\Delta x^3$).

Due to the particle initialization on a regular, cubic lattice, empty regions close to the curved wall surfaces remained after the initialization. This incomplete filling caused a lower particle number compared to the calculated N_{total}. However, to fully fill the geometry with the correct mass of fluid, we used a lower particle spacing for the initialization, followed by a slight expansion of the fluid, which filled the empty regions. The actual value of the initial particle spacing was iteratively determined in order to achieve

approximately the correct particle number N_{total} as calculated from the volume (the actually obtained values of N_{total} are given in Table 8.2). The initial particle spacing was ca. 3 – 7% lower than the desired value of Δx after the expansion, depending on the geometry.

To achieve the expansion after the initialization, the initial density ρ_{Init} had to be larger than the desired density of 1000 kg/m³ after the expansion. The actual values of the initial density were less critical, since the above described density correction drove the average density close to the desired 1000 kg/m³, almost independent of the used initial density. The used values of ρ_{Init} are given in Table 8.2 and were iteratively determined, in order to run quickly into a steady average density after the expansion.

Moreover, a background pressure p_0 was required in order to keep the geometry completely filled. Without that, the pressure distribution would show regions with negative pressures, where a partial filling would emerge. The used values of p_0 are given in Table 8.2, together with the values of the wall repulsion force C_{rep}, required to avoid wall penetration. C_{rep} was determined as proposed previously[21] ($C_{rep} \approx 10 \cdot p_0 \cdot h^2$).

In order to show that the chosen Reynolds number of 9.5 was a valid assumption for creeping flow conditions, we varied the Reynolds number in one case of the C15 element with a flow rate of almost zero. Here, the used viscosity of 1 Pas required an axial body force of 600 m/s² and an increased speed of sound c = 20 m/s compared to the cases with Re = 9.5. This led to a time step of 1 µs (i.e., $4 \cdot 10^5$ steps per revolution). Since we did not study mixing in this specific case, but used it only to compare the resulting dimensionless numbers for flow rate, pressure rise and screw driving power, we reduced the length to a half pitch (7.5 mm). All relevant parameters are given in Table 8.3 (row "C15 (Re)").

Table 8.3: Simulation parameters (reference cases).

Case	η	Re	h	a_z	c	Δt	$(n\Delta t)^{-1}$	V	N_{total}	ρ_{Init}	p_0	C_{rep}
	[Pas]	-	[mm]	[m/s²]	[m/s]	[µs]	[10^3]	[ml]	[10^3]	[kg/m³]	[Pa]	[mN]
C15 (Re)	1	1.8	0.36	600	20	1	400	3.13	114	1120	5000	8
M15 (c)	0.2	9.5	0.36	10	10	2	200	15.17	556	1100	300	0.5
M15 (Δx)	0.2	9.5	0.24	10	5	4	100	15.17	1844	1100	300	0.3

As we reduced the speed of sound to c = 5 m/s for the M15 element compared to c = 10 m/s for the other elements, we repeated one case of M15 with c = 10 m/s in order to show that the effect is negligible. The detailed parameters of this specific case are also given in Table 8.3 (row "M15 (c)").

Due to the above explained modification of the geometry, specifically the increased clearance distances of 0.3 mm, we repeated the same case of the M15 element with 0.2 mm clearances (barrel diameter D = 27.4 mm) and, consequently, a particle spacing of Δx = 0.2 mm. This required about the three-fold number of fluid particles, compared to the cases with Δx = 0.3 mm, as shown in Table 8.3 (row "M15 (Δx)").

For the simulation of the partially filled elements, we basically used similar parameters. Due to the absence of backpressure we reduced the speed of sound to c = 5 m/s for all elements here, in order to reduce the computation costs. Moreover, the background pressure was set to p_0 = 0 and we did not apply the initial expansion here, which was only essential to achieve a complete filling. Thus, the initial particle spacing was equal to the desired value of 0.3 mm and the initial density was ρ_{Init} = 1000 kg/m³. Despite of the reduced speed of sound, the required time step was even smaller than for the completely filled cases. The values were found iteratively, and decreased with decreasing filling ratio (Δt = 1 – 0.25 µs, i.e., $4 \cdot 10^5$ – $1.6 \cdot 10^6$ steps per revolution). This was also found in our previous work[21], and could be caused by instabilities along the free surfaces of the fluid, limiting the time step compared to the completely filled simulations.

8.5 Results and Discussion

8.5.1 Hydrodynamics

From all simulations, we evaluated the flow rate $\dot{V}$, which is defined as integral of the axial velocity v_z over the cross section area A_{cr}. However, since volume integrals in contrast to surface integrals are straightforward in SPH, we calculated the flow rate from the volume averaged axial velocity, which is related to the definition the flow rate:

$$\dot{V} = \int_{A_{cr}} v_z dA = \frac{1}{L} \cdot \int_{L} dz \cdot \int_{A_{cr}} v_z dA = \frac{1}{L} \cdot \int_{L} \int_{A_{cr}} v_z \, dA \, dz = \frac{1}{L} \cdot \int_{V} v_z \, dV \tag{8.10}$$

This is valid since the flow rate is constant along z, also if the cross section area A_{cr} is not constant along z, as for example for the M15 element. Moreover, the flow rate was time averaged during the simulated period, excluding the first half revolution, which was required to develop the flow.

The axial pressure rise was calculated from the predefined values of a_z according to Eq. 8.7. Showing the pressure rise versus the flow rate in dimensionless form leads to the so-called pressure characteristic, which was introduced by Pawlowski[26] and also shown by Kohlgrüber[27]. Specifically, the pressure characteristic shows $\Delta pD/(\eta nL)$ versus $\dot{V}/(nD^3)$, where Δp is the axial pressure rise along the length L, D the barrel diameter, η the viscosity and n the screw speed. For the detailed discussion of the used dimensionless groups please refer to Pawlowski[26], Kohlgrüber[27] and our previous work[5,6,21].

The pressure characteristics of all investigated screw elements in the completely filled state are shown in Figure 8.4 together with fitted lines. For the partially filled state the pressure characteristic does not exist, since an axial pressure rise is not possible there. Basically, the obtained curves are linear, which is a consequence of the linearity of the Stokes equations. This was also confirmed experimentally by Pawlowski[26] for the Newtonian, creeping flow in a single screw extruder. The obtained values for the parameters A_1 and A_2, which are the axis intercepts of the pressure characteristic of actively conveying elements, are given in Table 8.4 (i.e., A_1 characterizes the inherent conveying capacity). For the non-conveying element K90, where A_1 and A_2 are zero both, the parameter A_0 is shown, which is the slope of the pressure characteristic function then.

Table 8.4: Resulting screw parameters (completely filled states).

	A_1	A_2	B_1	B_2
C30	0.295	3583	0.807	2795
C15	0.137	7228	0.424	3205
M15	0.102	354	3.02	1309
K30	0.416	1378	2.22	2970
K90	$A_0 = 3535$		$B_0 = 2032$	

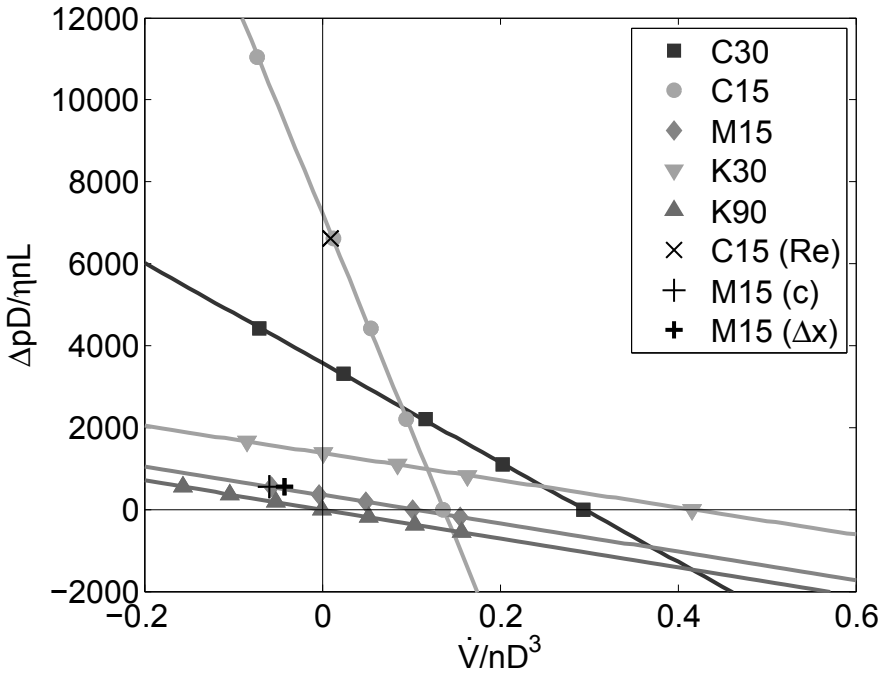

Figure 8.4: Obtained data for the pressure characteristics and fitted lines (completely filled states).

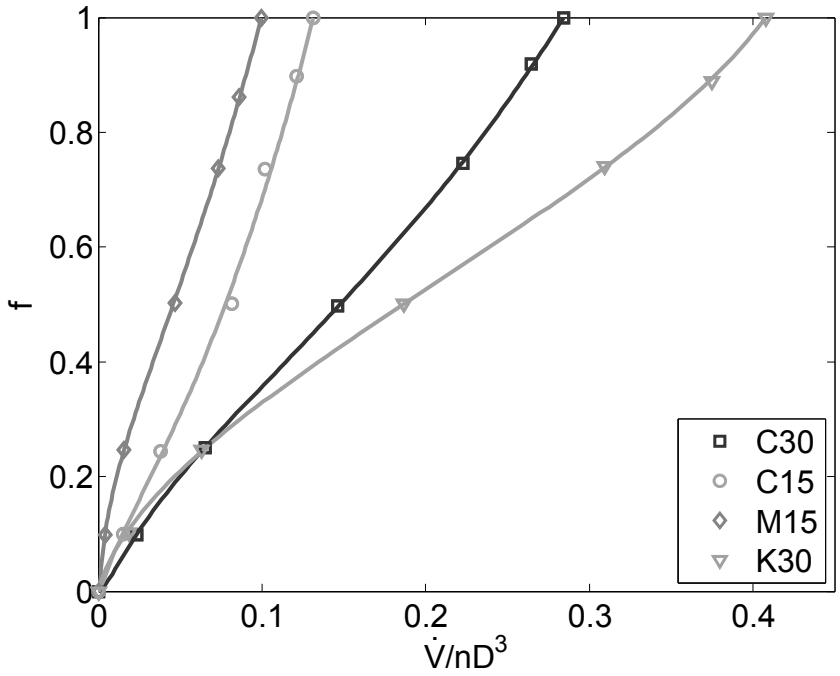

Figure 8.5: Filling ratio versus the dimensionless flow rate (partially filled elements).

Clearly, the highest pressure rises were achieved by the conveying elements C15 and C30. Their inherent conveying capacity is approximately proportional to the pitch, whereas their pressure rise at zero flow rate is approximately inversely proportional to the pitch.

Compared to the C15 element, the M15 element yielded a lower inherent conveying capacity, and almost vanishing values for the pressure rise, caused by the axial openings. The K30 element showed the highest inherent conveying capacity among the investigated elements, caused by its geometrical shape, which describes one revolution along an axial length of 72 mm (i.e., similar to a conveying element of pitch 72 mm). However, the pressure generation ability of K30 is limited, which can be addressed to the openings between the kneading discs, allowing a flow between adjacent channels (similar to the M15 element). Clearly, the non-conveying K90 element showed a pressure characteristic through the origin, i.e., it requires pressure to achieve a flow rate.

The time averaging of the flow rate was not essential for the conveying elements (C15 and C30), whose geometry is continuous along the axial direction. These elements showed a constant flow rate versus time. However, the elements with discontinuous geometries (M15, K30 and K90) showed an oscillating flow rate versus time. Specifically, the amplitude of the oscillations was approximately proportional to the backpressure, i.e., it vanished at the inherent conveying and increased with increasing backpressure. Relative to the time averaged flow rate of the backflow $A_1 n D^3 - \dot{V}$, the amplitude of the oscillations was about 1.5%, 9% and 11% for the K30, M15 and K90 elements, respectively. The frequency of the oscillations was independent of the backpressure, and yielded 12 oscillations per revolution for the K30 element, and 4 oscillations per revolution for the M15 and K90 elements. For the kneading elements K30 and K90, this is equal to the number of "kneading events" per revolution, i.e. how often kneading discs pass the intermeshing region, which is 360° divided by the stagger angle.

Instead of the pressure characteristic, the simulations of the partially filled elements yielded data for the filling ratio versus the dimensionless flow rate, which are shown in Figure 8.5 for the elements C30, C15, M15 and K30. For the non-conveying element K90 the partially filled state is not relevant, since a flow rate cannot be achieved there, i.e., in practical applications this element must always be completely filled. The resulting curves show a zero flow rate for the empty elements (trivially), and with increasing filling ratio the flow rate increased nonlinear. As the filling ratio approached 1, the flow rate yielded the inherent conveying capacity of each element, i.e., the same flow rate as obvious from the pressure characteristic for zero backpressure. For the fits Eq. 8.11 was used, where

$\Lambda = \dot{V}/A_1 nD^3$ is the normalized flow rate.[21] The values of the fitted parameters are given in Table 8.5.

$$\Lambda = f - \alpha_0 (1-f)\left[1-(1-f)^{\phi_0}\right] + \alpha_1 f\left(1-f^{\phi_1}\right) \tag{8.11}$$

Table 8.5: Fitted parameters (partially filled elements).

	α_0	α_1	ϕ_0	ϕ_1	β_0	β_1	χ_0	χ_1
C30	0.359	4.18	5	0.14	0.464	0.253	5	9
C15	0.129	11.3	13	0.04	0.190	0.253	9	19
M15	0.453	4.84	5	0.11	0.740	0.656	2	3
K30	0.344	0.245	3	3	0.464	0.142	6	20

Furthermore, we evaluated the screw driving power using the wall interaction forces of the fluid particles. The resulting values for the driving power versus the flow rate are shown in Figure 8.6 in dimensionless form, the so-called power characteristic ($P/(\eta n^2 D^2 L)$ versus $\dot{V}/(nD^3)$, where P is the driving power of the screws.[26,27]

Here, the linear data represent the completely filled elements, whereas the nonlinear data represent the partially filled elements. Similar to the A_1 and A_2 parameters, the linear fits of the power characteristics for the completely filled elements are characterized by their axis intercepts B_1 and B_2, given in Table 8.4. Specifically, the highest driving power values were obtained for the conveying elements C15 and C30. Specifically, for these elements the driving power also showed the strongest dependency on the flow rate, i.e., the driving power increased strongly with decreasing flow rate due to the high pressure generation ability of these elements. The power characteristic of the kneading element K30 is very similar to the conveying elements, since K30 also significantly conveys and generates pressure (see Figure 8.4). Qualitatively similar is also the power characteristic of the mixing element M15, however, this element showed the lowest power values among the investigated elements, which can be addressed to its reduced amount of gap regions, caused by the axial openings. On the contrast, the non-conveying kneading element K90 showed a driving power independent of the flow rate. The theoretical reason for this is the symmetry of the element K90, i.e., its driving power must be independent of the flow rate

direction. Considering the linearity of the power characteristic, which results from the linearity of the Stokes equations, the only possible way to fulfill both conditions is a constant power.

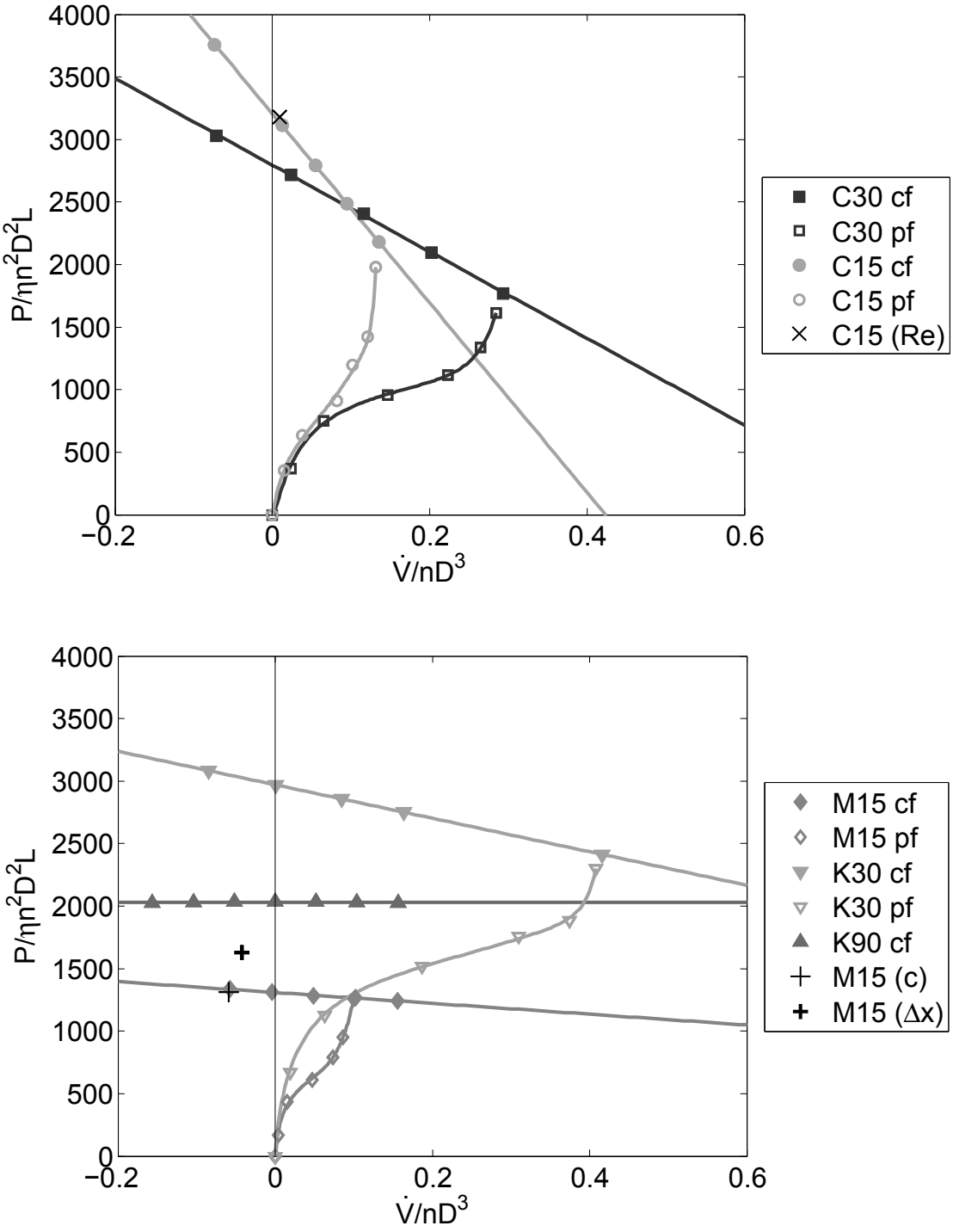

Figure 8.6: Power characteristic for the completely filled (cf) and the partially filled (pf) elements.

The shown nonlinear fits for the partially filled elements were calculated from Eq. 8.12 (for the parameters see Table 8.5), where $\Pi_P = P/P_{f=1}$ is the driving power normalized with the power $P_{f=1}$ at filling ratio $f = 1$[21]:

$$\Pi_P = f + \beta_0 (1-f)\left[1-(1-f)^{\chi_0}\right] - \beta_1 f\left(1-f^{\chi_1}\right) \tag{8.12}$$

The partially filled elements can only be achieved for flow rates between zero and the inherent convening capacity, the so-called “conveying conditions”. Clearly, negative flow rates are only possible with strong backpressure (“backward pumping conditions”), similarly, flow rates exceeding the inherent conveying capacity require a pressure rise directed in the conveying direction (“overrun screw”), and thus, a completely filled element.[27]

The power characteristics of the partially filled elements approach zero as the flow rate approaches zero, since the elements are empty there. The power characteristics of the partially filled elements and of the completely filled elements converge at the inherent conveying, where the backpressure of the completely filled element is zero, and the filling ratio of the partially filled element is one. However, for these specific two cases, the resulting power was not identical, since the background pressure p_0 was zero for the partially filled state, and non-zero for the completely filled state (see Table 8.2). Theoretically, a flow described by the Navier Stokes equations is pressure invariant, i.e., depends only on the pressure gradients, not on the absolute level of the pressure. However, the used weakly compressible SPH formulation is not exactly pressure invariant, which is the reason for this discrepancy. Nevertheless, this formulation is widely used due to its exact momentum conservation and for the mostly studied free surface flows the lack of pressure invariance is not critical. However, for the specific case of completely filled screw elements it might be beneficial to investigate the applicability of other formulations, to avoid this problem. At least, with the applied formulation, the background pressure p_0 should be kept as low as possible to keep the errors low.

The results of the reference cases with lower Reynolds number “C15 (Re)” and higher speed of sound “M15 (c)” showed excellent agreement. Specifically, the lower Reynolds number, tested for the C15 element, yielded almost identical values in terms of pressure and power characteristic, which confirms the assumed validity of the creeping flow regime.

Also, the higher speed of sound in case of the M15 element yielded quasi identical results, showing that the chosen speed of sound was sufficiently high to keep the compressibility negligible. Only, the case "M15 (Δx)" with the lower particle spacing Δx = 0.2 mm yielded significant deviations compared to the corresponding case with Δx = 0.3 mm, since here also the clearances between screws and barrel were tighter, in order to test the impact on the results. Specifically, the flow rate was slightly higher in the case Δx = 0.2 mm, which can be addressed to reduced backflow through the tighter clearances (the backflow $A_1 n D^3 - \dot{V}$ was ca. 10% lower). The deviation of the driving power was even more pronounced (ca. 25% higher with Δx = 0.2 mm), since the extremely high shear rates in the clearance regions contribute strongly to the screw driving power. Considering that the volume fraction of the clearance regions is comparably low for the M15 element due to the axial openings, the observed increase of the driving power for the tighter clearances would be a multiple for screw elements without these openings, i.e., continuous clearances. This means that the presented power characteristic results, obtained with increased clearance distances compared to the real geometry, are quantitatively not representative for newly manufactured, real screw elements, where the clearances are even tighter than the investigated 0.3 and 0.2 mm. It is also important to mention that the clearance distances strongly depend on the degree of abrasion, and that the clearances of massively used extruders are typically considerably larger compared to newly manufactured extruders (strongly depending on the processed materials, the actual processing conditions and the operating time). The strong dependency of the driving power on the clearances together with the typical evolution of the clearance distances over the life time of extruder screws makes a general definition of power characteristic values absurd. Thus, the lack of quantitative accuracy of the shown power characteristics is less important, rather the qualitative trends can support the understanding of the flow field in the investigated screw elements.

The resulting flow fields for all investigated screw elements are illustrated in Figure 8.7 – Figure 8.13, specifically snapshots of the velocity magnitude, the axial velocity, the pressure and the mixing index. Three dedicated operation states are shown there for the actively conveying elements (C15, C30, M15 and K30), two completely filled (Figure 8.7 – Figure 8.10) and one partially filled with filling ratio f = 0.5 (Figures 8.12 and 8.13).

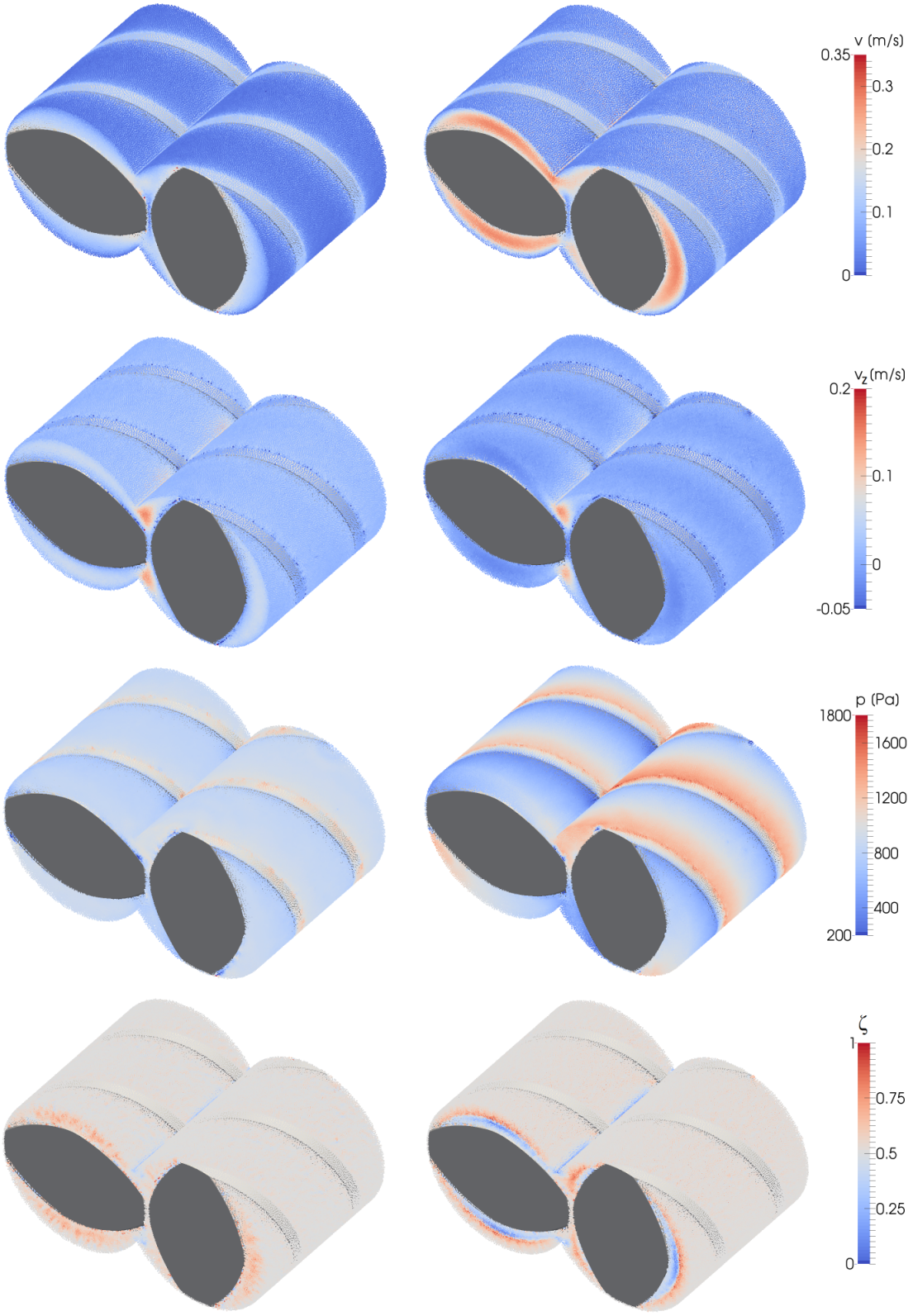

Figure 8.7: Snapshots of (from top to bottom): velocity magnitude v, axial velocity v_z, pressure p and mixing index ζ for the completely filled element C30 in two operation states: Left column: $a_z = 0$ and $\dot{\boldsymbol{V}}/\boldsymbol{nD}^3 = 0.29$; right column: $a_z = 60$ m/s² and $\dot{\boldsymbol{V}}/\boldsymbol{nD}^3 = 0.02$. The rotation is counter-clockwise.

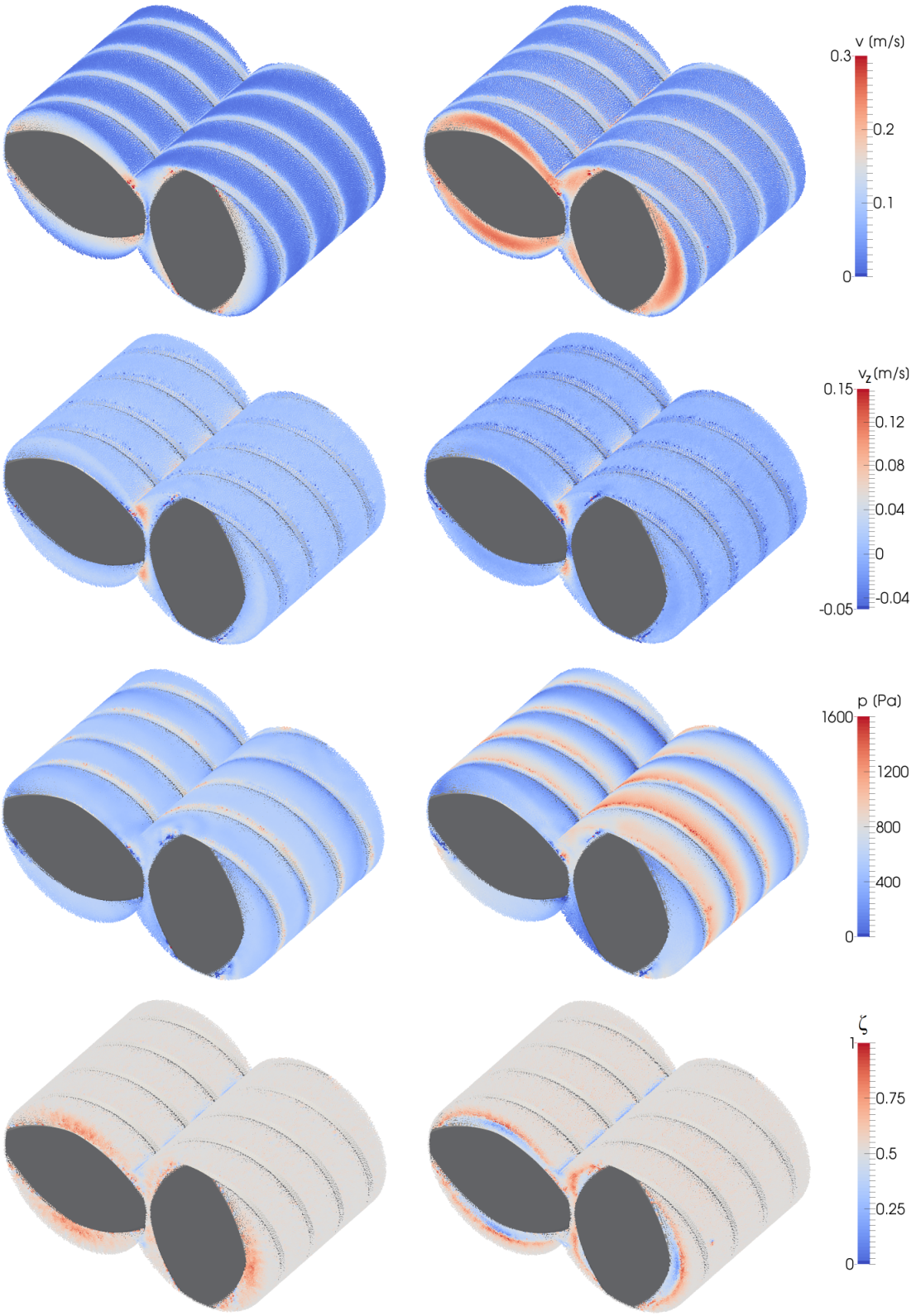

Figure 8.8: Snapshots of (from top to bottom): velocity magnitude v, axial velocity v_z, pressure p and mixing index ζ for the completely filled element C15 in two operation states: Left column: $a_z = 0$ and $\dot{\boldsymbol{V}}/\boldsymbol{nD}^3 = 0.14$; right column: $a_z = 120$ m/s² and $\dot{\boldsymbol{V}}/\boldsymbol{nD}^3 = 0.01$. The rotation is counter-clockwise.

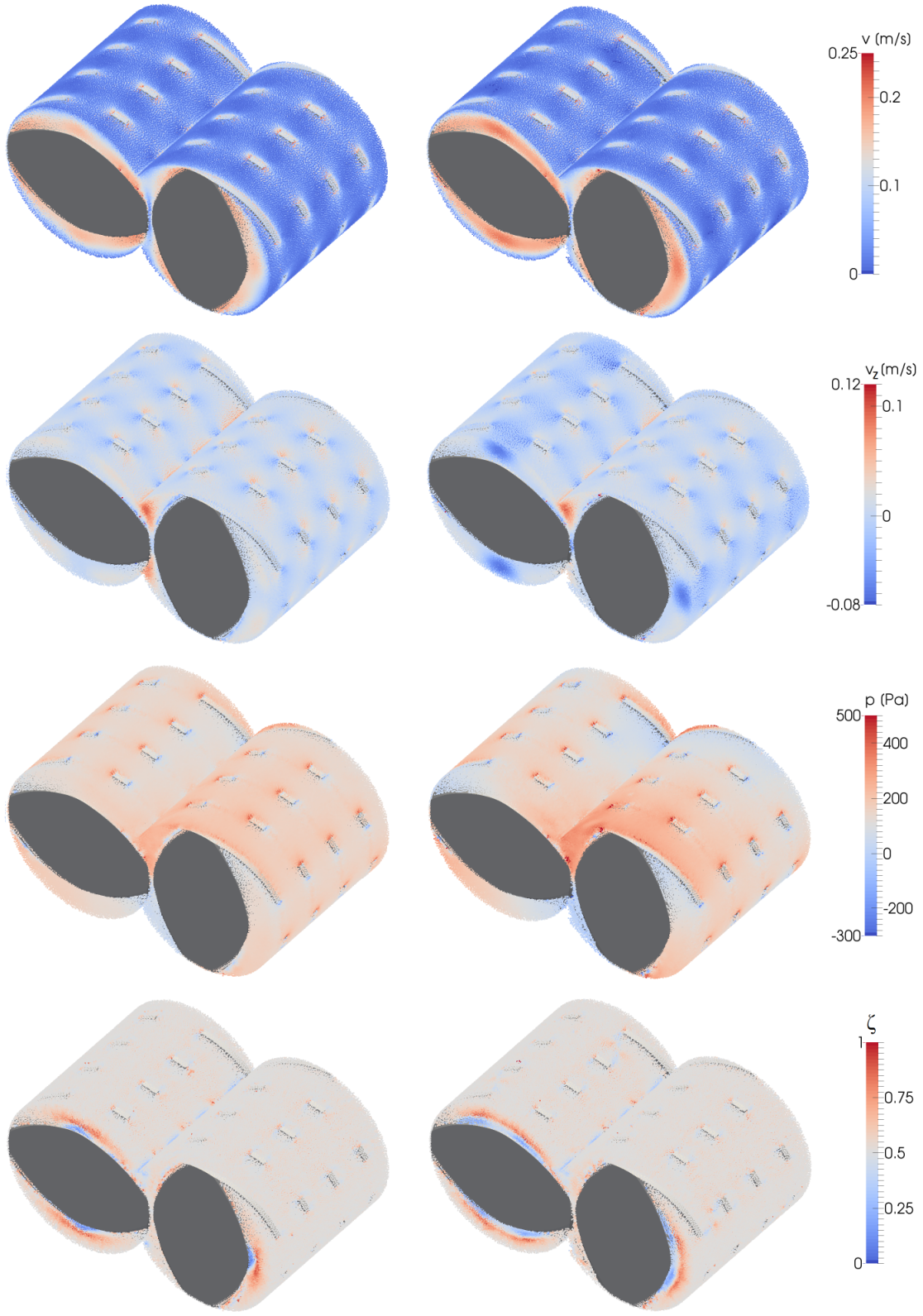

Figure 8.9: Snapshots of (from top to bottom): velocity magnitude v, axial velocity v_z, pressure p and mixing index ζ for the completely filled element M15 in two operation states: Left column: $a_z = 0$ and $\dot{\boldsymbol{V}}/\boldsymbol{nD}^3 = 0.10$; right column: $a_z = 6.67$ m/s² and $\dot{\boldsymbol{V}}/\boldsymbol{nD}^3 = 0.00$. The rotation is counter-clockwise.

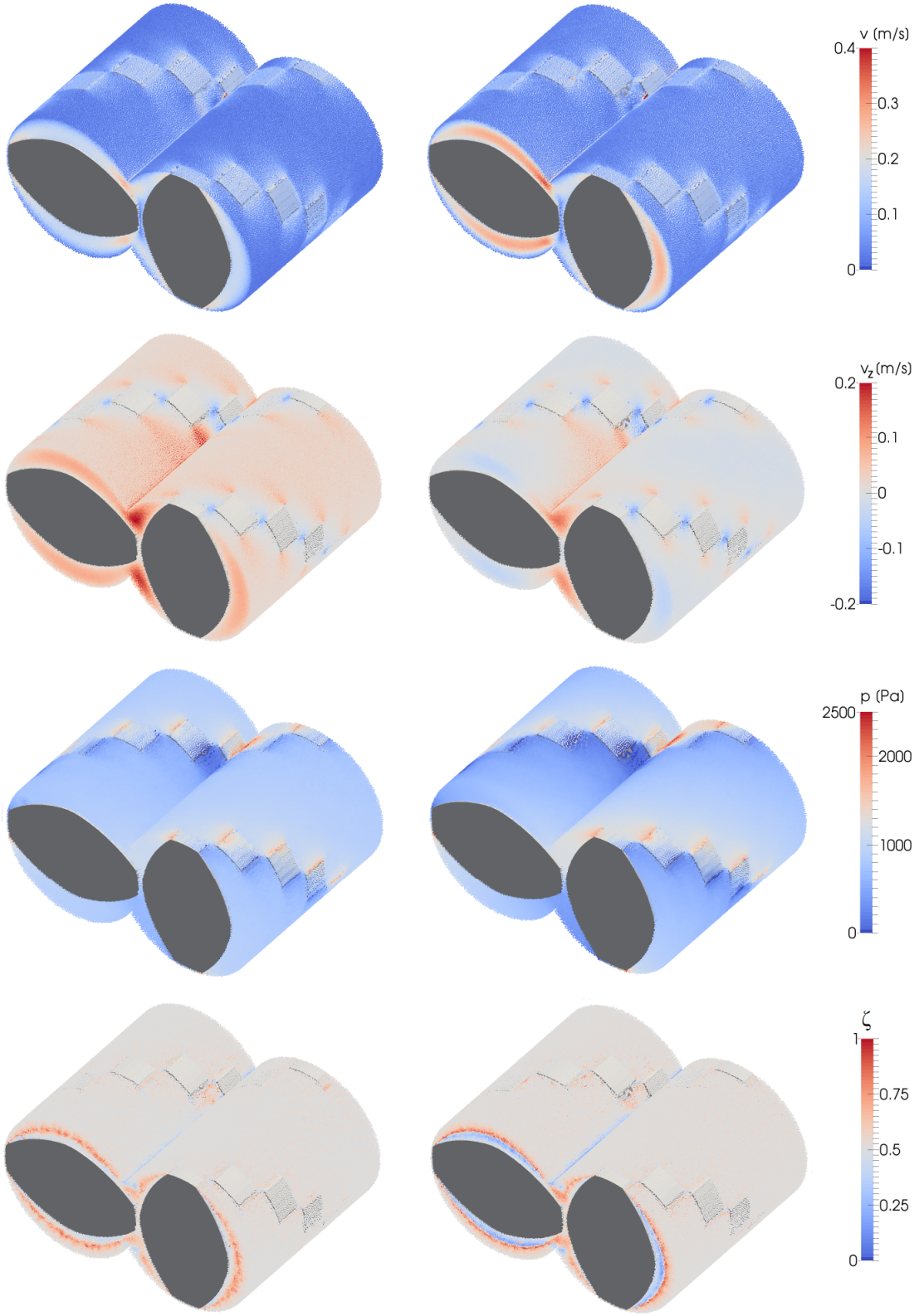

Figure 8.10: Snapshots of (from top to bottom): velocity magnitude v, axial velocity v_z, pressure p and mixing index ζ for the completely filled element K30 in two operation states: Left column: a_z = 0 and $\dot{\boldsymbol{V}}/\boldsymbol{nD}^3$ = 0.41; right column: a_z = 60 m/s² and $\dot{\boldsymbol{V}}/\boldsymbol{nD}^3$ = 0.01. The rotation is counter-clockwise.

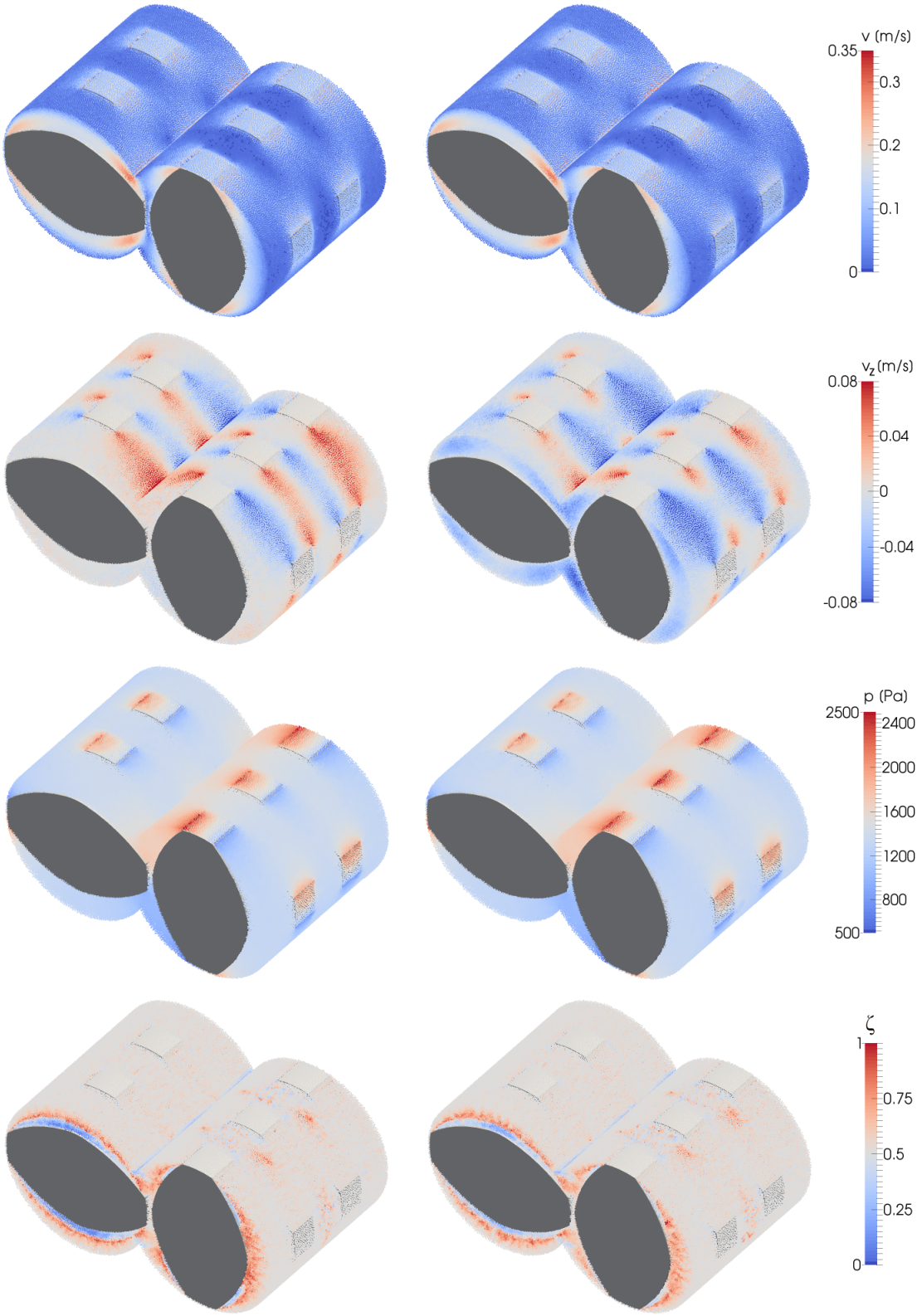

Figure 8.11: Snapshots of (from top to bottom): velocity magnitude v, axial velocity v_z, pressure p and mixing index ζ for the completely filled element K90 in two operation states: Left column: a_z = 0 and $\dot{\boldsymbol{V}}/\boldsymbol{nD}^3$ = 0.00; right column: a_z = 10 m/s² and $\dot{\boldsymbol{V}}/\boldsymbol{nD}^3$ =-0.16. The rotation is counter-clockwise.

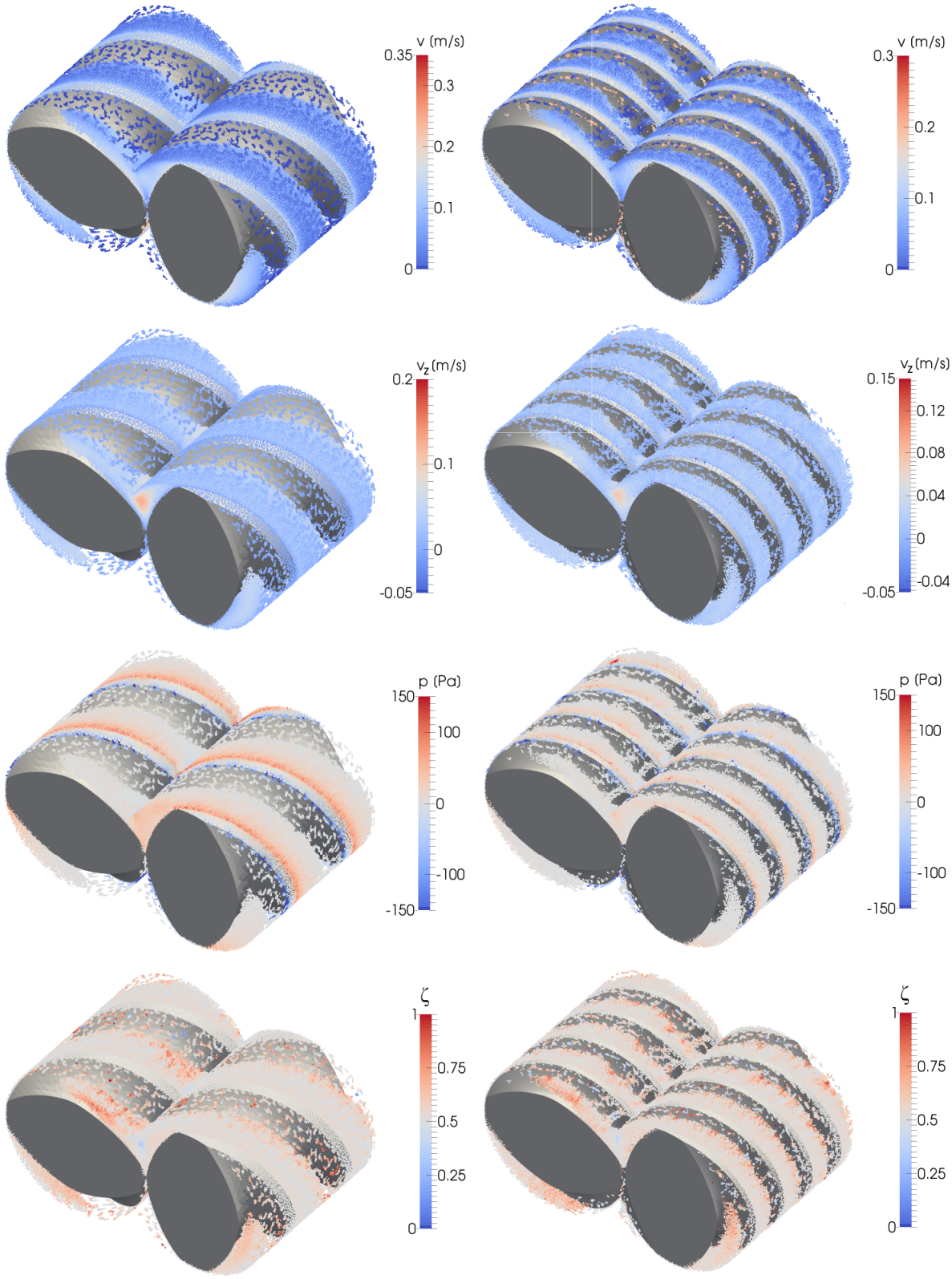

Figure 8.12: Snapshots of (from top to bottom): velocity magnitude v, axial velocity v_z, pressure p and mixing index ζ for the partially filled elements C30 (left column) and C15 (right column) with filling ratio $f = 0.5$. The rotation is counter-clockwise.

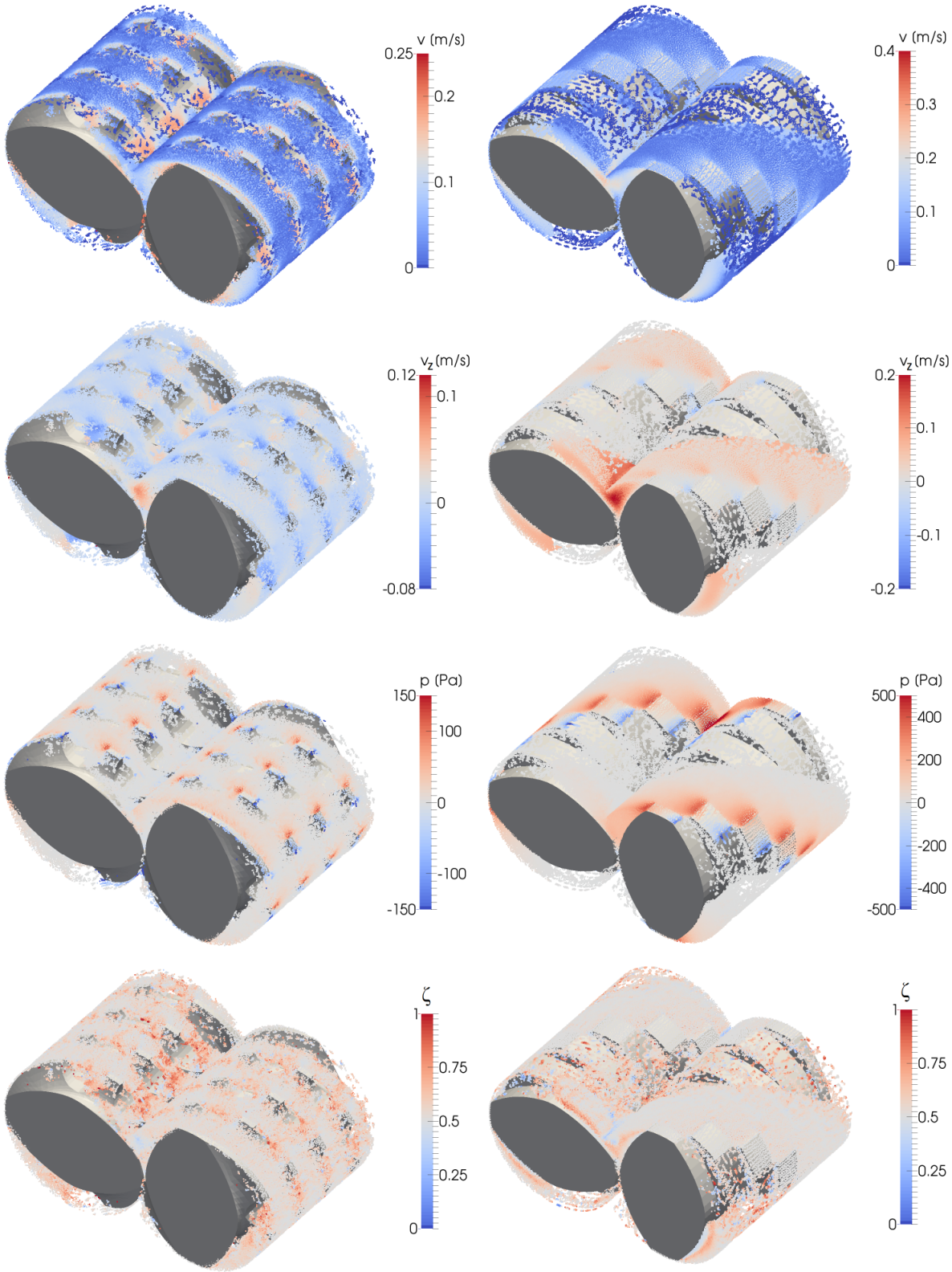

Figure 8.13: Snapshots of (from top to bottom): velocity magnitude v, axial velocity v_z, pressure p and mixing index ζ for the partially filled elements M15 (left column) and K30 (right column) with filling ratio $f = 0.5$. The rotation is counter-clockwise.

For the non-conveying K90 element, only two completely filled states are shown (Figure 8.11), since the partial filling is not reasonable there. For the completely filled elements, first we showed the inherent conveying (left columns in Figure 8.7 – Figure 8.11), which is the transition from complete to partial filling, and second a case with backpressure (right columns in Figure 8.7 – Figure 8.11). For the latter, the flow rate was almost zero compared to the inherent conveying capacity, i.e., represented by the symbols closest to the y-axis in Figure 8.4 and Figure 8.6 (i.e., a_z = 120, 60, 6.67 and 25 m/s² for C15, C30, M15 and K30, respectively). Thus, these operations states approximately represent the flow established when conveying against a closed nozzle, i.e., yielding the maximum pressure which can be generated by these elements (considering only positive flow rates, i.e., right handed elements). For the non-conveying element K90, whose inherent conveying capacity is zero, the shown case with a_z = 10 m/s² yielded a comparably high flow rate of $\dot{V}/nD^3$ = 0.16, which is in the upper range of throughput values used in practical applications. Thus, the shown operation states represent the upper and lower limits of the flow rate in real applications of these screw elements. Only, in the case of left-handed screw elements the resulting flow rate would be negative and thus, outside of these limits. However, for negative flow rates the flow field is qualitatively similar to the case of zero flow rate.

The flow generated by the conveying elements C15 and C30 (Figure 8.7, Figure 8.8 and Figure 8.12) shows the same features as already shown in our previous work for a conveying element.[21] Specifically, maxima of the axial velocity occurred in the intermeshing region, which were almost independent of the actual operation state. The axial velocity in the channel regions was positive for zero backpressure (left columns) and slightly negative for zero flow rate (right columns), where the backpressure drove a flow through the channels against the conveying direction. This backflow also caused maximum values of the velocity magnitude in the channels. At the barrel surfaces, the velocity magnitude approached zero, and the screw rotation speed at the screw surfaces, caused by the no-slip condition. For the case with backpressure (right columns), the pressure distribution does not show the increasing pressure level along the z direction, since this was in conflict with the periodic boundaries. Thus, it is important to take into account the applied hydrostatic pressure gradient against the conveying direction, which corresponds to pressure rises of 1800 and 3600 Pa along the 30 mm length for the C15 and C30 elements, respectively. Besides that, the pressure distribution of the conveying elements shows

maximum values in front of the rotating screw flights, and minimum values behind them, causing pressure gradients and flow through the clearances.

The velocity and pressure values inside the partially filled conveying elements are very similar to the inherent conveying, since the backpressure is zero in both cases and they only differ in the filling ratio. In the empty regions a pattern of fluid particles adhering to the screw and barrel surfaces is obvious, which might correspond to thin films in reality. However, the used particle spacing was not sufficiently fine to resolve these films in our simulations.

The flow field of the M15 element (Figure 8.9) looks similar to the C15 element. However, due to the axial openings the pressure driven backflow mainly occurred through the openings, which is most obvious from the axial velocity snapshot. Although, these openings are distributed around the entire circumference of the element, the backflow mainly occurred at two opposite circumferential positions (considering one element). At these two positions, the openings are created along the entire element length, i.e., they cut all four screw flights and generate a continuous channel in the axial direction (see also Figure 8.1 and Figure 8.3). At all other positions, the openings cut only three screw flights and, thus, the axial channel is discontinuous here. Clearly, the flow took the way of minimal resistance, i.e., through the continuous channels, whereas the backflow through other openings was vanishing. It can be assumed, that this impacts the residence time distribution due to stagnant flow in these openings, which are even not emptied by the self-cleaning mechanism. This is even more pronounced in the partially filled state (Figure 8.12, left column), where fluid portions are located inside the openings, having the velocity of the screw rotation. They can be expected to be rarely exchanged, since no pressure-driven backflow occurred in the partially filled state. This suggests to avoid partially filled mixing elements, which specifically has to be taken into account when designing a screw configuration. The complete filling of these elements can be achieved by locating a non-conveying or even left-handed element downstream to the mixing element. Without this, the M15 is partially filled due to its conveying properties (at least for flow rates below its inherent conveying capacity). For deeper insights into the interaction of screw elements along an entire screw, and the corresponding design considerations please refer to our previous work.[6] It is not clear if the discussed aspects of the flow through the openings of

the M15 element were intended or not, and also if the backflow through all openings would be beneficial for mixing. However, in future work this aspect should be investigated in more detail, which could lead to a further improvement of the geometry of this mixing element.

The flow field generated by the kneading element K30 (see Figure 8.10 and Figure 8.13) is comparable to the conveying elements. Specifically, the K30 element shows similar maxima of the axial velocity in the intermeshing region for all presented operation states, the inherent conveying (Figure 8.10 left column), the case with backpressure (Figure 8.10 right column) and the partially filled state (Figure 8.13 right column). In the channel regions, the axial velocity is positive for inherent conveying and negative with backpressure, i.e., the K30 element does significantly convey (which agrees well with Figure 8.4 and Figure 8.5). Moreover, the K30 element shows local maxima and minima of the axial velocity in front of each kneading disc, i.e., the kneading discs displace the fluid in front of them due to their rotation. This is also obvious from the pressure distribution, which shows local maxima in front of the kneading discs, and minima behind. This effect also yields a flow through the openings between adjacent kneading discs, which contributes to mixing.

For the kneading element K90 (Figure 8.11) the flow field is partially similar to the K30, element, however without the conveying effect. Thus, the axial velocity does not show the characteristic maxima in the intermeshing region of screw elements which actively convey. Instead of that, in the case without backpressure (Figure 8.11 left column), the entire cross section shows a zero axial velocity, whereas in the case with backpressure the backflow is also much more homogeneous than for elements which actively convey. Similar to the K30 element, pressure maxima in front and minima behind the kneading discs are obvious due to the displacement of fluid flowing around the rotating discs. The corresponding maxima and minima of the axial velocity are also obvious.

8.5.2 Mixing

Qualitative results about mixing could be directly obtained from the flow field by evaluating the mixing index ζ according to its definition Eq. 8.2. Snapshots of the mixing index are shown at the bottom of Figure 8.7 - Figure 8.13 for the above presented operation

states. Basically, the mixing index shows very similar patterns for all investigated screw elements and operation states. An example histogram of the spatial distribution (by mass fraction *w*) is shown in Figure 8.14 for the K90 element. This was qualitatively equal for all investigated cases, and was also similarly shown by Yang and Manas-Zloczower[32]. The mixing index ζ is dominated by the value 0.5 (shear flow), specifically in the regions close to the barrel surface. Inside the screw channels also values close to 1 occurred (elongational flow), indicating good mixing. However, close to the screw surface the mixing index dropped down close to 0 (rotational flow), indicating poor mixing.

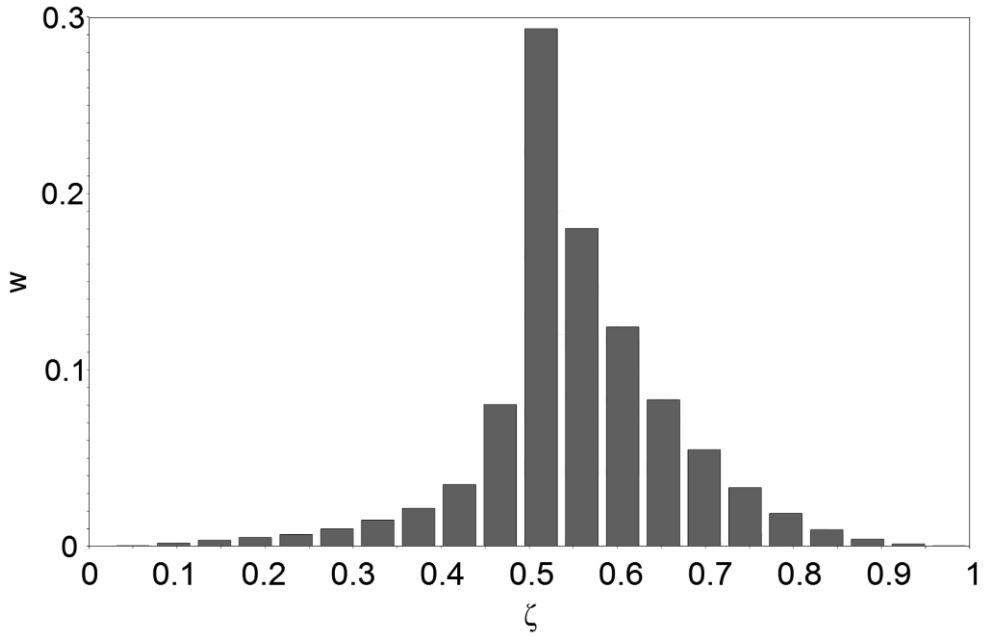

Figure 8.14: Exemplary mass distribution of the mixing index (K90, a_z = 10m/s²).

Figure 8.15 shows the average mixing index ζ_{av} (averaged over all fluid particles) versus the dimensionless flow rate for all investigated screw elements in the completely filled state. The values showed only minor variations and are located between 0.51 and 0.57. Similar values were reported by Yang and Manas-Zloczower[32]. However, the M15 and K90 elements showed significantly higher values than the C15, C30 and K30 elements below the inherent conveying capacity, i.e. in the operation range relevant for practical applications. This indicates higher amounts of elongational flow and, thus, better mixing capabilities for the M15 and K90 elements. However, these data do not provide sufficient information for the quantitative design of extrusion processes, rather support the qualitative understanding of the flow.

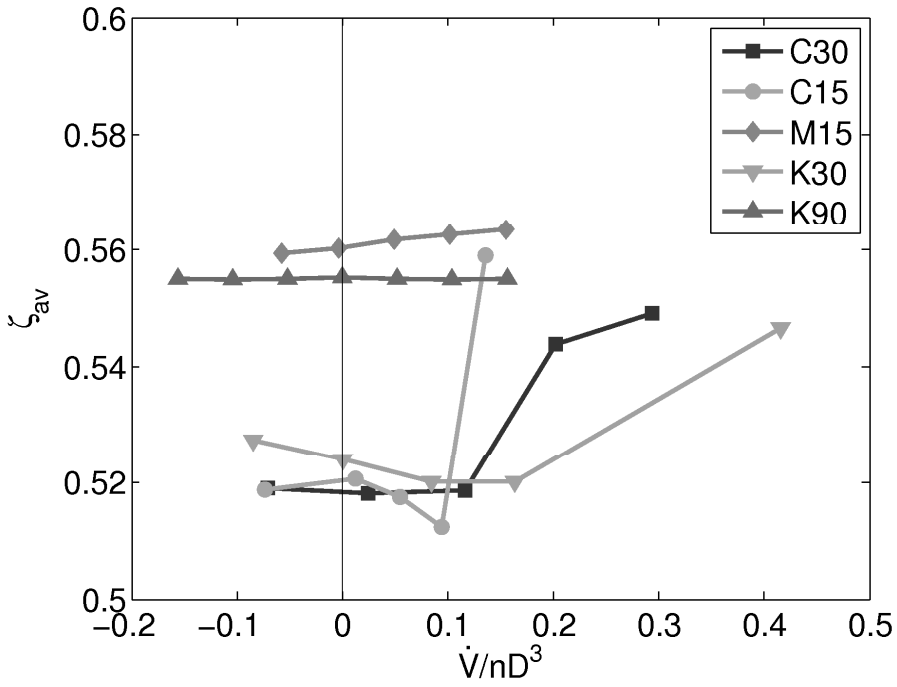

Figure 8.15: Average mixing index ζ_{av} versus the dimensionless flow rate for the completely filled screw elements.

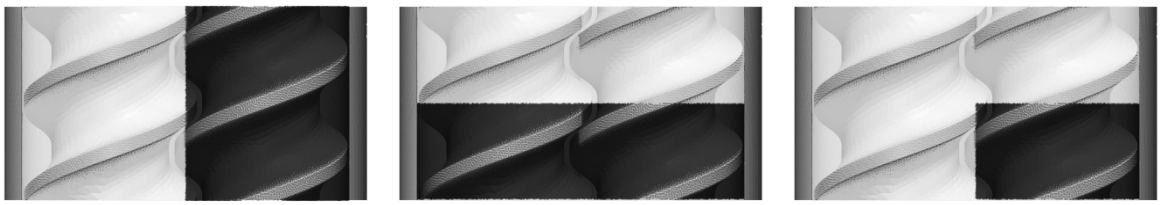

Figure 8.16: Used tracer configurations (from left to right: cross, axial, quarter).

In order to gain a quantitative description of the mixing process for the screw elements in the completely filled state, we used tracer particles, similar as shown in our previous work.[22] For the partially filled state mixing is less relevant due to the lower residence time, as we showed in our previous work. In the completely filled states we used three different tracer configurations, shown in Figure 8.16. The first was initialized in a half of the cross section (Figure 8.16 left, termed tracer "cross"), and can be expected to indicate only cross mixing directly after the initialization (deformation and distribution during the rotation caused increasing influence of axial mixing). The second was called tracer "axial" and was initialized in a half of the axial length (see Figure 8.16 middle), and indicated only axial mixing initially. The third tracer was a combination of "cross" and "axial", and was

initialized in a quarter of the simulation box, thus called “quarter”. The latter indicated cross and axial mixing both, thus was assumed to be the most relevant tracer for real applications, where cross and axial mixing occur simultaneously.

The tracers were initialized after 0.25 revolutions, this was sufficient to develop the flow. From that, we evaluated the time evolution of the mixedness on a grid of cubed cells with a cell size of 1 mm. This size was chosen since it represents a typical product size of HME processes, when considering pellets and granules. In order to get information about the grid size dependency, we conducted the same evaluation on a grid of cell size 1.5 mm, and compared the results. The evaluation of the mixedness M was based on the standard deviation σ of the amount of tracer particles in each cell, for details about the evaluation of σ (e.g., how to achieve a constant sample size or about the treatment of cells crossed by the screw and barrel surfaces) please refer to our previous work.[22] From this, the mixedness M was calculated according to:

$$M = 1 - \frac{\sigma}{\sqrt{\frac{N_{tracer}}{N_{total}} \cdot \left(1 - \frac{N_{tracer}}{N_{total}}\right)}} \tag{8.13}$$

where N_{tracer} is the number of tracer particles and N_{total} the total particle number. This leads to values $0 \leq M \leq 1$, where $M = 0$ means completely unmixed (i.e., σ is maximal), and $M = 1$ means homogeneously mixed (i.e., $\sigma = 0$). This yielded the time evolution of M during the runtime of each simulation (5 screw revolutions). For example, this is shown in Figure 8.17 for the M15 element without backpressure for the tracer quarter. In all simulations, a more less pronounced inflection point occurred after 0.5 – 3 revolutions. As we showed earlier,[22] for screw elements with a strong conveying capabilities, as the C15, C30 and K30 elements, this can be addressed to the periodic boundaries together with the strong axial convection caused by the conveying effect, which distributed the tracer very fast initially, whereas mixing was more limited when the tracer was already distributed along the entire length. However, in this work we found that this effect is not equal for all screw elements. Specifically, the elements M15 and K90 even showed the inverted behavior, i.e., slow mixing first and faster mixing later (a typical example for this is shown in Figure 8.17). For a detailed discussion of the observed phenomena please see below.

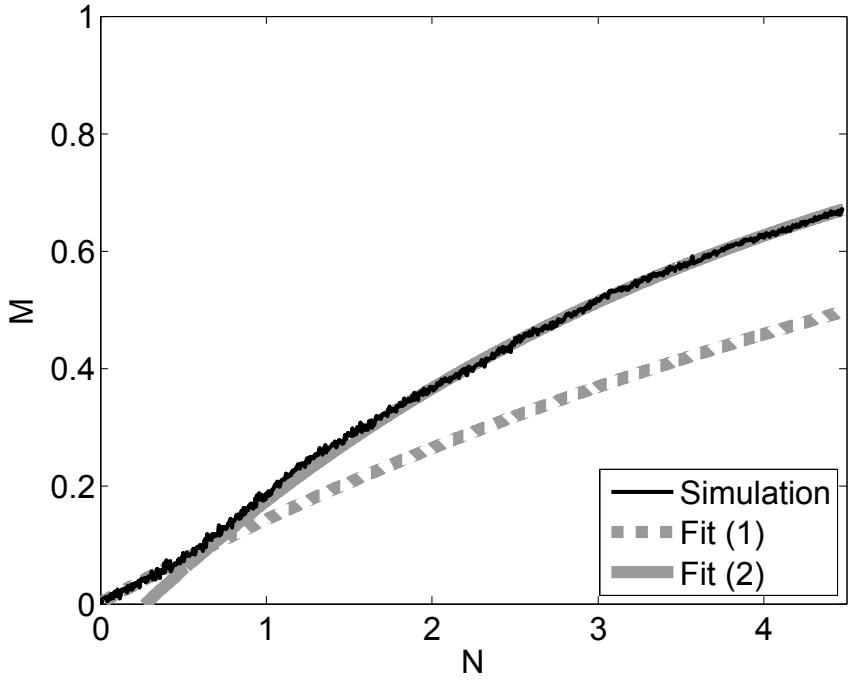

Figure 8.17: Example for the evolution of the mixedness of tracer "quarter" during the screw revolutions and fitted curves for the mixing before (fit 1) and after (fit 2) the inflection (M15 element at zero backpressure).

To account for the different mixing rates initially and later in the evaluation, we determined two mixing rates for each case, termed k_1 (initially) and k_2 (after the inflection), by fitting the following function to the evolution of the mixedness M during the number of revolutions N:

$$M = 1 - e^{-kN} \tag{8.14}$$

For an example of these fits see Figure 8.17. The resulting mixing rates versus the flow rate (the so-called mixing characteristic) for the tracers cross ($k_{1,cr}$ and $k_{2,cr}$), axial ($k_{1,ax}$ and $k_{2,ax}$) and quarter ($k_{1,qu}$ and $k_{2,qu}$) are shown in Figure 8.18 – Figure 8.22 for the screw elements C15, C30, M15, K30 and K90, respectively. In general, it is obvious there that the obtained mixing rates are not equal for the used tracers, i.e., a generally applicable mixing rate is not existing. However, relations between the mixing rates of the different tracers are obvious, as the mixing rates of the quarter tracer are approximately a weighted average of the mixing rates of the cross and axial tracers. Specifically, the mixing rate $k_{2,qu}$ is mostly similar to the arithmetic average of the mixing rates $k_{2,cr}$ and $k_{2,ax}$ ($k_{2,qu} \approx (k_{2,cr} + k_{2,ax})/2$), whereas the mixing rate $k_{1,cr}$ tends to be close to the maximum of $k_{1,cr}$ and $k_{1,ax}$.

The relevant mixing rates for practical applications are mainly those after the inflection, since the initial mixing is strongly related to the chosen initial tracer configuration, whereas in real applications the materials are typically not in such an ordered state prior to the mixing. Also, the initial mixing occurs relatively short compared to the mixing after the inflection. Whereas the initial mixing rates $k_{1,cr}$ and $k_{1,ax}$, which represent pure cross- and axial mixing, are clearly different, the mixing rates $k_{2,cr}$ and $k_{2,ax}$ tend to be more similar, specifically for the C15 and C30 and K30 elements. Taking into account the rough relation $k_{2,qu} \approx (k_{2,cr} + k_{2,ax})/2$, all obtained mixing rates tend to be similar after the inflection, which can be addressed to the fact, that the initial difference in the distribution of the tracer particles vanished during the mixing time, and would yield a homogenous mixture after enough revolutions for all tracers, independent of the initial configuration.

The largest differences in $k_{2,cr}$, $k_{2,ax}$ $k_{2,qu}$ occurred for the elements K90 and M15, specifically at flow rates around zero. This can be addressed to a poor axial mixing around zero flow rate for these elements with poor or even vanishing conveying capabilities, i.e, when the axial flow is almost stagnant at zero flow rate.

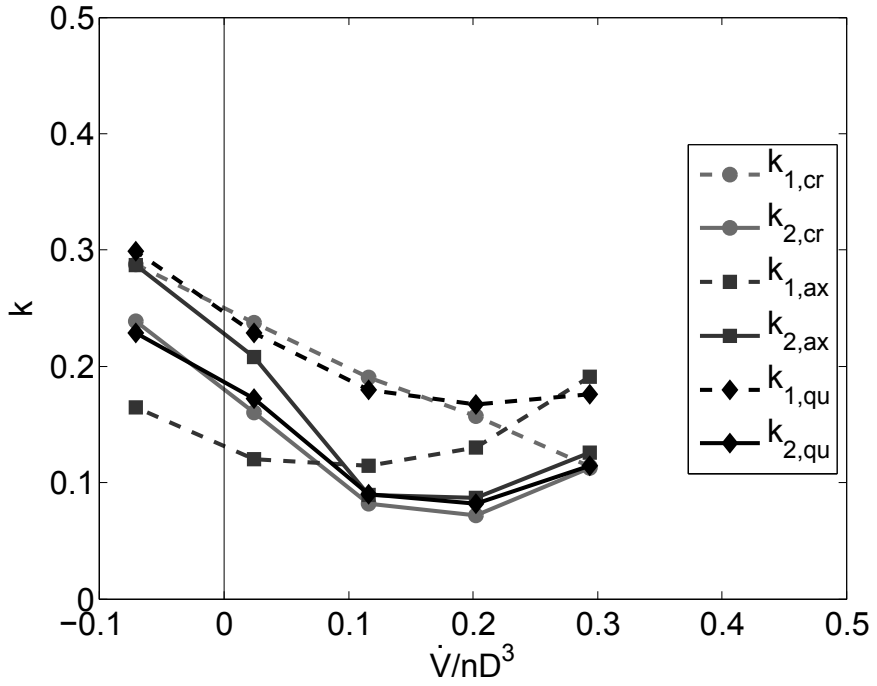

Figure 8.18: Mixing rates $k_{1,cr}$, $k_{2,cr}$, $k_{1,ax}$, $k_{2,ax}$, $k_{1,qu}$ and $k_{2,qu}$ versus the dimensionless flow rate for C30 in the completely filled state.

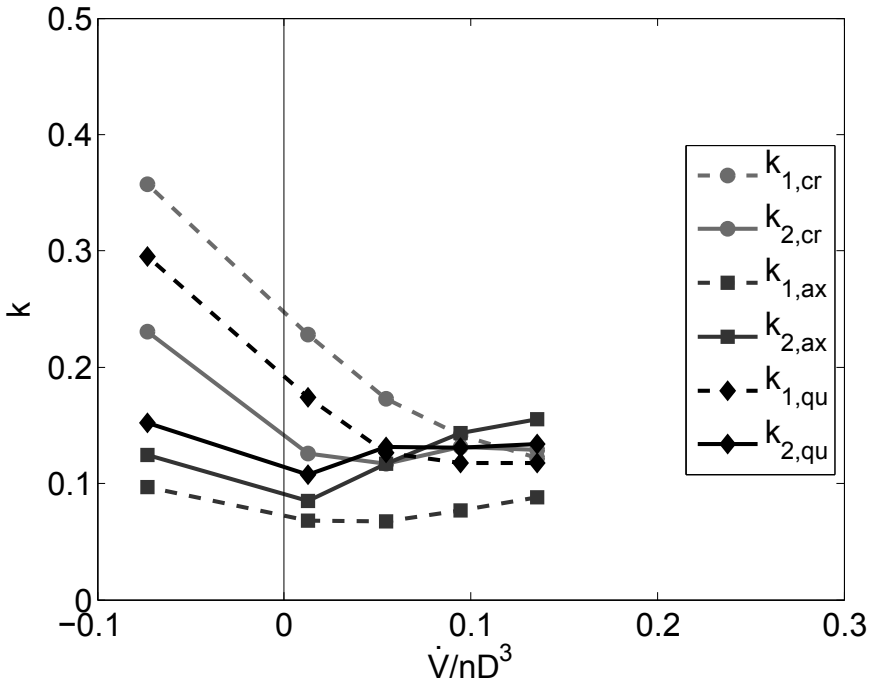

Figure 8.19: Mixing rates $k_{1,cr}$, $k_{2,cr}$, $k_{1,ax}$, $k_{2,ax}$, $k_{1,qu}$ and $k_{2,qu}$ versus the dimensionless flow rate for C15 in the completely filled state.

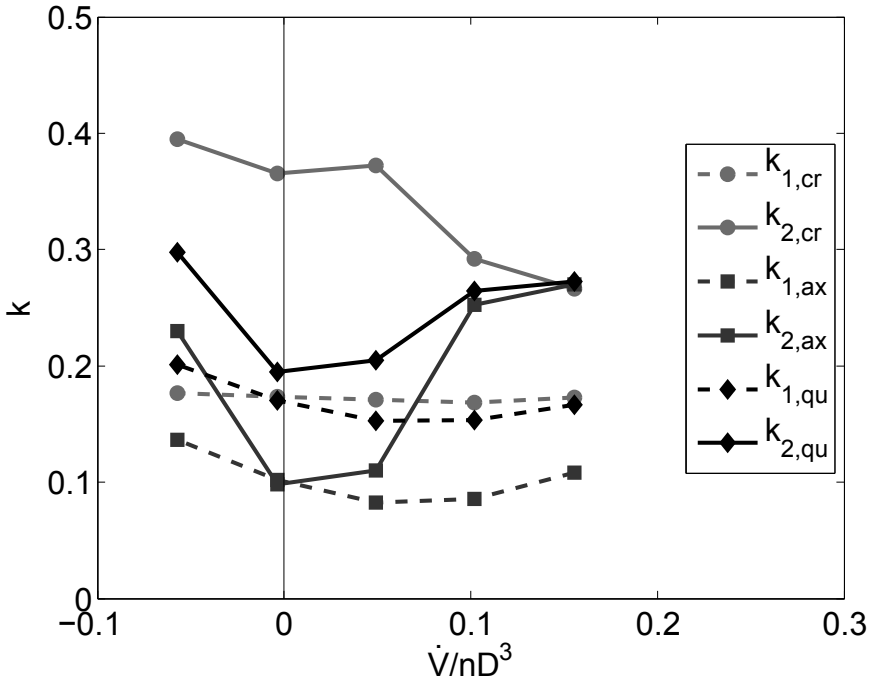

Figure 8.20: Mixing rates $k_{1,cr}$, $k_{2,cr}$, $k_{1,ax}$, $k_{2,ax}$, $k_{1,qu}$ and $k_{2,qu}$ versus the dimensionless flow rate for M15 in the completely filled state.

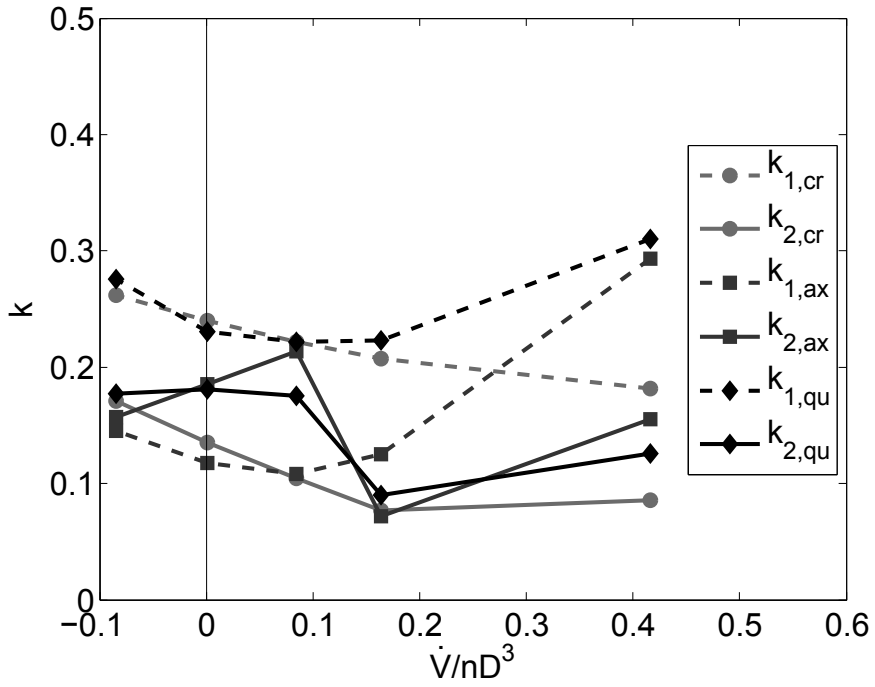

Figure 8.21: Mixing rates $k_{1,cr}$, $k_{2,cr}$, $k_{1,ax}$, $k_{2,ax}$, $k_{1,qu}$ and $k_{2,qu}$ versus the dimensionless flow rate for K30 in the completely filled state.

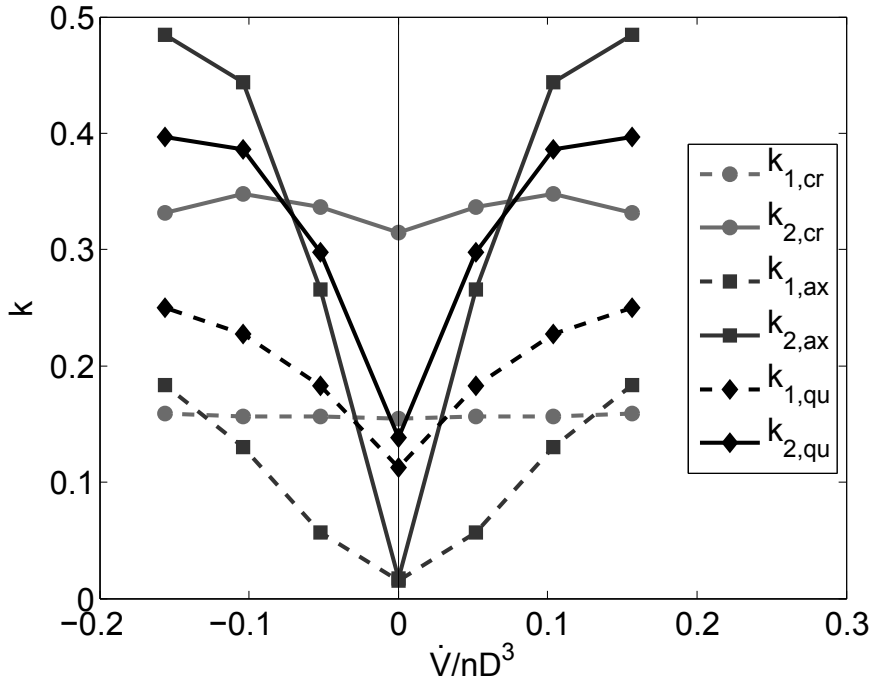

Figure 8.22: Mixing rates $k_{1,cr}$, $k_{2,cr}$, $k_{1,ax}$, $k_{2,ax}$, $k_{1,qu}$ and $k_{2,qu}$ versus the dimensionless flow rate for K90 in the completely filled state.

The conveying element C30 (Figure 8.18) showed almost equal mixing rates $k_{2,cr}$, $k_{2,ax}$ $k_{2,qu}$, which yielded a minimum at approximately the half inherent conveying capacity, increased strongly with the decreasing flow rate and reached highest values at negative flow rates, i.e., for left-handed elements. This is very similar as shown in our previous work,[22] and can be addressed to the strong pressure-driven backflow at low and negative flow rates, which is directed along the screw channels and significantly supports mixing (see also Figure 8.7). The initial mixing is faster than the mixing subsequent to the inflection for the cross tracer, which cannot be explained by the periodic boundaries in the axial direction. Rather this seems to be a slow distributive mixing subsequent to a fast initial deformation of the cross tracer. The axial tracer for high flow rates also showed a fast initial mixing followed by a slower mixing after the inflection, which is the consequence of the periodic boundaries and the strong axial convection, specifically at high flow rates (as already shown in detail previously[22]). Interestingly, for low and negative flow rates, the initial mixing rate of the axial tracer is comparable to the high flow rates, while the mixing rate after the inflection is strongly increased here, even higher than the initial mixing rate. This might be caused by the strong cross mixing occurring at low flow rates, which also effects the deformed axial tracer after the inflection, in contrast to its the initial configuration.

The conveying element C15 (Figure 8.19) shows a very similar mixing characteristic, however, the increased mixing at negative flow rates is less pronounced.

In contrast to the conveying elements, the mixing element M15 (Figure 8.20) shows significantly higher mixing rates, specifically for the tracer cross in the entire flow rate range. This indicates, that the geometry of the M15 element mostly supports cross mixing. From the comparison to the C15 element, it can be concluded that obviously the axial openings and the remaining teeth between them strongly support the cross mixing. The increased mixing rates $k_{2,ax}$ at high and negative flow rates also might be caused by the increased cross mixing, since the axial tracer here underlies also cross mixing after the initial deformation, in contrast to flow rates around zero. The initial mixing rates are lower than the mixing rates after the inflection here throughout the investigated flow rate range, even for the quarter tracer, which is sensitive to cross and axial mixing from the beginning.

This indicates that the M15 element supports fine-scale mixing, which occurs after the coarse distribution of the initial tracer configurations.

The kneading element K30 (Figure 8.21) basically showed a mixing characteristic similar to the conveying elements, however the mixing rate $k_{2,ax}$ interestingly showed a maximum at $\dot{V}/nD^3 \approx 0.1$ and a minimum of $k_{2,ax}$ at $\dot{V}/nD^3 \approx 0.16$. The reasons for this are currently not clear.

The non-conveying kneading element K90 (Figure 8.22) showed a mixing characteristic different from the elements described above. Due to the symmetry of the geometry, the mixing characteristic is also symmetrical around zero flow rate. Axial mixing increased strongly with the increasing flow rate, whereas the cross mixing was almost independent of the flow rate. Similar to the M15 element, the initial mixing rates were lower than the mixing rates after the infection, which indicates better mixing at smaller length scales.

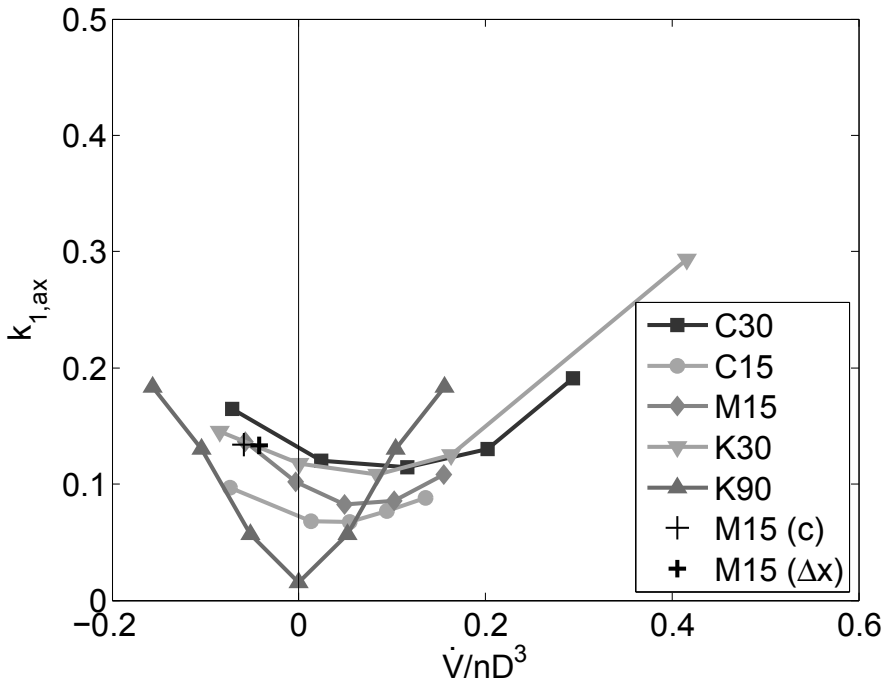

Figure 8.23: Mixing rate $k_{1,ax}$ versus the dimensionless flow rate for the investigated screw elements in the completely filled states.

Figure 8.23 and Figure 8.24 show the initial mixing rates of the axial and cross tracer for all elements, respectively, which represent pure axial and cross mixing. Obviously, the axial mixing of the elements with conveying capabilities (C15, C30, M15 and K30)

showed a minimum between zero flow rate and their inherent conveying capacity, which might be related to the pressure-driven backflow that led to a almost zero axial velocity in the channel regions here, corresponding to a poor axial mixing. For the K90 element, the minimum occurred exactly at zero flow rate, which is equal to the inherent conveying capacity of this non-conveying element. The K90 showed the strongest dependency of axial mixing with the flow rate, caused by the zero conveying capacity, which yielded a vanishing axial velocity at zero flow rate.

The initial cross mixing rate (Figure 8.24) clearly showed increasing mixing with decreasing flow rate for the actively conveying elements. This is caused by the increasing backflow along the channels. In contrast, the non-conveying K90 element showed an almost constant cross mixing versus the flow rate.

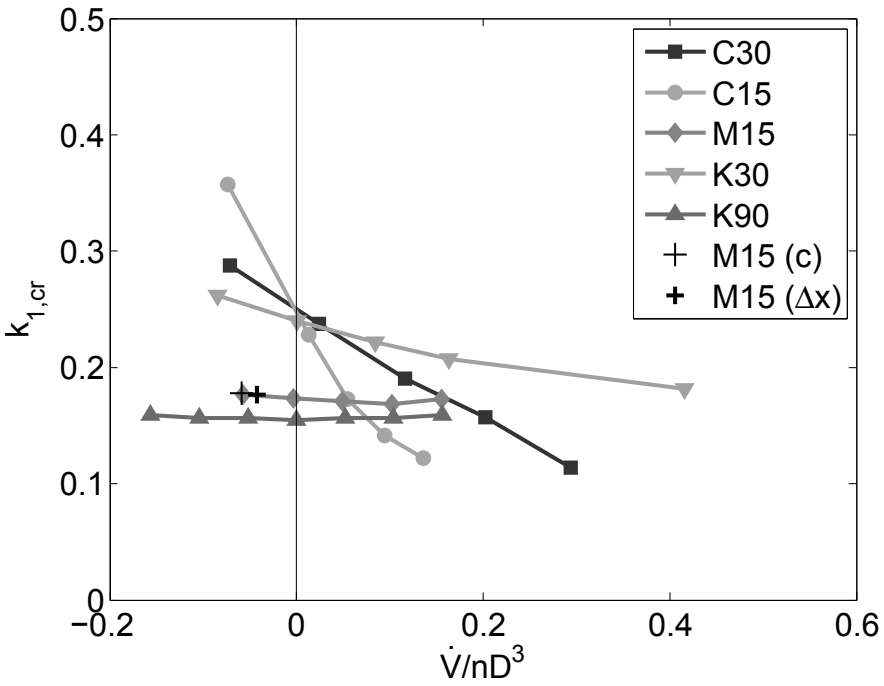

Figure 8.24: Mixing rate $k_{1,cr}$ versus the dimensionless flow rate for the investigated screw elements in the completely filled states.

Figure 8.25 shows the mixing rate $k_{2,qu}$ versus the flow rate for all investigated screw elements in comparison. This is the most relevant mixing rate for practical applications since it includes both, axial and cross mixing, and is less impacted by the ordered initial state than the initial mixing rate. Here, the K90 and M15 elements showed the highest

mixing rates, however, with minima at zero flow rate. The mixing rates of the K90 element were even higher than of the M15 element, however, causing significantly more energy input (as shown in Figure 8.6). The good mixing capabilities of the K90 and M15 elements are in agreement with the above discussed average mixing index (Figure 8.15).

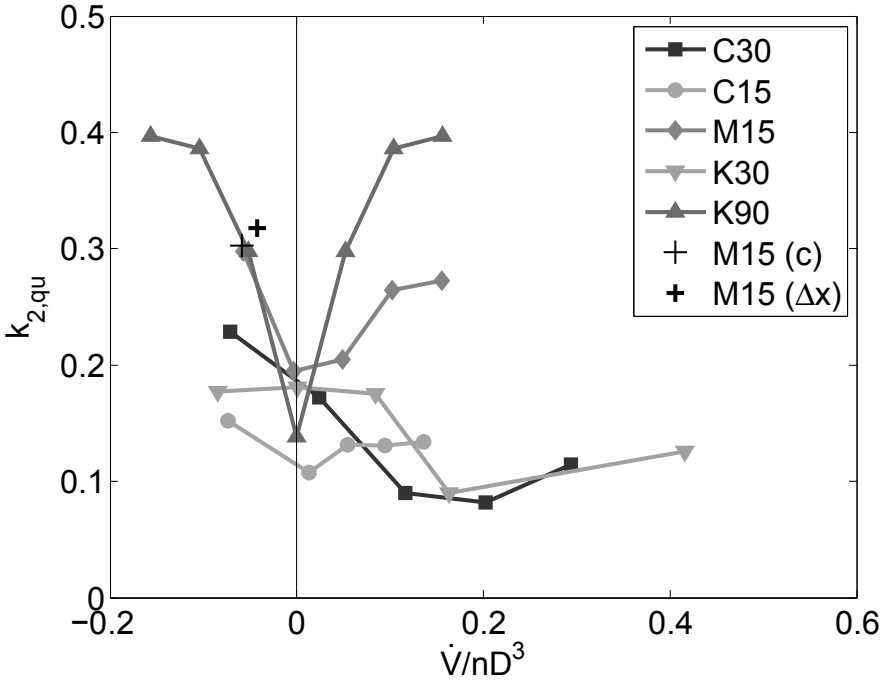

Figure 8.25: Mixing rate $k_{2,qu}$ versus the dimensionless flow rate for the investigated screw elements in the completely filled states.

In Figure 8.23, Figure 8.24 and Figure 8.25 also the resulting mixing rates of the reference simulations "M15 (c)" and "M15 (Δx)" are included, which showed well agreement. Thus, the compressibility effect vanished with the used speed of sound, the finer resolution of Δx = 0.2 mm had no benefits for the description of mixing, and the mixing was not influenced by the reduced clearances of the case M15 (Δx).

Figure 8.26 shows the mixing rates obtained with the 1 mm grid and with the 1.5 mm grid in comparison. Obviously, the data cloud shows a linear relationship with a proportionality factor of 1.2, i.e., the mixing rates evaluated with the 1.5 mm grid were 1.2 times higher compared to the 1 mm grid.

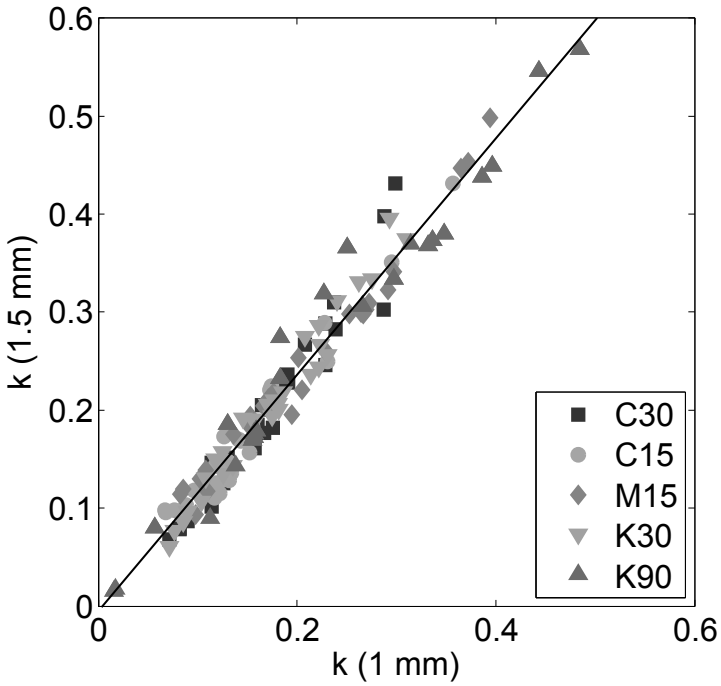

Figure 8.26: Grid size dependency of all determined mixing rates *k*.

8.6 Summary and Conclusions

In this work, we applied the SPH method and our new approach for the wall interaction of fluid particles with complex wall surfaces to study the flow and mixing inside typical screw elements of co-rotating intermeshing twin-screw extruders. Specifically, we presented the pressure and power characteristics of the investigated screw elements. These data clearly showed the differences between conveying elements, kneading elements with and without conveying capabilities and mixing elements with respect to their conveying capacity, pressure generation capabilities and power consumption. For the partially filled state, we showed that the flow rate and the driving power depend nonlinearly on the filling ratio.

The flow rate showed significant oscillations for the elements with discontinuous geometries, as the kneading elements and the mixing element. This probably leads to typically observed oscillations in experimental investigations of extrusion processes with kneading elements.[5]

For the investigated mixing element, we found that the geometry could be optimized by ensuring the same number of axial openings at all circumferential positions. This should be investigated in more detail in the future.

Furthermore, we presented a detailed mixing analysis of these screw elements in the completely filled state, based on tracer particles. We evaluated the time evolution of the mixedness using a grid of cubed cells and fitted exponential functions through these data. The obtained mixing rates were presented versus the flow rate, the so-called mixing characteristics. Based on that, we found that the mixing element and the non-conveying kneading element showed the highest mixing rates.

The shown results are based on the simplified scenario of a Newtonian fluid under creeping flow conditions. This is the most general scenario, where the obtained dimensionless results are independent of the actual values of fluid viscosity, screw speed and length scale. Thus, these results include relevant information for the scale-up of extruders. Since in reality the materials in extrusion processes are typically non-Newtonian and strongly temperature dependent, future work should also address these phenomena.

However, regardless of these simplifications our results confirmed the expected application properties of the investigated elements. Specifically, conveying elements should be used for conveying with low energy input in the partially filled state and for pressure generation in the completely filled state. The mixing element is well suited for mixing with low energy input, however it should always kept completely filled to avoid stagnant material in the openings, which are not emptied by the self-cleaning effect. In contrast, the kneading elements provide high energy input, e.g., required for melting. It should be noticed that the 30° kneading element showed the highest inherent conveying capacity, and thus, it is typically partially filled when operated without backpressure.

Moreover, the presented results provide important input information for simplified 1D modeling of extruders, which is still the only way to efficiently model twin-screw extruders in industrial applications. The shown mixing rates also support a simplified description of mixing along the screws in such models. Thus, the presented results not only demonstrated the applicability of the SPH method to co-rotating twin-screw extruders, but

also provide an excellent basis to support the design, optimization and scale-up of extrusion processes.

8.7 Abbreviations

1D	one-dimensional
3D	three-dimensional
CAD	computer aided design
CFD	computational fluid dynamics
FEM	finite element method
FVM	finite volume method
SPH	smoothed particle hydrodynamics
STL	surface tessellation language

8.8 Nomenclature

Latin symbols

A_1, A_2	axis intercepts of the pressure characteristic [-]
a	mass specific body force [m/s²]
B_1, B_2	axis intercepts of the power characteristic [-]
C	centerline distance [m]
C_{rep}	parameter for the repulsive wall force [N]
c	speed of sound [m/s]
D	barrel diameter [m]
D_i	inner screw diameter [m]
D_o	outer screw diameter [m]
$\mathbf{D}$	rate-of-strain tensor [s^{-1}]
f	filling ratio [-]
h	smoothing length [m]
k_1, k_2	mixing rates before and after the inflection [-]
L	length [m]
$\mathbf{L}$	velocity gradient tensor [s^{-1}]
m	mass [kg]
M	mixedness [-]

N	number of revolutions [-]
N_{total}	total number of fluid particles [-]
N_{tracer}	number of tracer particles [-]
n	screw speed [s^{-1}]
P	power [W]
p	pressure [Pa]
p_0	background pressure [Pa]
Re	Reynolds number [-]
t	time [s]
Δt	time step [s]
$\dot{V}$	flow rate [m^3/s]
$\vec{v}$	velocity [m/s]
v_z	axial velocity [m/s]
W_{ab}	kernel function evaluated for particles a and b [m^{-3}]
$\mathbf{W}$	vorticity tensor [s^{-1}]
Δx	particle spacing [m]

Greek symbols

α	artificial viscosity [-]
$\alpha_0, \alpha_1, \beta_0, \beta_1$	fitted parameters [-]
ζ	mixing index [-]
η	dynamic viscosity [Pas]
Λ	normalized flow rate [-]
ν	kinematic viscosity [m^2/s]
Π_P	normalized driving power [-]
ρ	density [kg/m^3]
ρ_0	reference density in the equation of state [kg/m^3]
ρ_{av}	density averaged over all fluid particles [kg/m^3]
ρ_{init}	initial density [kg/m^3]
σ	standard deviation of the tracer content [-]
τ_{corr}	coefficient for the density correction [s]
$\phi_0, \phi_1, \chi_0, \chi_1$	fitted parameters [-]

Subscripts

ax	tracer “axial”
cr	tracer “cross”
qu	tracer “quarter”

8.9 References

(1) Ghebre-Sellassie, I.; Martin, C. *Pharmaceutical Extrusion Technology*; Marcel Dekker Inc.: New York, 2003.

(2) Kleinebudde, P. Pharmazeutisches Produktdesign: Gezielte Freisetzung von Wirkstoffen durch unterschiedliche Extrusionstechniken. *Chemie Ing. Tech.* **2011**, *83*, 589–597.

(3) Breitenbach, J. Melt Extrusion: From Process to Drug Delivery Technology. *Eur. J. Pharm. Biopharm.* **2002**, *54*, 107–117.

(4) Repka, M. A.; Gutta, K.; Prodduturi, S.; Munjal, M.; Stodghill, S. P. Characterization of Cellulosic Hot-Melt Extruded Films Containing Lidocaine. *Eur. J. Pharm. Biopharm.* **2005**, *59*, 189–196.

(5) Eitzlmayr, A.; Khinast, J.; Hörl, G.; Koscher, G.; Reynolds, G.; Huang, Z.; Booth, J.; Shering, P. Experimental Characterization and Modeling of Twin-Screw Extruder Elements for Pharmaceutical Hot Melt Extrusion. *AIChE J.* **2013**, *59*, 4440–4450.

(6) Eitzlmayr, A.; Koscher, G.; Reynolds, G.; Huang, Z.; Booth, J.; Shering, P.; Khinast, J. Mechanistic Modeling of Modular Co-Rotating Twin-Screw Extruders. *Int. J. Pharm.* **2014**, *474*, 157–176.

(7) Ishikawa, T. 3-D Non-Isothermal Flow Field Analysis and Mixing Performance Evaluation of Kneading Blocks in a Co-Rotating Twin Srew Extruder. *Polym. Eng. Sci.* **2001**, *41*, 840–849.

(8) Bertrand, F.; Thibault, F.; Delamare, L.; Tanguy, P. A. Adaptive Finite Element Simulations of Fluid Flow in Twin-Screw Extruders. *Comput. Chem. Eng.* **2003**, *27*, 491–500.

(9) Ficarella, A.; Milanese, M.; Laforgia, D. Numerical Study of the Extrusion Process in Cereals Production: Part I. Fluid-Dynamic Analysis of the Extrusion System. *J. Food Eng.* **2006**, *73*, 103–111.

(10) Ficarella, A.; Milanese, M.; Laforgia, D. Numerical Study of the Extrusion Process in Cereals Production: Part II. Analysis of Variance. *J. Food Eng.* **2006**, *72*, 179–188.

(11) Barrera, M. A.; Vega, J. F.; Martínez-Salazar, J. Three-Dimensional Modelling of Flow Curves in Co-Rotating Twin-Screw Extruder Elements. *J. Mater. Process. Technol.* **2008**, *197*, 221–224.

(12) Bierdel, M. Computational Fluid Dynamics. In *Co-Rotating Twin-Screw Extruders*; Kohlgrüber, K., Ed.; Carl Hanser Publishers: Munich, 2008.

(13) Conzen, C. Numerische und experimentelle Untersuchungen zu Transportvorgängen in Schneckenmaschinen, Universität Kassel, 2008.

(14) Rodríguez, E. O. Numerical Simulations of Reactive Extrusion in Twin Screw Extruders, Waterloo, Canada, 2009.

(15) Sarhangi Fard, A.; Hulsen, M. A.; Meijer, H. E. H.; Famili, N. M. H.; Anderson, P. D. Adaptive Non-Conformal Mesh Refinement and Extended Finite Element Method for Viscous Flow inside Complex Moving Geometries. *Int. J. Numer. methods fluids* **2012**, *68*, 1031–1052.

(16) Sarhangi Fard, A.; Hulsen, M. A.; Meijer, H. E. H.; Famili, N. M. H.; Anderson, P. D. Tools to Simulate Distributive Mixing in Twin-Screw Extruders. *Macromol. Theory Simulations* **2012**, *21*, 217–240.

(17) Sarhangi Fard, A.; Anderson, P. D. Simulation of Distributive Mixing inside Mixing Elements of Co-Rotating Twin-Screw Extruders. *Comput. Fluids* **2013**, *87*, 79–91.

(18) Hétu, J.-F.; Ilinca, F. Immersed Boundary Finite Elements for 3D Flow Simulations in Twin-Screw Extruders. *Comput. Fluids* **2013**, *87*, 2–11.

(19) Pokriefke, G. Numerische Analyse reibungsbehafteter Strömungen in teilgefüllten Extrudern, Universität der Bundeswehr Hamburg, 2005.

(20) Cleary, P. W.; Robinson, M. Understanding Viscous Fluid Transport and Mixing in a Twin-Screw Extruder. In *8th International Conference on CFD in Oil & Gas, Metallurgical and Process Industries*; Trondheim, Norway, 2011.

(21) Eitzlmayr, A.; Khinast, J. Co-Rotating Twin-Screw Extruders: Detailed Analysis of Conveying Elements Based on Smoothed Particle Hydrodynamics. Part 1: Hydrodynamics. Submitted to *Chem. Eng. Sci.*

(22) Eitzlmayr, A.; Khinast, J. Co-Rotating Twin-Screw Extruders: Detailed Analysis of Conveying Elements Based on Smoothed Particle Hydrodynamics. Part 2: Mixing. Submitted to *Chem. Eng. Sci.*

(23) Eitzlmayr, A.; Koscher, G.; Khinast, J. A Novel Method for Modeling of Complex Wall Geometries in Smoothed Particle Hydrodynamics. *Comput. Phys. Commun.* **2014**, *185*, 2436–2448.

(24) Feldman, J.; Bonet, J. Dynamic Refinement and Boundary Contact Forces in SPH with Applications in Fluid Flow Problems. *Int. J. Numer. Methods Eng.* **2007**, *72*, 295–324.

(25) Vacondio, R.; Rogers, B. D.; Stansby, P. K.; Mignosa, P.; Feldman, J. Variable Resolution for SPH: A Dynamic Particle Coalescing and Splitting Scheme. *Comput. Methods Appl. Mech. Eng.* **2013**, *256*, 132–148.

(26) Pawlowski, J. *Die Ähnlichkeitstheorie in der physikalisch-technischen Forschung*; Springer-Verlag: Berlin/Heidelberg/New York, 1971.

(27) Kohlgrüber, K. *Co-Rotating Twin-Screw Extruders*; Carl Hanser Publishers: Munich, 2008.

(28) Rauwendaal, C. *Polymer Extrusion*; 4th ed.; Hanser Publishers: Munich, 2001.

(29) Monaghan, J. J. Simulating Free Surface Flows with SPH. *J. Comput. Phys.* **1994**, *110*, 339–406.

(30) Monaghan, J. J. SPH without a Tensile Instability. *J. Comput. Phys.* **2000**, *159*, 290–311.

(31) Morris, J. P.; Fox, P. J.; Zhu, Y. Modeling Low Reynolds Number Incompressible Flows Using SPH. *J. Comput. Phys.* **1997**, *136*, 214–226.

(32) Yang, H.-H.; Manas-Zloczower, I. Flow Field Analysis of the Kneading Disc Region in a Co-Rotating Twin Screw Extruder. *Polym. Eng. Sci.* **1992**, *32*, 1411–1417.

(33) Ardakani, H. A.; Mitsoulis, E.; Hatzikiriakos, S. G. Thixotropic Flow of Toothpaste through Extrusion Dies. *J. Nonnewton. Fluid Mech.* **2011**, *166*, 1262–1271.

(34) Shao, S.; Lo, E. Y. M. Incompressible SPH Method for Simulating Newtonian and Non-Newtonian Flows with a Free Surface. *Adv. Water Resour.* **2003**, *26*, 787–800.

(35) Amini, Y.; Emdad, H.; Farid, M. A New Model to Solve Fluid-Hypo-Elastic Solid Interaction Using the Smoothed Particle Hydrodynamics (SPH) Method. *Eur. J. Mech. B/Fluids* **2011**, *30*, 184–194.

(36) Kloss, C.; Goniva, C.; Hager, A.; Amberger, S.; Pirker, S. Models, Algorithms and Validation for Opensource DEM and CFD-DEM. *Prog. Comput. Fluid Dyn. An Int. J.* **2012**, *12*, 140–152.

(37) Monaghan, J. J. Smoothed Particle Hydrodynamics. *Reports Prog. Phys.* **2005**, *68*, 1703–1759.

(38) Liu, G.-R.; Liu, M. B. *Smoothed Particle Hydrodynamics: A Meshfree Particle Method*; Liu, G.-R.; Liu, M. B., Eds.; 1st ed.; World Scientific Publishing Co. Pte. Ltd.: Singapore, 2003; p. 453.

(39) Monaghan, J. J. On the Problem of Penetration in Particle Methods. *J. Comput. Phys.* **1989**, *82*, 1–15.

"*One thing I have learned in a long life: that all our science, measured against reality, is primitive and childlike – and yet it is the most precious thing we have.*"

(Albert Einstein)

9 Conclusions and Future Directions

9.1 Conclusions

The smoothed particle hydrodynamics (SPH) method is a promising alternative to mesh-based computational fluid dynamics (CFD) methods for free surface flows and complex, moving geometries. Specifically, for co-rotating twin-screw extruders, where the processed materials are strongly deformed by the rotating screws, the mesh-less nature of SPH is highly beneficial. Since SPH is a Lagrangian method, it inherently accounts for convection. Thus, mixing of high-viscous materials, where diffusion is negligible, can be investigated without further modeling effort. This is an additional benefit for the application to co-rotating twin-screw extruders, which are mostly utilized for mixing of high-viscous materials.

Chapters 6 and 7 showed in detail how SPH can be employed for the analysis of Newtonian flow and mixing in a conveying element of a co-rotating twin-screw extruder. A preliminary development, required to facilitate the correct interaction of SPH particles with complex geometries in the *.stl format, was presented in Chapter 5. The comparison of SPH results for the completely filled conveying element with CFD data from the literature showed excellent agreement, specifically, for the dependencies of flow rate and the power input on the applied backpressure. Particular attention was dedicated to the flow through the tight clearances. Since the spatial resolution is usually constant in SPH, and emerging techniques for variable resolution were not considered to be practicable in this specific case, the clearances could not be resolved. For that reason, a new model was

presented in Chapter 6, which correctly accounts for the Newtonian flow through unresolved clearances. The mixing analysis, presented in Chapter 7, revealed the dependency of the mixing rate on the backpressure for the completely filled element, and on the filling ratio for the partially filled element. A distinction of the contributions of axial and cross mixing could be achieved, which led to a deeper analysis of the observed phenomena. Moreover, it was demonstrated that mixing in completely filled screw sections is more dominant due to the higher residence time, compared to partially filled sections. To account also for other typical and frequently used screw element geometries, for example, kneading and mixing elements, similar results for Newtonian flow and mixing were shown in Chapter 8 for complete and partial filling of these elements.

A general drawback of spatially resolved flow simulations in co-rotating twin-screw extruders is the required computational expense, which is still too high for extensive investigations of entire extruders, specifically for industrial and engineering applications. Thus, simplified models, based on the one-dimensional (1D) approach, are still important when the entire extrusion process should be considered. Specifically, the impact of screw configuration, material and operation parameters on profiles of process variables along the screws (e.g., filling ratio, pressure, temperature) can be efficiently described with 1D models. In Chapter 4, a new implementation of a mechanistic 1D model was presented. Specifically, a simplified calculation of the viscous dissipation rate was developed and validated with CFD data from the literature for a Newtonian fluid. Since 1D models are not fully predictive and require underlying empirical correlations and parameters, experimental measurements of the pressure characteristic of different screw elements were conducted with a real extruder and a typical non-Newtonian polymer used for pharmaceutical hot-melt extrusion (Chapter 3). Also an empirical correlation for the heat transfer between melt and barrel was obtained from these measurements. Providing this information, the model could reproduce the measurements well. The comparison of model results to independent experimental data would be desirable, however, in this work the conduction of additional, time intensive experiments was not possible. Instead of that, a comparison of results for the residence time distribution to experimental data from the literature yielded good agreement.

The SPH results presented in Chapter 8 were also intended to provide data for the parameterization of the 1D model, as well as its further improvement and extension. However, all presented SPH results are limited to Newtonian fluids and do not account for thermal energy and temperature. Compared to the reality of hot-melt extrusion, these are strong simplifications. In this first step towards a comprehensive modeling of the flow in co-rotating twin-screw extruders based on SPH, the focus was mainly on the complexity of the geometry, and not on the materials. Clearly, models for non-Newtonian fluids and thermal energy are available for SPH and these aspects should be addressed in future work. Together with the 1D model, this can lead to comprehensive modeling tools for co-rotating twin-screw extruders, supporting the design, optimization and scale-up of extruders.

9.2 Future Directions

9.2.1 1D Modeling

The results of the presented SPH simulations could be used to refine and extend the 1D model. Specifically, the obtained non-linear correlations for flow rate and power input versus filling ratio could replace the currently assumed linear correlations. This allows a more precise prediction of filling ratio, power input and residence time in partially filled screw sections. Moreover, the determined mixing rates for different screw elements and different operation states can be used to describe the evolution of the mixedness along the screws. This could increase the relevance of the results for engineering applications. Moreover, it would be important to intensify the experimental validation of the 1D model. SPH simulations accounting for a higher amount of the relevant physical phenomena (see below) could also be used to improve critical aspects of the 1D model. For example a systematic investigation of heat transfer could lead to a more funded empirical correlation for the heat transfer between melt and barrel.

9.2.2 Non-Newtonian Fluids and Thermal Energy

The SPH model should be extended to account for non-Newtonian fluids and the thermal energy equation, as well as the corresponding temperature dependent material properties. In particular, the viscosity of polymers is usually strongly temperature dependent, which has essential impact on flow, viscous dissipation and the predicted fluid temperature.

Variable viscosity values would require a generalization of the clearance model, which is currently limited to Newtonian fluids, and presumes a parabolic velocity profile (see below).

9.2.3 Clearance Modeling

In the investigated Newtonian scenarios, where the local fluid temperature was not considered, the impact of the presented clearance model on the evaluated integral properties of the flow field was even negligible (see Chapter 6). Since the maximum shear rate, and thus, the maximum dissipation rate occur in the clearances, the maximum fluid temperature can be expected in the clearances too. Moreover, the clearances contribute significantly to the total power input due to their extremely high shear rate values. The quantification of local temperature and power input in clearances could be a result of practical relevance. In this case, it can be expected that the proper clearance modeling is important. Moreover, when a temperature dependent viscosity is used, significant errors can be expected even in integral properties of the flow field without proper clearance modeling. For examples of shear rate, dissipation rate and temperature distributions in clearances of twin-screw extruders please refer to Bierdel[1].

Two different types of clearances can be distinguished at co-rotating twin-screw extruders: clearances between barrel and screw (barrel/screw), and clearances between both screws (screw/screw). Their main difference is, that the barrel/screw clearances are bounded by parallel walls, whereas the walls of screw/screw clearances are not parallel. The presented clearance model (Chapter 6) was developed for clearances between two parallel walls, and thus, applied only to the barrel/screw clearances. A similar model for the screw/screw clearances seems to be hardly possible due to the complex boundary geometry in the intermeshing region. Here, variable resolution techniques could be more reasonable, which are based on splitting and merging of fluid particles in defined spatial regions.[2,3]

The application of variable resolution techniques could replace the presented clearance model by using the resolution refinement in all clearances. However, the distances of the barrel/screw clearances are usually smaller than for the screw/screw clearances, i.e., refining only the (wider) screw/screw clearances would cause less increase of the total particle number. Thus, it could be beneficial for the computational expense, to use the

refinement only for the screw/screw clearances, and to apply a proper clearance model for the barrel/screw clearances.

If a clearance model should be applied together with variable viscosity values (i.e., non-Newtonian or temperature dependent viscosity), the velocity profiles in the clearances will deviate from the presumed parabola. The nonlinearities introduced by the viscosity function do not allow a general solution of the velocity profile prior to the simulation, which means that a numerical resolution across the clearance (i.e., normal to the parallel walls) is definitely required then. Instead of the presumed parabola, this would require to store the complete velocity and temperature profiles across the clearance by using a defined number of points. Clearly, the numerical transport equations for these profiles have to be derived from the governing equations.

9.2.4 Chaotic Mixing

In this work, the analysis of mixing was conducted with tracer particles and an evaluation of their distribution using a grid of cubed cells. This yielded mixing rates, describing the increase of the mixedness during the screw rotation without distinguishing chaotic or non-chaotic mixing. However, chaotic mixing is highly beneficial for laminar mixing processes and should be analyzed in more detail. For example, this could be achieved by evaluating Lyapunov Exponents, which was already shown for SPH simulations of twin-cam mixers[4] and helical ribbon mixers[5]. For more details about chaotic mixing please refer to the literature.[6–8]

9.2.5 Viscoelasticity

In addition to the dependencies of the viscosity on temperature and shear rate, materials in real extrusion processes are often viscoelastic. Modeling of viscoelasticity in SPH has already been reported and could be included.[9,10]

9.2.6 Melting

The melting (plastification) was not considered in this thesis, however it is an essential part of real hot-melt extrusion processes. Simplified melting models have been shown and could be used to account for melting in the presented 1D model.[11,12] Also experimental

investigations of melting in a twin-screw extruder have been reported.[13] Spatially resolved first principles models for melting are not available up to now. However, it was shown that SPH can be employed to model solidification.[14] Similarly, it could be applied to melting by distinguishing between solid and liquid particles, and the transition of individual particles from the solid to the liquid state. Possibly a coupling with the discrete element method (DEM), which is a Lagrangian particle method for granular flow, could lead to comprehensive models for melting of a granular material. A coupling of SPH and DEM for modeling fluid-particle flows has been reported,[15] similarly a coupling of the moving particle semi-implicit (MPS) method with DEM.[16]

9.2.7 Numerical Aspects

A drawback of the currently used explicit time integration scheme in the SPH model is the small time step size, which is typically in the order of microseconds, and requires hundred-thousands of steps for a single revolution of the screws. Together with the high particle number, which was in the order of 10^6 for the presented results, the computational effort is high. This limits the applicability, specifically, when more complex physical models should be included. Implicit and semi-implicit SPH schemes have potential to reduce the overall computational expense, for example the SPH projection method presented by Cummins and Rudman[17] or the incompressible SPH method shown by Shao and Lo[18]. Similar to that is also the MPS method proposed by Koshizuka and Oka[19].

9.3 Abbreviations

1D	one-dimensional
DEM	discrete element method
CFD	computational fluid dynamics
SPH	smoothed particle hydrodynamics

9.4 References

(1) Bierdel, M. Computational Fluid Dynamics. In *Co-Rotating Twin-Screw Extruders*; Kohlgrüber, K., Ed.; Carl Hanser Publishers: Munich, 2008.

(2) Feldman, J.; Bonet, J. Dynamic Refinement and Boundary Contact Forces in SPH with Applications in Fluid Flow Problems. *Int. J. Numer. Methods Eng.* **2007**, *72*, 295–324.

(3) Vacondio, R.; Rogers, B. D.; Stansby, P. K.; Mignosa, P.; Feldman, J. Variable Resolution for SPH: A Dynamic Particle Coalescing and Splitting Scheme. *Comput. Methods Appl. Mech. Eng.* **2013**, *256*, 132–148.

(4) Robinson, M.; Cleary, P.; Monaghan, J. Analysis of Mixing in a Twin Cam Mixer Using Smoothed Particle Hydrodynamics. *AIChE J.* **2008**, *54*, 1987–1998.

(5) Robinson, M.; Cleary, P. W. Flow and Mixing Performance in Helical Ribbon Mixers. *Chem. Eng. Sci.* **2012**, *84*, 382–398.

(6) Ottino, J. M.; Leong, C. W.; Rising, H.; Swanson, P. D. Morphological Structures Produced by Mixing in Chaotic Flows. *Nature* **1988**, *333*, 419–425.

(7) Ottino, J. M. The Mixing of Fluids. *Sci. Am.* **1989**, 56–67.

(8) Wiggins, S.; Ottino, J. M. Foundations of Chaotic Mixing. *Philos. Trans. R. Soc. London A* **2004**, *362*, 937–970.

(9) Ellero, M.; Tanner, R. I. SPH Simulations of Transient Viscoelastic Flows at Low Reynolds Number. *J. Nonnewton. Fluid Mech.* **2005**, *132*, 61–72.

(10) Angelova, M. Modellierung und Simulation von Strömungen viskoelastischer Fluide in komplexen , bewegten Geometrien mit Smoothed Particle Hydrodynamics (SPH), Technische Universität Hamburg-Harburg, 2012, pp. 1–102.

(11) Tadmor, Z. Fundamentals of Plasticating Extrusion. *Polym. Eng. Sci.* **1966**, 185–190.

(12) Tadmor, Z.; Gogos, C. G. *Principles of Polymer Processing*; 2nd Ed.; John Wiley & Sons, Inc.: Hoboken, New Jersey, 2006.

(13) Chen, H.; Sundararaj, U.; Nandakumar, K.; Wetzel, M. D. Investigation of the Melting Mechanism in a Twin-Screw Extruder Using a Pulse Method and Online Measurement. *Ind. Eng. Chem. Res.* **2004**, *43*, 6822–6831.

(14) Monaghan, J. J.; Huppert, H. E.; Worster, M. G. Solidification Using Smoothed Particle Hydrodynamics. *J. Comput. Phys.* **2005**, *206*, 684–705.

(15) Robinson, M.; Ramaioli, M.; Luding, S. Fluid-Particle Flow Simulations Using Two-Way-Coupled Mesoscale SPH-DEM and Validation. *Int. J. Multiph. Flow* **2014**, *59*, 121–134.

(16) Sun, X.; Sakai, M.; Sakai, M. T.; Yamada, Y. A Lagrangian-Lagrangian Coupled Method for Three-Dimensional Solid-Liquid Flows Involving Free Surfaces in a Rotating Cylindrical Tank. *Chem. Eng. J.* **2014**, *246*, 122–141.

(17) Cummins, S. J.; Rudman, M. An SPH Projection Method. *J. Comput. Phys.* **1999**, *152*, 584–607.

(18) Shao, S.; Lo, E. Y. M. Incompressible SPH Method for Simulating Newtonian and Non-Newtonian Flows with a Free Surface. *Adv. Water Resour.* **2003**, *26*, 787–800.

(19) Koshizuka, S.; Oka, Y. Moving-Particle Semi-Implicit Method for Fragmentation of Incompressible Fluid. *Nucl. Sci. Eng.* **1996**, *123*, 421–434.

Appendix A

Wall interaction for additional SPH models: density summation equation and artificial viscosity model

As part of the work presented in Chapter 5, boundary contributions for the density summation equation and the artificial viscosity model were determined, which are not included in Chapter 5. The density summation equation is[1]:

$$\rho_a = \sum_b m_b W_{ab} \tag{B.1}$$

The contribution of boundary particles to a single fluid particle is:

$$\rho_a\big|_{BP} = m_a \sum_{b\in BP} W_{ab} = \frac{m_a}{h^3} F_W \quad \text{with} \quad F_W = h^3 \sum_{b\in BP} W_{ab} \tag{B.2}$$

Determining the dimensionless boundary contribution for density F_W using the procedure described in the Section "Wall Interaction" yields the polynomial fit:

$$F_W\left(z^*\right) = \begin{cases} 0.13\left(z^*\right)^5 - 0.7\left(z^*\right)^4 + 1.14\left(z^*\right)^3 \\ \quad -0.072\left(z^*\right)^2 - 1.33z^* + 0.863 \quad \left(z^* < 1.31\right) \\ 0 \quad \left(\text{otherwise}\right) \end{cases} \tag{B.3}$$

The artificial viscosity model (a part of the momentum equation Eq. 5.7) after Monaghan[1] is:

$$\Pi_{ab} = \begin{cases} \dfrac{-\alpha c \mu_{ab} + \beta {\mu_{ab}}^2}{\overline{\rho}_{ab}} & \vec{v}_{ab}\cdot\vec{r}_{ab} < 0 \\ 0 & \vec{v}_{ab}\cdot\vec{r}_{ab} > 0 \end{cases} \quad \text{with} \quad \mu_{ab} = \frac{h\vec{v}_{ab}\cdot\vec{r}_{ab}}{\vec{r}_{ab}^{\,2} + \eta^2} \tag{B.4}$$

Here, $\vec{v}_{ab} = \vec{v}_a - \vec{v}_b$ is the velocity of particle a relative to neighbor b and $\vec{r}_{ab} = \vec{r}_a - \vec{r}_b$ is the distance vector between a and b. The average density is $\overline{\rho}_{ab} = \left(\rho_a + \rho_b\right)/2$ and the quantity $\eta^2 = 0.01h^2$ is proposed to prevent a zero denominator. The so-called artificial viscosity α is a dimensionless parameter accounting for the fluid viscosity, whereas β is

required to account for high Mach number shocks in gas dynamics (thus usually $\beta = 0$ for liquids).

Substituting Eq. B.4 in the momentum equation Eq. 5.7 using $\beta = 0$ yields for the viscous term:

$$\frac{d\vec{v}_a}{dt} = \begin{cases} -\sum_b m_b \left(-\frac{\alpha c}{\bar{\rho}_{ab}} \mu_{ab} \right) \vec{\nabla}_a W_{ab} & \vec{v}_{ab} \cdot \vec{r}_{ab} < 0 \\ 0 & \vec{v}_{ab} \cdot \vec{r}_{ab} > 0 \end{cases} \quad \text{with} \quad \mu_{ab} = \frac{h \vec{v}_{ab} \cdot \vec{r}_{ab}}{\vec{r}_{ab}^2 + \eta^2} \tag{B.5}$$

Only the first case of Eq. B.5 ($\vec{v}_{ab} \cdot \vec{r}_{ab} < 0$) is considered below, since the second case is trivial ($\vec{v}_{ab} \cdot \vec{r}_{ab} > 0$). The quantities m, ρ, α and c are assumed to be equal for boundary and fluid particles, leading to:

$$\left. \frac{d\vec{v}_a}{dt} \right|_{BP} = m_a \frac{\alpha c}{\rho_a} \sum_{b \in BP} \mu_{ab} \vec{\nabla}_a W_{ab} \tag{B.6}$$

In this case, the even property of the kernel function cannot be used, since the summation is only conducted over the boundary particles fulfilling the condition $\vec{v}_{ab} \cdot \vec{r}_{ab} < 0$ (i.e., when particles a and b are approaching to each other). Thus, all components (i.e., normal and parallel to the wall) remain, and the gradient cannot be reduced to a single component. Although the viscous forces depend on the velocity components parallel and normal to the wall, the dependencies of the parallel force on the parallel velocity and of the normal force on the normal velocity cannot be considered separately. Since fluid elements in the vicinity of a wall mainly move in parallel to the wall, we simplified the problem by assuming the normal velocity component $v_{a,z} = 0$ and determined the viscous force contributions of boundary particles only for the parallel velocity component $v_{a,x}$, which yields:

$$\left. \frac{d\vec{v}_a}{dt} \right|_{BP} = -m_a \frac{\alpha c}{\rho_a} \frac{v_{a,x}}{h^4} \vec{F}_{\mu \nabla W} \quad \text{with} \quad \vec{F}_{\mu \nabla W} = -\frac{h^4}{v_{a,x}} \sum_{b \in BP} \mu_{ab} \vec{\nabla}_a W_{ab} \tag{B.7}$$

The dimensionless boundary contribution for the artificial viscosity model $\vec{F}_{\mu \nabla W}$ is a vector that consists of a component normal to the wall ($F^{norm}_{\mu \nabla W}$) and a component parallel to the

wall ($F^{\tan}_{\mu\nabla W}$). We determined the values of $F^{norm}_{\mu\nabla W}$ and $F^{\tan}_{\mu\nabla W}$ in the manner described in Section 5.3, leading to the polynomial fits:

$$F^{norm}_{\mu\nabla W}\left(z^*\right)=\begin{cases}0.165\left(z^*\right)^5-0.791\left(z^*\right)^4+1.328\left(z^*\right)^3 \\ \quad -0.711\left(z^*\right)^2-0.311z^*+0.335 \quad (z^*<1.31) \\ 0 \quad (\text{otherwise})\end{cases} \tag{B.8}$$

$$F^{\tan}_{\mu\nabla W}\left(z^*\right)=\begin{cases}0.0794\left(z^*\right)^5-0.23\left(z^*\right)^4-0.05\left(z^*\right)^3 \\ \quad +0.83\left(z^*\right)^2-1.03z^*+0.407 \quad \left(z^*<1.22\right) \\ 0 \quad (\text{otherwise})\end{cases} \tag{B.9}$$

(1) Monaghan, J. J. Simulating Free Surface Flows with SPH. *J. Comput. Phys.* **1994**, *110*, 339–406.

Appendix B

Geometrical parameters of co-rotating, intermeshing twin-screw extruders

This appendix shows how the geometrical parameters of co-rotating, intermeshing twin-screw extruders, required for the model presented in Chapter 4, can be calculated. Booy[1] described the geometry of co-rotating twin-screws in detail and showed that the tip angle α (see Figure 4.7) can be calculated from the screw diameter D, the centerline distance C_L and the number of flights n_F (which is 2 for a typical two-flighted screw profile):

$$\alpha = \frac{\pi}{n_F} - 2\psi \tag{A.1}$$

$$\cos\psi = \frac{C_L}{D} \tag{A.2}$$

Based on the angles α and ψ, the external screw diameter D and the screw core diameter D_C, the cross-sectional area of the screw profile A_{Scr} and its circumference L_{Scr} can be calculated:

$$A_{Scr} = \left[\frac{D + D_C}{2} \cdot \left(\frac{D + D_C}{2} \cdot \psi - \frac{D}{2} sin\psi \right) + \frac{\alpha}{8} \left(D^2 + {D_C}^2 \right) \right] \cdot n_F \tag{A.3}$$

$$L_{Scr} = \frac{D + D_C}{2} \cdot \pi \tag{A.4}$$

Using the cross-sectional area of the screw profile A_{Scr}, the free cross-section area of the twin-screw can be calculated as free cross-section of the barrel minus $2 \cdot A_{Scr}$:

$$A_{cr} = \frac{1}{2} \left({D_B}^2 \cdot (\pi - \psi) + C_L \cdot \sqrt{{D_B}^2 - {C_L}^2} \right) - 2 \cdot A_{Scr} \tag{A.5}$$

The surface area of the conveying screw elements cannot be expressed by an exact analytical equation due to the spatial curvature of the surface. However, we developed the following approximation, the deviation of which is in the order of 1% compared to numerical calculations (where T_S is the pitch and L the length of the screw):

$$A_{Surf} \approx \left[\alpha + 2 \cdot \sqrt{\psi^2 + \left(\frac{D - D_C}{2 \cdot T_S} \cdot \pi \right)^2} \right] \cdot \frac{D + D_C}{2} \cdot n_F \cdot L \tag{A.6}$$

(1) Booy, M. L. Geometry of Fully Wiped Twin-Screw Equipment. *Polym. Eng. Sci.* **1978**, *18*, 973–984.

.

Appendix C

Used fit functions for mixing rate versus flow rate

Appendix C shows the fit functions used in Chapter 7 for the mixing rates k and k_{ax} versus the normalized flow rate Λ. The difference $k_1 - k_2$ together with $k_{ax,1}^c - k_{ax,2}^c$ for the completely filled state was fitted via a polynomial of 6th order:

$$k_1 - k_2 = k_{ax,1}^c - k_{ax,2}^c = 1.831\,\Lambda^6 - 3.3197\,\Lambda^5 + 0.5570\,\Lambda^4 + 1.1424\,\Lambda^3 + 0.2828\,\Lambda^2 - 0.4077\,\Lambda + 0.1194 \quad \text{(C.1)}$$

For k_1 in the completely filled state a polynomial of 5th order was fitted:

$$k_1 = -0.1583\Lambda^5 - 0.1123\Lambda^4 + 0.6389\Lambda^3 + 0.0864\Lambda^2 - 0.5110\Lambda + 0.3845 \quad \text{(C.2)}$$

For $k_{ax,2}$ in the completely filled state the following fit was used:

$$k_{ax,2} = \left[0.5 - \frac{\arctan\left(4(\Lambda - 0.5822)\right)}{\pi}\right] \cdot \left[-0.04703(\Lambda - 7.4597)^2 + 3.3694\right] + \left[0.5 + \frac{\arctan\left(4(\Lambda - 0.5822)\right)}{\pi}\right] \cdot \left[0.2107(\Lambda + 4.7979)^2 - 6.9209\right] \quad \text{(C.3)}$$

The difference $k_1 - k_2$ together with $k_{ax,1}^c - k_{ax,2}^c$ in the partially filled state was fitted via a polynomial of 4th order:

$$k_1 - k_2 = k_{ax,1}^c - k_{ax,2}^c = -1.0737\Lambda^4 + 2.2156\Lambda^3 - 1.1199\Lambda^2 - 0.0761\Lambda + 0.2631 \quad \text{(C.4)}$$

For k_2 in the partially filled state a power law was used:

$$k_2 = 0.122\Lambda^{-0.385} \quad \text{(C.5)}$$

$k_{ax,2}$ for the partially filled state was fitted via a parabola:

$$k_{ax,2} = -0.3607\Lambda^2 + 0.3106\Lambda + 0.3146 \quad \text{(C.6)}$$

The remaining k_2 and $k_{1,ax}$ for the completely filled state and the k_1 and $k_{1,ax}$ for the partially filled state were calculated from Eqs. C.1 – C.6 using the conversion Eq. 7.4.

Appendix D

SPH example

This appendix shows snapshots of an example SPH simulation, involving several screw elements, to demonstrate that the presented approach can also be applied to more complex cases than presented in the Chapters 6 - 8.

Parameters:

- Outer screw diameter: 27 mm
- Length: 150 mm
- Rotation speed: 60 rpm
- Viscosity: 0.2 Pas
- Reynolds number: 3.6
- Particle spacing: 0.6 mm
- Smooting length: 0.72 mm
- Number of particles: 212 489
- Particle mass: $2.38 \cdot 10^{-7}$ kg
- Speed of sound: 3 m/s
- Time step: $5 \cdot 10^{-6}$ s

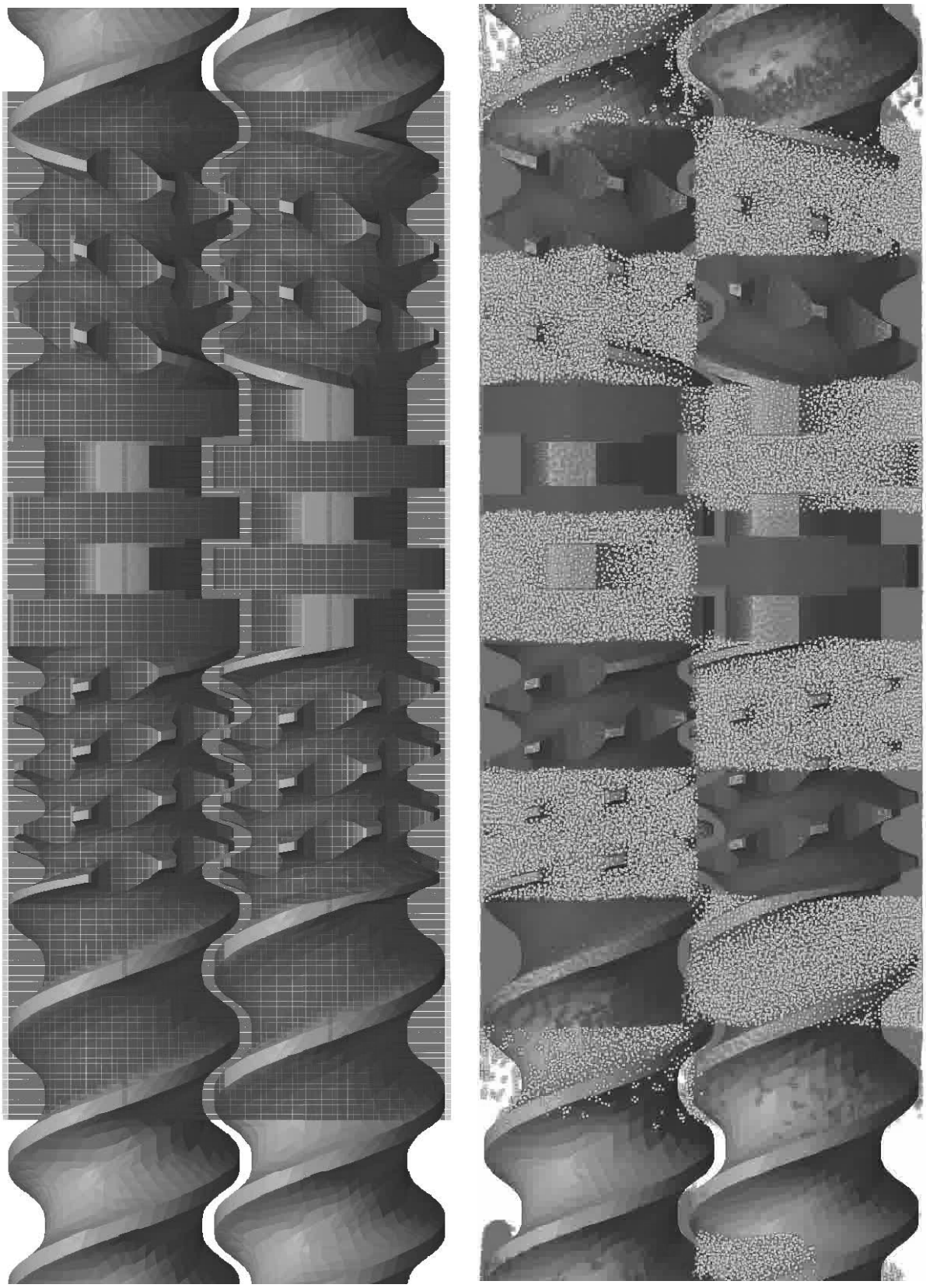

Figure D.1: Snapshots of the simulation: initial state (left), after 1 revolution (right). The white color indicates tracer particles used for the illustration of mixing.

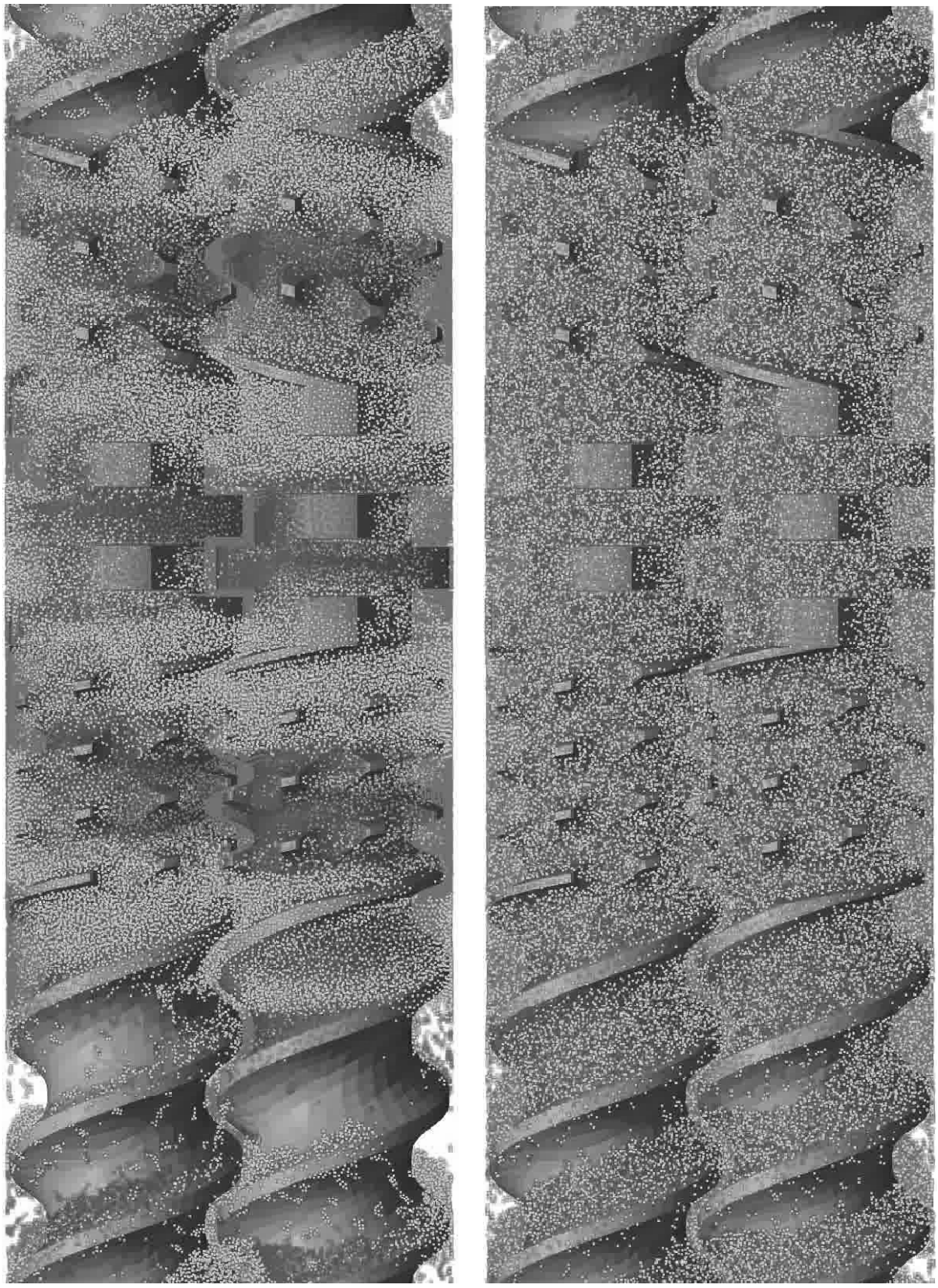

Figure D.2: Snapshots of the simulation: after 2 revolutions (left), after 10 revolution (right). The white color indicates tracer particles used for the illustration of mixing.

Appendix E

Structure of the 1D model code (implemented in Matlab® R2009a)

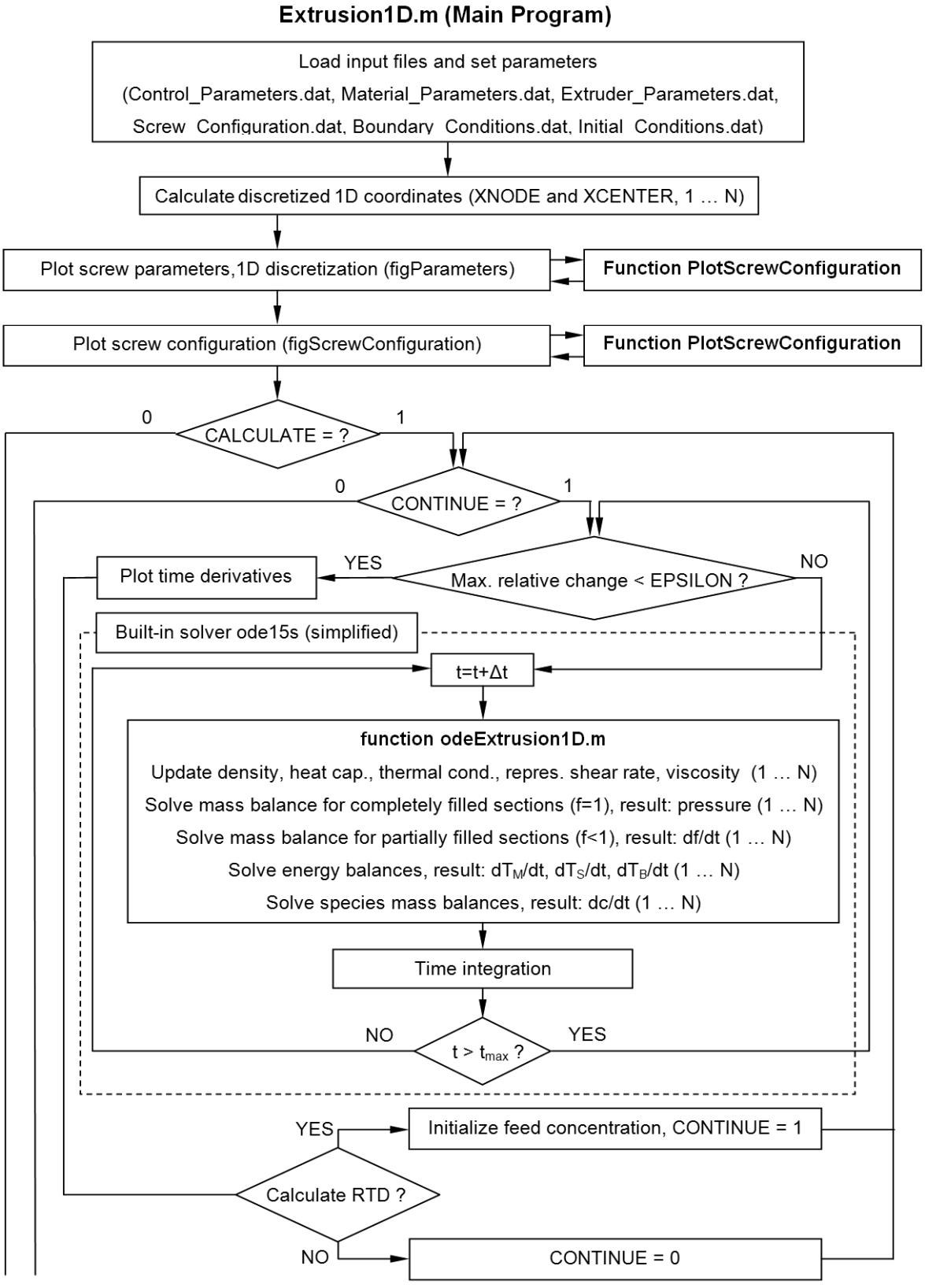

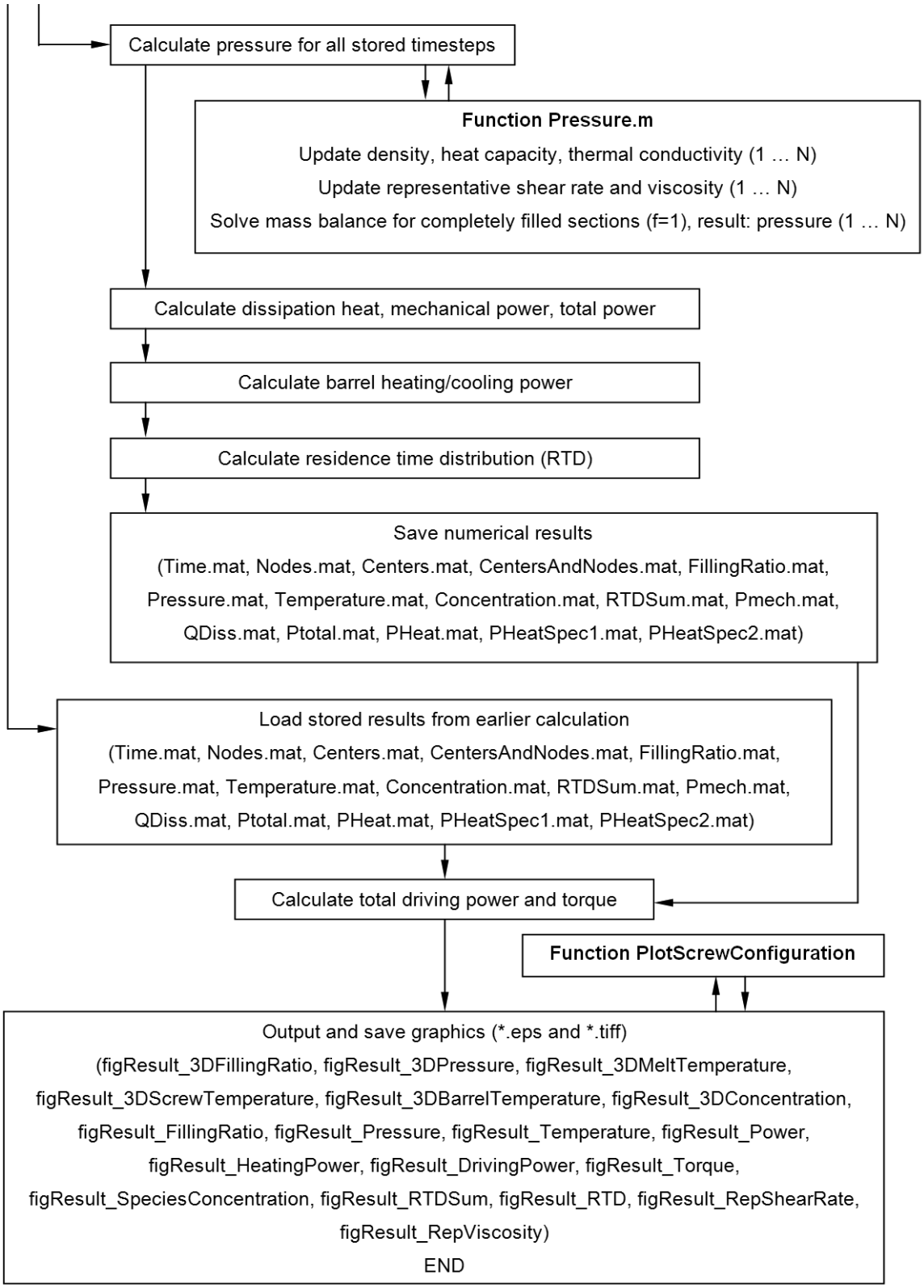
Calculate pressure for all stored timesteps
Function Pressure.m
Update density, heat capacity, thermal conductivity (1 … N)
Update representative shear rate and viscosity (1 … N)
Solve mass balance for completely filled sections (f=1), result: pressure (1 … N)
Calculate dissipation heat, mechanical power, total power
Calculate barrel heating/cooling power
Calculate residence time distribution (RTD)
Save numerical results
(Time.mat, Nodes.mat, Centers.mat, CentersAndNodes.mat, FillingRatio.mat,
Pressure.mat, Temperature.mat, Concentration.mat, RTDSum.mat, Pmech.mat,
QDiss.mat, Ptotal.mat, PHeat.mat, PHeatSpec1.mat, PHeatSpec2.mat)
Load stored results from earlier calculation
(Time.mat, Nodes.mat, Centers.mat, CentersAndNodes.mat, FillingRatio.mat,
Pressure.mat, Temperature.mat, Concentration.mat, RTDSum.mat, Pmech.mat,
QDiss.mat, Ptotal.mat, PHeat.mat, PHeatSpec1.mat, PHeatSpec2.mat)
Calculate total driving power and torque
Function PlotScrewConfiguration
Output and save graphics (*.eps and *.tiff)
(figResult_3DFillingRatio, figResult_3DPressure, figResult_3DMeltTemperature,
figResult_3DScrewTemperature, figResult_3DBarrelTemperature, figResult_3DConcentration,
figResult_FillingRatio, figResult_Pressure, figResult_Temperature, figResult_Power,
figResult_HeatingPower, figResult_DrivingPower, figResult_Torque,
figResult_SpeciesConcentration, figResult_RTDSum, figResult_RTD, figResult_RepShearRate,
figResult_RepViscosity)
END

Appendix F

1D model parameter study

This appendix shows results of a 1D simulation example with variations of flow rate and screw speed as well as an example for scale-up. In addition to the model proposed in Chapter 4, these results include also a description of mixing along the screws based on the mixing rates obtained from the SPH simulations presented in Chapter 8. As measure for the mixedness the intensity of segregation S was used (as shown in Chapter 7 in detail), which is initially 1 (unmixed) and decreases exponentially during the rotations (Eq. 7.2). With that, the profile of S along the screws was calculated by using the average residence time τ due to Eq. 7.6 for the number of screw revolutions N in each numerical element.

The used screw geometry is the same as in Chapter 8 (Leistritz MICRO 27, screw diameter 27 mm). The modular screws used for these example results consist of conveying elements (pitches 20, 30 and 40 mm), kneading elements (stagger angles 30°, 60° and 90°, right- and left handed) and mixing elements (right- and left handed). Most of these elements were investigated in Chapter 8 and the parameters presented there were used as input here. For the screw elements not included in Chapter 8, the parameters were estimated based on these results. For the gap distance between screws and barrel the value 0.1 mm was used here. In detail, the configuration of the modular screw consisted of the following screw elements, each 30 mm long (RH and LH mean right handed and left handed, respectively):

- 2 conveying elements (pitch 30 mm RH)
- 1 kneading element (30° RH, 5 discs)
- 1 kneading element (60° RH, 5 discs)
- 1 conveying element (pitch 30 mm RH)
- 1 kneading element (30° RH, 5 discs)
- 1 kneading element (60° RH, 5 discs)
- 1 kneading element (90°, 5 discs)

- 1 kneading element (30° LH, 5 discs)
- 1 kneading element (60° LH, 5 discs)
- 2 conveying elements (pitch 30 mm RH)
- 3 mixing elements (pitch 15 mm RH)
- 1 mixing element (pitch 20 mm LH)
- 2 conveying elements (pitch 40 mm RH)
- 2 conveying elements (pitch 20 mm RH)

The die consisted of 4 parallel channels, each with a diameter of 3 mm, a length of 20 mm and a dead volume of 5 mm length between screws and die. For a schematic of this screw configuration see the figures below. This configuration was chosen in order to show the most important screw element types available for this extruder in both, completely filled and partially filled states.

The calculations were performed with the material properties of Soluplus®, as presented in Chapters 3 and 4. The following operation conditions were used for case 1:

- Screw speed: 150 rpm
- Feed flow rate: 10 kg/h
- Barrel temperature: 150°C
- Devaporization pressure 200 mbar at position x = 500 mm.

This yields a dimensionless flow rate of $\dot{V}/nD^3$ = 0.051. The resulting steady state profiles for filling ratio, pressure and temperatures along the screws for case 1 are shown in Figure F.1.

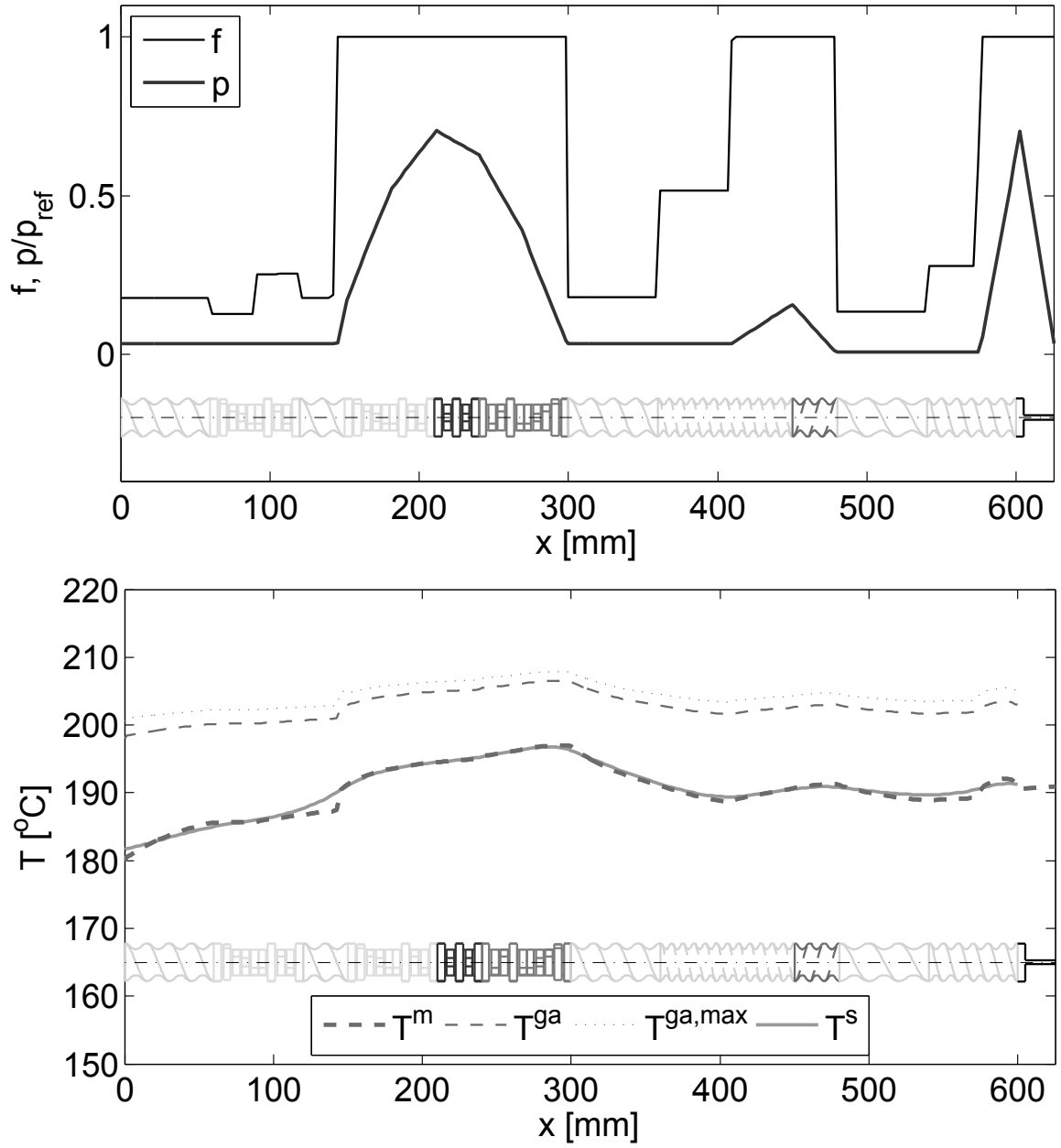

Figure F.1: Resulting axial profiles of filling ratio f, pressure p (relative to $p_{ref} = 3 \cdot 10^6$ Pa), average melt temperature in channels T^m, average melt temperature in gaps T^{ga} (Eq. 4.58), maximum melt temperature in gaps $T^{ga,max}$ (Eq. 4.60) and screw temperature T^s (the barrel temperature was $T^b = 150°C$) for case 1.

The die and the left handed elements cause complete fillings. The pressure profile shows increased values in the completely filled sections according to the presumed pressure characteristic of the involved screw elements. The kneading elements between x = 60 mm and x = 120 mm are partially filled, since they do not convey against backpressure. This is a consequence of the results of Chapter 8, where it is shown that the 30° kneading element has a relatively high conveying capacity. The temperature profiles show a temperature

increase in the completely filled sections, and a decrease in the partially filled sections, which is related to the ratio of the volume, in which the dissipation heat is generated, to the surface of the barrel over which the heat is removed. The profile of the intensity of segregation S along the screws and the residence time distribution are shown in Figure F.2. Specifically, the profile of S shows that the mixing is dominated by the completely filled section, whereas the contribution of the partially filled sections to the mixing is minor. This can mainly be addressed to the comparably short residence time in partially filled sections.

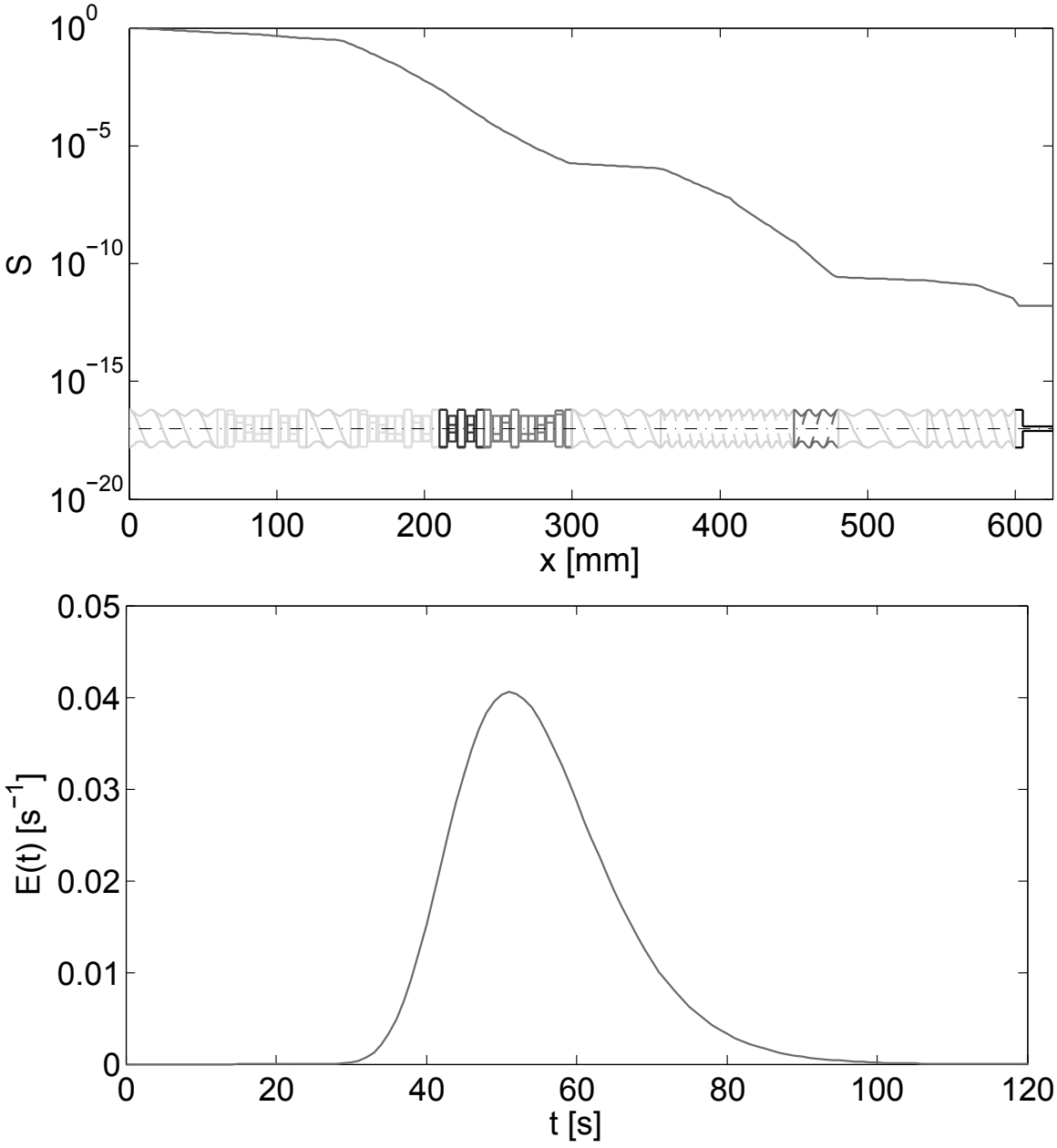

Figure F.2: Resulting axial profile of the intensity of segregation S (top) and residence time distribution (bottom) for case 1.

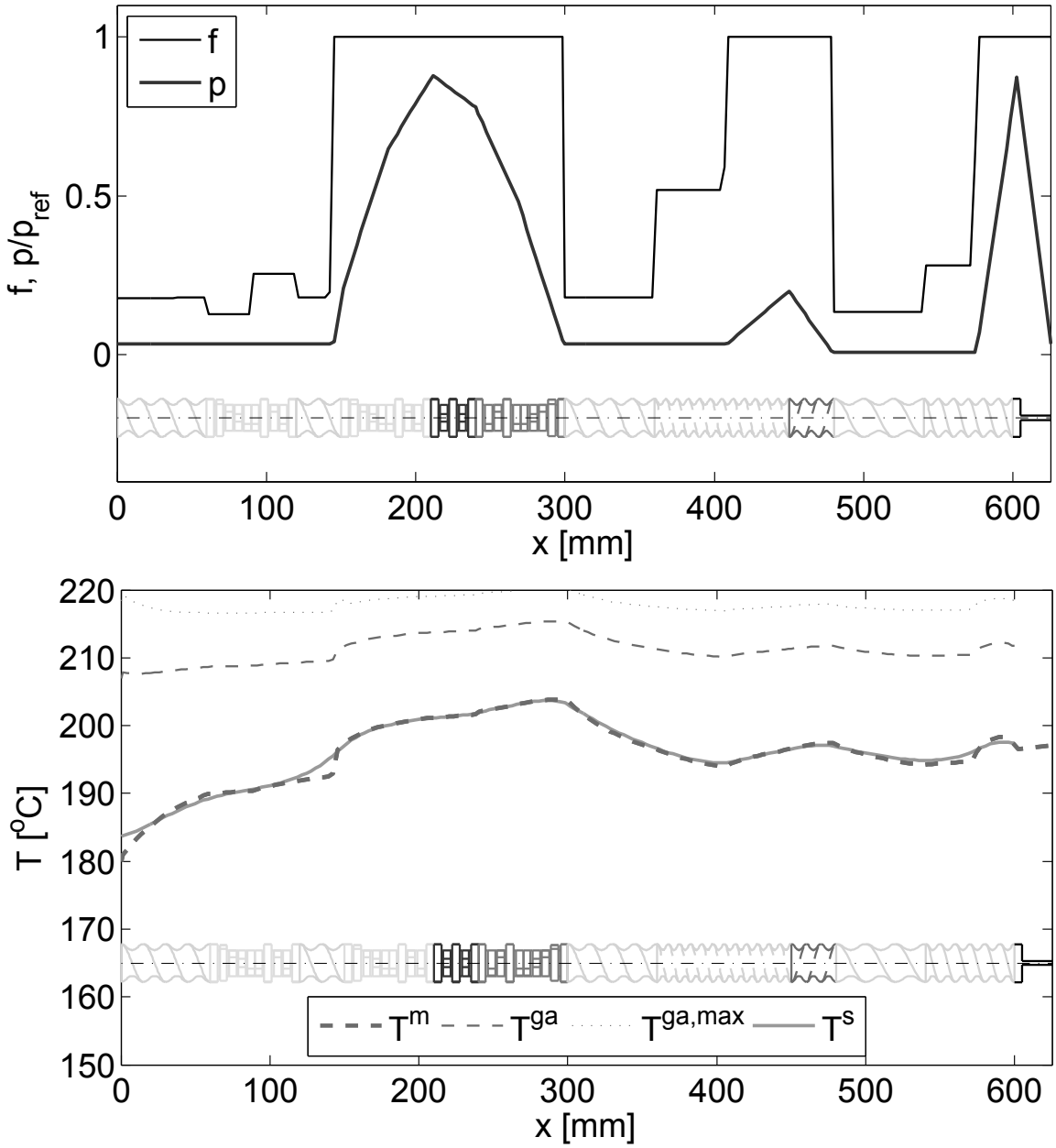

Figure F.3: Resulting axial profiles of filling ratio f, pressure p (relative to $p_{ref} = 3 \cdot 10^6$ Pa), average melt temperature in channels T^m, average melt temperature in gaps T^{ga} (Eq. 4.58), maximum melt temperature in gaps $T^{ga,max}$ (Eq. 4.60) and screw temperature T^s (the barrel temperature was $T^b = 150°C$) for case 2.

The Figures F.3 and F.4 show the same results for case 2 with a screw speed of 300 rpm and a feed flow rate of 20 kg/h (which yields the same dimensionless flow rate of $\dot{V}/nD^3 = 0.051$). Due to the same dimensionless flow rate, the operation states of the screw elements are similar and the profiles of filling ratio and pressure are almost equal to the first case, only the pressure values are a bit higher due to the increased screw speed. However, the temperature profiles show significantly higher values than in case 1, specifically the

maximum gap temperature is more than 10K higher, which is related to the increased screw speed and the corresponding shear rates. The profile of S is equal compared to the first case, because this depends on the number of screw revolutions during the average residence time, which is the same due to the similarity of the pressure and filling ratio profiles. The residence time is shorter here, due to the screw speed increased by factor 2. However, the shape of the distribution is similar to the first case, only the time axis is scaled with the screw speed factor of 2.

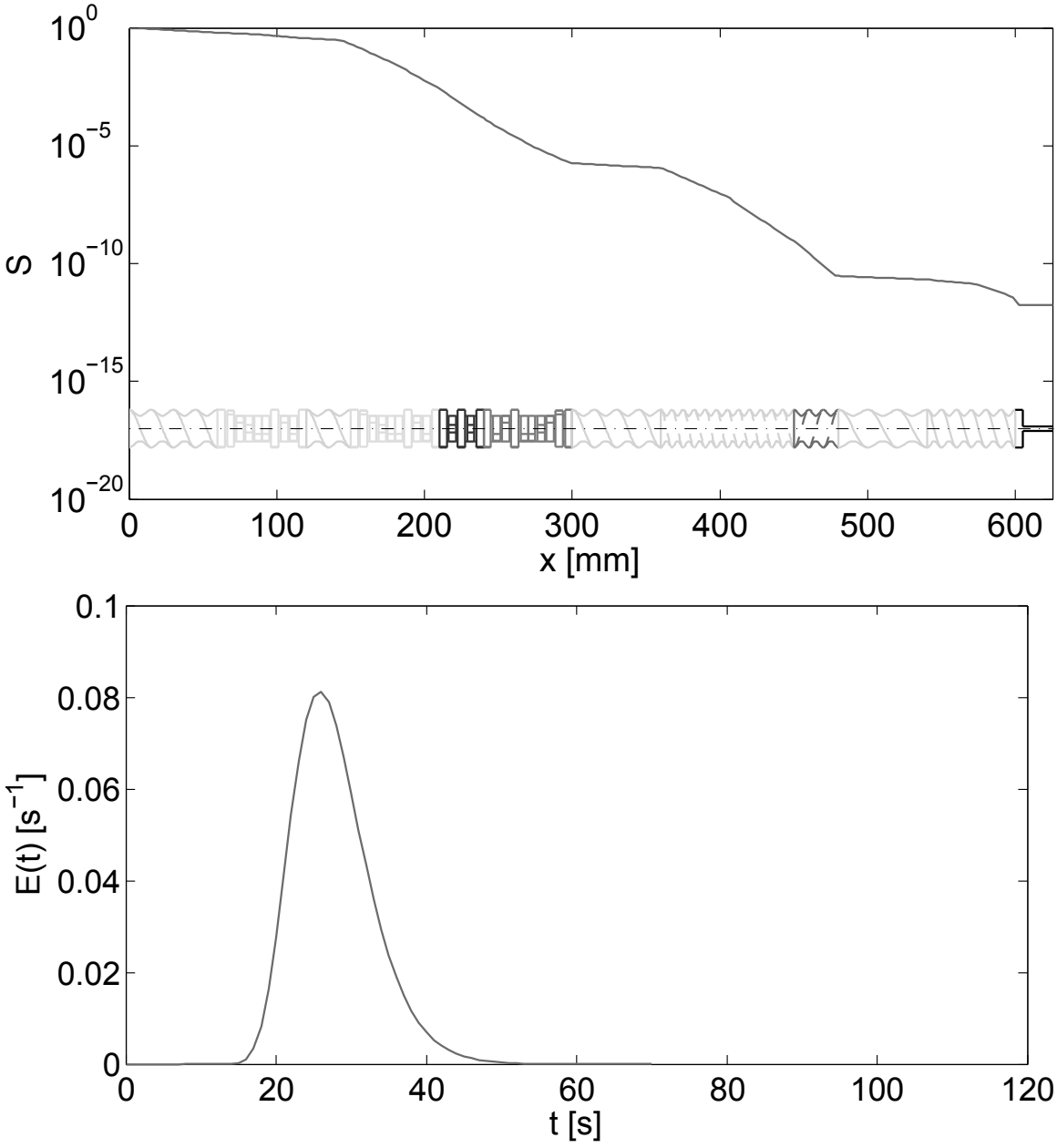

Figure F.4: Resulting axial profile of the intensity of segregation S (top) and residence time distribution (bottom) for case 2.

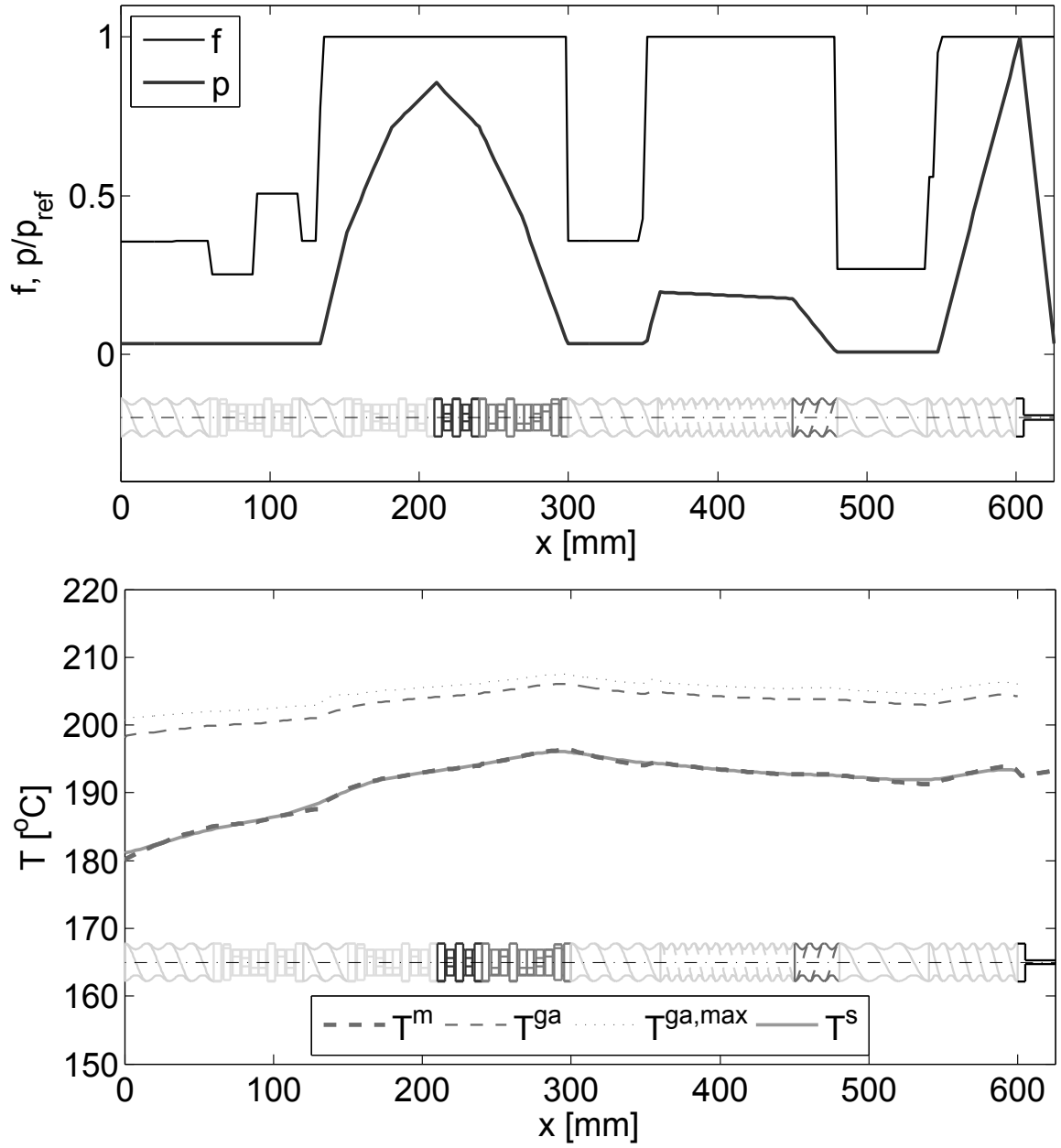

Figure F.5: Resulting axial profiles of filling ratio f, pressure p (relative to $p_{ref} = 3 \cdot 10^6$ Pa), average melt temperature in channels T^m, average melt temperature in gaps T^{ga} (Eq. 4.58), maximum melt temperature in gaps $T^{ga,max}$ (Eq. 4.60) and screw temperature T^s (the barrel temperature was $T^b = 150°C$) for case 3.

The Figures F.5 and F.6 show case 3 with the original screw speed of 150 rpm, but a feed flow rate of 20 kg/h. This changes the dimensionless flow rate to $\dot{V}/nD^3 = 0.102$. Consequently, also the profiles of filling ratio and pressure are different here, specifically, the length of the completely filled sections are increased. The reason is that the flow rate per screw revolution is now higher, i.e., the flow rate compared to the inherent conveying capacity of the screw elements is increased. However, the temperatures are in a similar

range than in the first case, since they depend mainly on the screw speed. The profile of S shows significantly less mixing here compared to the first case (although, the completely filled sections are longer here). The reduced mixing can be addressed to the higher flow rate, which causes a shorter residence time and thus, a lower number of screw revolutions during the average residence time. This and the previous cases show the importance of the dimensionless flow rate $\dot{V}/nD^3$. Similar process conditions are obtained when $\dot{V}/nD^3$ is constant.

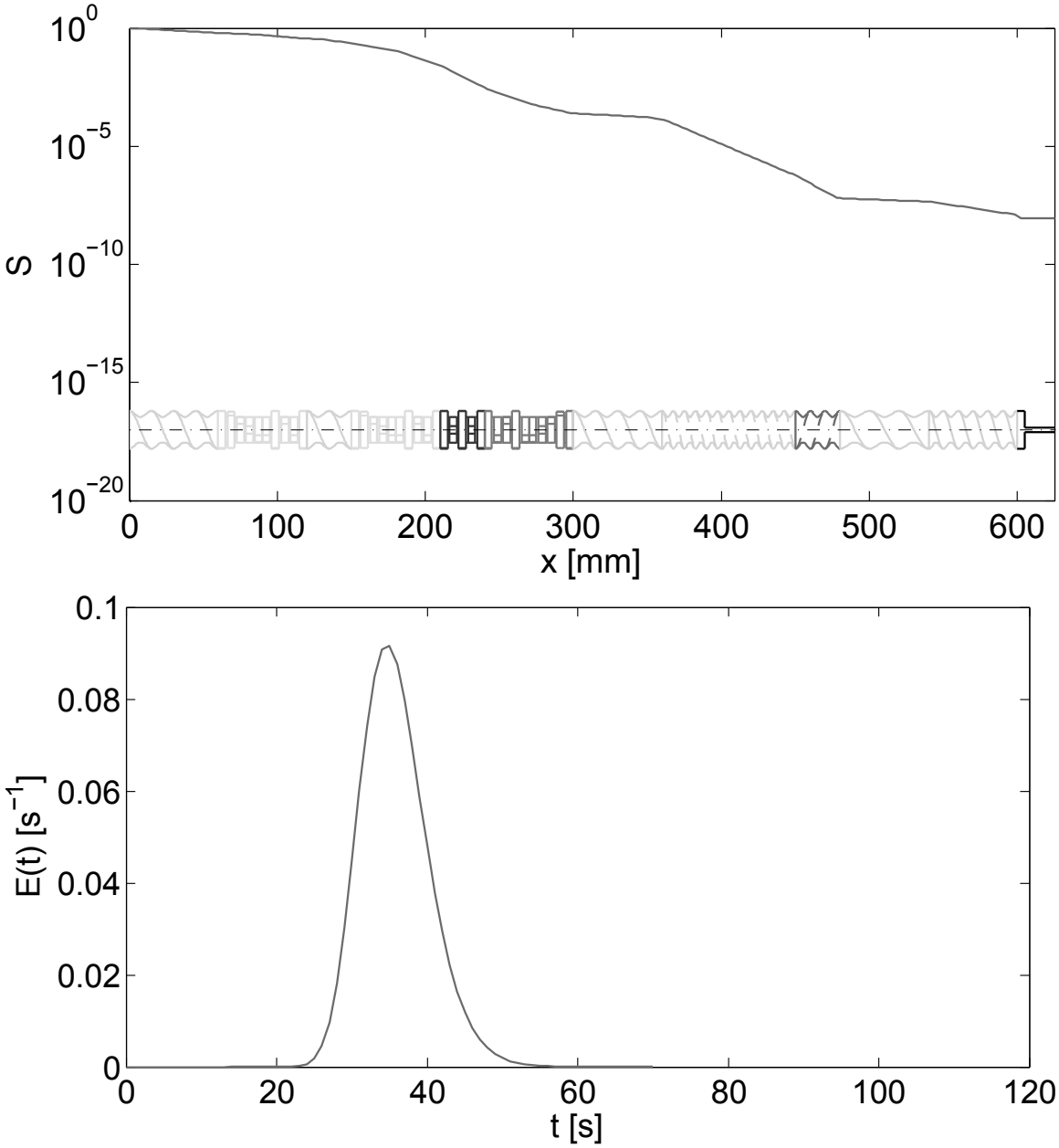

Figure F.6: Resulting axial profile of the intensity of segregation S (top) and residence time distribution (bottom) for case 3.

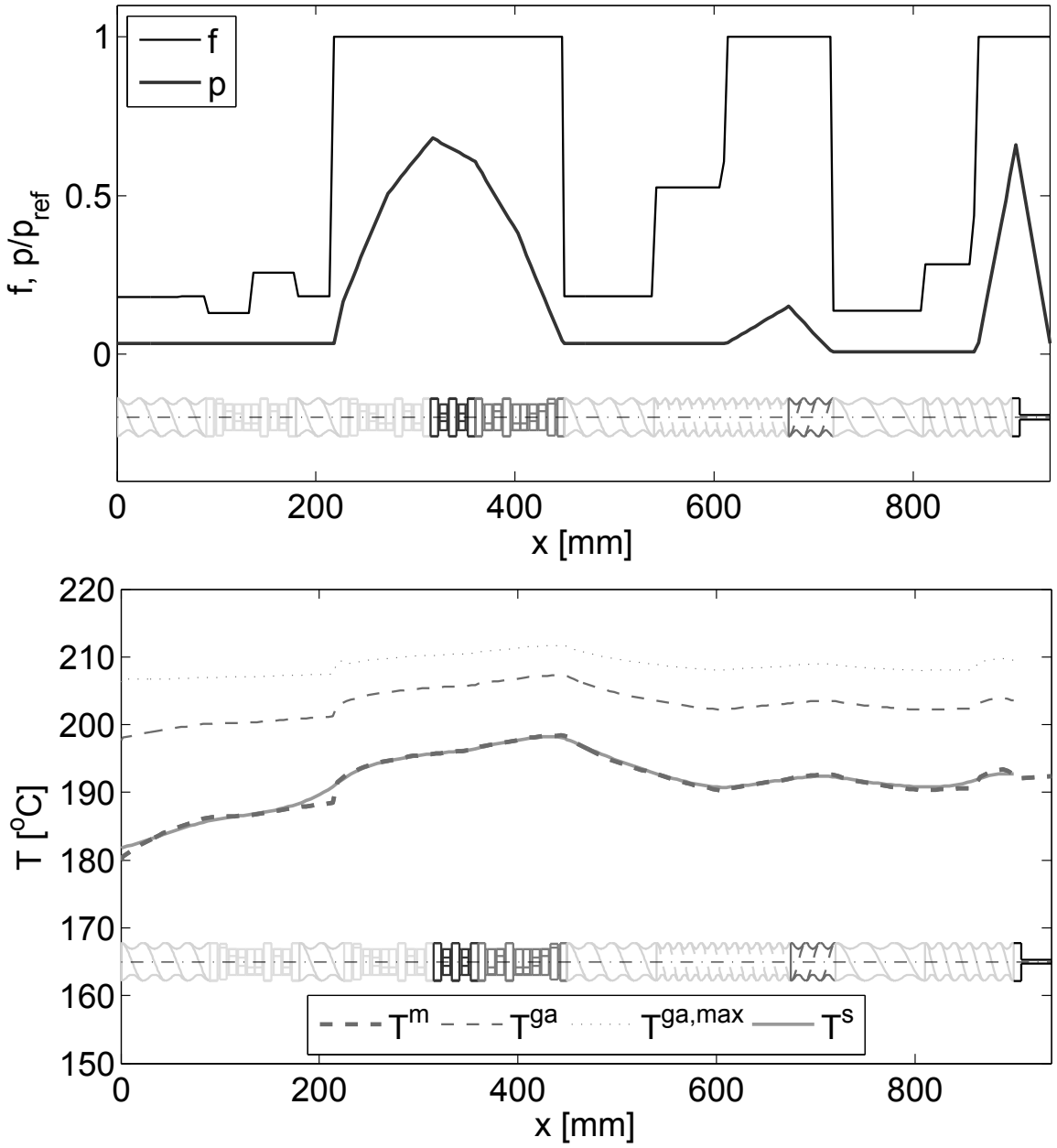

Figure F.7: Resulting axial profiles of filling ratio f, pressure p (relative to $p_{ref} = 3 \cdot 10^6$ Pa), average melt temperature in channels T^m, average melt temperature in gaps T^{ga} (Eq. 4.58), maximum melt temperature in gaps $T^{ga,max}$ (Eq. 4.60) and screw temperature T^s (the barrel temperature was $T^b = 150°C$) for case 4.

The case 4 (Figures F.7 and F.8) shows a scale-up of case 1 to a screw diameter of 40 mm. Geometrical similarity was presumed for all screw elements and the die, also for the gap distances, which were changed to 0.15 mm. The screw speed was 150 rpm, the feed flow rate scaled to 33 kg/h, based on a constant dimensionless flow rate $\dot{V}/nD^3$. Consequently, the resulting profiles of filling ratio and pressure are similar to the first case. Also the temperature profiles are similar, however, slightly increased temperatures resulted due to

the higher heat transfer surface relative to the volume. No significant differences were obtained for the axial profile of S and the residence time distribution compared to case 1. This shows that the constant dimensionless flow rate is an important scale-up criterion.

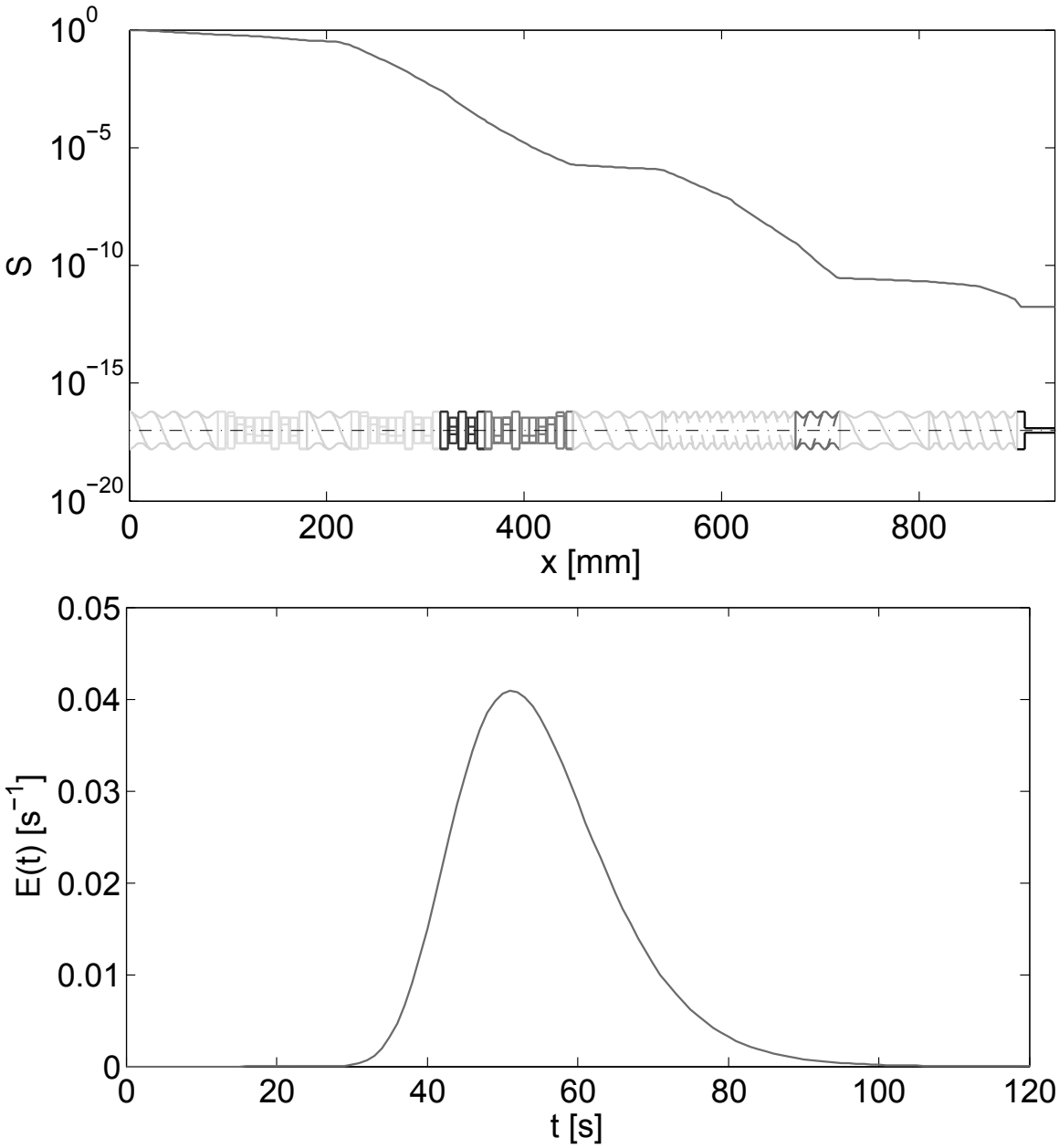

Figure F.8: Resulting axial profile of the intensity of segregation S (top) and residence time distribution (bottom) for case 4.

List of Publications

Journal Papers

Eitzlmayr, A.; Petschacher, C.; Radl, S.; Suzzi, D.; Zimmer, A.; Khinast, J. Modeling and Simulation of Polyacrylic Acid/protamine Nanoparticle Precipitation. *Soft Matter* **2011**, *7*, 9484–9497.

Teubl, B. J.; Meindl, C.; Eitzlmayr, A.; Zimmer, A.; Fröhlich, E.; Roblegg, E. In-Vitro Permeability of Neutral Polystyrene Particles via Buccal Mucosa. *Small* **2013**, *9*, 457–466.

Petschacher, C.; Eitzlmayr, A.; Besenhard, M.; Wagner, J.; Barthelmes, J.; Bernkop-Schnürch, A.; Khinast, J.; Zimmer, A. Thinking Continuously: A Microreactor for the Production and Scale-up of Biodegradable, Self-Assembled Nanoparticles. *Polym. Chem*. **2013**, *4*, 2342–2352.

Eitzlmayr, A.; Khinast, J.; Hörl, G.; Koscher, G.; Reynolds, G.; Huang, Z.; Booth, J.; Shering, P. Experimental Characterization and Modeling of Twin-Screw Extruder Elements for Pharmaceutical Hot Melt Extrusion. *AIChE J.* **2013**, *59*, 4440–4450.

Eitzlmayr, A.; Koscher, G.; Reynolds, G.; Huang, Z.; Booth, J.; Shering, P.; Khinast, J. Mechanistic Modeling of Modular Co-Rotating Twin-Screw Extruders. *Int. J. Pharm*. **2014**, *474*, 157–176.

Baumgartner, R.; Eitzlmayr, A.; Matsko, N.; Tetyczka, C.; Khinast, J.; Roblegg, E. Nano-Extrusion: A Promising Tool for Continuous Manufacturing of Solid Nano-Formulations. *Int. J. Pharm*. **2014**, *477*, 1–11.

Eitzlmayr, A.; Koscher, G.; Khinast, J. A Novel Method for Modeling of Complex Wall Geometries in Smoothed Particle Hydrodynamics. *Comput. Phys. Commun*. **2014**, *185*, 2436–2448.

Eitzlmayr, A.; Khinast, J. Co-Rotating Twin-Screw Extruders: Detailed Analysis of Conveying Elements Based on Smoothed Particle Hydrodynamics. Part 1: Hydrodynamics. Submitted to *Chem. Eng. Sci.*

Eitzlmayr, A.; Khinast, J. Co-Rotating Twin-Screw Extruders: Detailed Analysis of Conveying Elements Based on Smoothed Particle Hydrodynamics. Part 2: Mixing. Submitted to *Chem. Eng. Sci*.

Eitzlmayr, A.; Matić, J.; Khinast, J. Investigation of Flow and Mixing in Typical Screw Elements of Co-Rotating Twin-Screw Extruders via SPH. To be submitted.

Conference Talks

Suzzi, D.; Toschkoff, G.; Hörmann, T.; Radl, S.; Radeke, C.; Eitzlmayr, A.; Machold, D; Khinast, J. Multiphase Simulation in the Pharmaceutical Industry. *11th ERCOFTAC Alpe Danube Adria PC Meeting*, Graz, 30.4.2010.

Gruber, M.; Eitzlmayr, A.; Radl., S.; Suzzi, D.; Khinast, J. Modeling Fast Reactions and Particle Flow – Applications of OpenFOAM in the Pharmaceutical Industry. *5th OpenFOAM Workshop*, Chalmers University, Gothenburg, 21.6.2010.

Eitzlmayr, A.; Radl., S.; Suzzi, D.; Khinast, J. Numerical Simulation of Nanoparticle Precipitation. *ProcessNet-Jahrestagung 2010*, Aachen, 21.9.2010.

Eitzlmayr, A.; Suzzi, D.; Koscher, G.; Shering, P.; Reynolds, G.; Booth, J.; Khinast, J. Modeling of Pharmaceutical Hot Melt Extrusion. *5th International Congress on Pharmaceutical Engineering*, Graz, 29.9.2011.

Eitzlmayr, A.; Treffer, D.; Jedinger, N.; Koscher, G.; Roblegg, E.; Khinast, J. Hot Melt Extrusion: Product and Process Development. *6th Annual PSSRC Symposium*, Lisbon, 26.8.2012.

Eitzlmayr, A.; Treffer, D.; Hörl, G.; Windhab, S.; Koscher, G.; Khinast, J. Predictive Modeling of Hot Melt Extruders. *2012 AIChE Annual Meeting*, Pittsburgh, PA, 28.10.2012.

Treffer, D.; Eitzlmayr, A.; Smola, C.-M.; Koscher, G.; Roblegg, E.; Khinast, J. Continuous Pharmaceutical Hot-Melt Extrusion & Hot-Die Face Pelleziting. *2012 AIChE Annual Meeting*, Pittsburgh, PA, 28.10.2012.

Eitzlmayr, A.; Radl, S.; Koscher, G.; Khinast, J. Simulation of Mixing in Hot Melt Extruders Using Smoothed Particle Hydrodynamics. *2013 AIChE Annual Meeting, San Francisco*, CA, 3.11.2013.

Eitzlmayr, A.; Matić, J.; Koscher, G.; Khinast, J. Novel Developments for the Simulation of Hot Melt Extrusion. *Leistritz Pharma Workshop 2014*, Nuremberg, 11.6.2014.

Eitzlmayr, A.; Matić, J.; Koscher, G.; Khinast, J. A Novel Simulation Approach for Hot Melt Extrusion. *6th International Congress on Pharmaceutical Engineering*, Graz, 16.6.2014.

Eitzlmayr, A.; Kondor, I.; Matić, J.; Koscher, G.; Khinast, J. The Simulation of Mixing and Free Surface Flows in Co-Rotating Twin-Screw Extruders. *2014 AIChE Annual Meeting*, Atlanta, GA, 16.11.2014.